Chemical Characterisations of Exoplanetary Atmospheres

by

Arazi Pinhas

Submitted to the Institute of Astronomy
for the degree of

Doctor of Philosophy

at the

University of Cambridge, Hughes Hall

March 2019

Thesis Supervisor: Nikku Madhusudhan
Thesis Co-Supervisor: Catherine Clarke

Chemical Characterisations of Exoplanetary Atmospheres

by

Arazi Pinhas

Submitted to the Institute of Astronomy
on March 5, 2019 for the degree of Doctor of Philosophy

Summary

We examine the properties of exoplanetary atmospheres using state-of-the-art retrieval methods and theoretical models. The examinations include investigations of the chemical compositions and abundances, the cloud and haze properties, and the temperature structures of exoplanetary atmospheres.

The detailed theoretical models we have developed study the chemistry of exoplanetary atmospheres across the gas and solid phases of matter. The first theoretical model investigates the extent to which solids evaporate in the envelopes of giant planets and how they contribute to enriching the atmosphere with metallic elements. The results of this study illustrate that the observable chemistry in the atmospheres of giant planets may indeed be used as a tool for tracing their formation conditions and histories. The second model considers the observable signatures of clouds in the spectra of transiting planets. We explore three metrics that may provide constraints on cloud properties: the slope in the optical wavelength region, the uniformity of this slope, and features in the infrared.

We then present several state-of-the-art retrieval studies of the chemical and thermal properties of transiting and directly-imaged planetary atmospheres. First, we apply our transmission retrieval method to the spectra of ten hot giant exoplanets and, for the first time, provide detailed statistical estimates of atmospheric properties for a size-able exoplanet sample with broadband data. Our analysis reveals a trend of low abundances of water vapour in the hot Jupiter atmospheres compared to their stars and the Sun, suggesting that a majority of hot Jupiters in our galaxy may harbour atmospheres depleted in water vapour. Importantly, the low water and oxygen abundances suggest that the majority of hot Jupiters undergo disk-free migration to their present locations. Second, we introduce a novel retrieval framework, Aura, for the joint study of planetary and stellar properties imprinted in a transmission spectrum. This method is the first in the literature to provide combined constraints on stellar and planetary properties. Our study finds that the spectra of four hot Jupiters in the previous sample show potential evidence of stellar contamination due to heterogeneity features in the photospheres of their stars. Such a joint framework lays a first foundation to disentangling spectral features which originate in the atmospheres of exoplanets from those present in the stellar photospheres.

We also present a new retrieval method for directly-imaged exoplanets and brown dwarfs. The retrieval structure is applied to the most iconic imaged system, HR 8799, composed of four giant companions. We find the presence of water vapour at high confidence ($>5\sigma$) in all four atmospheres and strong evidence for carbon monoxide at high abundances in the atmospheres of the two outer companions. The O/H ratios in the companion atmospheres are enhanced by over $6\times$ the solar value, and the C/O ratios of HR 8799b and HR 8799c are distinctly super-solar.

We finally present two additional applications of our retrieval methods to atmospheric observations with collaborators outside of Cambridge. We interpret the day-side atmosphere of the highly irradiated hot Jupiter WASP-18b and find evidence of a strong thermal inversion due to carbon monoxide and an atmosphere with a super-solar metallicity and C/O ratio. Finally, we characterise the most complete transmission spectrum of the giant planet XO-1b spanning the optical to infrared and find an atmosphere composed of inhomogeneous clouds and a low water abundance compared to the solar expectation.

Thesis Supervisor: Nikku Madhusudhan
Title: Reader in Astrophysics and Exoplanetary Science

Thesis Co-Supervisor: Catherine Clarke
Title: Professor of Theoretical Astrophysics

Acknowledgements

I bless the Divine Hand, formless and incarnate, that has guided me from knowledge to Knowing, from philosophy to Philosia, from darkness to Light.

I owe the existence of this thesis to Nikku Madhusudhan. I am grateful for his clarity and vision that have served vital for this thesis as well as for the many scientific opportunities he has provided.

I am infinitely grateful to Vladush, an Incarnation of the Divine. She has been the fire that refined and purified me, and I am lucky to have grown in her flame. Only an individual of a higher plane can smelt a man to his golden center. Her childish innocence will continue to kindle rooms of my heart.

I am deeply grateful to Imma for her unconditional care in the past few years. Our friendship has grown greater in time. You have been unique in supporting me when I have found everyone to oppose the soundless truths of my inner light. This is the nature of a true mother and I am fortunate to have one of the few in the world.

The science in the thesis has benefited from many individuals. I am thankful to the many colleagues who have contributed in various ways including Siddharth Gandhi, Dániel Apai, Benjamin Rackham, Cathie Clarke, Luis Welbanks, Mark Wyatt, Chris Tout, Ivan Hubeny, and Ryan MacDonald. In addition, I am also deeply grateful to Scott for his support as well as Ya'arah, Vicki, and Steve. I acknowledge and pay my regards to many others not included in this list who have otherwise taught me much.

The IoA and Cambridge have been rare Edens for me and I am fortunate to have grown in these gardens. In my view, the whole structure of society and the intellectual environment are weights against such a flowering – and yet it happens through one's own pure and spirited devotion. I feel it is like the flower which grows out of a concrete pavement: everything is against its ascent and yet its total longing to meet the endless sky beyond provides the path. I especially thank a trinity – Imma, Vladush, and Madhu – who, in this dream of life, have served as water and light to help the blossoming of the inner seed and the photosynthesis of man.

Declaration

This dissertation is the result of my own work and includes nothing which is the outcome of work done in collaboration unless explicitly specified in the text. It is not being concurrently submitted for a degree or diploma or other qualification at the University of Cambridge or any other university or similar institution, and does not exceed the limit of 60,000 words.

Contents

List of Figures

List of Tables

Chapter 1

Introduction

1.1 A Crescendo of Exoplanets

The history of exoplanetary science is the story of the out-looking mind. Since the remotest of times the human mind has meditated on the possibility of planetary systems beyond our own. These imaginations were seeds which have come to a flowering only within the past three decades. At present, a few thousand exoplanets have been revealed and it is now thought that every star in the night sky is host to at least one planet (Cassan et al., 2012). The album of these discovered exoplanets embodies the variety of Nature. The properties of exoplanets span the extremes of temperature, mass, size, composition, and orbital configurations such that our imagination of what may be is never far away from what is. Figure 1.1 shows a glimpse of this planetary variety revealed by the *Kepler Space Telescope* between 2009 and 2013.

The discovery of planets in the solar system was accomplished mainly by Babylonian astronomers through careful, direct observations (Sachs, 1974). Exoplanets similar to the planets in our solar system are a billion times fainter compared to their stars and would have small projected separations from their stars due to their great distances (see Figure 3-6 in Dalcanton et al., 2015). These challenges make it difficult to obtain similar direct observations of exoplanets, especially since the diffraction limits of even the largest of ground telescopes in the spectral range where planets emit light are similar to the projected angles of such planets in the sky, and

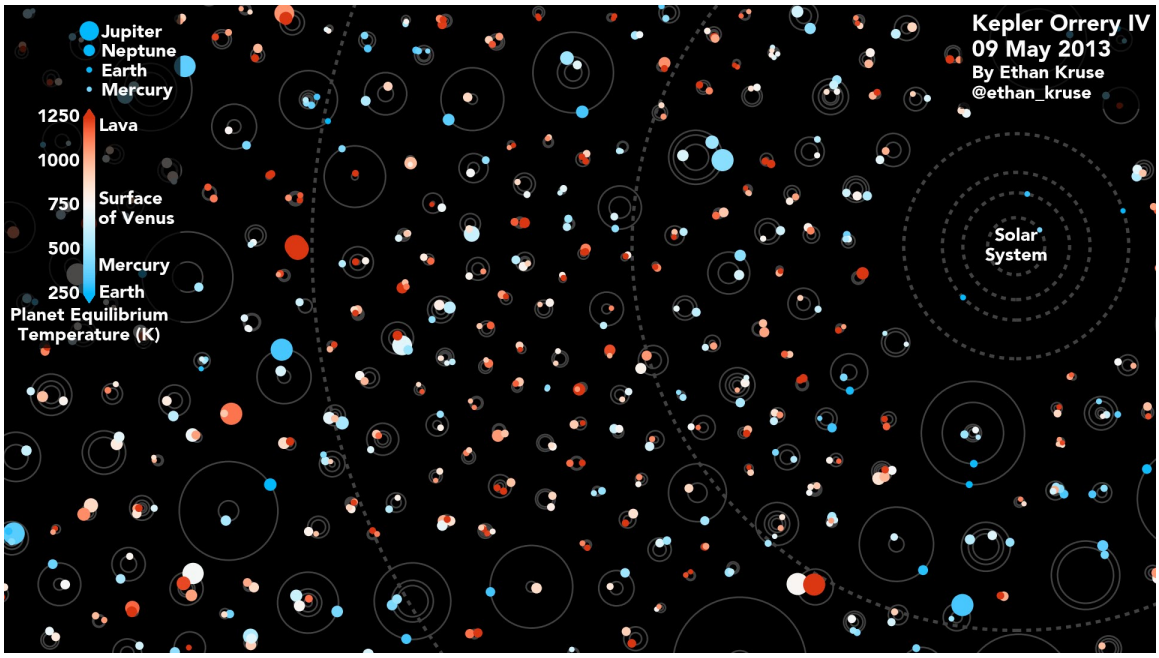

Figure 1.1: The variety of exoplanets discovered by the *Kepler Space Telescope* between 2009 and 2013. The planets span the domains of temperature, radius, and orbital periods. A large number of planets are Earth-sized.

Earth's atmosphere also provides blurring (Dalcanton et al., 2015). In light of these challenges, the crescendo in exoplanet discoveries – particularly in the past decade – is surely owed to clever technological developments.

Detection technologies based on the dynamical perturbation of the star by an orbiting planet bore the first discovery of an exoplanetary system in 1992. In particular, precision timing of pulsar light achieved the first convincing detection of at least two terrestrial-mass exoplanets around a pulsar (Wolszczan and Frail, 1992) and illustrated, from the start, that planets could exist in environments thought to be impossible. Radial velocity measurements, whereby an orbiting planet induces a periodic Doppler shift in the light received from a star, presented the first tentative suggestions (subsequently confirmed) of sub-stellar mass companions to stars of varied evolutionary stages (Campbell et al., 1988; Latham et al., 1989; Hatzes and Cochran, 1993).

However, the first conclusive detection of an exoplanet orbiting a main-sequence star was reported by Mayor and Queloz (1995). The discovered planet, 51 Pegasi b,

is the size of Jupiter and circles its parent star every 4.23 Earth days. This discovery became a precedent for similar future detections of close-in Jovian-size planets, and together with the pulsar discovery (Wolszczan and Frail, 1992), facilitated a break from a state of mind in which exoplanets should show similarity with solar system planets. It also provoked a transformation of thought about planetary formation and evolution, in the sense that planetary evolution is dynamic and may involve substantial inward migration (Goldreich and Tremaine, 1980; Rasio and Ford, 1996). In the period since, radial velocity measurements have identified an increasing population of exoplanets with periods spanning from 1 day to 10,000 days, and has been the most successful discovery technique between 1995 and 2009.

Transiting exoplanets have since exceeded radial velocity detections in abundance. A transiting planet is one whose orbit lies orthogonal to the plane of the sky such that it eclipses its star as viewed from Earth. The planet is discovered through dips in the stellar brightness during its transit in front of the star. The first discovered transiting exoplanet, HD 209458b, was identified independently by two research groups: Henry et al. (1999, 2000) and Charbonneau et al. (2000). Since then the population of known transiting exoplanets has burgeoned, due in large part to NASA's *Kepler Space Telescope (Kepler)* that was launched in 2009. In 2014 and 2016 alone, the mission verified 715 and 1,284 new exoplanets, respectively – the latter constituting the single largest finding of planets to date. Today, there are 3,026 bona fide exoplanet transits and about 2,000 candidates that are awaiting further observations.

The most familiar exoplanet discovery method is direct imaging. In contrast to the transit and radial velocity detection techniques (and which are indirect methods), direct imaging qualifies best at discovering sub-stellar mass objects far from the star at tens of astronomical units (AUs) and characterising their atmospheres through spectroscopy and photometry. At the moment, imaged objects are unresolved point sources but the holy grail of this method in the far future is spatially-resolved images of their facing hemispheres. Remarkable examples of imaged systems include a quadruple of companions around HR 8799 (Marois et al., 2008, 2010), Fomalhaut b (Kalas et al., 2008), β Pictoris b (Lagrange et al., 2009), and Gliese 229b (Nakajima

et al., 1995). Of these the HR 8799 system is of special note. Observations with the *Keck* and *Gemini* telescopes revealed four objects with projected separations of 15, 24, 38, and 68 AU around the star HR 8799 (Marois et al., 2008, 2010), and a series of images in time since 2008 confirm their orbital motion around HR 8799. Today, there are about 44 confirmed imaged sub-stellar companions sporting semi-major axes between 2 and 2,500 AU (Exoplanetarchive.ipac.caltech.edu, 2019).

Now, 27 years after the first exoplanet discovery, the archived planetary systems from the above methods reflect the infinite diversity and personality of Nature. Exoplanets have been found to orbit a wide range of stellar types from main-sequence stars (e.g., 51 Pegasi b, Mayor and Queloz, 1995) to post-main sequence phases such as giant stars, pulsars and white dwarfs (e.g., Wolszczan and Kuchner, 2010; Vanderburg et al., 2015). Many exoplanets are hot gas giants (known as 'hot Jupiters', e.g., 51 Pegasi b) residing ten times closer to their stars than Mercury is to our Sun (0.39 AU) such that their orbital periods are only a few Earth days. Others are cold and located more than 3,000 times away than 0.39 AU (Exoplanetarchive.ipac.caltech.edu, 2019). Some planetary orbits are inclined with respect to the star's equatorial plane, while others rotate or orbit oppositely to their stars. Their potential bulk compositions are also broad: water worlds, diamond spheres, lava worlds, and rocky planets stripped of their atmospheres are some of the examples.[1]

Of the thousands of confirmed exoplanets, there are more than 600 multiple planetary systems having between two and eight planets. Systems with multiple planets are actively being discovered as transit and radial velocity surveys increase their temporal baselines and improve their sensitivities. The first discovery of multiple planets around a main-sequence star was υ Andromedae, composed of one hot Jupiter and two more massive planets on periods exceeding 240 days (Butler et al., 1999). A long-term radial velocity trend was used to infer an additional planet with a period of 10.5 years (Curiel et al., 2011). Other systems comprise more planets. The five-

[1]Water worlds are exo-terrestrial planets containing a substantial amount of liquid water either at their surfaces or subsurfaces, lava planets have surfaces mostly or entirely covered by molten magma, and diamond planets are composed of a considerable amount of carbon, much of which may be in the form of diamond as a result of the high temperatures and pressures in planetary interiors.

planet system of 55 Cancri (Fischer et al., 2008) has an Earth-sized lava world, 55 Cancri e (Demory et al., 2016), and HD 10180 hosts seven planets (with potentially two more) of which five have masses similar to Neptune (Lovis et al., 2011). Perhaps the most iconic system, TRAPPIST-1 contains seven Earth-sized planets in compact orbits of which three reside in the canonical 'habitable zone' where liquid water can exist (Gillon et al., 2017). After the solar system, Kepler-90 is the only known planetary system to date with eight planets (Cabrera et al., 2014; Shallue and Vanderburg, 2018). The six inner planets range from super-Earths to mini-Neptunes while the two outer planets are gas giants. The furthest planet orbits the star at the same distance as Earth from the Sun.

1.2 From Discovery to Characterisation

Beyond the veritable richness in planetary types and architectures, a more detailed study of exoplanets requires observations of their atmospheres. Observations of exoplanetary atmospheres using spectrographs and photometers provide a treasury of information and allow for their detailed characterisations. Major properties which influence an atmospheric spectrum are the chemical compositions and abundances, the temperature structure, and the presence of aerosols (i.e., clouds and hazes) in the atmosphere. Importantly, spectra of the same planet provide different information depending on the planet's alignment geometry at the time of observation.

The atmospheric structure and properties of a transiting planet are accessible when it eclipses or transits its star, as well as during secondary eclipse just before it is eclipsed by its star. When the planet eclipses its star, stellar light filters through the atmosphere at the planet's limb. At wavelengths where particles in the atmosphere absorb or scatter light efficiently, the transmitted radiation decreases and the planet appears larger. The true potency of the transit method lies in its power to identify and quantify the amount of molecular and atomic gases in the observable atmosphere (i.e., at optical depths below one; $\tau(\lambda) < 1$) from their unique absorption features which are engraved in the transmission spectrum. The population of

known transiting planets orbit close to their stars and are expected to be in tidal locking similar to the Moon-Earth system, and they are therefore expected to display permanent day and night hemispheres. The general transmission spectrum therefore provides information on molecular and atomic gases as well as clouds and hazes (i.e., liquids/solids) along the day-night transition region of the planetary atmosphere. In addition, the transiting geometry can be used to measure the planet's inclination relative to the stellar rotation axis (i.e., the Rossiter-McLaughlin effect, Triaud (2017)), while variations in the timing of transits can suggest additional planets or satellites in the system through the method of TTVs (Agol and Fabrycky, 2017).

On the other hand, when the planet is nearly occulted by its star during secondary eclipse, the inherent thermal radiation from the planet can be observed. The thermal spectrum of the planet is obtained by subtracting the combined stellar and planetary day-side flux before occultation to the stellar flux during occultation, and is particularly suitable in characterising the temperature structure of the day-side atmosphere (Madhusudhan, 2018). This quality is especially important since thermal spectra, unlike during primary eclipse, can manifest emission and absorption features corresponding to atmospheric temperature increases and decreases with height, respectively.

Spectra of directly-imaged exoplanets and brown dwarfs allow similar characterisations as secondary eclipse observations. Since imaging facilities are currently sensitive to objects at a few tens of AU from the star, the observed light is also thermal emission from the object and probes the infrared region, but temperature inversions are not expected unlike for secondary eclipse due to the negligible irradiation from their host stars. However, the relative faintness of even the most massive objects to their host stars as well as the interference and scattering of stellar light (known as 'speckle' noise) along the path to a telescope's detector can hamper the discovery and characterisation of objects at tens of AU. Fortunately, growing instrumental capabilities and an intelligent selection of targets makes imaging and characterisation possible. First, adaptive optics (AO) systems on large-aperture ground telescopes such as the *Very Large Telescope (VLT)*, *Keck*, and *Gemini* help correct for the effects of scat-

tered light in Earth's atmosphere and enhance signal-to-noise ratios. Second, novel coronograph designs have been achieved to suppress light from the star (Lyot, 1939; Guyon et al., 2006). Third, various post-processing methods have emerged to diminish 'speckle' noise due to scattered and interfering starlight within the optical path of a telescope resulting from surface errors on telescope mirrors and instrument optics (Marois et al., 2006; Traub and Oppenheimer, 2010). Finally, these advancements are helped by a focus on young stellar systems since young companion objects are at their brightest and cool over time (e.g., Burrows et al., 1997).

The chemical composition imprinted in the spectrum of an atmosphere is also a reflection of a planet's past, representing a chronicle of the formation and evolutionary processes experienced throughout its history. Deciphering the formation pathways from the observable chemistry in a spectrum represents a challenging aspiration since the composition of a planet as observed today depends on the compositions of the gas and solids gathered in the natal protoplanetary disc and which evolve in time and orbital distance (Öberg et al., 2011; Eistrup et al., 2018). Nevertheless, various studies have explored the effects of formation pathways on the observable compositions of giant exoplanets (e.g., Madhusudhan et al., 2014a; Helling et al., 2014; Turrini et al., 2015; Cridland et al., 2016; Mordasini et al., 2016; Booth et al., 2017; Madhusudhan et al., 2017).

High carbon-to-oxygen ratios ($\sim$1) and sub-stellar O and C abundances in hot Jupiter atmospheres can potentially signify a migration mechanism that does not involve significant solid accretion (i.e., disk-free migration; Madhusudhan et al. (2014a)) or involve a formation by pebble-sized solids without significant erosion of the core and with or without migration through the disk (Madhusudhan et al., 2017). On the other hand, planets which form through core-accretion and migrate through the disk result in oxygen-rich compositions in the observable atmospheres, leading to sub-stellar C/O ratios (Cridland et al., 2016; Mordasini et al., 2016). Beyond investigations of the atmospheric carbon and oxygen abundances, new studies are suggesting the potency of using the nitrogen abundance to constrain a planet's formation history (Piso et al., 2016; Booth and Clarke, 2018). Thus the atmosphere is a planet's

diary, and its revelation can lead to potential insights into a planet's formation and migration scenarios.

A number of facilities have allowed formative strides in illuminating the atmospheres of exoplanets. The *Hubble Space Telescope (HST)* has lead the characterisation of planets in primary and secondary eclipse geometries since the early 2000s. Observations have been made with various spectroscopic modes of the *Space Telescope Imaging Spectrograph (STIS)* between 0.3 and 1 μm (e.g., Sing et al., 2013; Nikolov et al., 2014; Sing et al., 2016; Fischer et al., 2016), the *Wide Field Camera 3 (WFC3)* between 0.8 and 1.7 μm (e.g., Deming et al., 2013; McCullough et al., 2014; de Wit et al., 2016; Wakeford et al., 2017; de Wit et al., 2018), and the *Advanced Camera for Surveys (ACS)* between 0.35 and 1.1 μm (e.g., Pont et al., 2008). NASA's *Spitzer Space Telescope (Spitzer)* has also performed numerous measurements of the atmospheres of transiting planets using the *Infrared Array Camera (IRAC)* photometric bandpasses centered at 3.6, 4.5, 5.8, and 8 μm (e.g., Deming et al., 2007; Knutson et al., 2007; Machalek et al., 2008; Knutson et al., 2010; Demory et al., 2016; Sing et al., 2016; Wong et al., 2016; Sheppard et al., 2017). Since the exhaustion of its cryogen in 2009, *Spitzer* has assumed its 'warm mission' phase with only the 3.6 and 4.5 wavelength channels remaining fully functional.

On the other hand, the direct detection of planets and brown dwarfs requires high spatial resolution and high contrast between the planet and the star and has thus relied on large-aperture ground facilities. The *Spectro-Polarimetric High-contrast Exoplanet Research* (*SPHERE*) project at the *VLT* and the *Gemini Planet Imager (GPI)* at *Gemini South* were built especially for high-contrast exoplanet detection and characterisation. An essential feature of these facilities is the technique of integral field spectroscopy (IFS), whereby a spectrum is acquired for each pixel in a two-dimensional field of view which enables the spectrum of an imaged object to be extracted. Other popular direct-imaging facilities with adaptive optics include *Keck-AO* (van Dam et al., 2006), *LBT-ARGOS* (Hill et al., 2010), and *Subaru-AO188-CIAO* (Watanabe et al., 2004).

The detail of exoplanetary studies will soar with future telescope facilities. The

James Webb Space Telescope (JWST) will enable high-precision spectroscopy of transiting and imaged planets (e.g., Clampin, 2009; Seager et al., 2009; Barstow et al., 2015; Greene et al., 2016; Mollière et al., 2017). Its four basic instruments – *NIRSpec*, *NIRISS*, *NIRCam*, and *MIRI* – can span 0.6 to 29 μm with resolving powers (R) of 100 to 2,700, and can therefore yield vital information on gaseous absorption features as well as cloud and haze properties for transiting planets. While the *JWST* was not designed for high-contrast direct imaging, *NIRCam* and *MIRI* have coronographs with their own wavelength filters that will provide important baseline measurements. The next generation of extremely large ground observatories – the *European Extremely Large Telescope (E-ELT)* (eso.org/sci/facilities/eelt), the *Giant Magellan Telescope (GMT)* (Johns, 2008), and the *Thirty Metre Telescope (TMT)* (Crampton et al., 2009) – will have instruments which will be capable of performing spectroscopy of Earth-sized planets in the habitable zones of cool stars. For example, the *IRIS* IFS on the *TMT* (Wright et al., 2014) will cover $0.8 - 2.5$ μm and could provide high-precision flux measurements for all four companions in the HR 8799 system at resolving powers between 4,000 and 8,000 (Currie, 2016).

Faced with a transmission or thermal emission spectrum from the numerous instruments above, a model of the atmosphere is required to interpret the information concealed therein. A variety of atmospheric modeling methods have been developed for this purpose and advances in modeling approaches are progressing on many planes. We attempt to condense these modeling efforts in the following section.

1.3 Models of Exoplanetary Atmospheres

The first theoretical models of exoplanetary atmospheres developed in parallel with the earliest radial velocity detections at the turn of the century (Burrows et al., 1997; Marley et al., 1999; Burrows and Sharp, 1999; Goukenleuque et al., 2000; Sudarsky et al., 2000; Seager and Sasselov, 2000; Brown, 2001; Hubbard et al., 2001; Barman et al., 2001). The first model of transmission spectra was by Seager and Sasselov (2000) and emphasised the prospects of observing sodium and potassium absorption

features in the optical wavelength range in addition to helium, water, and methane features in the near-infrared. Sophistication in transmission spectra grew soon after with Brown (2001) and Hubbard et al. (2001), which showed that high-altitude clouds can decrease the amplitude of absorption features in the infrared.

Various theoretical developments have since been explored for transiting planets in primary and secondary configurations. These models generally assume chemical equilibrium with solar elemental abundances, where chemical equilibrium is the state in which molecules and atoms in an atmosphere are present in steady concentrations such that they do not change with time. The assumption of chemical equilibrium serves as a manageable first representation of atmospheres since the abundances of molecular and atomic gases can be calculated in a relatively simple way for given temperatures, pressures and elemental abundances through minimization of the Gibbs free energy of the system (e.g., Sharp and Huebner, 1990; Burrows and Sharp, 1999; Lodders and Fegley, 2002; Madhusudhan, 2012; Mollière et al., 2015; Blecic et al., 2016; Heng and Tsai, 2016). Chemical equilibrium represents a starting point to atmospheric studies since it is valid only in the hottest, densest regions (at high atmospheric depths) or for most of an atmosphere for very hot, strongly-irradiated planets (e.g., super-hot Jupiters); in cooler and less dense regions of an atmosphere, the chemistry can be shifted significantly out of equilibrium since the chemical reactions become slower than other processes (e.g., turbulence and photochemistry).

The majority of theoretical developments are termed 'self-consistent' models, so named because consistency is ensured among the temperature, chemistry, and radiation field of the atmosphere. These models apply a constraint of radiative-convective equilibrium (i.e., total energy conservation) and allow the determination of a temperature profile consistent with the incident irradiation and the chemical compositions. Popular 'self-consistent' models for the primary eclipse geometry include those of Fortney et al. (2010), Mollière et al. (2017), and Goyal et al. (2018), while major thermal emission models for secondary eclipse include those of Seager et al. (2005), Burrows et al. (2008), and Gandhi and Madhusudhan (2017).

The differences among the various models lie in the complexity of their numer-

ical methods and incorporated assumptions. In particular, major differences lie in the approaches for solving the radiative transfer equation and for ensuring radiative-convective equilibrium, the gas opacities (i.e., line-by-line or correlated-k), and the consideration of physical processes such as clouds and convection. For example, Burrows et al. (2008) uses a very accurate method to determine the temperature structure for radiative-convective equilibrium, a line-by-line treatment of opacities, and Mie theory for spherical and chemically-homogeneous cloud particles; on the other hand, Mollière et al. (2017) uses a less accurate but faster method to determine the temperature structure for radiative-convective equilibrium, a correlated-k treatment of opacities, and distribution of hollow spheres (DHS) theory for irregularly-shaped condensate aggregates. A review of available self-consistent models is presented in Heng and Marley (2017) and Gandhi and Madhusudhan (2017). The majority of such theoretical models assume a one-dimensional atmosphere composed of an ideal gas. The typical self-consistent model has three primary governing equations: the equation of hydrostatic equilibrium, the equation of radiative transfer, and the equation of energy conservation.

Models typically start with an estimate for the temperature profile throughout the atmosphere. The assumption of chemical equilibrium transforms the temperature structure into chemical compositions and abundances assuming fiducial elemental compositions and abundances, with the latter abundances usually assumed to be those of the solar photosphere (Asplund et al., 2009) in the case of gas giant exoplanets. The opacity in each layer of the atmosphere is then calculated for a limited number of chemicals across all wavelengths. The radiative transfer equation is then solved to determine the energy flux through each layer. The above scheme is iterated until each layer satisfies energy conservation such that the energy flowing into a layer of the atmosphere matches the energy flowing out. A satisfied system of equations provides the final observed spectrum and temperature structure of the atmosphere.

The assumption of chemical equilibrium in these self-consistent models is a convenient first attempt to understanding exoplanetary atmospheres. At high pressures, such as in the deep layers of hot Jupiters' day-sides, chemical equilibrium is reason-

able since the high densities make it easy to overcome energy barriers in both the forward and reverse directions of a chemical reaction. However, for cooler and less dense regions of an atmosphere, incident light from the star dissociates molecules and turbulence mixes atmospheric fluid; chemical equilibrium can therefore be disturbed and the chemical compositions and abundances can change significantly. The majority of transiting planets may therefore be expected to host disequilibrium chemistry in their upper atmospheres due to stellar-induced photolysis and tranport-induced quenching (e.g., Moses et al., 2011; Miguel and Kaltenegger, 2014). The atmospheric chemistry present in the atmospheres of transiting planets is then a contest between the timescales of photochemistry and atmospheric dynamics and those associated with the reactions of chemicals.

Departures from chemical equilibrium in models were first examined through coupled thermochemical and photochemical/transport models, and were used to assess how disequilibrium chemistry affects the composition and observable spectral properties of exoplanetary atmospheres (Moses et al., 2011; Moses, 2014). Important results include a significant effect of photochemistry on molecules with weak bonds, such as methane and ammonia. Moreover, turbulent mixing tends to significantly enhance the abundances of hydrogen cyanide, methane, ammonia, and carbon monoxide over their equilibrium values, and molecules are photochemically destroyed or converted to other species at high atmospheric altitudes (see Figure 3 of Moses, 2014). Therefore disequilibrium chemistry due to photolysis leads to an enhancement of atomic oxygen, carbon, and nitrogen at pressures below $\sim$1 μbar.

The majority of self-consistent models considered above are one-dimensional and as such cannot explicitly account for variations in temperature, chemistry, and dynamics across the longitude and latitude of a planet. A three-dimensional treatment, though more challenging, facilitates more realism, especially for close-in hot giant exoplanets which receive high stellar irradiation and have permanent day and night sides. A large number of studies have investigated three-dimensional models of hot Jupiters' atmospheric circulation, called General Circulation Models or GCMs (e.g., Dobbs-Dixon and Lin, 2008; Showman et al., 2009; Mayne et al., 2014; Lee et al.,

2016; Lines et al., 2018). A common emergent feature of these studies is the presence of hot equatorial winds with large velocities of $1 - 4$ km/s directed towards the planet's night-side.

Although the components of 'self-consistent' models are internally consonant, they still suffer a number of limitations when faced with observations. First, as discussed above, models are commonly generated under the assumption of thermochemical equilibrium. However, the atmospheres of transiting planets are expected to host departures from chemical equilibrium due to photolysis and gas dynamics. Importantly, the diversity of exoplanetary properties as exhibited in Section 1.1 means that there should also be significant departures from solar elemental abundances as commonly assumed in such consistent models. Second, 'self-consistent' models are also time consuming in that relatively few models can be calculated for different assumptions of elemental abundances. The limited number of models that can necessarily be evaluated also limits a thorough exploration of a high-dimensional model parameter space. Although measures of fit to observations can be gleaned using the chi-square statistic, the statistic will not necessarily be reliable given a typically coarse grid over model parameters and a largely unexplored parameter space (e.g., departures from solar abundances and solar C/O ratios, day-night heat re-distributions, and disequilibrium abundances).

A parallel approach to interpreting observations of exoplanetary atmospheres is called a retrieval method, the first of which was developed by Madhusudhan and Seager (2009). While the retrieval method of Madhusudhan and Seager (2009) is an independent development, retrieval techniques have previously been developed and used widely in the remote sensing of solar system planets (e.g., Houghton et al., 1984; Hanel et al., 1992; Rodgers, 2000; Irwin et al., 2008). The retrieval approach seeks to retrieve the composition and temperature structure of the atmosphere using observations as a shepherd or direct guide, rather than estimating these using chemical assumptions and energy balance as in the case of 'self-consistent' models. The retrieval method couples a parametric model of the atmosphere with an algorithm capable of sampling the free parameters of the model and provides statistical estimates of all

model parameter values and their mutual correlations. The parametrisation of the temperature profile and chemical abundances significantly shortens the evaluation time of a model since the former are evaluated iteratively in self-consistent models to reach a converged solution and are therefore computationally expensive. Hence a retrieval approach permits the calculation of millions of models in the effort to interpret a spectrum. The parameterised forward model also naturally eliminates the assumption of chemical equilibrium such that the chemistry and temperature imprinted in a spectrum can be revealed without an a priori prejudice.

There exist a number of retrieval frameworks that differ mainly in the way the model parameter space is sampled. The initial retrieval method of Madhusudhan and Seager (2009) can retrieve both primary and secondary eclipse spectra and operates by searching over a grid of models covering a large parameter space. The Markov Chain Monte Carlo method to parameter estimation was introduced into retrievals with Madhusudhan and Seager (2011) and has since been adopted by other groups (Blecic, 2016; Wakeford et al., 2017). Lee et al. (2012) and Barstow et al. (2017) use an Optimal Estimation technique and Line et al. (2013) feature several additional sampling methods (Bootstrap Monte Carlo and Differential Evolution Monte Carlo). More recently, a new method called nested sampling (Skilling, 2004) has been incorporated into retrieval techniques and is one of the most powerful sampling algorithms to date. This is because in addition to parameter estimation – as is possible with the other algorithms above – nested sampling allows a quantitative way of comparing models with different inherent assumptions. Given our general ignorance about the content of an observed spectrum, nested sampling is a useful way to calibrate ignorance in a scientific way. The nested sampling algorithm is being used for retrievals in the primary eclipse (Benneke and Seager, 2013; Waldmann et al., 2015b; MacDonald and Madhusudhan, 2017a), secondary eclipse (Waldmann et al., 2015a; Oreshenko et al., 2017; Gandhi and Madhusudhan, 2018), and direct imaging (Lavie et al., 2017) geometries.

The above modeling approaches have been used to infer the chemistry and thermal structure of various exoplanetary observations. We present a brief panorama of these

characterisations in the next section.

1.4 Observations of Exoplanetary Atmospheres

Transiting exoplanets have been a veritable diamond mine, providing a wealth of information on atmospheric chemistry and structure. Spectroscopy and photometry during primary eclipse probes the limb of the planet and the long path length light has to traverse means primary eclipse is more sensitive to absorption features from chemicals than in the case of secondary eclipse.

The first characterisation of the atmosphere of a transiting planet was for HD 209458b and used *HST STIS* measurements to reveal absorption in the sodium doublet at 0.589 μm (Charbonneau et al., 2002). More recent observations spanning the optical and near-infrared show a definitive presence of water vapour, albeit at a low quantity (Barman, 2007; Deming et al., 2013; Madhusudhan et al., 2014b; Barstow et al., 2017). Along with HD 209458b, HD 189733b is one of the most observed hot Jupiters and its observations throughout the years were combined in Pont et al. (2013). The full spectrum has been used to suggest hazes due to the steep slope of observations in the optical as well as the clear presence of water vapour with an abundance similar to that of HD 209458b (Madhusudhan et al., 2014b; Barstow et al., 2017).

Signatures of water vapour have also been found in HAT-P-1b (Wakeford et al., 2013), WASP-12b (Kreidberg et al., 2015), WASP-19b (Huitson et al., 2013), WASP-43b (Kreidberg et al., 2014c), and XO-1b (Deming et al., 2013) as well as in over a dozen other hot Jupiters. The prominence of water in the atmospheres of many discovered planets is remarkable albeit not unexpected, and is due to its unique absorption band at 1.4 μm where *HST WFC3* is sensitive as well as its predicted ubiquity in exoplanetary atmospheres across many temperatures (Madhusudhan, 2012) and equilibrium/disequilibrium conditions (Moses, 2014).

Inferences of other chemicals in transiting planets are comparatively moderate. There are tentative indications of nitrogen-based chemistry such as ammonia and

hydrogen cyanide in the atmospheres of WASP-31b, WASP-63b, and HD 209458b (MacDonald and Madhusudhan, 2017b). *HST WFC3* observations of a hot Neptune (Knutson et al., 2014a) and a super-Earth (Kreidberg et al., 2014a) have revealed flat transmission spectra which imply the presence of either clouds or a large abundance of heavy metals. In terms of atoms, *HST STIS* observations indicate strong sodium absorption in HD 189733b, HAT-P-1b, and WASP-96b (Huitson et al., 2012; Nikolov et al., 2014, 2018) and ground-based observations reveal similar line strengths in the atmospheres of WASP-17b and XO-2b (Wood et al., 2011; Sing et al., 2012). Potassium absorption at 778.8 nm has been identified in over half a dozen atmospheres (e.g., Nikolov et al., 2015). Heavier atoms and ions have also been inferred as in the case of the most studied planet, HD 209458b, where O I, C II, and Si III are present in its fleeting exosphere (Vidal-Madjar et al., 2004; Linsky et al., 2010).

The first measurement of the thermal emission of a planet in secondary eclipse was made for HD 209458b using the *Spitzer Multiband Imaging Photometer (MIPS)* at 24 μm (Deming et al., 2005). A substantial number of hot Jupiters have since had their thermal emission measured with *Spitzer IRAC* photometric channels and *HST WFC3*. The majority of molecular detections are of water vapour. Reported water in the daysides of hot Jupiters include WASP-43b (Kreidberg et al., 2014c), WASP-33b (Haynes et al., 2015), and Tres-3b (Line et al., 2014), among others.

In addition to the atmospheric composition, thermal emission spectra during secondary eclipse are sensitive to the temperature structure of the atmosphere, especially the potential of temperature inversions (i.e., an increasing temperature with increasing atmospheric height). During the development of the earliest self-consistent models it was hypothesised that metallic oxides such as TiO and VO can induce temperature inversions in hot atmospheres (Hubeny et al., 2003; Fortney et al., 2008). Clear inferences of thermal inversions have since been made for three extremely irradiated hot Jupiters with temperatures around 3,000 K: WASP-33b (Haynes et al., 2015), WASP-121b (Evans et al., 2017), and WASP-18b (Sheppard et al., 2017). While the presence of TiO or VO is evident in WASP-33b and WASP-121b, their signatures are lacking in WASP-18b which instead has a large concentration of carbon monoxide

gas.

Secondary eclipse observations and full phase curves have also enabled inferences about atmospheric dynamics. The first full phase curve of a planet was obtained for HD 189733b using the *Spitzer IRAC* 8 μm bandpass (Knutson et al., 2007). The measurement indicated the presence of a highly energetic wind that is offset from the point on the planet directly facing the star (called the 'sub-stellar' point) and which redistributes heat from the day to night side. The spatial variation in thermal emission across the dayside hemisphere of a planet can also be mapped through the ingress and egress portions of a secondary eclipse measurement as a planet is eclipsed by its star (Williams et al., 2006). Results for HD 189733b show an equatorial hot spot which is shifted from the sub-stellar point (Majeau et al., 2012; de Wit et al., 2012), consistent with the inference from the full phase curve of Knutson et al. (2007). More recently, Demory et al. (2016) reported the first thermal map of a super-Earth, 55 Cancri e, and found a hot spot significantly shifted from the sub-stellar point and a day-night temperature contrast of $\sim$1,300 K.

On the other hand, the characterisation of imaged exoplanets and brown dwarfs is still in an early phase but a few inferences have nevertheless been made. The most iconic imaged system, HR 8799, consists of four companion objects whose atmospheres show evidence for water vapour (Lavie et al., 2017). The two outermost companions, HR 8799b and HR 8799c, also show signatures of carbon monoxide vapour from absorption features at 2.3 and 4.5 μm (Konopacky et al., 2013; Lavie et al., 2017). The prominence of carbon monoxide and lack of methane is potentially indicative of active non-equilibrium processes in the atmospheres since methane is expected to be the dominant carrier of carbon at their low atmospheric temperatures assuming chemical equilibrium (Madhusudhan, 2012; Heng and Tsai, 2016). Water vapour has also been estimated for the giant planet κ Andromedae b (Todorov et al., 2016) and the presence of H_2O, CO, CH_4, and NH_3 have been demonstrated in brown dwarfs (e.g., Oppenheimer et al., 1995; Geballe et al., 1996; Janson et al., 2011, 2013; Line et al., 2015; Madhusudhan et al., 2016b; Line et al., 2017; Burningham et al., 2017). Recent work is also using the brightness variations from rotating brown dwarfs to

map the global cloud structures in their atmospheres (Lew et al., 2016; Apai et al., 2017b; Manjavacas et al., 2018).

1.5 Areas of Needed Study

The developments in observation and theory discussed above are a testament to the maturation of exoplanetary science and its promising future. Still, there are many areas that remain unexplored or undeveloped which are in need of attention. Here we briefly introduce the areas which serve as motivations for the work contained in this thesis.

1.5.1 Project I: Solid Enrichment of Giant Planetary Envelopes

One of the aspirations in the study of atmospheric chemistry is its potential to shed light on the formation and migration conditions of a planet. The chemistry of an atmosphere, particularly its elemental abundances in the form of oxygen and carbon, have been considered to interpret possible formation locations (Öberg et al., 2011) as well as formation and migration mechanisms of planets (Madhusudhan et al., 2014a, 2017; Booth et al., 2017). For example, a low oxygen abundance in a hot Jupiter atmosphere can suggest inward migration to its current location through gravitational interactions with other massive objects in the system (see Figure 3 of Madhusudhan et al., 2014a), although oxygen contained in clouds may represent $\sim$0.15 of the total oxygen abundance (see Figure 9 of Helling et al., 2016) and thereby slightly change the narrative. Given that protoplanetary disks are composed of both gases and solids, the inferred chemistry from observations of atmospheres probe the accreted gas, but potentially also accreted solids by the planet during its formation.

It is therefore important to understand to what extent accreted solids evaporate and contribute to the chemistry of the atmosphere. We have thus been motivated to study the following question: to what extent does the atmosphere of a planet reflect

the solids which it accreted during the later stages of its formation? The study of this question is presented in Chapter 2 and is based on Pinhas et al. (2016). The results suggest that the atmosphere of a gas giant planet should reflect the accreted solids throughout most of its life.

1.5.2 Project II: Clouds in Exoplanetary Transmission Spectra

Equal in importance to the study of evaporated solids in atmospheres is the condensation of the gas to liquids or solids, known as clouds and hazes. Clouds and hazes present the most challenging aspects in interpreting observations of exoplanetary atmospheres. The inference of clouds/hazes in exoplanets derives from their ubiquity in solar system planets as well as from particular spectral features present in atmospheric observations. The increasing precisions and resolving powers of future observations (e.g., with the *JWST*) means that small differences in cloud and haze properties will be more expressed in the observations. We have thus been motivated to study the detailed spectral characteristics of clouds and hazes. In particular, we explore three observable metrics that can be used to constrain the properties of clouds: the slope in the optical wavelength region, the uniformity of this slope, and features in the infrared. This study is contained in Chapter 3 and is based on Pinhas and Madhusudhan (2017).

1.5.3 Project III: H_2O Abundances and Cloud Properties in Ten Hot Giant Exoplanets

Another challenge is the accurate inference of molecular gas abundances in transmission spectra. For example, an observed water vapour feature of small amplitude can be due either to an inherently low abundance of the gas (Madhusudhan et al., 2014b; Barstow et al., 2017) or a significant presence of clouds (Deming et al., 2013; Sing et al., 2016). In light of this degeneracy, we carry out a detailed retrieval analysis of the water vapour abundances in ten hot giant exoplanets with broadband transit

observations. This research is presented in Chapter 5 and is published in Pinhas et al. (2019). An outline of the retrieval method used in this study is presented in Chapter 4. We retrieve the water abundances by using an inhomogeneous cloud and haze model along with observations in the optical, which provide a long spectral range and act to reduce degeneracies. Importantly, our study finds a pattern of low water abundances for the majority of the hot Jupiters and indicates the importance of disk-free migration for hot Jupiters.

1.5.4 Project IV: Retrieving the Stellar and Planetary Influence on a Transmission Spectrum

An assumption that enters Project III is that the disk of the star is homogeneous and can be represented by one spectrum and radius. In reality stellar photospheres are not homogeneous. Active regions of the stellar surface, in the form of cool spots or hot faculae, make the stellar photosphere heterogeneous. Such features on active stars can induce modifications to a transmission spectrum that would otherwise be due to features originating from the planetary atmosphere alone. For example, the slope of a transmission spectrum in the visible wavelength region is usually interpreted as hazes or clouds composed of small particles, and yet the slope in the optical can also be caused by cool star spots which are unocculted by a transiting planet.

It is therefore crucial to be able to disentangle stellar and planetary features from a spectrum. We have developed a new retrieval method, Aura, for inferring both planetary and stellar properties from a transmission spectrum. This development is presented in Chapter 6 and is published in Pinhas et al. (2018). We apply our retrieval framework to nine of the gas giants in Project III to determine the significance of stellar heterogeneity and hazes/clouds in their spectra. We find evidence – albeit not strong – of stellar contamination in the spectra of four of the hot Jupiters.

1.5.5 Project V: Retrieving the Spectra of the Directly-Imaged HR 8799 Companions

The advent of direct imaging has ushered in a new era of atmospheric characterisation of giant exoplanets and brown dwarf companions at large orbital separations from their stars. Inferences of properties of imaged companions have usually relied on evolutionary models together with 'self-consistent' atmospheric models. The atmospheric models are typically limited by the assumptions of chemical equilibrium with solar abundances and the ability to calculate only a few models. The evolutionary models also have to assume an age for the system to derive the mass of a companion. We have aimed to move beyond these and other limitations.

We discuss a new retrieval paradigm for interpreting the thermal emission spectra of directly-imaged companions. This work is contained in Chapter 7. We apply our retrieval framework to the most iconic imaged system, HR 8799, and characterise the atmospheres of the four companions around the star. We find clear signatures ($>5\sigma$) of water vapour and super-solar oxygen metallicities in all four companion atmospheres.

1.5.6 Projects VI & VII: Retrieving the Spectra of the Transiting Planets WASP-18b and XO-1b

The set of retrieval methods presented in Chapters 4−7 have also been applied to several observations as part of collaborations with colleagues outside the IoA. Chapter 8 discusses our contribution and the results from these two projects which are officially published in Sheppard et al. (2017) and Southworth et al. (2018). A fellow PhD student and I interpreted the secondary eclipse spectrum of the highly irradiated hot Jupiter WASP-18b and found evidence of a strong thermal inversion, a high abundance of carbon monoxide gas, and an atmosphere with a super-solar metallicity and C/O ratio. I also characterised the transmission spectrum of the giant planet XO-1b spanning the optical to infrared and found its atmosphere is best explained by

inhomogeneous clouds and a low water abundance compared to the solar expectation.

Chapter 2

Solid Enrichment of Giant Planetary Envelopes

2.1 Atmospheric Chemistry as a Diary

One of the new frontiers in exoplanetary science is the consideration of an exoplanetary atmosphere as a diary which can give insights into the formation and migration history of a planet. In particular, the abundances of elements such as oxygen and carbon in the atmospheres of giant planets are being pursued as a way to constrain the conditions and processes of planetary formation and migration (Öberg et al., 2011; Madhusudhan et al., 2014a; Mordasini et al., 2016; Madhusudhan et al., 2017; Booth et al., 2017).

The fundamental assumption in the effort to constrain the formation history of a planet from observed atmospheric abundances is that the observed elemental abundances represent the sum-total of elemental abundances in the gas and solids accreted throughout the planet's history, provided there's minimal processing of the atmosphere (e.g., photo-induced erosion). This assumption is critically important as the metallicity of an atmosphere (e.g., O/H or C/H ratios) is directly related to the amount of accreted solids dissolved in the atmosphere. For example, super-stellar metallicities are strong indicators of substantial planetesimal accretion (Podolak et al., 1988; Pollack et al., 1996; Wong et al., 2004). On the other hand, when sub-stellar

metallicities are observed it is unclear if they are due to a lack of substantial planetesimal accretion or if the accreted planetesimals have not ablated significantly in the atmosphere, assuming minimal atmospheric processing. Therefore, a primary question to be answered currently is to what extent do accreted planetesimals ablate in the gaseous envelopes of giant planets as opposed to sinking to the core partially or fully with limited contribution to the envelopes. The present chapter is focused on addressing this question.

In particular, our work focuses on planetesimal accretion into the envelopes of a Jovian-like planet.[1] We investigate how planetesimals ablate and thus chemically enrich Jovian-like exoplanetary envelopes and their overlying atmospheres by following the evolution of impactors with different compositions and initial conditions. The compositions, sizes, and velocities of accreted planetesimals will have differential effects on the composition of planetary envelopes throughout the process of formation and evolution. The ablated chemistry from the impacting planetesimals will subsequently experience mixing through convection, transporting material to the observable atmosphere.

We present our planetesimal ablation model as follows. We first discuss the planetary structure of a Jovian-analogue planet in Section 2.2, which is then used as a background to study how planetesimals ablate and evolve in Sections 2.3 and 2.4. We discuss and consider two forms of ablation: frictional ablation and thermal ablation. We present a sample of results in Section 2.5, with a focus on iron bolides. We then present potential improvements of our model and review the essential outcomes of our study in Sections 2.6 and 2.7. This work is published in Pinhas et al. (2016).

2.2 Planetary Structure

The study of the ablation and dynamics of impacting planetesimals first requires a model for the planetary structure. Here we detail our fiducial model for the planetary structure which is assumed to be similar to that of Jupiter.

[1] We use the terms 'planetesimal', 'bolide', and 'impactor' as synonyms throughout our work.

2.2.1 Internal Structure Model

The interior structure of gas giant planets broadly divides into three layers. Our fiducial planet consists of a solid core surrounded by two adiabatic fluid layers. We call the two fluid layers the 'outer envelope' and 'inner envelope' and these are assumed to be homogeneously mixed with differential compositions of hydrogen and helium. The composition of the core is not modeled and we treat its surface as a boundary where our structure equations and planetesimal evolution stop. The internal structure model does not include heavier metals due to their trace quantities, but nevertheless captures the dominant physics from hydrogen and helium. The outer and inner envelopes are used as backgrounds for the evolution of planetesimals.

The equations of state of hydrogen and helium effective in the two envelopes are created through a patchwork of experiments and theoretical simulations for hydrogen and helium and span large domains in density, pressure, and temperature applicable to gas giant planets and brown dwarfs (Becker et al., 2014). The equations of state represent extensive simulations using density functional theory molecular dynamics (DFT-MD) in the regimes of high density and pressure, where experiments are limited and quantum phenomena occur such as pressure dissociation of molecular hydrogen and ionizations of hydrogen and helium. These DFT-MD calculations are combined with simulations of fluid variational theory (FVT) in the transition region between the ideal gas limit and the quantum limit of DFT-MD. The resulting equations of state generally ensure a consistency in thermodynamics to better than 1 percent (Becker et al., 2014).

2.2.2 Planetary Construction

Here we construct the structure of a giant planet with the three fiducial layers described above. We solve three coupled equations for the structure of the planet assuming spherical symmetry:

$$\frac{dm}{dp} = -\frac{4\pi r^4}{Gm}, \tag{2.1}$$

$$\frac{dr}{dp} = -\frac{1}{g\rho}, \tag{2.2}$$

$$\frac{dT}{dp} = \frac{T}{\rho^2}\left(\frac{\partial p}{\partial u}\right)_\rho \left(\frac{\partial \rho}{\partial p}\right)_u \text{(Becker et al., 2013, equation (2))}, \tag{2.3}$$

where the slope of the temperature with respect to the pressure is assumed at constant entropy and u is the internal energy per unit mass of the fluid. The total density is calculated through the additive volume rule which is given by

$$\frac{1}{\rho} = \frac{X}{\rho_{\rm H}} + \frac{Y}{\rho_{\rm He}}, \tag{2.4}$$

where X and Y are the mass of hydrogen and helium in a unit volume defined as $X = m_{\rm H}/(m_{\rm H} + m_{\rm He})$ and $Y = m_{\rm He}/(m_{\rm H} + m_{\rm He})$. We solve these equations using a fourth-order Runge-Kutta approach (see section 17.1 of Press et al., 1992).

The numerical integration of these equations requires specifying explicit boundary conditions and mass fractions for hydrogen and helium. We set the temperature at the top of the planet to $T = 170$ K at a pressure of 1 bar from *Galileo* probe data (Seiff et al., 1998). The mass abundances of hydrogen and helium in the outer and inner envelopes are taken as $X_\uparrow = 0.762$, $Y_\uparrow = 0.238$, $X_\downarrow = 0.709$, and $Y_\downarrow = 0.291$ (Nettelmann et al., 2012)[2], where the transition pressure between the outer and inner envelopes is assumed to be $p_{\uparrow-\downarrow} = 4$ Mbar (see the J11-4a model of Nettelmann et al., 2012). The location of layer boundaries and the mass fractions in the layers match observational constraints within the errors (Nettelmann et al., 2012). The radius at the upper boundary of the outer envelope is $R_{\rm J} = 69911$ km and we stop integration of the equations at the core boundary at a pressure of $p = 41.687$ Mbar.

The internal structure of the planet is shown in Figure 2.1. The temperature and density are illustrated as functions of altitude and pressure throughout the planet. The temperature profile extends from 170 K at the upper boundary to about 20,000

[2]The value of $Y_\uparrow$ is obtained from *Galileo* probe data (von Zahn and Hunten, 1996) and the value of $Y_\downarrow$ is obtained from matching the observed gravitational moments J_2, J_4, and J_6 (see Section 2.3 of Nettelmann et al., 2012).

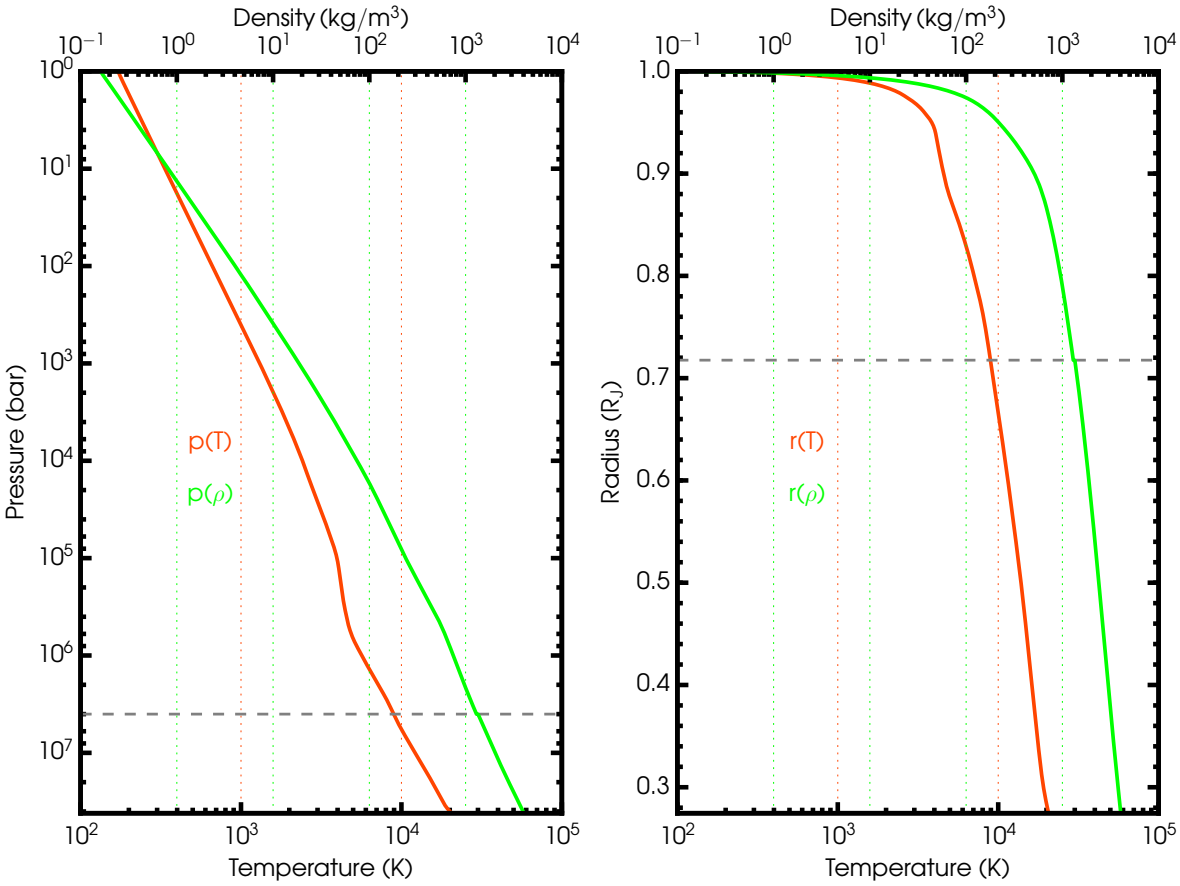

Figure 2.1: Internal structure of the planet. Left panel: Pressure as a function of temperature and density in the planet based on the hydrogen and helium equations of state of Becker et al. (2014). The dashed horizontal grey line at 4 Mbar shows the demarcation between the outer and inner envelopes and defines the transition of hydrogen from an insulator (i.e., mostly in H_2) to a metallic liquid. The pressure ranges from 1 bar to 41.687 Mbar at the core boundary. Right panel: Altitude in the planet as a function of temperature and density. The dashed horizontal grey line at a radius of 0.72 shows the demarcation between the outer and inner envelopes similar to the one in the left panel. The relation between pressure and altitude is therefore significantly non-linear.

K at the core boundary of $p = 41.687$ Mbar at an altitude of 0.275 $R_{\rm J}$. The density spans over nearly four orders of magnitude from $10^{-1}\,{\rm kg\,m^{-3}}$ to $\sim 4 \times 10^{3}\,{\rm kg\,m^{-3}}$. The ideal gas limit extends from $10^{-1}\,{\rm kg\,m^{-3}}$ to $\sim 10^{2}\,{\rm kg\,m^{-3}}$, beyond which non-ideal effects such as pressure dissociation and ionization begin to gain influence. The insulator-metallic transition above which most of the hydrogen is in molecular form and below which metallic liquid hydrogen becomes physically favorable occurs at 4 Mbar and is shown by the horizontal gray dashed lines in both panels.

2.3 Planetesimal Dynamics

The established planetary structure can now be used to model the dynamical evolution of impacting planetesimals. Impacting bolides are accelerated by the gravity of the planet and decelerated by aerodynamic drag which drives them toward terminal velocity. The radial equation of motion in the polar-coordinate plane is thus

$$M_{pl}|\vec{a}_{\rm radial}| = |\vec{\mathcal{F}}_{\rm gravity}| + |\vec{\mathcal{F}}_{\rm drag}|, \tag{2.5}$$

$$M_{pl}(\ddot{r} - r\dot{\theta}^2) = -\frac{GmM_{pl}}{r^2} + \frac{1}{2}C_D\rho|\dot{\vec{r}}|_r^2 S, \tag{2.6}$$

where the total acceleration vector in the polar-coordinate plane is $\vec{a} = (\ddot{r} - r\dot{\theta}^2)\hat{e}_{\rm r} + (2\dot{r}\dot{\theta} + r\ddot{\theta})\hat{e}_\theta$ (MIT Dynamics Lecture, 2018). This equation assumes a reference frame fixed at the centre of the planet. Here M_{pl} is the planetesimal mass; C_D is the drag coefficient; ρ is the envelope density surrounding the planetesimal; S is the cross-sectional area of the planetesimal; and $|\dot{\vec{r}}|_r$ is the radial portion of the planetesimal velocity. The total velocity is $\dot{\vec{r}} = \dot{\vec{r}}_{\rm radial} + \dot{\vec{r}}_{\rm circumferential} = \dot{r}\hat{e}_{\rm r} + r\dot{\theta}\hat{e}_\theta$.

The size of planetesimals is larger than the typical mean free path of the envelope particles and thus the particles form a hydrodynamic cushion underneath the impacting bolide. In this limit, the total drag force on the impactor is due to Stokes drag (Podolak et al., 1988), $|\vec{\mathcal{F}}_{\rm Stokes}| = \frac{1}{2}C_D\rho(\dot{r}^2 + r^2\dot{\theta}^2)S$, where the ram pressure exerted on the planetesimal is $\rho|\dot{\vec{r}}|^2$. The radial component of this drag force is represented in equation (2.5). The drag coefficient C_D, which acts as a multiplicative prefactor,

is a function of the bolide velocity and the fluid viscosity (i.e., the 'Reynolds number'). For Reynolds numbers above 10^3, the drag coefficient is nearly a constant at 1.0 (see Figure 2 of Seiff and Kirk, 1982; Podolak et al., 1988). Given that the typical Reynolds numbers in our problem are $\sim 10^6$, we assume a $C_D = 1$, consistent with typical estimates (Mac Low and Zahnle (1994), Field and Ferrara (1995), Chyba et al. (1990) assume 1.0, 1.2, and 0.92, respectively).

The influx of planetesimals into the planet could generally span all initial trajectories relative to a local zenith. Therefore the entry angle of a planetesimal is a free variable in our model. The geometry of our planetesimal-planet system is shown in Figure 2.2. The local zenith in Figure 2.2 is assumed to be the North Jovian Pole (NJP) but our framework is valid for any local zenith. Drag forces always act anti-parallel to the instantaneous velocity vector of the planetesimal. Regardless of initial impactor angle, we assume all impactors begin from a local zenith in the $r - \theta$ plane with projected velocities $v_{r,i} = |\dot{\vec{r}}_i| \cos\phi_i$ and $v_{\theta,i} = |\dot{\vec{r}}_i| \sin\phi_i$. The cross-section for the aerodynamic force of a spherical bolide is always perpendicular to the drag vector and is $S(t) = \pi R_{pl}^2(t)$.

This fiducial geometry allows us to generate our first two dynamical evolution equations for the radial and angular components of motion, providing the first two important evolution relations for planetesimals,

$$\ddot{r} = r\dot{\theta}^2 - \frac{Gm}{r^2} + \frac{C_D \rho (\dot{r}^2 + r^2\dot{\theta}^2) \cos\phi S}{2M_{pl}}, \tag{2.7}$$

$$\ddot{\theta} = -\frac{2\dot{r}\dot{\theta}}{r} - \frac{C_D \rho (\dot{r}^2 + r^2\dot{\theta}^2) \sin\phi S}{2rM_{pl}}. \tag{2.8}$$

The magnitudes of the drag force in the radial and circumferential directions are determined by the angle ϕ carved between $-\hat{\vec{r}}$ and $\vec{v}$ with $\phi = |\arctan(r\dot{\theta}/\dot{r})|$.

2.4 Planetesimal Ablation

Material ablates or evaporates from the surfaces of planetesimals as they move through the envelopes. Here we consider two ablation processes. Firstly, strong pressures from

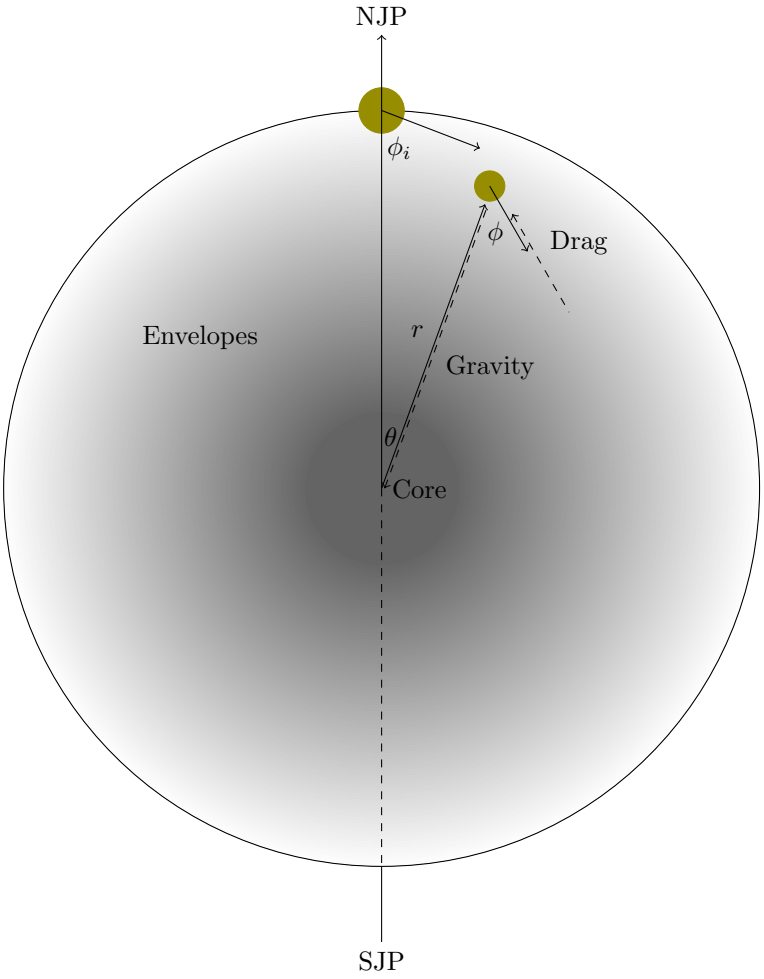

Figure 2.2: Geometry of the planet-planetesimal system. The two envelope layers determine the dynamical evolution and ablation of impactors. Planetesimals enter the upper envelope with an angle ϕ_i relative to the local zenith (in this case the North Jovian Pole) and are accelerated toward the core of the planet by gravity and decelerated by aerodynamic drag. The instantaneous angle between the total velocity vector of the planetesimal and the radial velocity vector is ϕ and is $\phi = |\arctan(r\dot{\theta}/\dot{r})|$. The instantaneous position of impactors relative to the local zenith of impact is represented by θ.

gas flows below a planetesimal remove material from the surface when they exceed the material strength of a bolide. We term this mechanism 'frictional ablation'. Secondly, the temperature of the surrounding envelope melts surface material and contributes to 'thermal ablation' of a planetesimal. We consider these ablation mechanisms for planetesimals with radii ranging from 30 metres to 1 km. We note that planetesimal-planetesimal collisions could potentially occur outside the planetary atmosphere, but our range over initial impactor radii essentially marginalises over modelling the details of this process.

There are certainly more physical mechanisms that may ablate planetesimals or increase the efficiency with which material is evaporated, such as the fragmentation and lateral spread of impactors. Nevertheless, these additional mechanisms would act to place the complete ablation of a planetesimal higher in the structured envelopes than considered here. Our approach therefore places lower limits on wholesale ablation altitudes which more sophisticated models should only lie above.

2.4.1 Frictional Ablation

Our study into the evolution of planetesimals is mainly concerned with the extent of vaporisation and dissociation in the envelopes. Following Opik (1958), the kinetic energy of a fluid through which a planetesimal sweeps in a unit time is $S\rho|\dot{\vec{r}}|^3/2$. Of this value, a fraction C_H is utilised in ablating and atomizing the planetesimal and therefore the total rate of mass ablation, and our third evolution equation, is

$$\frac{dM_{pl}}{dt} = -\frac{C_H \rho |\dot{\vec{r}}|^3 S}{2Q_{abl}}. \tag{2.9}$$

Here C_H is the heat transfer coefficient and quantises the fraction of kinetic energy used towards ablation from the cushion of fluid particles below the bolide. The parameter Q_{abl} is the specific energy that is necessary to break the chemical bonds of a kilogram of planetesimal material. This represents the sum of latent heats of fusion and vaporisation and the intermediate energy used in heating the bolides and is generally a well-known quantity. On the other hand, determination of C_H is a

substantial challenge since it generally depends on the composition, mass, and velocity of an impactor. An upper limit to C_H is given by $C_H = C_D/2$ (Podolak et al., 1988), but C_H can also be considerably smaller than this upper limit (e.g., see Table 2 of Svetsov et al., 1995). For our baseline model, however, we use an intermediate value of $C_H = 0.01$. The kinetic energy transferred to the bolide causes heating and ablation of surface material and we therefore call this kind of evaporation 'frictional ablation'.

The decrease in the mass of a planetesimal through equation (2.9) implies a decreasing cross-section S as the planetesimal shrinks. We focus on spherical impactors and calculate the rate of radial change assuming homogeneous ablation from the bolide surface. The radial rate of change, our fourth evolution equation, is derived by differentiating the bolide mass $M_{pl} = \frac{4}{3}\pi R_{pl}^3 \rho$ with respect to time,

$$\frac{dR_{pl}}{dt} = \frac{R_{pl}}{3M_{pl}} \frac{dM_{pl}}{dt}, \tag{2.10}$$

which, when using equation (2.9), becomes

$$\frac{dR_{pl}}{dt} = -\frac{R_{pl}}{6M_{pl}} C_H \rho |\dot{\vec{r}}|^3 \frac{S}{Q_{abl}}. \tag{2.11}$$

2.4.2 Coupled Solution of Dynamics and Frictional Ablation

The four coupled dynamical and mass-loss relations ((2.7), (2.8), (2.9), (2.11)) must now be solved numerically. We use a fourth-order Runge-Kutta finite-difference numerical scheme (see Section 16.1 of Press et al., 1992) to integrate a planetesimal's velocity and frictional ablation. The method of Runge-Kutta requires we generate *first order* ordinary differential equations, and we therefore redefine some parameters in the above relations. Our redefinition of parameters y_i with $i \in [1, 6]$ are: $y_1 \equiv \dot{r}$, $y_2 \equiv r$, $y_3 \equiv M_{pl}$, $y_4 \equiv R_{pl}$, $y_5 \equiv \dot{\theta}$, and $y_6 \equiv \theta$. These re-definitions allow a solution of the four relations in addition to two redundant relations (for a total of six coupled

equations):

$$\dot{y}_1 = -\frac{Gm}{y_2^2} + \frac{C_D\rho(y_1^2 + (y_2y_5)^2)\cos\phi\, S}{2y_3} + y_2y_5^2 \tag{2.12}$$

$$\dot{y}_2 = y_1 \tag{2.13}$$

$$\dot{y}_3 = -\frac{1}{2}C_H\rho(y_1^2 + (y_2y_5)^2)^{3/2}\frac{S}{Q_{abl}} \tag{2.14}$$

$$\dot{y}_4 = -\frac{y_4}{6y_3}C_H\rho(y_1^2 + (y_2y_5)^2)^{3/2}\frac{S}{Q_{abl}} \tag{2.15}$$

$$\dot{y}_5 = -\frac{C_D\rho(y_1^2 + (y_2y_5)^2)\sin\phi S}{2y_3y_2} - \frac{2y_1y_5}{y_2} \tag{2.16}$$

$$\dot{y}_6 = y_5 \tag{2.17}$$

Equations (2.14) and (2.15) represent frictional ablation and are set to zero when the average aerodynamic pressure across the bolide is less than the yield strength of the bolide: $p_{\text{Stokes}}/2 = \mathcal{F}_{\text{Stokes}}/(2S) <$ bolide yield strength. This condition implies that the structural integrity of a planetesimal is sufficient to halt its vaporisation through frictional ablation.

2.4.3 Thermal Ablation

We have so far considered the physics of frictional ablation in our planetesimal-planet model. We now look to an additional source of ablation due to thermal heating from the envelopes. As an impactor decelerates in the planet, thermal ablation begins to operate as a result of the increasing envelope temperatures and thermal conductivities. The produced melting and vaporisation is due to heating of the bolide from the temperature gradient between the planetesimal and the ambient envelopes.

The efficiency of heat transfer from the surrounding envelope to the bolide surface is modeled by a relation analogous to Newton's law of heating. We match the heat gain at the surface of the bolide with the conductive heat flux into the bolide interior. This relation is essentially a 'Robin boundary condition' which is a weighted sum of

Neumann and Dirichlet boundary conditions. The relation is

$$\kappa \frac{\partial T}{\partial r} = \aleph (T_{amb} - T), \tag{2.18}$$

where κ is the thermal conductivity of the impactor and T_{amb} is the ambient temperature of the surrounding envelope. The proportionality constant $\aleph$ is a property of both the surrounding fluid and the planetesimal and is $\aleph = \kappa_{amb} A_{pl}/V_{pl} = 3\kappa_{amb}/R_{pl}$, where κ_{amb} is the ambient thermal conductivity. Equation (2.18) implies that the temperature at the outer edge (i.e., at a radial grid point $n_{\rm out}$) of the planetesimal is

$$T_{n_{\rm out}} \approx \frac{(\aleph' T_{amb} + T_{n_{\rm out}-1})}{1 + \aleph'}, \tag{2.19}$$

where $\aleph' \equiv \aleph \delta r/\kappa$ and δr is the radial grid spacing at the outer edge of the bolide.

We use the thermal conductivities κ_{amb} by French et al. (2012) for a Jovian-analogue hydrogen and helium mixture. The general thermal conductivity κ_{amb} is a combination of electronic and ionic contributions, κ_e and κ_i, and each has its region of dominance in Jovian envelopes. In regions where electrons are bound and thermal energy is transported through inter-molecular collisions, κ_e is not significant. The conductive transport of heat, and therefore κ_e, dominates quite deep in the Jovian structure where metallic hydrogen becomes abundant.

Thermal ablation depends not only on the transport of heat to the surface of the bolide but also on the conductive transfer of this heat throughout the whole bolide. The description of heat transfer within an impactor is modeled using the spherically-symmetric heat diffusion equation,

$$\frac{\partial T}{\partial t} = \frac{\alpha}{r^2} \frac{\partial}{\partial r} \left\{ r^2 \frac{\partial T}{\partial r} \right\}. \tag{2.20}$$

Here $\alpha = \kappa/(\sigma \rho_{pl})$ is the thermal diffusivity and is a function of the planetesimal composition; κ is the thermal conductivity of the impactor; σ is the specific heat capacity of the planetesimal; and ρ_{pl} is the bulk density of the bolide. To solve this equation, we use a method similar to that discussed by Recktenwald (2011) which presents a

finite-difference method for a numerical solution of equation (2.20). Adopting the *forward time, centered-space (FTCS) approximation* to a finite-difference solution allows us to write the heat diffusion equation as

$$T_i^{n+1} \approx T_i^n + \frac{\alpha \delta t}{\delta r}\left[\frac{2[T_{i+1}^n - T_i^n]}{r_i} + \frac{T_{i+1}^n - 2T_i^n + T_{i-1}^n}{\delta r}\right], \tag{2.21}$$

where subscripts and superscripts represent spatial steps and time steps, respectively.

A unique solution of equation (2.20) requires specification of three boundary conditions. Our boundary conditions are $\partial T/\partial r(r = 0, t) = 0$, $T(r = R_{pl}, t = 0) = 170\,\mathrm{K}$, and $T(r = R_{pl}, t)$ given by the Robin condition of equation (2.19). Where and when the temperature of a region exceeds the melting temperature of the planetesimal material, we enforce a reduction in the mass and radius such that the material ablates accordingly.

2.5 Results

Our model allows an exploration of planetesimal ablation for various initial conditions. We explore three main themes in our results. First, we discuss a representative case which illustrates the bimodal nature of the ablation process. Second, we investigate the effects of impact angle, impact velocity, and impact radius for four material compositions to explore the rich diversity of scenarios, and establish iron as the most conservative case among all our planetesimal compositions. We then narrow our attention to a detailed study of iron planetesimals since these provide lower limits on the wholesale ablation altitudes for all other considered planetesimal materials.

2.5.1 A Case Study of Bimodal Ablation

An example case which illustrates the bimodal ablation process is shown in Figure 2.3. This case is of an iron planetesimal with an impact radius of $R_{pl} = 30$ m, initial velocity of $|\dot{\vec{r}}| = 50\,\mathrm{km\,s^{-1}}$, and impact angle of $\phi_i = 45°$. All the results are run until the impactors either have 1 percent of their total mass left, by which point we

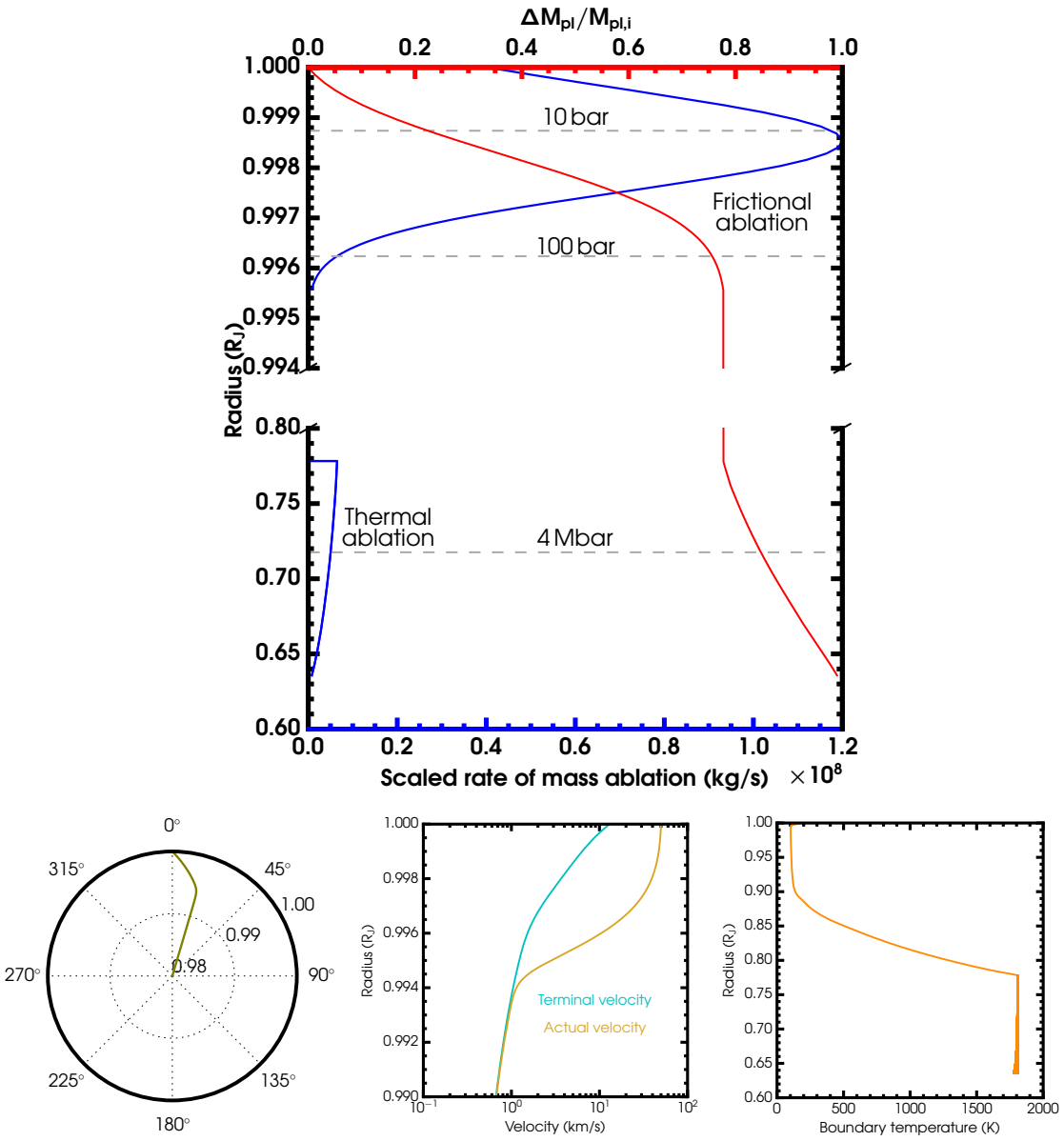

Figure 2.3: Illustration of bimodal ablation. Shown is the case of an iron bolide with an initial radius of 30 metres, impact velocity of $50\,\mathrm{km\,s^{-1}}$, and entry angle of 45°. Top panel: the scaled rate of mass ablation (bottom axis, blue) and corresponding fractional mass ablation (top axis, red) of the impactor as a function of altitude. The two blue peaks show the frictional and thermal rates of mass ablation, respectively. Horizontal gray dashed lines denote isobars. The thermal ablation rate has been scaled by a factor 30 for clarity. Bottom, left panel: the dynamical trajectory of the planetesimal in the $r - \theta$ coordinate plane. The angular values are inflated by a factor of 50 for visibility since the true maximal angle is 0.34°. Bottom, middle panel: Actual velocity (gold curve) and terminal velocity (cyan curve) as a function of altitude. Bottom, right panel: the boundary temperature of the planetesimal as a function of altitude.

consider them to be completely ablated, or until contact with the core at 41 Mbar.

The main panel in Figure 2.3 shows that frictional ablation initiates on impact at 1 bar, reaches a peak in mass ablation of $\sim 10^8\,\mathrm{kg\,s^{-1}}$ at 10 bar, and persists until 100 bar. This ablation process is generally efficient, as seen from the red curve which represents the fractional mass ablation along the path, $(M_{pl_\mathrm{i}} - M_{pl_\mathrm{f}})/M_{pl_\mathrm{i}}$, where M_{pl_i} is the mass at impact and M_{pl_f} is the planetesimal mass at a final location. Nearly 80 percent of the bolide mass vaporises through frictional ablation by 100 bar. What remains of the impactor then gradually heats up through equation (2.19). The temperature of the planetary envelope exceeds iron's melting temperature of 1,811 K at 3,176 bar (see Figure 2.1), but the planetesimal surface does not warm to this temperature until the bolide has penetrated to beyond 1 Mbar. The rise in temperature is slow because ℵ' is exceptionally small due to small thermal conductivities κ_{amb} in the upper outer envelope. Nevertheless, thermal ablation completes the planetesimal's wholesale ablation in the inner envelope.

The evolution of the planetesimal surface temperature is shown in the bottom right panel of Figure 2.3. The temperature reaches close to the ∼1811 K melting temperature of iron at altitudes below 0.80. The spread of temperature in this region is an artifact of finite grid resolution, for as each surface layer of the bolide is evaporated a finite time is taken for the slightly colder material in the adjacent inner cell to be heated to the melting temperature.

The dynamical trajectory of the bolide in the $r - \theta$ plane is shown in the bottom left panel. The planetesimal enters the outer envelope at an angle of 45° to the local zenith. The circumferential aerodynamic force of equation (2.16) acts to maneuver the planetesimal onto a purely radial trajectory. In this case, the planetesimal takes on a radial path just after the frictional ablation phase at an altitude of 0.995 R_J.

The bottom middle panel shows the evolution of the actual velocity compared with the terminal velocity as a function of altitude. The terminal velocity decreases with decreasing altitude due to an increasing density of the envelope. The actual velocity reaches a terminal velocity at an altitude of ∼0.994 R_J, which is also the level at which the trajectory becomes purely radial (see bottom left panel again).

Composition	Density ($\mathrm{kg\,m^{-3}}$)	Q_{abl}($\mathrm{MJ\,kg^{-1}}$)	Yield Strength ($\mathrm{MN\,m^{-2}}$)
Iron	7800	8.26	100
Rock	3400	8.08	10
Carbonaceous	2200	5.00	1
Ice	1000	2.80	1

Table 2.1: Material properties of planetesimals. Listed are the densities, specific heats of sublimation, and the yield strengths for iron, rock, carbonaceous, and ice planetesimals used throughout this work. The two latter properties are fundamental to determining the onset and efficiency of planetesimal ablation. The data are sourced from Chyba et al. (1993), Podolak et al. (1988), and Petrovic et al. (2003).

The bolide then always remains on a radial path at a terminal velocity. Thermal ablation then completely vaporises the bolide.

2.5.2 Exploration of Initial Conditions

Here we investigate the effects of various planetesimal characteristics including the composition, initial radius, initial velocity, and impact angle. We study how these planetesimal properties affect the mass ablation in the planetary envelopes. Given the efficiency of frictional ablation seen in Section 2.5.1, the results of this section only consider frictional ablation. The material properties used for the planetesimal compositions are listed in Table 2.1.

2.5.2.1 Initial Velocity

The frictional mass ablation of a planetesimal increases with the cube of the velocity (equation (2.9)) and is therefore crucial for the fate of a planetesimal. We consider initial velocities of $v_{\mathrm{initial}} \in [10, 50]\,\mathrm{km\,s^{-1}}$ in light of values from the Shoemaker-Levy 9 impactor (Harrington et al., 2004) and the Tunguska impactor (Chyba et al., 1993).[3] We study how this range of velocities modifies the fractional mass ablation

[3]The Shoemaker-Levy 9 and Tunguska events occured in Jupiter and Earth, respectively. The average velocity of the Shoemaker-Levy 9 fragments was about $44\,\mathrm{km\,s^{-1}}$ (Harrington et al., 2004) and the median of near-Earth asteroids is $15\,\mathrm{km\,s^{-1}}$ (Chyba et al., 1993).

of planetesimals, $(M_{pl_i} - M_{pl_f})/M_{pl_i}$. The top left panel of Figure 2.4 shows the fractional mass ablations to pressure levels of 100 and 1,000 bar for bolides of different compositions and initial velocities, with impact radii of 1 km and angles of 45°.

All compositions show larger fractional mass ablations for higher velocities. Water ice impactors with large velocities ($\gtrsim 45\,\mathrm{km\,s^{-1}}$) completely evaporate by 10^3 bar in the upper outer envelope due to two factors. First is the persistence of aerodynamic drag due to ice's low yield strength that activates equation (2.14) for a long time. Secondly, the low Q_{abl} of ice means frictional ablation is efficient when active. Carbonaceous, rock, and iron bolides ablate sequentially less than water ice planetesimals due to more robust material bonding and higher values of Q_{abl}.

It has been emphasised that carbonaceous impactors will evaporate when entering the Earth's atmosphere at more than $10\,\mathrm{km\,s^{-1}}$ (Chyba et al., 1990). In our case, 1 km carbonaceous impactors with initial velocities greater than $30\,\mathrm{km\,s^{-1}}$ lose more than half their mass by 10^3 bar. Whereas ice planetesimals of the highest velocities fully ablate by 10^3 bar, similar iron bolides lose only half of their initial mass by this level.

2.5.2.2 Initial Radius

We also examine the impact of initial planetesimal size. The top right panel of Figure 2.4 shows the effect of initial planetesimal radius on the mass ablation fraction of planetesimals at 10^2 bar and 10^3 bar. The ablated mass fraction is nearly constant across the majority of radii at 10^3 bar and is small for large radii at 10^2 bar. The constant mass ablation across radii for ice, carbonaceous, and most rocky planetesimals is a result of planetesimals having terminal velocities and purely radial trajectories.

This is demonstrated as follows. Once a bolide has a purely radial trajectory (i.e., $\dot{\theta} = 0$) at a velocity equal to the terminal velocity (i.e., $\ddot{r} = 0$), equation (2.6) implies that the velocity of a planetesimal is

$$|\dot{\vec{r}}_{term}|^2 = \dot{r}_{term}^2 = \frac{2gM_{pl}}{C_D \rho S}. \tag{2.22}$$

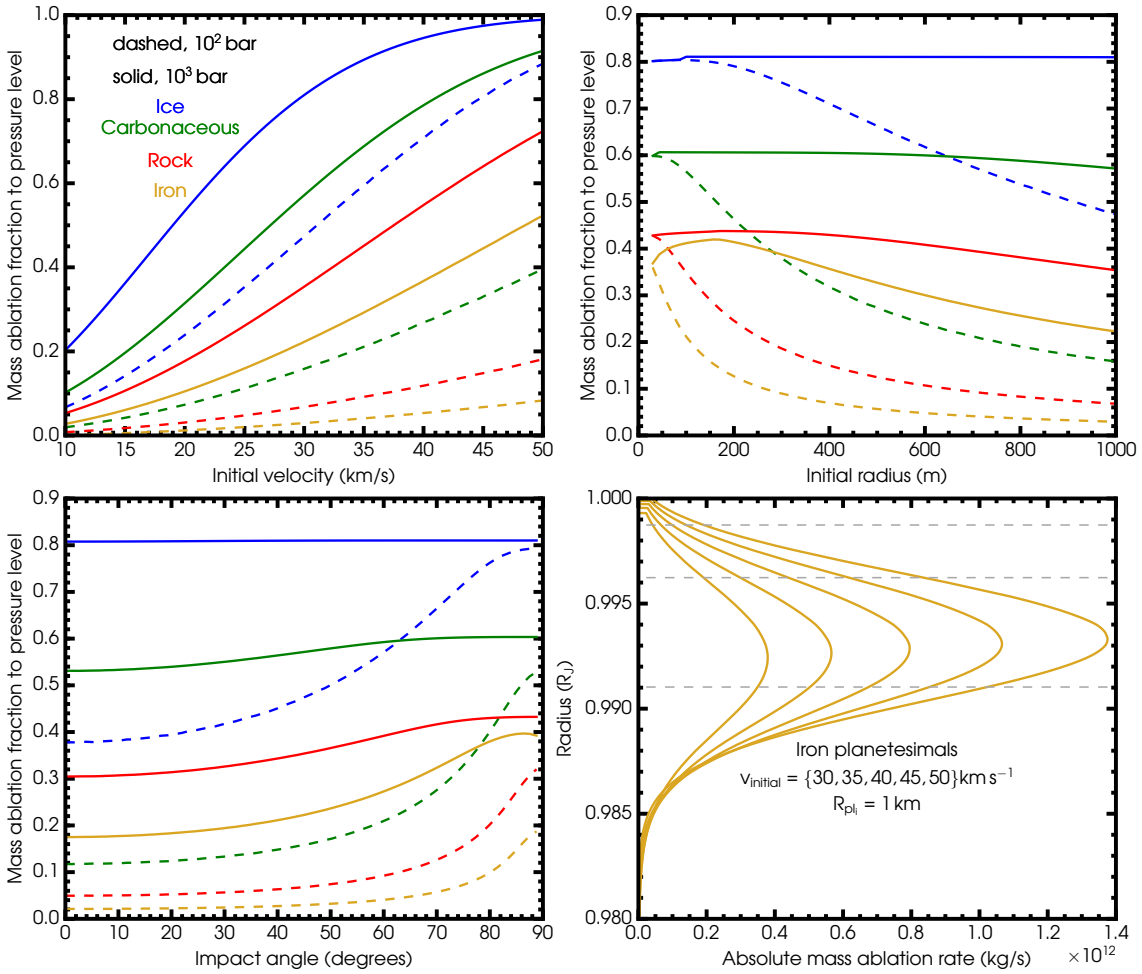

Figure 2.4: Impact of initial planetesimal parameters on ablated mass. Top, left panel: the mass ablation fraction to 100 bar and 1,000 bar as a function of impactor velocity. Planetesimals have an initial radius of 1 km and impact at 45° to the local zenith. The dashed curves represent fractional mass ablations at a pressure of 10^2 bar and solid curves represent the same but for 10^3 bar. Blue, green, red, and gold curves represent ice, carbonaceous, rock, and iron planetesimals, respectively. Top, right panel: the mass ablation fraction to 100 bar and 1,000 bar as a function of impactor radius. Planetesimals have initial velocities of 30 $\mathrm{km\,s^{-1}}$ and impact at 45° to the local zenith. The colours represent the same as in the top left panel. Bottom, left panel: the mass ablation fraction to 100 bar and 1,000 bar as a function of entry angle. Planetesimals have initial velocities of 30 $\mathrm{km\,s^{-1}}$ and radii of 1 km. The colours and line styles are the same as in the top panels. Bottom, right panel: the rate of mass ablation for iron planetesimals with entry angles of 45°, impact radii of 1 km, and $v_{\mathrm{initial}} = \{30, 35, 40, 45, 50\}\,\mathrm{km\,s^{-1}}$ (from left to right). Gray dashed lines indicate pressures of 10, 10^2, and 10^3 bar.

We now take equation (2.9) and link the time and spatial derivatives of the differential mass loss rate by the terminal velocity to obtain:

$$\frac{dM_{pl}}{d\vec{r}_{term}}\dot{\vec{r}}_{term} \propto |\dot{\vec{r}}_{term}|^3 \frac{S}{Q_{abl}} \tag{2.23}$$

Substituting equation (2.22) into equation (2.23) gives

$$\frac{dM_{pl}}{M_{pl}} \propto \frac{g(r)dr}{Q_{abl}}. \tag{2.24}$$

This relation is independent of the planetesimal radius. It signifies that for a planetesimal of a given composition whose speed is the terminal velocity and whose path is purely radial, the mass ablation fraction at some altitude is a constant. This is the origin of the horizontal curves in Figure 2.4. Bolide compositions with small characteristic heats of ablation Q_{abl} experience the greatest mass ablations, and thus the horizontal features shift up and down according to the value of Q_{abl}. The top right panel shows that icy, carbonaceous, and most rocky bolides attain terminal velocity and purely radial trajectories by 10^3 bar whereas iron bolides do not.

2.5.2.3 Impact Angle

The last parameter we investigate is the initial impact angle ϕ_i. Equation (2.24) is generally valid for planetesimals with terminal velocities and radial trajectories, and is thus also applicable to the bottom left panel of Figure 2.4. The mass ablation fraction for refractory materials is more weakly dependent on the angle of impact than for volatile materials. By 1,000 bar, one-kilometre bolides of ice sublimate 80 percent of their mass for all impact angles while carbon-rich bodies retain about 45 percent of their initial masses. Ice and carbonaceous bolides of the highest impact angles reach terminal velocities by 500 bar. On the other hand, the refractory species retain much of their mass and their larger inertia delays their attainment of terminal velocity as shown by a general lack of horizontal features in their ablated masses.

2.5.2.4 Mass Ablation Rate

The bottom right panel of Figure 2.4 shows the rates of mass ablation for iron bolides with different initial velocities. Iron planetesimals with significantly different velocities reach their peak rates of frictional ablation at about the same altitude in the upper envelope. This interesting finding holds generally for any planetesimal composition.

The results of Figure 2.4 highlight two important points. First, frictional ablation is efficient in ablating planetesimals by 10^3 bar and the mass ablation fraction is large especially for the fastest, smallest, and weakest of materials. Second, of the considered set of bolide materials, iron planetesimals represent the most conservative case, in the sense that iron bolides show the least fractional mass losses at any altitude compared with planetesimals of other compositions.

2.5.3 Iron Planetesimals

Section 2.5.2 illustrates that iron planetesimals are the most resilient to vaporisation. Here we narrow our exploration to the dynamics and ablation of iron impactors since the complete evaporation of planetesimals composed of other materials will occur at higher altitudes in the planet than those for iron.

We model the evolutions of iron impactors due to frictional and thermal ablation, in which the depths to which planetesimals penetrate depends mainly on their size and velocity. Figure 2.5 shows the mass ablation fractions of iron planetesimals at 10^3 bar, 10^7 bar, and 4.1687×10^7 bar along with a comparison to water ice planetesimals at 10^3 bar. We discuss results for the case of $\phi_i = 60^\circ$ since the majority of impact angles for iron display similar patterns with one another at different pressures.

Frictional ablation is active in the upper portions of the outer envelope for the majority of initial radii and velocities. On the other hand, thermal ablation is important comparatively deep in the structured planet where the ambient temperatures of the envelope are greater than the melting point of iron, and is active only for the smallest of planetesimals. For our planetary structure using the hydrogen and helium equations of state of Becker et al. (2014), the earliest thermal ablation can onset

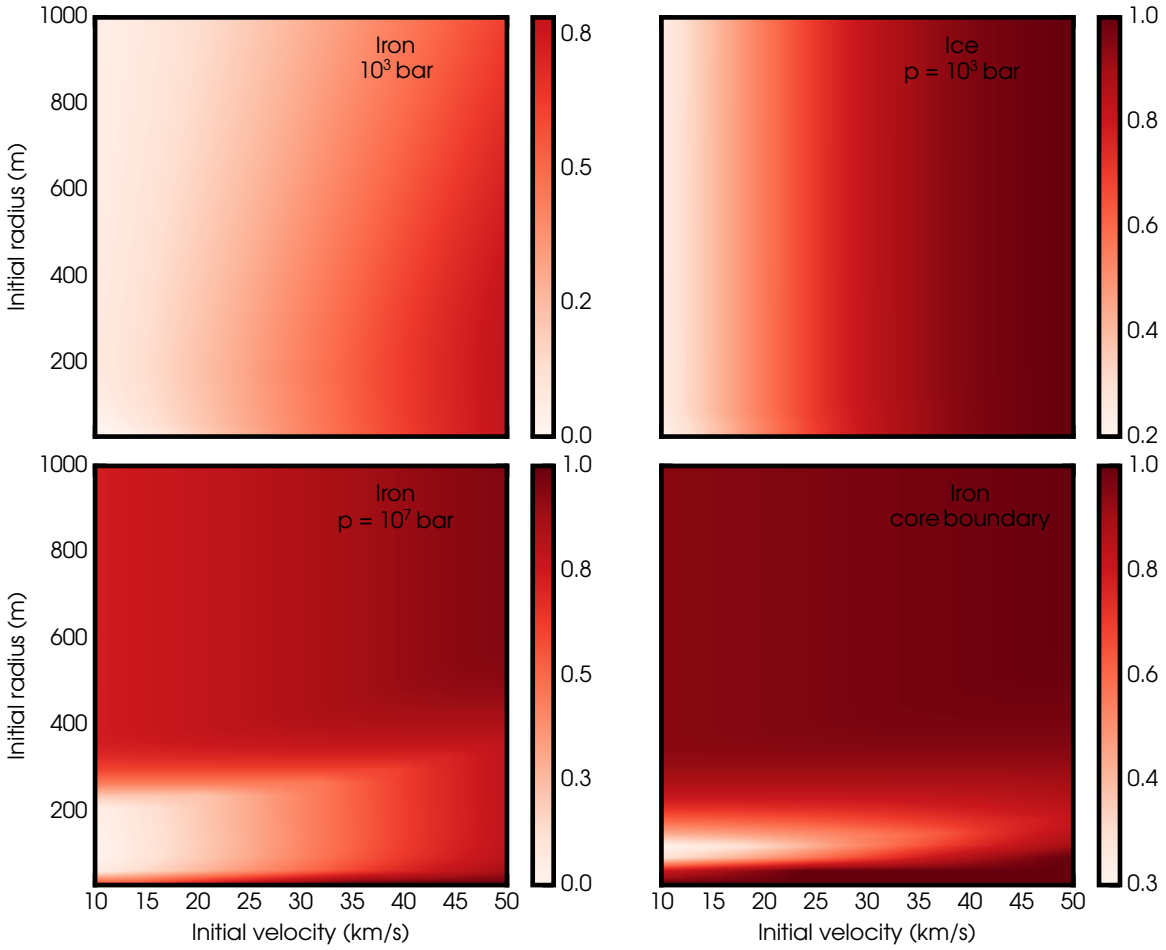

Figure 2.5: Mass ablation fractions of iron planetesimals at various pressures in the planet. Also shown for comparison is the ablation of ice planetesimals at 10^3 bar. Upper, left panel: Mass ablation fraction of iron planetesimals at 10^3 bar as a function of initial radius and initial velocity. Upper, right panel: the same for ice but considering only frictional ablation. Lower, left panel: the same as the upper, left panel but at a pressure of 10 Mbar. Lower, right panel: the same as the lower left panel but at the core boundary at a pressure of 41.69 Mbar. The impact angle of all planetesimals is 60°.

is at an altitude of 0.986 $R_{\rm J}$ corresponding to 3,176 bar; the low κ_{amb} of the outer envelope, however, means the actual onset of thermal ablation only starts to occur at the bottom of the outer envelope.

Therefore only frictional ablation contributes to mass loss in the upper left panel of Figure 2.5. The mass ablation of iron bolides is highest for planetesimals with large initial velocities and small radii. This behaviour follows from dividing the frictional ablation equation by M_{pl}, $\dot{M}_{pl}/M_{pl} \propto |\dot{\vec{r}}|^3/R_{pl}$. Planetesimals of small radii have higher fractional ablation rates than larger planetesimals for a given velocity, with higher velocities showing greater mass ablation fractions for a fixed planetesimal size. Iron bolides of the highest velocities and smallest initial radii lose 60 to 80 percent of their mass by 10^3 bar. The 10^3 bar level is significant since it is here that θ becomes a constant for the majority of planetesimals, leading to purely radial trajectories. It is significant that over 50 percent of mass is ablated by 10^3 bar over much of the dynamic range, since the mostly convective nature of the envelopes implies that vaporised material may mix upwards to the $\sim$1 bar region on short timescales and incorporate into the observed atmospheric chemistry of a planet.

The upper right panel of Figure 2.5 shows the analogue of the upper left panel but for water ice planetesimals. More than 80 percent of mass is lost for impact velocities of 30 $\mathrm{km\,s^{-1}}$ or greater. Two physical parameters explain this fragility of icy objects: Q_{abl} and the yield strength. A low Q_{abl} allows for high mass ablation rates for a given radius and velocity, while a low yield strength allows frictional ablation to persist longer than for iron bolides with a similar initial radius, velocity, and impact angle.

The lower left panel of Figure 2.5 shows the mass ablation fraction at 10 Mbar in the upper inner envelope, and is well beyond the level where thermal ablation can in principal affect planetesimals. Significant ablation has occurred for planetesimals with radii of $\gtrsim$300 metres compared with the upper left panel representing 10^3 bar. Smaller bolides remain comparatively unaffected between these pressure levels. The efficient ablation for the larger planetesimals can be understood in terms of equation (2.22) which is proportional to R_{pl} and the gravity g. As the gravitational acceleration increases deeper into the planet, the terminal velocity increases as

well. As planetesimals move deeper into the planet, the frictional ablation condition, $\mathcal{F}_{\rm drag}/(2S) >$ yield strength, turns on again due to an increasing terminal velocity, and does so first for the largest of planetesimals. We find that low velocity bolides of $\sim$300 metres and greater show this character whereby approximately 80 percent or more of the mass is lost due to the resurgence of frictional ablation. Smaller bolides of characteristically lower inertias attain terminal velocities more readily and this reduces the possibility of frictional ablation. Thermal ablation completes the destruction of the smallest planetesimals with radii of $\sim$30 metres.

The state of planetesimals at the core boundary is shown in lower right panel of Figure 2.5. The parameter space for which most of the bolide mass is retained for the 10 Mbar case is here more distinguished and is confined to a narrower range of initial radii (i.e., $\sim 90 - 250$ m) and relatively low initial velocities. Smaller bolides of $\sim$30 metres which had not undergone frictional ablation by 10 Mbar are thermally ablated between 10 Mbar and the core. Bolides with radii larger than 250 metres can eventually undergo frictional ablation because their terminal velocity increases due to the increasing gravitational field strength at small planetary radii. Only bolides in a very limited size range of $\sim 90 - 250$ metres are large enough such that they do not reach the sublimation temperature for thermal ablation, and yet small enough for their low terminal velocities to be rendered immune to frictional ablation. However, given the uncertainties and limitations that enter our modeling (e.g., of excluding additional ablation processes), this cavity feature may in reality either be somewhat smaller or non-existent.

2.5.3.1 Grazing Planetesimals at Super-Escape Velocities

If impacting planetesimals have velocities beyond the escape velocity of Jupiter of 60 $\mathrm{km\,s^{-1}}$, some planetesimals with large impact angles can deposit material in the outer envelope and still escape. Figure 2.6 shows the case of planetesimals which impact at nearly right angles to the local zenith. The illustration is shown for an elapsed time of 126 physical seconds, which is ten times the period required for a 30 metre bolide travelling at 100 $\mathrm{km\,s^{-1}}$ to completely ablate. Planetesimals with

sizes between 30 and 200 metres and speeds of 80 to 100 $\mathrm{km\,s^{-1}}$ undergo complete ablation, while larger bolides with these high kinetic energies manage to escape the Jovian radius (e.g., a 1 km planetesimal retains $\sim$60 percent of its initial mass in the process). At future times, the region of the plot involving velocities greater than the escape velocity does not evolve while the low velocity regime is subject to progressive ablation as in Figure 2.5. Therefore, planetesimals with speeds exceeding the escape velocity deposit chemicals that should also be detectable in the observable atmosphere of a giant planet.

2.6 Limitations and Future Steps

Our model is a simple description of planetesimal ablation and dynamics with implications for the enrichment of gas giant atmospheres. There is ample potential for model improvement and here we discuss a few possible refinements.

A more accurate planetesimal ablation model would include thermal conductivities κ of a bolide as a function of temperature and pressure. This would require knowledge of the complete phase diagram of conductivities from condensed-matter experiments at high pressures. This is presently a challenge. In addition, our thermal ablation model for a planetesimal assumes a constant melting temperature, thereby providing a host of qualitative features. Ideally a set of complete phase diagrams would be used for different impactor compositions to detail the melting temperature as a function of pressure. A more realistic planetary model would also include metallic species such as carbon, nitrogen, and oxygen in the envelopes. This would increase the ambient mass density and thus increase the efficiency of planetesimal ablation.

Another way of increasing the sophistication of the planetesimal model would be to incorporate the lateral spread of planetesimals. Aerodynamic drag can cause a planetesimal to become flattened and ellipsoidal from an initially spherical shape. The impactor becomes laterally distorted once aerodynamic forces overcome the yield strength of the impactor, and the bolide is deformed due to the differential pressures between the impactor's anterior and posterior. Lateral spread is suggested to be

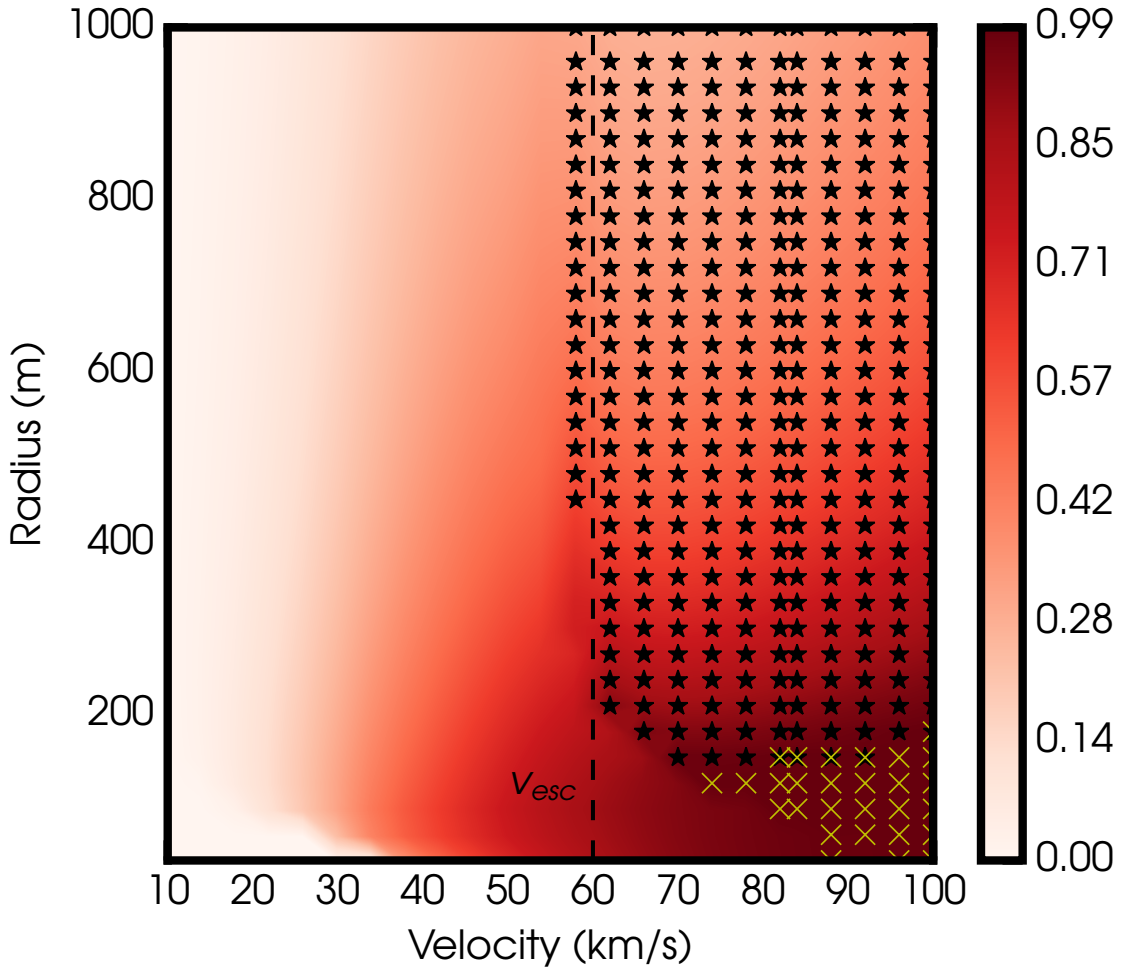

Figure 2.6: Mass ablation fraction for grazing planetesimals with initial speeds exceeding the Jovian escape velocity. The illustration is for a physical time of 126 seconds after planetesimal impact. Stars and yellow crosses respectively represent planetesimals which escape and which completely ablate. Planetesimals with speeds exceeding the Jovian escape velocity provide chemical depositions that should also be observable at $\sim$1 bar.

important for objects $\lesssim$1$-$2 km (Korycansky et al., 2000) and would increase the efficiency of frictional ablation due to a larger projected cross-section as seen by the drag force.

The effects of fragmentation and thermal radiation could also increase model sophistication. Fragmentation involves mechanical separation of the planetesimal into a number of smaller bolides and thermal radiation would consider the absorbed heat from thermal radiation of the envelopes. Both of these of considerations would place the complete ablation of planetesimals at higher levels in the envelopes, perhaps being of such efficiency as to keep all evaporation within the outer envelope of the planet. Accurate modelling of the first of these phenomena is complicated. For example, it is unclear whether it is more realistic to model fractionation of planetesimals by considering their raw material strength (Artemieva and Shuvalov, 2001) or by growth rates of hydro-dynamical instability modes (Korycansky and Zahnle, 2005).

One might also wonder about modelling the effects which the ablated material could have on the planetary structure for subsequently impacting planetesimals. The evaporated heavy metallic elements are more conductive than H and He and would decrease the bulk specific heat capacity in a unit volume originally containing H and He, thereby increasing the change in temperature with height. An increased temperature gradient and added material could produce greater thermal ablation and higher frictional ablation due to greater envelope densities. This therefore reiterates the point that our model is capable of placing lower limits on the efficiency of wholesale ablation of planetesimals compared to models with more detailed physics.

Our results are compared with the work of Pond et al. (2012) which used 3D hydrodynamical simulations to investigate the Shoemaker-Levy 9 (SL9) and 2009 Jovian impacts. The comparison is shown in Figure 2.7. We use the same parameters as Pond et al. (2012) for the incident angles, material densities, and radii of planetesimals. Four cases are considered: a porous 2009 impactor incident at 69°, a porous SL9 impactor at 43°, a non-porous 2009 impactor at 69°, and a non-porous SL9 impactor at 43°. In our model a porous 2009 impactor incident at 69° to the zenith ablates 67 percent of its mass at an altitude where Pond et al. (2012) finds it is completely

ablated. Similarly, we find the porous SL9 43° bolide ablates 88 percent of its mass, the non-porous 2009 69° bolide ablates 69 percent of its mass, and the non-porous SL9 43° planetesimal ablates 85 percent of its mass at altitudes where they are entirely ablated in Pond et al. (2012). Unsurprisingly, this comparison demonstrates that the ablation in Pond et al. (2012) is more efficient since they consider additional ablation processes such as lateral spread and fragmentation, both of which serve to place complete ablation of a planetesimal higher in the outer envelope.

Furthermore, we find several qualitative similarities with the work of Mordasini et al. (2015). However, exact comparisons cannot be made due to different planetary structures, considered physics, planetesimal compositions, and planetary evolutionary stages. Mordasini et al. (2015) find that planetesimals are completely ablated in planetary envelopes for envelope masses greater than 30 $M_\oplus$. This is consistent with our finding for our Jupiter-like envelopes of total mass $\sim$300 $M_\oplus$ for a range of planetesimal sizes and impact velocities. Mordasini et al. (2015) also demonstrate that planetesimals of a limited size range are able to reach the core. We find a similar scenario in which a population of planetesimals are too small to be subject to efficient frictional ablation and too large for efficient thermal ablation, leading to little mass ablation and contact with the core (see the bottom panels of Figure 2.5). More recently, Valletta and Helled (2018) carried out an investigation of planetesimal ablation during the early protoplanetary stages. They found that in all cases after 1 Myr the accreted solids ablate before reaching the core, while for times before 1 Myr all the accreted solids end up in the core.

2.7 Summary

We have developed a model for the frictional and thermal ablations of planetesimals that impact into Jovian-like envelopes. Frictional ablation is generally efficient in the upper outer envelope. The initial velocity, initial radius, impact angle, and composition of a planetesimal are the factors which control the magnitude and location of this mass ablation. We explore initial velocities of $10 - 50$ km s^{-1} and initial radii of

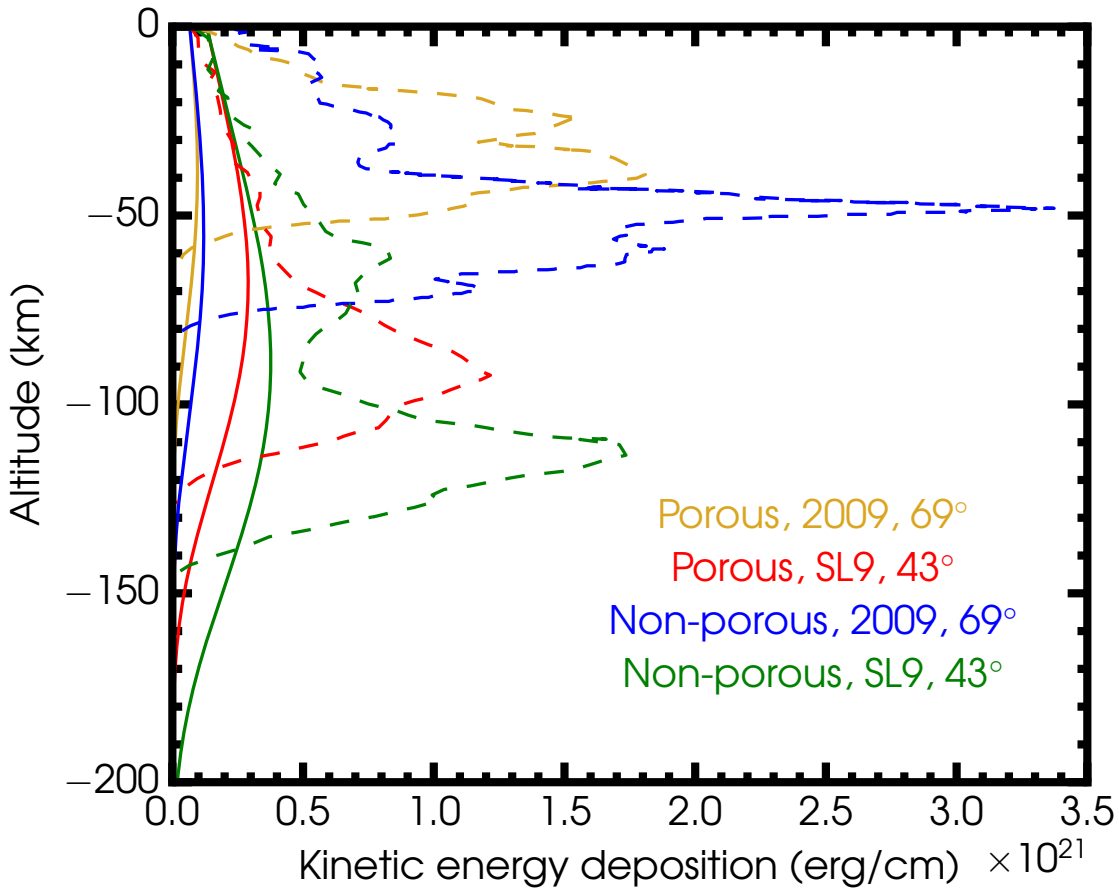

Figure 2.7: Comparison of deposited energy from planetesimals with the results of Pond et al. (2012). Solid and dashed curves show the results of our model and those of Pond et al. (2012), respectively. The altitude is relative to the 1 bar level and represents the z-projected height of the planetesimal (cf. equation (6) of Korycansky et al. (2006)). Four cases are shown: a porous 2009 impactor with an impact angle of 69° (orange); a porous SL9 impactor with an impact angle of 43° (red); a non-porous 2009 impactor with an impact angle of 69° (blue); and a non-porous SL9 impactor with an impact angle of 43° (green).The porous density is 0.6 g/cm^3, the non-porous density is 0.917 g/cm^3, and the radii of planetesimals is 500 metres.

$30-1000$ metres for iron, icy, carbonaceous, and rocky planetesimals. A small radius, large impact angle, and a large impact velocity lead to high mass ablation fractions. Thermal ablation operates deep in the planet where the ambient temperature exceeds the melting temperature of the planetesimal and when the thermal conductivity of the envelopes is sufficiently large. The effects of thermal ablation become relevant in regions where the velocity asymptotes to terminal velocity in the high-pressure regimes beyond about 3100 bar, and in cases of small planetesimals, finishes what frictional ablation began.

Frictional ablation fully ablates ice bolides by 1000 bar and evaporates 50 percent of the mass of iron bolides for planetesimals of the highest velocities and largest radii. By 1000 bar, iron planetesimals of the highest velocities but smallest radii ablate 60 to 80 percent of their mass due to frictional ablation. For ice bolides we find that frictional ablation causes planetesimals of all impact angles and radii with initial velocities greater than 30 $\mathrm{km\,s^{-1}}$ to lose more than 80 percent of their mass. Contact with the core boundary at a pressure of 41 Mbar is viable for some iron planetesimals with radii of $\sim 90-250$ metres. These bolides are too small to attain velocities required for frictional ablation and yet too large to be heated to the melting temperatures through thermal ablation.

A significant motivation of this work has been to investigate whether the observable chemistry in exoplanetary atmospheres is expected to reflect the accreted solids. The timescale for convective mixing in the envelopes of Jupiter is about 3 years while evolutionary times are greater than 10^9 years (Salpeter, 1973). The dissolution of planetesimal material in the envelopes through our modeled methods are therefore expected to be readily mixed on timescales of a few years. Our work has implications for giant exoplanets by using the inferred chemistry from observations to help discussions of formation and evolution of giant planets. In particular, our work suggests that observations of sub-stellar metallicities in an exoplanetary atmosphere are incompatible with substantial planetesimal accretion as accreted planetesimals ablate significantly in the atmosphere.

Chapter 3

Clouds in Exoplanetary Transmission Spectra

In addition to the gas constituents of an atmosphere as considered in Chapter 2, the atmospheres of exoplanets also host liquids and solids in the form of clouds and hazes (e.g., Pont et al., 2013; Ehrenreich et al., 2014; Knutson et al., 2014b,c; Kreidberg et al., 2014a). Clouds and hazes represent one of the greatest challenges in interpreting the atmospheric spectra of exoplanets. This is primarily due to the difficulty of modeling their physics and feedback effects in a self-consistent way (Marley et al., 2013).

The terms 'clouds' and 'hazes', collectively referred to as 'aerosols', are used in different contexts in the literature. From a formation standpoint, 'haze' implies particles formed through photochemical processes whereas a 'cloud' constitutes particles formed through the condensation of vapour onto a nucleus under suitable thermodynamic conditions (Marley et al., 2013). On the other hand, these terms are also used in reference to the spectral features they can cause, particularly in parametric models used in retrieval methods (e.g., Benneke and Seager, 2012; Kreidberg et al., 2014a; Sing et al., 2016; MacDonald and Madhusudhan, 2017a). In retrieval methods, a 'cloud' is generally used to mean a source of gray opacity and high optical depth effective below some height in the atmosphere, while a 'haze' is represented by a non-gray opacity in the optical (e.g., see MacDonald and Madhusudhan, 2017a). In

the present work we use the terminology of a 'cloud' according to the first of these standpoints, as we do not explicitly consider photochemical processes induced by the stars, and focus on cloud condensates composed of single chemical species.

Our goal in the present chapter is to conduct a detailed investigation of observable cloud features of importance for the interpretation of high-precision transmission spectra. We explore three key observable metrics to study the properties of clouds from transmission spectra: the slope of a spectrum in the optical wavelength range, the uniformity of this slope, and cloud features in the infrared. While gaseous Rayleigh scattering from H_2 particles leads to a slope of ~ -4 in the optical wavelength range due to the dominant λ^{-4} term in equation (3.4), we show that cloud condensates can lead to slopes over a broad range from -13 to flat spectra. We also illuminate degeneracies in the values of optical slopes that arise from a combination of the cloud species, the modal sizes of the cloud particles, and the cloud scale heights. Secondly, we explore the extent to which these optical slopes are uniform which can provide further constraints on the inferred cloud properties. These two observable metrics promise to be powerful means of understanding clouds in the optical with high-precision observations. Finally, we also study cloud signatures in the infrared and show that there are four cloud types with strong observable features. This third observable metric will be a promising way to study clouds in the near future due to the coming launch of the *James Webb Space Telescope* (*JWST*), whose spectral range spans 0.6 to 28 μm. The present and forthcoming observations in the optical and infrared domains from the *Hubble Space Telescope* (*HST*), *Spitzer*, the *Very Large Telescope* (*VLT*), the *JWST*, and forthcoming *Extremely Large Telescopes (ELTs)* motivate our present study.

Our work is presented as follows. Our model for the transmission spectra of exoplanetary atmospheres that incorporates clouds is presented in Section 3.1. In Section 3.2 we use Mie theory and the transmission spectrum model to explore the three key observable metrics discussed above. Section 3.3 presents an application of our method to current observations, with a focus on two hot giant exoplanets with the highest quality observations: HD 189733b and HD 209458b. Section 3.4

outlines several limitations of our approach and compares our model with another cloud treatment. We summarise our work in Section 3.5. The published form of this work is presented in Pinhas and Madhusudhan (2017).

3.1 Transmission Spectrum Model

The study of cloud features in the spectra of transiting planets first requires a model for the spectrum of an exoplanetary atmosphere. As a planet transits in front of its star, the stellar brightness decreases by a certain fraction. This fraction varies with wavelength due to the presence of gases and clouds in the planetary atmosphere that absorb and scatter radiation at unique frequencies. The 'transmission spectrum' (or 'transit depth') of an exoplanet is obtained by considering how much of the stellar light is absorbed and scattered in the planetary atmosphere, and is given by

$$\Delta(\lambda) \equiv \left(\frac{R_p(\lambda)}{R_\star}\right)^2 = \frac{2\pi \int_0^\infty r(1 - e^{-\tau(\lambda,r)})dr}{\pi R_\star^2}. \tag{3.1}$$

Here $\tau(\lambda, r)$ is the total optical depth along the line of sight of the observer at a radius r from the planetary centre, and is therefore called the 'slant optical depth'. The numerator of equation (3.1) is the sum of each planetary annulus $2\pi r dr$ weighted by the extinction, $1-e^{-\tau(\lambda,r)}$, due to absorbing and scattering particles in the annulus. In principle, this equation may be solved numerically. In the present study, however, we assume a simplified form of equation (3.1). We here describe our simplified model and its assumptions.

The transparency of an atmosphere increases with height due to lower gas pressures and densities. Therefore at a certain small slant optical depth, the size of the atmosphere due to extinction will be a good approximation to the full size of the atmosphere at a slant optical depth of zero. Lecavelier Des Etangs et al. (2008) explored a range of planetary radii and atmospheric scale heights and determined an effective slant optical depth that approximates the translucent atmosphere of a planet. They found that the transit depth at a slant optical depth of 0.56 is a good approximation

to the total transit depth contributed by the full atmosphere. This effectively means that the atmosphere is modelled as a sharp, occulting disk with the top of the atmosphere defined by a slant optical depth of 0.56 at any wavelength. The transmission spectrum of the sharp occulting disk model is

$$\Delta(\lambda) = \left(\frac{R_p(\lambda)}{R_\star}\right)^2 = \left(\frac{R_p + z_{\rm eff}(\lambda)}{R_\star}\right)^2 \tag{3.2}$$

The slant optical depth at the top of the occulting disk is $\tau_{\rm eff} = 0.56$ and defines the effective altitude $z_{\rm eff}$ at a given wavelength. The approximate model of equation (3.2) differs from the formulation in equation (3.1) by less than 1 percent. In our model, the reference pressure $p_{\rm ref}$ associated with R_p is a free parameter and depending on its value, $z_{\rm eff}(\lambda)$ can lie either below or above R_p depending on where the surface of $\tau_{\rm eff} = 0.56$ occurs.

3.1.1 Slant Optical Depth

The information about absorption and scattering of radiation by gases, liquids, and solids is all contained in the slant optical depth τ. By considering the transit geometry and the line-of-sight to an observer (Fortney, 2005), it is possible to obtain an analytical expression of the slant optical depth for a cloudy H_2-rich atmosphere as

$$\begin{aligned}
\tau(\lambda, y) =& \tau_{\rm cloud}(\lambda, y) + \tau_{\rm gas}(\lambda, y) \\
=& \sigma'_{\rm cloud}(a, \lambda) n_{\rm tot,b} X_{\rm cloud} e^{-y/H_c} \sqrt{2\pi R_p H_c} + \\
& \sigma_{\rm H_2}(\lambda) n_{\rm tot,b} X_{\rm H_2} e^{-y/H} \sqrt{2\pi R_p H} + \\
& \sigma_{\rm Na}(\lambda) n_{\rm tot,b} X_{\rm Na} e^{-y/H} \sqrt{2\pi R_p H} + \\
& \sigma_{\rm K}(\lambda) n_{\rm tot,b} X_{\rm K} e^{-y/H} \sqrt{2\pi R_p H} + \\
& \sigma_{\rm H_2O}(\lambda) n_{\rm tot,b} X_{\rm H_2O} e^{-y/H} \sqrt{2\pi R_p H} + \\
& \sigma_{\rm H_2-H_2}(\lambda) (n_{\rm tot,b} X_{\rm H_2})^2 e^{-y/H} \sqrt{2\pi R_p H} + \\
& \sigma_{\rm H_2-He}(\lambda) (n_{\rm tot,b})^2 X_{\rm H_2} X_{\rm He} e^{-y/H} \sqrt{2\pi R_p H},
\end{aligned} \tag{3.3}$$

where $\sigma_{H_2}(\lambda)$ is (Seager, 2010)

$$\sigma_{H_2}(\lambda) = \frac{8.14 \times 10^{-57}}{\lambda^4} + \frac{1.28 \times 10^{-70}}{\lambda^6} + \frac{1.61 \times 10^{-84}}{\lambda^8}\,\mathrm{m}^2. \tag{3.4}$$

Here, $\sigma'_{\mathrm{cloud}}(a, \lambda)$ is the total effective cross-section of the cloud species; $n_{\mathrm{tot,b}}$ is the total atmospheric number density at the bottom of the atmosphere; X_i is the mixing ratio of opacity species i; and H_c is the cloud scale height where we have assumed $n_{\mathrm{c}}(r) = n_{\mathrm{c,b}} e^{-y/H_c}$. Our model considers three sources of opacity: absorption and scattering by cloud particles, H_2 Rayleigh scattering, and absorption by atomic and molecular gas species. In the present work, we consider the latter gas component to include five contributions: sodium, potassium, water, and collision-induced absorption (CIA) from H_2-H_2 and H_2-He. Finally, we obtain the effective altitude $z_{\mathrm{eff}}(\lambda)$ in equation (3.2) through

$$z_{\mathrm{eff}}(\lambda) = y_{\mathrm{eff}}(\lambda) - H \ln \frac{p_{\mathrm{bottom}}}{p_{\mathrm{ref}}} \tag{3.5}$$

The effective altitude is determined by subtracting the height y where $\tau_{\mathrm{eff}} = 0.56$ from the distance between the bottom of the atmosphere at p_{bottom} and the reference radius R_p at p_{ref}.

In order to determine z_{eff} at a given wavelength, we calculate τ iteratively starting from the bottom of the atmosphere and work upwards differentially assuming spherical symmetry until $\tau = 0.56 \equiv \tau_{\mathrm{eff}}$. We assign y_{eff} to the height where the calculated slant optical depth is 0.56 and compute z_{eff} through equation (3.5). In all cases we assume an isothermal atmosphere determined by the equilibrium temperature T_{eq} of the planet (see equation (3.20)). The molecular cross-sections for H_2O are computed from HITEMP2010 line data (Rothman et al., 2010) and the CIA line data are sourced from the HITRAN archive (Richard et al., 2012). These line data are applied with a Voigt function to incorporate both temperature (Doppler) and pressure broadening. The cross-section of each opacity species is calculated separately and is tabulated by binning to a resolution of 0.01 cm^{-1} on a pre-defined temperature and pressure grid spanning 10^{-5} to 10^2 bar and 300 – 3500 K. The established grid is interpolated to extract the cross-section for a general temperature, pressure and wavelength for each

species. The Na, K, and H_2O cross-sections have units of [m^2], while those for H_2-H_2 and H_2-He CIA have units of [m^5]. A complete description of the molecular cross-section calculations is presented in Gandhi and Madhusudhan (2017). We discuss the calculation of the effective cloud cross-section $\sigma'_{\rm cloud}(a, \lambda)$ (with units of [m^2]) in the next section.

3.1.2 Extinction from Cloud Particles

A physical theory for the absorption and scattering of light by micro-particles is needed to explore the effects of clouds on transmission spectra. Mie theory is such a theory. It is a solution of Maxwell's equations that considers interactions of electromagnetic radiation with spherical particles. When a solid or liquid particle is illuminated by an electromagnetic wave, electric charges in the particle transform into dipolar antennas that re-radiate waves producing 'scattered' radiation. The excited electric charges can also transform a portion of the incident energy into thermal energy in a process of absorption. The efficiencies with which a particle scatters and absorbs radiation as a function of wavelength are denoted through components of a complex index of refraction, $m(\lambda) = n(\lambda) + i\kappa(\lambda)$. The real index of refraction $n(\lambda)$ informs about scattering while the imaginary index $\kappa(\lambda)$ represents absorption.

We have created our own Mie theory code in Python and have benchmarked it against the classical codes of Deirmendjian (1969) and Bohren and Huffman (1983). For a spherical particle of radius a embedded in radiation of wavelength λ, we can define a dimensionless size parameter x,

$$x \equiv \frac{2\pi a}{\lambda}, \tag{3.6}$$

$$\lambda = \frac{\lambda_0}{n_{\rm amb}}. \tag{3.7}$$

The numerator of equation (3.7) is the incident wavelength in a vacuum and $n_{\rm amb}$ is the real refractive index of the ambient medium surrounding the particle. The complex index of refraction of a particle with a given composition, $m(\lambda)$, can be used to generate the scattering and total extinction cross-sections as a function of particle

size and wavelength according to (Deirmendjian, 1969)

$$\sigma_{\rm scat}(a,\lambda) = (\pi a^2)\frac{2}{x^2}\sum_{n=1}^{\infty}(2n+1)\{|a_n(m,x)|^2 + |b_n(m,x)|^2\}, \tag{3.8}$$

$$\sigma_{\rm ext}(a,\lambda) = (\pi a^2)\frac{2}{x^2}\sum_{n=1}^{\infty}(2n+1)\,{\rm Re}\{a_n(m,x) + b_n(m,x)\}, \tag{3.9}$$

where a_n and b_n are coefficients expressed in terms of Bessel functions of the first kind with fractional orders $\zeta = n \pm 1/2$. We emphasise that the above description of cloud particle extinction used in our model is only valid for spherical particles composed of a single material. There are several ways to express the coefficients a_n and b_n, the most popular being in Bohren and Huffman (1983, page 127) and Deirmendjian (1969, page 17). Appendix A details the calculation of these coefficients. The number of terms n needed for convergence of the scattering and extinction cross-sections in equations (3.8) and (3.9) is a monotonic function of the size parameter x. The maximum number of terms needed for convergence is $n_{\rm max} = \max\{x + 4x^{1/3} + 2, |mx|\} + 15$ (Bohren and Huffman, 1983). Finally, the absorption cross-section is simply $\sigma_{\rm abs} = \sigma_{\rm ext} - \sigma_{\rm scat}$.

3.1.2.1 Cloud Particle Cross-Sections

The Mie theory formalism allows us to generate cloud particle cross-sections for use in our model transmission spectra. An important general feature of scattered radiation from a cloud particle is that the intensity of scattered light varies as a function of scattering angle. This angular asymmetry in the scattered light profile is represented by a so-called 'phase function'. The phase function generally peaks in the direction of incident radiation (i.e., in the forward direction) except for small particles of sizes $\lesssim 10^{-1}$ μm, for which the phase function is relatively isotropic.

The extinction measured by an observer is the theoretical extinction reduced by the scattered light collected at the detector. The measured or effective extinction is therefore the theoretical extinction cross-section modulated by the 'asymmetry parameter', g, which is proportional to the phase function and characterises the degree by which the scattered light profile is skewed from an isotropic profile (Bohren and

Huffman, 1983). The effective cross-section can be written as (Van de Hulst, 2003; Graaff et al., 1992)

$$\sigma'_{\rm cloud} = \sigma_{\rm ext} - \sigma_{\rm scat} g, \tag{3.10}$$

where $\sigma_{\rm scat}$ and $\sigma_{\rm ext}$ are from equations (3.8) and (3.9). The case of $g = 1$ represents radiation scattered purely in the forward direction and therefore the effective cross-section is due to absorption alone: $\sigma'_{\rm cloud} = \sigma_{\rm abs}$. An asymmetry factor of 0 represents isotropic scattering and $\sigma'_{\rm cloud} = \sigma_{\rm ext} = \sigma_{\rm abs} + \sigma_{\rm scat}$. Scattered light characterised by $g = -1$ does not reach the observer and in this case the effective cross-section is an enhanced theoretical cross-section, $\sigma'_{\rm cloud} = \sigma_{\rm abs} + 2\sigma_{\rm scat}$.

Figure 3.1 shows the effective cross-sections of various cloud particle species calculated using our Mie theory code. We consider cloud types that are expected to form in hot Jupiter atmospheres and which have experimental refractive index data spanning the optical and infrared: Na_2S, MnS, ZnS, $MgSiO_3$, SiO_2, Al_2O_3, FeO, Fe_2O_3, TiO_2, NaCl, KCl, and Mg_2SiO_4. Our model therefore considers twelve condensate species which are composed of twelve distinct elements. The refractive index data are obtained from various sources listed in Table 1 of Wakeford and Sing (2015). The cloud particle cross-sections and asymmetry parameters calculated with our code are made available online for the benefit of the astrophysical community.[1] The effective cross-sections for each cloud type in Figure 3.1 are shown for size distributions defined by three modal sizes: 10^{-2}, 10^{-1}, and 1 μm. The $\sigma_{\rm ext}$, $\sigma_{\rm scat}$, and g are computed through equations (3.12) and (3.14), respectively (see Section 3.1.2.3). Groups of species have common absorption features in the infrared due to similar chemical properties.

3.1.2.2 Cloud Particle Abundance

The volumetric mixing ratio of cloud particles in equation (3.3) is $X_{\rm cloud}$. We assume that cloud grains are composed of one type of condensate in a process known as homogeneous nucleation (see section 4.1 of Marley et al., 2013). The abundance of cloud particles in equation (3.3) is

[1] Our Mie theory cloud data is publicly available at `www.github.com/exo-worlds/Mie_data`

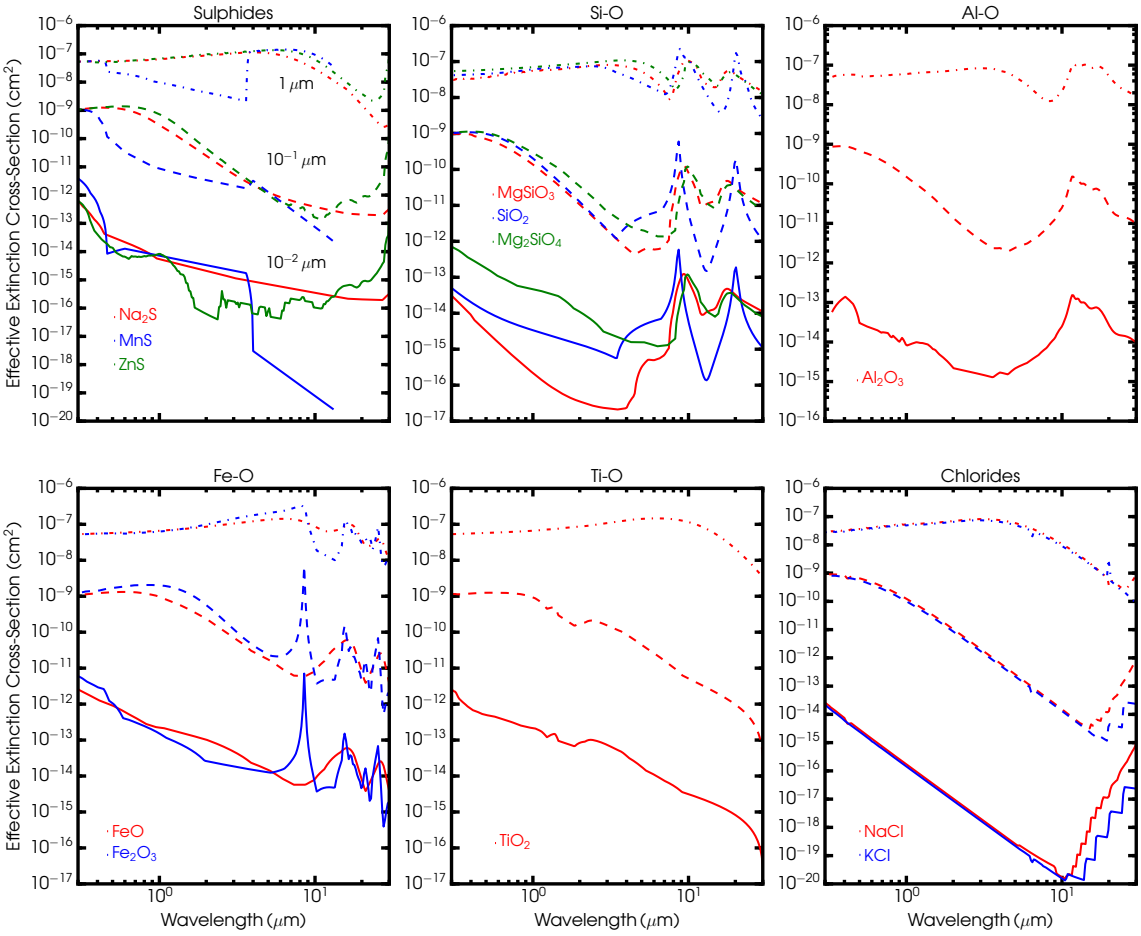

Figure 3.1: Effective cross-sections $\sigma'_{\rm cloud}$ for twelve cloud species. The cross-sections are calculated using our Mie theory code and consider a distribution of particle sizes with modal sizes of $10^{-2}\,\mu$m (solid lines), $10^{-1}\,\mu$m (dashed lines), and $1\,\mu$m (dot-dashed lines).

Cloud Species	Condensation Temperature (K)	Molar Mass (g/mol)	Density ($\mathrm{g\,cm^{-3}}$)
Na_2S	1176	78.04	1.43
MnS	1139	87	4
ZnS	700	97.45	4.05
$MgSiO_3$	1316	100.33	3.2
SiO_2	1725	60.08	2.62
Al_2O_3	1677	101.96	4.05
FeO	1650	71.79	5.7
Fe_2O_3	1566	159.68	5.3
TiO_2	1125	79.86	4.25
NaCl	825	58.44	2.17
KCl	740	74.55	2.17
Mg_2SiO_4	1354	140.63	3.27

Table 3.1: Chemical properties of the twelve cloud species. The condensation temperatures are shown at 1 mbar and are from Table 1 of Wakeford and Sing (2015).

$$X_{\mathrm{cloud}} = \frac{3X_{\mathrm{lim}}\mu_{\mathrm{cloud}}}{2\rho_{\mathrm{cloud}}\pi a^3 \tilde{N}_{\mathrm{lim}}}. \tag{3.11}$$

A derivation of this equation can be found in Appendix B. Here, μ_{cloud} is the molecular mass of the cloud species; X_{lim} is the volumetric mixing ratio of the least abundant atomic element that composes the cloud species; $\tilde{N}_{\mathrm{lim}}$ is the number of the limiting atomic element in the chemical formula of a condensate species (e.g., $\tilde{N}_{\mathrm{lim}} = 2$ for Al_2O_3); and ρ_{cloud} is the density of the cloud species.[2] The volumetric mixing ratio of the least abundant atomic element in a cloud particle, X_{lim}, limits the amount of condensates that can form and we generally assume solar values for these species from Asplund et al. (2009) unless specified otherwise. Chemical characteristics of the twelve cloud species are summarised in Table 3.1.

[2]The densities of cloud species are adopted from `http://webmineral.com/Alphabetical_Listing.shtml\#\#.V5nTr451o9g`

3.1.2.3 Size Distribution of Cloud Particles

The clouds in an atmosphere generally contain particles which span a broad range of sizes. Here we discuss how to incorporate a distribution of particle sizes into our cloud model for transmission spectra.

The incorporation of a size distribution for cloud particles requires weighting the cross-sections, the grain mixing ratio, and the asymmetry parameter for a given particle size by its abundance in a particle size distribution according to,

$$\bar{\sigma}_{\{\text{ext,scat}\}}(\lambda) = \frac{\int_{a_1}^{a_2} \sigma_{\{\text{ext,scat}\}}(a,\lambda) n(a) da}{\int_{a_1}^{a_2} n(a) da}, \tag{3.12}$$

and

$$\bar{X}_{\text{cloud}} = \frac{\int_{a_1}^{a_2} X_{\text{cloud}}(a) n(a) da}{\int_{a_1}^{a_2} n(a) da}, \tag{3.13}$$

and

$$\bar{g}(\lambda) = \frac{\int_{a_1}^{a_2} g(a,\lambda) n(a) da}{\int_{a_1}^{a_2} n(a) da}, \tag{3.14}$$

where $n(a)$ is the number of cloud particles in a unit volume with radii between a and $a + da$ and $g(a, \lambda)$ is the asymmetry parameter for a given particle size and wavelength. The asymmetry parameter for a particle size a and wavelength λ is

$$g(a,\lambda) = \frac{\int_0^{\pi} \int_0^{2\pi} p(\theta, a) \cos(\theta) \sin(\theta) d\theta d\phi}{\int_0^{\pi} \int_0^{2\pi} p(\theta, a) \sin(\theta) d\theta d\phi}. \tag{3.15}$$

where $p(\theta, a)$ is the phase function of scattered light for a scattering angle of θ.

The spectra of planetary atmospheres in the solar system have been fit with various particle size distributions such as log-normal distributions, gamma distributions, and power laws. We adopt the gamma distribution for cloud particle sizes (Deirmendjian, 1964),

$$n(a) = \omega a^{\beta} e^{-ba}, \tag{3.16}$$

Here ω, β, and b are positive real numbers. In particular, we use the specific form

presented in Budaj et al. (2015) (with $\beta \equiv 6$, $\omega \equiv a_0^{-6}$, and $b \equiv 6a_0^{-1}$),

$$n(a) = \left\{ \frac{a}{a_0} \right\}^6 e^{-6a/a_0}, \tag{3.17}$$

where a_0 is the modal particle size of the distribution and the range of a extends from $\sim 10^{-3}$ to $\sim 10^3$ μm (e.g., Lee et al., 2016; Lines et al., 2018). Deirmendjian (1964) justifies this choice of distribution by showing that it fits well with measurements of Earth's water clouds for an a_0 of 4 μm. This adopted distribution is a plausible assumption due to the impossibility of *in-situ* measurements of cloud particle sizes in the atmospheres of exoplanets. Nevertheless, deviations from the assumed distribution are expected in light of the variety of exoplanetary atmospheres as illustrated in Chapter 1.

3.1.3 Free Parameters

Our model of clouds for transiting planets contains five free parameters. Here we summarise their range of values as well as their effects on transmission spectra:

1. **Cloud scale height ($\mathbf{H_c}$)**: Earth and most other solar system planets have cloud scale heights of $H_c \lesssim H/3$ (Fortney, 2005; Ackerman and Marley, 2001; Carlson et al., 1994; Brooke et al., 1998; Sánchez-Lavega et al., 2004). However, the gas dynamics and high temperatures in hot Jupiter atmospheres could allow for significantly larger cloud scale heights, especially for small cloud particles which mix more easily (Parmentier et al., 2013). The cloud scale height in our model may therefore range from zero to the bulk atmospheric scale height, H. The value of H_c has important effects on transit spectra. Smaller values of H_c decrease the optical slope of a spectrum as well as provide lower amounts of extinction to a spectrum.

2. **Modal particle size ($\mathbf{a_0}$)**: Sophisticated cloud formation models find that the cloud particle sizes in exoplanetary atmospheres span a continuum from $\sim 10^{-3}$ to $\sim 10^3$ μm (e.g., Helling et al., 2016; Lee et al., 2016; Lines et al.,

2018). We therefore consider model particle sizes spanning 10^{-2} to 10^{2} μm and assume cloud particles follow a particular gamma distribution characterised by the modal particle size. Increasing the modal size translates into decreased optical slopes, with a spectrum becoming entirely flat for $a_0 \gtrsim 1$ μm.

3. **Reference pressure ($\mathbf{p_{ref}}$)**: The pressure associated with the radius of the planet R_p may range from $\sim$1 bar to $\sim$1 mbar (Heng and Kitzmann, 2017). Increasing $p_{\rm ref}$ shifts R_p lower in the planet and increases the absolute offset level of a transmission spectrum.

4. Grain abundance ($\mathbf{X}_{\rm cloud}$): The non-equilibrium nature of clouds makes it challenging to determine the abundance of cloud grains. Equation (3.11) assumes that the abundance of cloud grains is limited by the least abundant element in a cloud species. The grain abundance can range from about 10^{-25} to 10^{-7} (e.g., see Figure 7 of Lee et al., 2016).

5. **Molecular abundance ($\mathbf{X_i}$)**: The molecular abundances of different volatile species have been suggested to range from sub-solar to super-solar values (Madhusudhan et al., 2014b; Kreidberg et al., 2014c; Sing et al., 2016; Barstow et al., 2017). We thus also investigate the effects of different molecular abundances on the observability of cloud features.

3.2 Results

Here we present results which explore the signatures of clouds in exoplanetary transmission spectra. We first discuss a metric that characterises the slope of the transmission spectrum in the optical wavelength range. This metric can be useful for constraining the cloud species, cloud scale heights, and modal particle sizes of clouds using high-precision observations. Moreover, we discuss the use of temperature information as a way to reduce degeneracies in inferred cloud properties. We then present a second metric, the uniformity of slopes in the optical, as an additional way to break degeneracies using high-precision observations. Finally, we investigate which cloud

species have pronounced features in the infrared which may be observable with future spectra from the *JWST*. We then apply our framework to an ensemble of hot Jupiter spectra to evaluate the potential cloud properties in their atmospheres, with a particular focus on HD 189733b and HD 209458b which have the highest quality observations.

3.2.1 First Metric: Optical Slopes

Transmission spectra of exoplanets in the visible wavelength range have various slopes that hint towards the existence of different cloud properties. Here we construct a metric to extract cloud information from an observed spectrum in the optical window of $0.3-0.56$ μm. This wavelength range serves as a prudent metric for the optical slope since it avoids potential contributions from sodium and potassium gas absorption features at 0.59 and 0.77 μm.

Atmospheric observations of hot giant exoplanets in transit obtain the radius of the planet as a function of wavelength $R_p(\lambda)$. Using the effective height $z_{\rm eff}$ in equation (1) of Lecavelier Des Etangs et al. (2008), the slope of this observed radius can be written as

$$m_{\rm obs} = \frac{dR_p(\lambda)}{d\ln\lambda} = \frac{z_{\rm eff}(\lambda)}{d\ln\lambda} = \gamma H_c. \tag{3.18}$$

Here there is a degeneracy in the slope for values of γ and H_c, where γ is the exponent on the wavelength-dependent portion of the cloud cross-section. Because the cloud scale height H_c is generally unknown a priori, it is prudent to modify the slope $m_{\rm obs}$ in terms of the more certain bulk atmospheric scale height H. The slope of $R_p(\lambda)$ expressed in a more convenient dimensionless form is then

$$\begin{aligned} \mathcal{S} \equiv \frac{m_{\rm obs}}{H} &= \frac{dR_p(\lambda)}{d\ln\lambda}\frac{1}{H} \\ &= \frac{dz_{\rm eff}(\lambda)}{d\ln\lambda}\frac{1}{H} = \gamma\frac{H_c}{H}, \quad \text{for } 2H/5 \lesssim H_c \leq H. \end{aligned} \tag{3.19}$$

The dimensionless slope $\mathcal{S}$ combines a directly observable quantity ($m_{\rm obs}$) and an estimated quantity (H). In the limit of small H_c ($H_c \lesssim 2H/5$) the slope $\mathcal{S}$ tends to

the H_2 Rayleigh scattering value of -4.2 and therefore equation (3.19) is valid for $H_c \gtrsim 2H/5$. The bulk scale height H is typically the scale height at the equilibrium temperature, i.e. $H = H_{\rm eq} = k_B T_{\rm eq}/(\mu g)$, where the equilibrium temperature is obtained from considering conservation of energy and is given by (Seager, 2010)

$$T_{\rm eq} = T_\star \left(\frac{R_\star^2}{2a_{\rm major}^2} \right)^{1/4} (f(1-A))^{1/4}. \tag{3.20}$$

Here $a_{\rm major}$ is the semi-major axis of the planet, A is the Bond albedo (i.e., the fraction of total incident light that is reflected by a planet), and f is the heat redistribution fraction.

The calculated slopes $\mathcal{S}$ in the $0.3-0.56$ μm range for the twelve cloud species in Table 3.1 are shown in Figure 3.2. The slopes of the transmission spectra are computed for atmospheres composed of one type of cloud for a range of scale heights and modal particle sizes. The distinction between a regime where clouds dominate the calculated slopes (i.e., $H_c > 2H/5$) to one where H_2 scattering dominates (i.e., $H_c \lesssim 2H/5$ is made clear. The slopes $\mathcal{S}$ for large scale heights reflect the unique opacities of the cloud species through their refractive indices. Once cloud scale heights of $H_c \lesssim 2H/5$ are reached, the drastic fall of the number of cloud particles with height allows the scattering by H_2 to begin to dominate the spectrum in the optical. The cloud contribution diminishes for lower H_c and the slope $\mathcal{S}$ takes on a value of -4.2 typical of equation (3.4) in the $0.3-0.56$ μm range at $H_c = H/5$. Figure 3.2 is useful in showing the degeneracies among the cloud compositions, modal particle sizes, and scale heights that are commensurate with an observed slope $\mathcal{S}$.

There are several essential points to be extracted from the detail of Figure 3.2:

1. Sulphide clouds are the only considered cloud species for which $\mathcal{S} < -5$ across all modal particle sizes and scale heights. Therefore, spectral observations which show steep slopes of $\mathcal{S} < -5$ might potentially imply the presence of Na_2S, MnS, and/or ZnS clouds in the atmosphere.

2. Cloud properties are observable for $H_c \gtrsim 0.4H$.

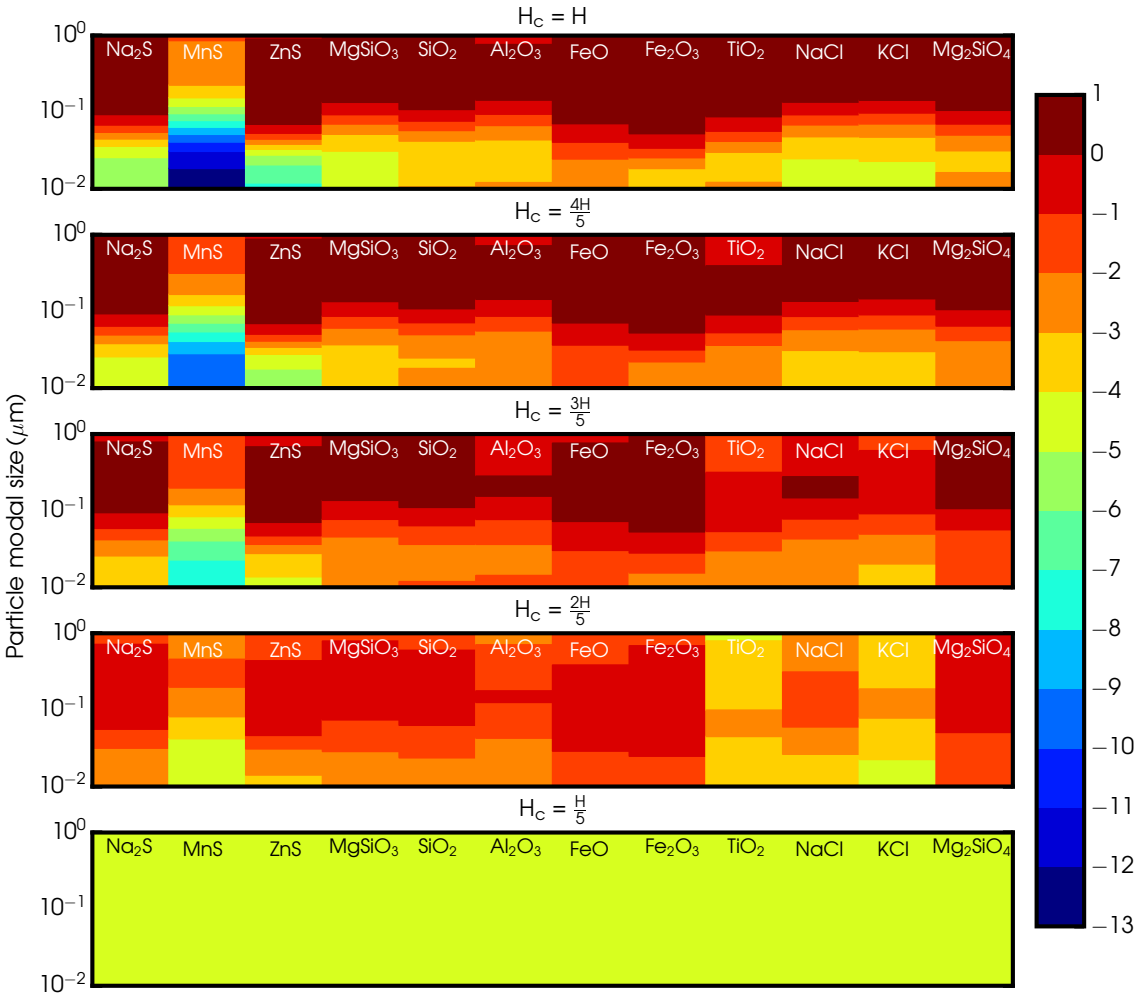

Figure 3.2: Slopes $\mathcal{S}$ of transmission spectra in the 0.3−0.56 μm range for twelve cloud species. The slopes are represented by the colours and depend on the cloud species, the modal particle size, and the cloud scale height. The panels represent atmospheres with cloud scale heights of $H_c = H$, $H_c = 4H/5$, $H_c = 3H/5$, $H_c = 2H/5$, and $H_c = H/5$.

3. Degenerate values of $\mathcal{S}$ are produced for various cloud types, scale heights, and modal particle sizes. Large particles (i.e., less negative γ) with large scale heights are degenerate with small cloud particles (i.e., more negative γ) with small scale heights.

4. An $\mathcal{S}$ of ~ -4 does not of itself imply H_2 Rayleigh scattering. For example, such slopes are produced by various cloud species with large scale heights (see top panel of Figure 3.2).

The appeal of Figure 3.2 lies in its ability to illuminate potential cloud properties directly from observations. Observers can take their spectrum of the planet's radius versus wavelength, take the slope of that spectrum in the optical from 0.3 to 0.56 μm, divide by an estimate for H, and immediately be able to glean some fundamental cloud properties that may be producing the spectrum.

3.2.1.1 Temperature as a Guide

The temperature structure of an atmosphere can be used as a guide to predict which cloud species are able to condense and thereby reduce potential degeneracies among cloud properties as displayed in Figure 3.2. Condensable gas becomes thermally stable when the temperature of the atmosphere becomes colder than the saturation vapour temperature of a species at a given pressure (Sánchez-Lavega et al., 2004; Helling, 2018). The temperature structure may be obtained in the first place through a retrieval method (Madhusudhan and Seager, 2009). In what follows the slopes of transmission spectra in Figure 3.2 are used to reveal a limited, potential set of cloud properties assuming knowledge of the atmospheric temperature at $\sim$1 mbar.

Before proceeding it is crucial to note that the discussion is considerably restricted since it does not consider the full range of condensate species that are thermally stable for a given temperature at 1 mbar. For example, in the case that a temperature profile is found to be about 700 K at 1 mbar, we only discuss species in Table 3.1 that have comparable condensation temperatures (i.e., ZnS and KCl) despite the fact that the remaining ten species in Table 3.1 will also be thermally stable for a $T \approx 700$ K at

1 mbar. Likewise, in the case of $T \approx 1500$ K at 1 mbar, Al_2O_3, FeO, and SiO_2 will too be thermally stable in addition to Fe_2O_3 considered here. *The following analysis therefore only presents a limited sample of potential explanations to an observed slope:*

$\boldsymbol{T \approx 700}$ **K**: If the temperature at ∼1 mbar is determined to be less than 700 K from the $p - T$ profile, ZnS and KCl may potentially form condensates in the observable atmosphere. Transmission observations which show slopes of $\mathcal{S} < -4$ might suggest the presence of ZnS cloud particles with modal sizes between 10^{-2} to 3×10^{-2} μm and $H_c \approx H$ or KCl cloud particles of similar sizes.

A trend that is present for all cloud species is that slopes for large H_c and large a_0 are mimicked by those for small H_c and small a_0. For example, KCl particles with a modal size of 8×10^{-2} μm and $H_c = H$ produce the same slopes (-1 to -2) as KCl particles with $H_c = 3H/5$ and modal sizes of 5×10^{-2} μm. This trend follows from equation (3.19): a large modal size (i.e., a low γ) coupled with a large H_c gives the same slope as a small modal size (i.e., a high γ) coupled with a small H_c. This degeneracy is always present unless H_c may be predicted from fundamental physical principles. Sánchez-Lavega et al. (2004) present a first estimate of H_c in their equation (22) which could potentially be utilised in future work.

$\boldsymbol{T \approx 800}$ **K**: Atmospheres with temperatures of ∼800 K at 1 mbar might potentially host NaCl cloud particles. Grain modal sizes between 10^{-2} and $5 \times 10^{-2}\mu$m could potentially help explain observations showing slopes of $-5 < \mathcal{S} < -3$.

$\boldsymbol{T \approx 1100}$ **K**: Atmospheres with temperatures of ∼1100 K at 1 mbar might potentially indicate MnS cloud particles for observed slopes of $\mathcal{S} \lesssim -8$. On the other hand, slopes of $-8 \lesssim \mathcal{S} \lesssim -3$ present alternative possibilities. Observations which have a uniform slope could imply Na_2S cloud particles as opposed to MnS and TiO_2 particles (see Section 3.2.2). If $\mathcal{S} \gtrsim -3$ the slopes could be produced either by large particles with $H_c \approx H$ or by small particles with scale heights of $H_c \approx 3H/5$. There is a general pattern for these species in that per a given slope, the modal size increases sequentially for TiO_2, Na_2S, and MnS particles. Once the scale height becomes lower than $H_c \approx 3H/10$, the magnitude of H_2 scattering dominates and the optical spectrum features an H_2 scattering slope of -4.2.

***T* ≈ 1300 K**: Atmospheres with temperatures of ∼1300 K at 1 mbar might potentially indicate $MgSiO_3$ cloud particles with modal sizes between 10^{-2} and $3 \times 10^{-2}\mu$m for observed slopes of $\mathcal{S} \lesssim -4$. Mg_2SiO_4 always has a shallower slope than $MgSiO_3$ for a given H_c and a_0.

***T* ≈ 1500 K**: Atmospheres with temperatures of ∼1500 K at 1 mbar might potentially suggest Fe_2O_3 cloud particles with modal sizes of $10^{-2}\mu$m to $3 \times 10^{-2}\mu$m and $H_c \approx H$ for observed slopes of $-4 \lesssim \mathcal{S} \lesssim -2$. Slopes larger than -2 are degenerate for different combinations of H_c and a_0 until $H_c \approx 2H/5$, at which point the slopes begin to approach the molecular H_2 value of -4.2.

***T* ≈ 1600 K**: Atmospheres with temperatures of ∼1600 K at 1 mbar might suggest Al_2O_3 rather than FeO as the the most likely species for values of $\mathcal{S}$ between -3 and -4. These Al_2O_3 cloud particles would have sizes of $\sim 2 \times 10^{-2}\mu$m with large scale heights. Slopes between -2 and -3 may be due to either cloud type with $H_c = H$ and modal sizes of $\sim 2 \times 10^{-2}$ μm for FeO or $5 \times 10^{-2}\mu$m for Al_2O_3.

***T* ≈ 1700 K**: Atmospheres with temperatures of ∼1700 K at 1 mbar might potentially suggest SiO_2 particles with $H_c \approx H$ and modal sizes between 10^{-2} and $4 \times 10^{-2}\mu$m if $-4 \leq \mathcal{S} \leq -3$, while an $\mathcal{S}$ between -2 and -3 would suggest modal sizes of $5 \times 10^{-2}\mu$m. The slopes and particle modal sizes for $H_c = 4H/5$ and $H_c = 3H/5$ are almost indistinguishable and remain degenerate unless H_c can be reliably calculated from first principles.

3.2.2 Second Metric: Shape of Optical Slopes

Most current models of transit spectra in the optical use parametric prescriptions for clouds in both forward theoretical models and retrieval methods resulting in constant slope values (e.g., Kreidberg et al., 2015; Sing et al., 2016; Blecic, 2016; Wakeford et al., 2017; MacDonald and Madhusudhan, 2017a; Pinhas et al., 2019). Here we investigate the uniformity of slopes in the optical for different cloud species. The degree of non-uniformity of the optical slopes can provide constraints on the cloud properties from high-precision observations.

Figure 3.3 shows the transmission spectra of twelve clouds for three modal particle

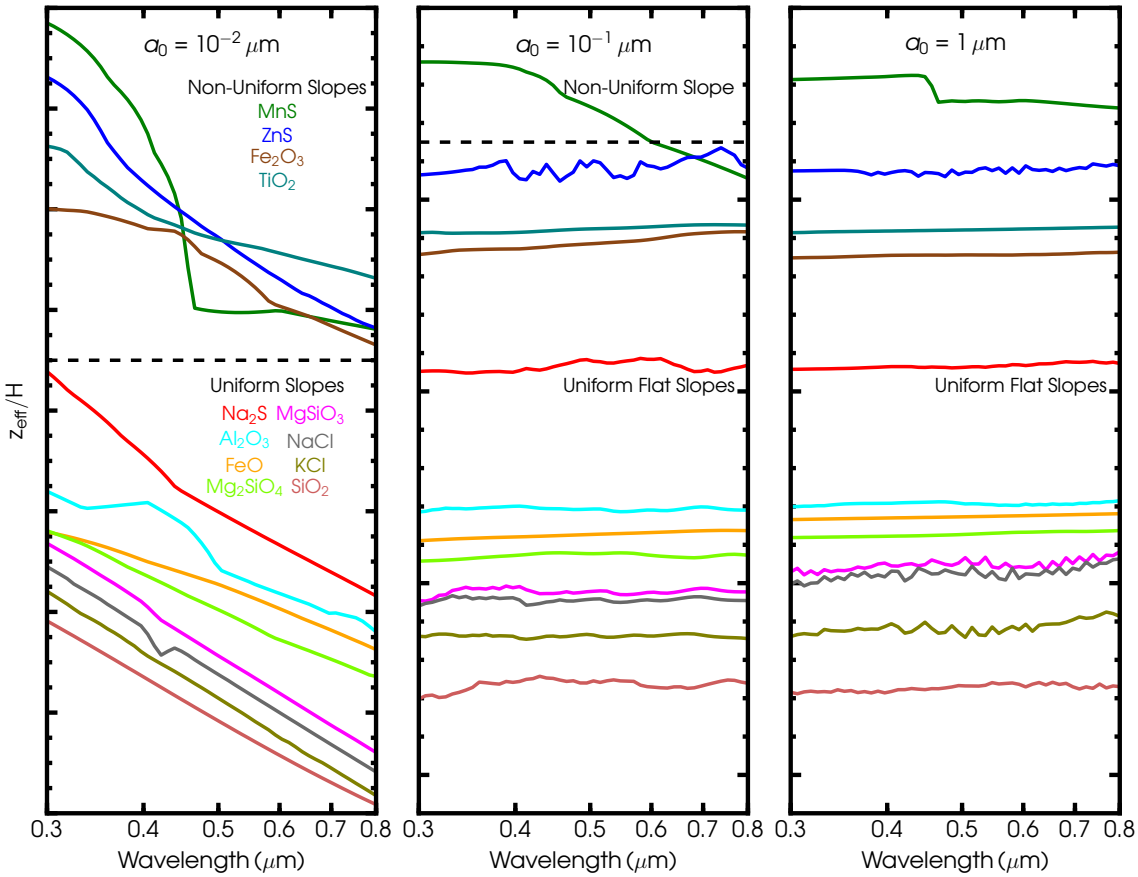

Figure 3.3: Optical transmission spectra of cloud species. Species display either uniform or non-uniform optical slopes depending on the particle sizes and condensate type. All clouds but MnS, ZnS, Fe_2O_3, and TiO_2 display observationally-limited uniform slopes. The dashed black horizontal line delineates between cloud types showing non-uniform and uniform slopes. Vertical offsets have been applied to make these delineations clear.

sizes (0.01, 0.1 and 1 μm). The species fall into two groups according to whether a uniform slope is displayed in the optical range of $0.3 - 0.8$ μm. Our interpretation of 'uniform' is in accordance with the quality of observations. We start at the lowest wavelength and construct a 1σ envelope with the same slope as that at the lowest wavelength. A model curve that is able to fit completely within this 1σ envelope is considered to have a uniform slope. The average 1σ uncertainty in $z_{\rm eff}/H$ which we use for this envelope is 1.25, and reflects the quality of spectra of ten hot Jupiters with the best observations as contained in Sing et al. (2016).

Of the tested cloud species with modal sizes of 10^{-2} μm, four have non-uniform slopes in the optical. MnS, ZnS, Fe_2O_3 and TiO_2 have the most significant changes in their scattering and absorption properties in the optical leading to variations in their slopes. MnS deviates from uniformity most with a broad valley at 0.5 μm. Fe_2O_3 shows three distinct regions composed of different slopes. On the other hand, high-precision observations showing no significant non-uniformity in the optical can be due to one or more species in the bottom group in Figure 3.3. Increasing the grain modal particle size to 0.1 μm leads to an essentially grey opacity for all species in the optical except for MnS. All cloud species display flat spectra for modal sizes larger than 1 μm.

In all, small modal particle sizes of $\sim 10^{-2}$ μm produce non-flat spectra. Non-uniform slopes in these spectra are seen for several species including MnS, ZnS, Fe_2O_3 and TiO_2. Virtually all cloud species with modal sizes greater than 0.1 μm produce flat, featureless spectra.

3.2.3 Third Metric: Cloud Features in the Infrared

The infrared region of a transmission spectrum holds information about cloud absorption features. However, these cloud features could be masked by absorption features due to gas species (e.g., water vapour). Here we study cloud signatures for different combinations of H_2O abundances and modal particle sizes to identify the most promising cloud species which are distinguishable in infrared spectra.

The modal sizes of cloud particles and the abundance of H_2O determine the

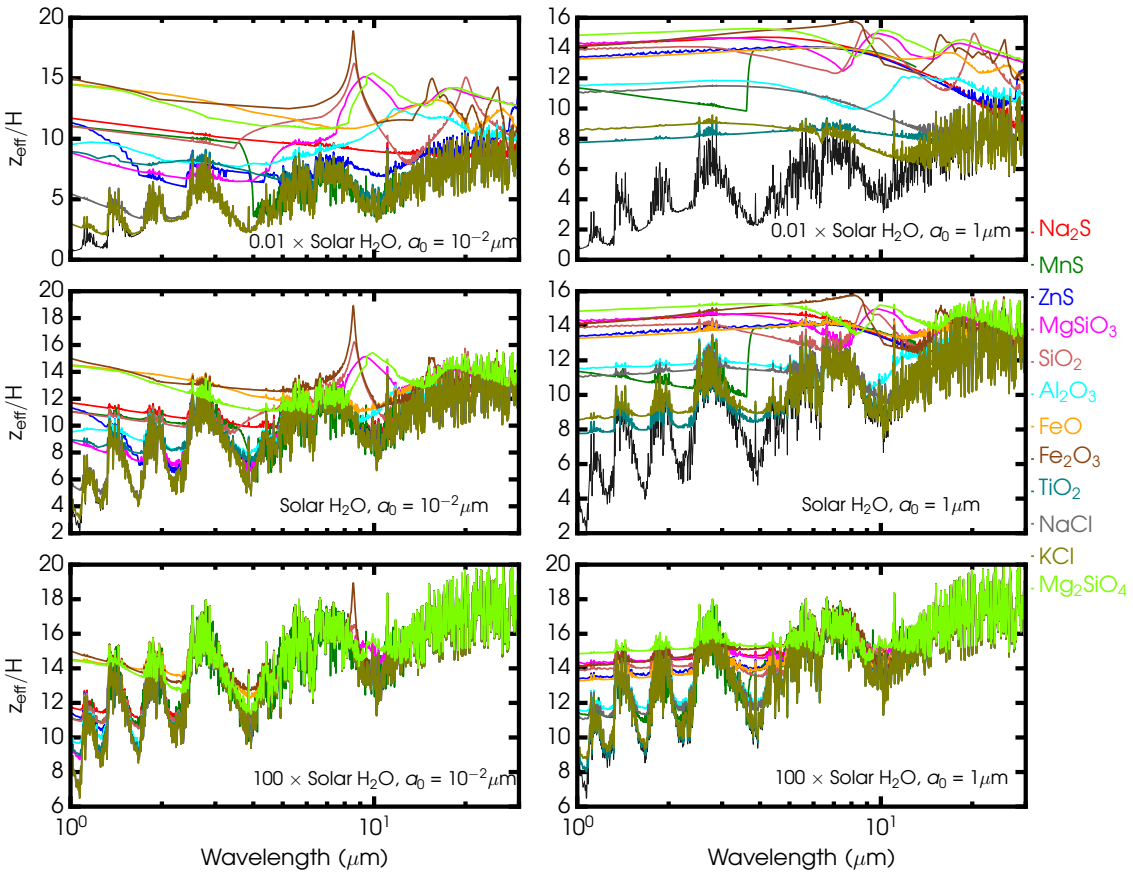

Figure 3.4: Model transmission spectra of cloudy hot Jupiter atmospheres in the infrared. The models contain opacity due various cloud species, H_2O, H_2-H_2 CIA, and H_2-He CIA. Each panel represents a particular distribution of cloud particle sizes and atmospheric H_2O abundance and assumes $H_c = H$. The black curves show reference cloud-free models.

strength and appearance of condensate features in the infrared. Figure 3.4 shows transmission spectra for six scenarios ranging over H_2O abundances of $10^{-2}\times$ solar, solar, and $100\times$ solar and cloud modal particle sizes of 10^{-2} and 1 μm. The six combinations illuminate significant cloud signatures that are observable with facilities capable of high-precision spectra in the infrared (e.g., the *JWST*).

1. **Solar H_2O, small a_0:** Figure 3.4 shows four cloud species dominate the spectrum for small cloud particles and solar H_2O abundances. These species are SiO_2, Fe_2O_3, $MgSiO_3$, and Mg_2SiO_4. SiO_2 and Fe_2O_3 have strong specral features at $8-9$ μm, and $MgSiO_3$ and Mg_2SiO_4 have overlapping absorption signatures at $\sim$10 μm. The lower condensation temperature of Fe_2O_3 compared to SiO_2 makes distinguishing between the two possible. On the other hand, $MgSiO_3$ and Mg_2SiO_4 have similar condensation temperatures. Distinguishability between these may come from the amplitude between optical and infrared observations since $MgSiO_3$ possesses a larger amplitude by a factor of $\sim$4. All four cloud types are of unique interest because their features occur where there is little contribution from H_2O absorption (i.e., in the valley between two H_2O absorption bands).

2. **Subsolar H_2O, small a_0:** Lower abundances of water vapour reveal more subtle features for the four condensates compared with case (1). SiO_2, Fe_2O_3, $MgSiO_3$, and Mg_2SiO_4 display additional absorption features at wavelengths beyond $\sim$12 μm. $MgSiO_3$ and Mg_2SiO_4 have coincident features at $\sim$18 μm which may again be distinguished by the difference in optical-infrared amplitudes. An SiO_2 peak at 19 μm lies in the valley between two prominent Fe_2O_3 peaks at $\sim$15 μm and $\sim$22 μm, helping to distinguish between the overlapping features in the $\sim 8-9$ μm region. The steep MnS feature at $\sim$4 μm is significant due the contrast in amplitudes it creates in the optical and infrared.

3. **Solar H_2O, high a_0:** The main effect of increasing particle sizes is to transition Mie theory into the geometric limit. The extinction coefficient for large modal sizes approaches a constant value, as seen by the 1 μm curves in Figure

3.1. Increasing the particle sizes decreases the relative strength of the absorption features in cases (1) and (2). Interestingly, the MnS feature at $\sim$4 μm is inverted relative to case (2). This feature is remarkable because it is not due to absorption as is generally assumed of all condensate features in the infrared (Wakeford and Sing, 2015). The scattering and absorption refractive indices for MnS illustrate this feature is due to strong scattering for particle sizes of $\gtrsim 0.1$ μm (see MnS panel in Figure 1 of Wakeford and Sing, 2015). The case of MnS demonstrates the mistake of this typical assumption, suggesting that scattering dominates the cloud opacity for large particle sizes.

4. **Subsolar H_2O, high a_0:** Transit spectra of atmospheres with depleted water abundances and large cloud particles are relatively flat with low-amplitude gas features. As in case (3), the amplitude of condensate signatures are damped with respect to smaller particles but the multiple spectral features of different species in case (2) are present. The Al_2O_3 band from $10 - 20$ μm appears for subsolar water abundances and across all particle sizes. As observed by Wakeford and Sing (2015), sulphides and chlorides have no prominent features at wavelengths beyond $\sim$4 μm.

5. **Supersolar H_2O:** H_2O abundances at 100$\times$ the solar value generally extinguish all cloud features in the infrared. For small modal particle sizes, the vibrational absorption peak of Fe_2O_3 at $\sim$9 μm is still distinguishable from the large-amplitude H_2O features. On the other hand, no cloud features are present for large modal sizes. Condensates for which the opacity is large compared to the H_2O opacity exhibit flat spectra in the near infrared.

Our Figure 3.4 shows there are no spectral features of sulphide and chloride species (i.e., Na_2S, ZnS, KCl, and NaCl) even in the most promising scenario of subsolar H_2O abundances. This allows us to make predictions for planets suggested to host these cloud species, such as GJ 1214b (Kreidberg et al., 2014b) and HD 95678b (Knutson et al., 2014c). The transit spectra of GJ 1214b and HD 95678b between 1.1 and 1.7 μm are consistent with being flat. Our work suggests this may be due to KCl clouds

Planet	Predicted Condensates	Observed slope $\mathcal{S}_{sd}$	$T_{\rm eq}$ (K)
HAT-P-12b	None	-2.24 ± 2.88	960
WASP-39b	MnS	-3.89 ± 1.28	1,120
WASP-6b	MnS	-4.14 ± 1.36	1,150
HD 189733b	MnS	-7.94 ± 0.61	1,200
HAT-P-1b	MnS	-4.11 ± 1.73	1,320
HD209458b	$MgSiO_3$ and Mg_2SiO_4	-3.04 ± 0.54	1,450
WASP-31b	$MgSiO_3$ and Mg_2SiO_4	-5.52 ± 1.27	1,580
WASP-17b	Al_2O_3	-4.25 ± 1.03	1,740

Table 3.2: Properties of eight hot Jupiters. Listed are the predicted clouds in the observable atmosphere (i.e., at ∼1 mbar), the slopes of the Sing et al. (2016) observations in the $0.3 - 0.56$ μm range, and the planetary equilibrium temperatures. The predicted condensates are obtained by considering atmospheric pressures between 10^{-1} and 10^{-3} bar and the planetary-averaged $p - T$ profiles in Figure 2 of Sing et al. (2016).

with a modal particle size of 1 μm and subsolar water abundances or Na_2S and ZnS with subsolar to solar water abundances. The *JWST* will be capable of observing these planetary atmospheres at wavelengths longer than 2 μm. Figure 3.4 predicts that future observations of GJ 1214b and HD 95678b should display a decrease at wavelengths greater than 9 μm if indeed Na_2S, KCl, or ZnS clouds are present in their atmospheres.

Our analysis of condensate signatures in the infrared reveals four cloud species as the most promising for spectroscopic identification with the *JWST*: SiO_2, Fe_2O_3, $MgSiO_3$, and Mg_2SiO_4. One instrument aboard the *JWST*, the *Mid Infrared Instrument (MIRI)*, will be especially important for identifying these species. *MIRI* will span the window of 5 to 29 μm with sufficient precisions to distinguish their signatures (Greene et al., 2016).

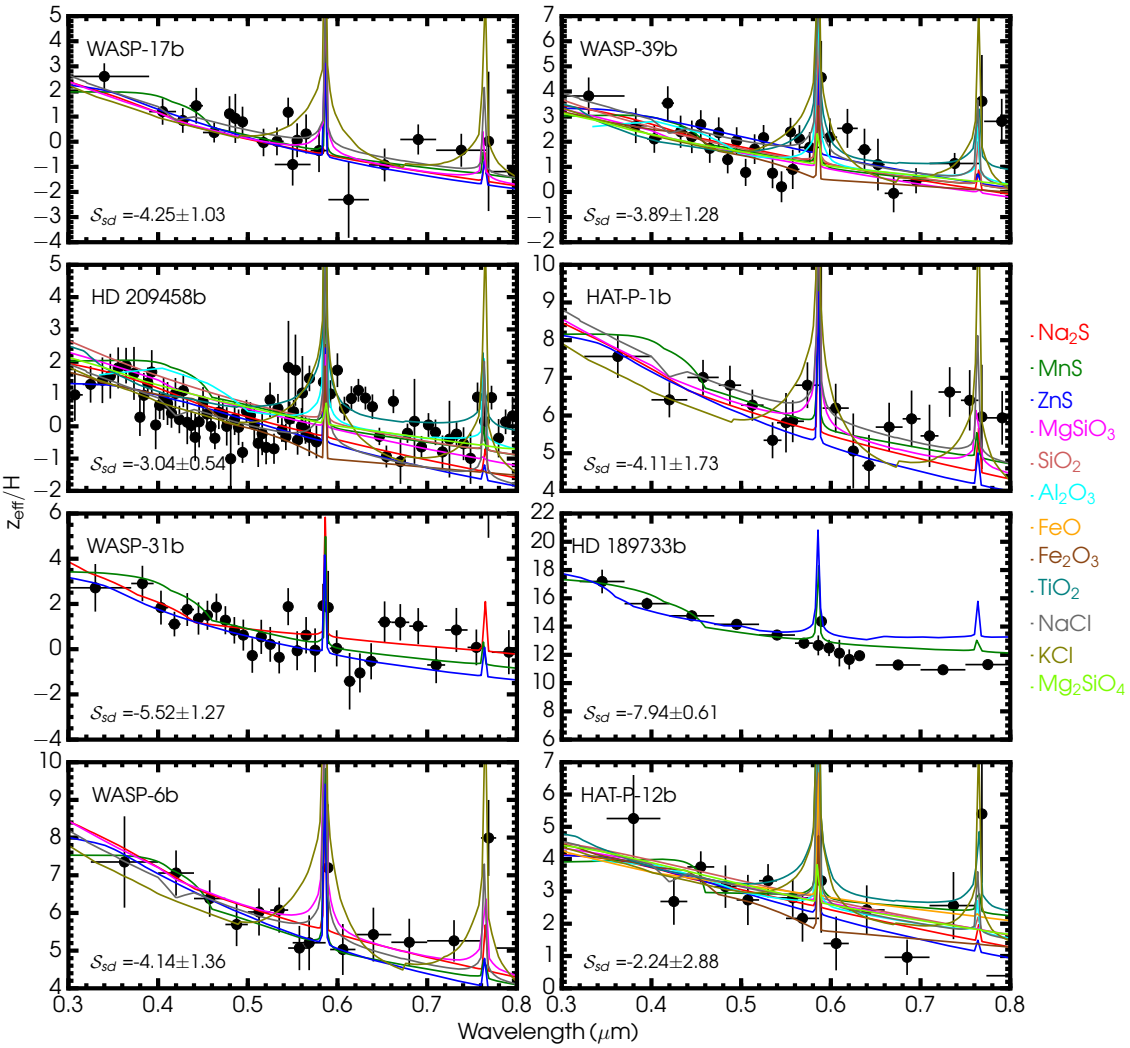

Figure 3.5: Model transmission spectra of cloud species compared with observations from Sing et al. (2016) for eight hot Jupiters. The planets include WASP-17b, WASP-39b, HD 209458b, HAT-P-1b, WASP-31b, HD 189733b, WASP-6b, and HAT-P-12b. The slope of the Sing et al. (2016) data with its associated uncertainty in the $0.30 - 0.56$ μm range is given by $\mathcal{S}_{\rm sd}$ in each panel.

3.3 Application to Current Observations

We apply the metric from Section 3.2.1 to observations of eight hot Jupiters. In particular, we concentrate on two hot Jupiters with the most precise observations: HD 189733b and HD 209458b. We find that the spectral precisions for the six other planets allow for degenerate solutions of cloud properties, and conveys the importance of improved precisions (e.g., through multiple-orbit *HST* observations). Our models of HD 209458b and HD 189733b illustrate the need for higher quality data from future facilities such as the *JWST* and the *ELTs*.

Figure 3.5 shows our cloud models compared with observations of eight hot Jupiters from Sing et al. (2016). Although Sing et al. (2016) consider ten hot Jupiters in their study, we do not include WASP-12b and WASP-19b since their atmospheric temperatures are much hotter than the condensation temperatures for the cloud species in Table 3.1. The set of models for each planet are calculated assuming $H_c = H$ and use our results in Figure 3.2 to identify the modal size of cloud particles which reproduces the mean slope of the observations (see Table 3.2). We also assume an isothermal temperature profile valued at the equilibrium temperature of each planet (see Table 3.2). We choose an $H_c = H$ for our models because condensate species are shown to experience strong mixing in hot Jupiter atmospheres (Parmentier et al., 2013). The models fit the observed spectra for the majority of hot Jupiters, yet the precisions on the observations allow for degenerate fits ranging over different a_0 and cloud compositions. In particular, we find multiple indistinguishable fits for WASP-17b, WASP-39b, HAT-P-1b, WASP-31b, WASP-6b, and HAT-P-12b.

3.3.1 HD 189733b and HD 209458b

Here we focus on the analysis of two hot Jupiters with the highest-quality observations, HD 189733b and HD 209458b. Figure 3.6 shows model transmission spectra for HD 189733b and HD 209458b compared to the Sing et al. (2016) observations.

The observed spectrum of HD 189733b is a challenge to understand since it is

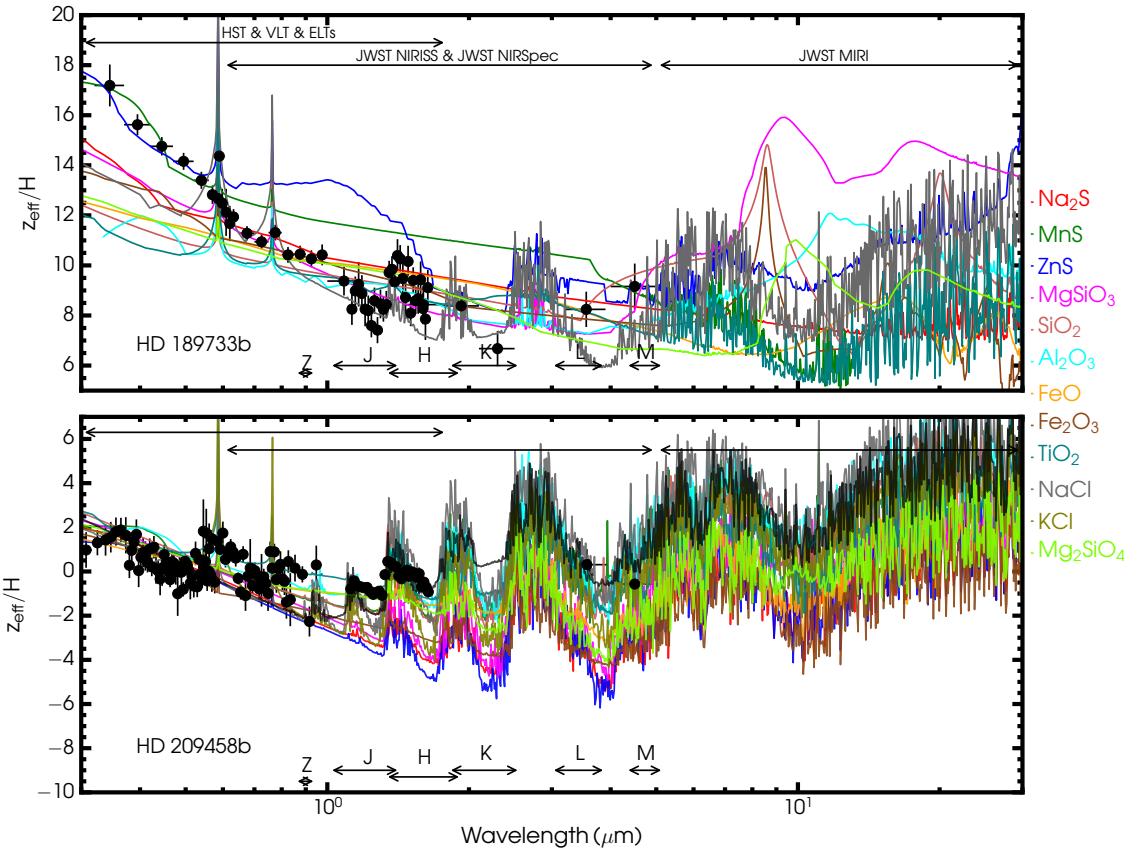

Figure 3.6: Cloud model spectra compared with observations of HD 189733b and HD 209458b. Each coloured model represents an H_2-rich atmosphere with a certain cloud species and additional opacities due to H_2O, H_2-H_2 CIA, H_2-He CIA, Na, and K. The cloud parameters for each model are chosen to fit the data using the metric of Figure 3.2. HD 189733b and HD 209458b models have 0.01× solar and super-solar H_2O abundances, respectively. The black curve is a benchmark model with no condensates nor Na and K opacity, but includes 0.01×solar H_2O, and H_2-H_2 and H_2-He CIA opacity. The black circles show data from Sing et al. (2016).

not fit well by any single cloud species. MnS and ZnS fit the optical spectrum below 0.6 μm, but slope upwards at longer wavelengths and hence overall provide a poor fit to the full spectrum. A preliminary investigation using combinations of species (i.e., two or more) also do not show improved fits to the observations. The work of Lecavelier Des Etangs et al. (2008) suggests that the *HST* data between 0.55 and 1.05 μm is due to sub-micron $MgSiO_3$ particles. On the other hand, Vahidinia et al. (2014) discuss the effects which the bases of clouds have on transmission spectra and suggest that the steepness of the slope below 0.6 μm weakens the role of $MgSiO_3$. Our work finds a similar conclusion to that of Vahidinia et al. (2014) since Figure 3.6 shows that the steepness of the slope at wavelengths below 0.60 μm cannot be fit with sub-micron $MgSiO_3$ particles. More sophisticated three-dimensional radiative-hydrodynamical simulations also find it challenging to fit the steep slope in the optical (e.g., see Figure 3 of Dobbs-Dixon and Agol, 2013)

The lack of an overall fit to the HD 189733b observations may suggest the influence of stellar activity on the spectrum. The planet's host star shows significant activity in the form of variations in the observed photometry at the 3 percent level which is attributed to cool spots and hot faculae rotating in and out of view (Sing et al., 2011). Starspots which are unocculted by the transiting planet and occulted plages can induce variations in the optical transmission spectrum which could match the observed slope below 0.6 μm (Oshagh et al., 2014; McCullough et al., 2014). A combination of plage occultations and/or unocculted starspots together with one or several cloud species could potentially fit the observations. Alternatively, the steep slope may be due to another cloud species not considered in our study.

On the other hand, the spectrum of HD 209458b allows for similar model fits in the optical for nearly all cloud species. However, the cloud spectra are unable to provide good fits in the infrared. The poor fit between the cloud models and observations might suggest inhomogeneous cloud coverage along the limb of the planet. Indeed, MacDonald and Madhusudhan (2017a) conducted a retrieval analysis of the same optical spectrum of HD 209458b and obtained a γ of $-15.03^{+4.65}_{-3.36}$. Together with the optical slope of $\mathcal{S}_{sd} = -3.04 \pm 0.54$ (see Table 3.2), the cloud scale height is

$\mathcal{S}/\gamma = H_c/H = 0.20^{+0.14}_{-0.06}$. A $H_c/H = 0.20$ supports the suggestion for inhomogeneous cloud coverage in the atmosphere of HD 209458b since our one-dimensional cloud model shows that homogeneous clouds cannot be probed in transmission spectra for $H_c/H \lesssim 0.4$ (see Section 3.2.1).

The degeneracies and disagreements exposed between our cloud models and present observations of HD 189733b and HD 209458b call for higher-precision observations as well as more detailed approaches to cloud modeling in transit spectra. The latter can be met with present models which explore clouds with more sophistication, such as those of Helling and collaborators (e.g., see Helling et al., 2016). For example, the degeneracy among various parameters in our model (H_c, a_0, cloud composition, and abundances) for HD 189733b and HD 209458b can be mitigated through findings from a more realistic kinetic approach as illustrated in Figures 4 and 6 of Helling et al. (2016). Nevertheless, the three key observable metrics should be important to interpret cloud properties with higher-precision observations using facilities such as the *JWST* and the *ELTs*. Of the three observable cloud properties, cloud features in the infrared show the most immediate promise to characterising condensate properties given the launch of the *JWST* in 2021. Interpretation of the peculiarly steep slope of HD 189733b and HD 209458b's optical data currently observed with *HST* will benefit from the *JWST*'s broad infrared coverage, enabling the study of spectra as a whole from 0.6 μm to 30 μm.

3.4 Discussion

We have developed a model of transmission spectra for cloudy atmospheres and have investigated three observable metrics that can elucidate cloud properties with high-precision observations. However, our study finds that illuminating cloud properties in exoplanetary atmospheres requires higher-precision observations. There are also several facets of cloud physics which we have not considered, some of which should be incorporated into more sophisticated models in the future.

Cloud particles can form either from direct condensation from supersaturated

vapour or by condensing onto particles of a different composition in processes called homogeneous nucleation and heterogeneous nucleation, respectively. Our model assumes a homogeneous creation of cloud particles since the particles are assumed to be composed of a single material. However, heterogeneous cloud particles are also expected to be present in exoplanetary atmospheres, especially in Earth-sized planets where sub-micron particles from the rocky surfaces should act as efficient seed particles for heterogeneous nucleation (Marley et al., 2013).

We have also not attempted to model the actual formation of cloud particles. Such a study may be necessary since the simplistic picture of all vapour condensing at saturation ratios of one is generally not true. Helling et al. (2016) studied the atmospheres of HD 209458b and HD 189733b using 3D cloud micro-physics models and showed that supersaturation ratios in excess of ten are needed to form clouds in hot Jupiter atmospheres (see also Figure 1 of Helling et al., 2008b). To this end and more generally, the cloud formation model of Helling and collaborators represents the most sophisticated and unassuming study of cloud formation in the atmospheres of sub-stellar mass objects (Woitke and Helling, 2003, 2004; Helling and Woitke, 2006; Helling et al., 2008a,b, 2014; Helling, 2018). The model considers the micro-physics of cloud formation and follows the kinetic evolution of chemically-heterogeneous condensate particles through a self-consistent treatment of nucleation, sedimentation, growth, evaporation, and hydrodynamical transport to provide the size, compositions, and number density of cloud particles throughout the atmosphere.

Finally, we have assumed spherical cloud particles as opposed to irregular particles (e.g., ellipsoids, discs, and fractals). The spherical assumption is idealised and yet serves as a tractable way of understanding extinction from solid/liquid particles. We have not considered extinction from particles of irregular shapes for two reasons. First, the domain of validity of modified Mie theories are not extensively tested and are not self-consistent in all cases (for more detail see Schuerman, 1980). For example, Schuerman (1980) shows that the modified Mie theory of Chylek et al. (1976) violates energy conservation and predicts total extinction cross-sections that are different from the scattering cross-sections for a purely real refractive index (i.e., no absorption),

a result which is unphysical. Second, even under the assumption of self-consistency, these modified theories are of limited practical use due to our ignorance about the shapes of particles in exoplanetary atmospheres

Finally, there are other semi-analytical cloud model formulations with which we can draw comparisons. An alternative formulation of the effective altitude in equation (3.2) is presented by de Wit and Seager (2013) through considering how much flux is absorbed in the planetary atmosphere. Their effective altitude is

$$z_{\text{eff}}(\lambda) = R_p(\sqrt{1+\aleph_0} - 1), \tag{3.21}$$

where

$$\aleph_0 \equiv \int_0^\infty \frac{2}{R_p}\left(\frac{z}{R_p}+1\right)(1-e^{-\tau(\lambda,z)})dz. \tag{3.22}$$

As the optical depth $\tau(\lambda, z)$ appears in the exponent and z is always greater or equal to zero, $z_{\text{eff}} \geq 0$ and $R_p(\lambda)$ (on the left-hand side of equation (3.2)) is always greater than or equal to the fiducial R_p. In this model R_p therefore acts as a hard surface, while in our model it is a reference radius for which z_{eff} can lie either below or above. The slope of the effective altitude in equation (3.21) across wavelength – and the model's analogue of equation (3.19) – is then

$$\frac{d(z_{\text{eff}}/H)}{d\ln\lambda} = \gamma\frac{\frac{\int_0^\infty (z/R_p+1)e^{-\tau}\tau dz}{(1+\aleph_0)^{1/2}}}{H} \equiv \gamma\eta \tag{3.23}$$

where γ is the exponent on the effective extinction cross-section, $\sigma' = \sigma_0(a)(\lambda/\lambda_0)^{\gamma(a,\lambda)}$. In the non-Rayleigh limit η equals to H_c/H but these two relations are not equal in the Rayleigh limit.[3] The effective altitude used in this work and those of Lecavelier Des Etangs et al. (2008) and Wakeford and Sing (2015) use R_p as a reference altitude for which a negative effective altitude is allowed. The formulation of de Wit and Seager (2013) outlined above is, by construction, such that R_p is a hard planetary surface for which the effective altitude can only lie above or at the surface. We have

[3]The Rayleigh limit relations for the absorption and scattering cross-sections are strictly applicable in the condition $|m(\lambda)|x << 1$ rather than the typically used $x << 1$ (Bohren and Huffman, 1983).

tested this and seen that as the slant optical depth decreases (e.g., by considering smaller particles dominating the extinction), de Wit and Seager (2013)'s model indeed asymptotically approaches the planetary surface without going below, unlike in this study and those of Wakeford and Sing (2015) and Lecavelier Des Etangs et al. (2008). It is important for a model to have R_p represent a reference altitude since its value is typically obtained by averaging across a broad wavelength range and thus in practice there may be wavelengths at which $\tau_{\text{eff}} = 0.56$ occurs below this fiducial radius.

3.5 Summary

We have investigated several observable metrics to characterise clouds in transmission spectra of exoplanetary atmospheres. These observable metrics include the slope in the optical wavelength range, the uniformity of this slope, and cloud features in the infrared. We have explored the first metric through the effects of cloud composition, modal particle size, and cloud scale height on the observable spectral slope in a clean window in the optical. Second, we have studied which cloud species produce uniform/non-uniform slopes in the optical given the quality of current observations. These two metrics will be valuable for the interpretation of high-precision optical observations. Finally, there are several cloud species with strong features in the infrared, a region that represents the most immediate practical promise in deciphering cloud properties given the forthcoming launch of *JWST*.

The study of optical slopes reveals that significantly steep slopes of $\mathcal{S} < -5$ could imply the presence of sulphide clouds (i.e., MnS, ZnS, and Na_2S) in an atmosphere. Slopes of $\mathcal{S} > -5$ are mostly degenerate for different cloud species and modal particle sizes at a given cloud scale height. The slopes are also degenerate with the cloud scale height, in that large modal particle sizes with large scale heights produce similar slopes as clouds composed of smaller particles with smaller scale heights. Below cloud scale heights of $H_c \approx 2H/5$, the effects of clouds become undetectable and the optical slopes of transmission spectra tend towards the H_2 Rayleigh scattering

value of -4.2. The properties of homogeneous clouds are therefore manifested in transmission spectra for $H_c \gtrsim 2H/5$. Cloud scale heights that are smaller than $0.4H$ suggest either inhomogeneous clouds or atmospheres dominated by H_2 Rayleigh scattering. Finally, a slope of about ~ -4 does not of itself suggest H_2 Rayleigh scattering since such a slope is produced in the Rayleigh regime for many cloud species with large scale heights (e.g., sulphides and chlorides). One obvious path to resolving these degeneracies is through knowledge of the temperature structure obtained from retrieval methods.

Optical spectral observations of transiting exoplanets are usually modeled with simple cloud prescriptions using uniform power-law slopes (e.g., Sing et al., 2016). However, the extinction profiles of some cloud species show non-uniform slopes in the optical. For example, MnS grains of sizes $\sim 10^{-2}$ μm feature an absorption trough at ~ 0.5 μm leading to a distinctly non-uniform shape. Four of the twelve cloud species considered in this study have non-uniform slopes in the optical: MnS, ZnS, Fe_2O_3, and TiO_2. Future high-precision observations in the optical should enable honed constraints on the cloud properties through considering species which show substructure in optical slopes and those which are significantly linear. Species can then be further constrained through the first and third observable metrics.

Infrared observations are poised to disambiguate interpretations made from the optical region alone. Cloud infrared features can be due to both absorption and scattering. For example, MnS clouds with modal particle sizes greater than 0.1 μm contribute to extinction at ~ 4 μm through scattering. The cloud features most amenable for future spectral interpretation are those which are observable across a wide range of volatile gas abundances. These include four cloud types: SiO_2, Fe_2O_3, Mg_2SiO_4, and $MgSiO_3$. For solar-composition water abundances, SiO_2 and Fe_2O_3 have narrow peaks between 8 and 9 μm and Mg_2SiO_4 and $MgSiO_3$ possess broader features across 8 to 12 μm.

We have applied these metrics to current observations of eight hot Jupiters. For six of the planets the current precisions on the spectra allow for a wide range of solutions, suggesting the need for higher-precision spectra. For the planets with the most precise

data, HD 209458b and HD 189733b, we find degenerate fits to the optical spectrum of HD 209458b and the full spectrum of HD 189733b is challenging to explain by any one of the considered cloud species. Our work highlights the overall importance of broadband (i.e., optical-infrared) high-precision transmission spectra as well as detailed theoretical models for reliable inferences of cloud properties in transiting exoplanetary atmospheres. Dedicated observations with current space- and ground-based facilities (e.g., *HST* and *VLT*) as well as upcoming facilities (e.g., *JWST*, *ELTs*) promise new advancements in this direction. The three empirical metrics presented in our current work can prove useful in cloud characterisations exoplanetary atmospheres using high-precision transmission spectra.

Chapter 4

Retrieval of Exoplanetary Atmospheres

In this chapter we discuss the retrieval approach to studying exoplanetary atmospheres, namely the procedure for estimating the atmospheric properties from observed spectra of exoplanets. The retrieval approach aims to obtain statistical constraints on the properties of an atmosphere from an observed spectrum of an exoplanet. This is achieved by constructing a parametric model of a planet's atmosphere which is combined with a parameter-estimation algorithm that samples over these model parameters in order to infer the most likely estimates of atmospheric properties given the data. Typical properties explored in a retrieval are the compositions and abundances of chemical species and the temperature structures of atmospheres. The first retrieval method developed for the interpretation of exoplanetary atmosphere observations was by Madhusudhan and Seager (2009). The retrieval methods that have arisen since are mostly distinguished by the sophistication of the algorithms used to sample the large number of model parameters and estimate their probability distributions.

The retrieval methods used in this thesis are adapted from the retrieval method of Gandhi and Madhusudhan (2018). The retrieval method of Gandhi and Madhusudhan (2018) is specific to emission spectra in the secondary eclipse geometry and we have therefore made several modifications to the method before an applica-

tion to spectra of transiting planets in the primary eclipse geometry as well as to emission spectra of directly-imaged objects. In the case of spectra of transiting planets in the primary eclipse geometry, we have developed a separate radiative transfer model for the passage of stellar light along the day-night terminator of a planet and have also adopted additional prescriptions for clouds and hazes from MacDonald and Madhusudhan (2017a). The retrieval method for emission spectra of directly-imaged objects differs from the method in Gandhi and Madhusudhan (2018) only in that the former requires the flux from the object alone, whereas the flux of the planet is divided by the flux of the star for secondary eclipse spectra (Gandhi and Madhusudhan, 2018). These methods are used in five studies which characterise the atmospheres of exoplanets and are presented in Chapters $5-8$.

Here we present the retrieval methodology and outline the structure of several new Bayesian retrieval methods for observations of transiting and directly-imaged planets adapted from Gandhi and Madhusudhan (2018). Retrieving model parameters for spectral observations of transiting and imaged objects requires two basic components: a parametric model of a planetary atmosphere and a statistical sampling method for the model parameters. These are outlined here in turn. A condensed illustration of the retrieval methodology is shown in Figure 4.1.

4.1 Parametric Model

4.1.1 Pressure-Temperature Profile

The pressure-temperature ($p-T$) profile of a planetary atmosphere is calculated through the parametric relations in Madhusudhan and Seager (2009). The $p-T$ profile is able to fit various planetary atmosphere structures, mimicking atmospheric conditions of solar system planets as well as exoplanetary atmosphere models in the literature. The atmosphere is sectioned into three zones with the following equations

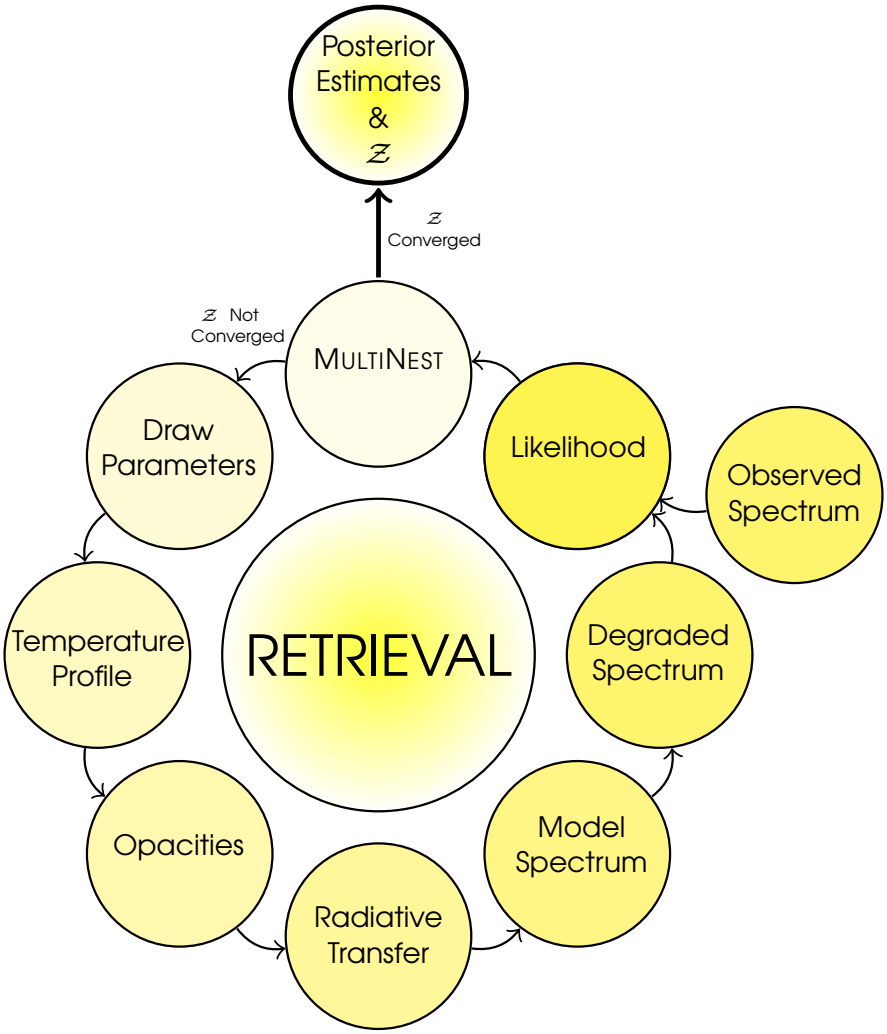

Figure 4.1: Illustrated retrieval methodology. Model parameters are drawn using the MULTINEST sampling algorithm and used to generate the temperature profile throughout the atmosphere. The temperature profile informs the relevant opacities which are used to evaluate the transfer of stellar radiation through the planetary atmosphere in the case of transiting planets in the primary eclipse geometry, or the transfer of thermal radiation (i.e., self-luminosity) in the case of transiting planets in the secondary eclipse geometry as well as directly-imaged planets. The model spectrum is then convolved and binned, degrading the model spectrum to the quality of the observed spectrum. The relevance of the degraded model is then straightforwardly compared with the observed spectrum via the likelihood. The likelihoods are ascertained with the MULTINEST nested sampling algorithm which maneuvers through the space of model parameters and finds those with highest likelihoods. Once convergence is achieved on the 'evidence' statistic ($\mathcal{Z}$), MULTINEST stops its iterative search and returns the final evidence and parameter estimates.

for the temperature,

$$T = T_0 + \left(\frac{\ln(P/P_0)}{\alpha_1}\right)^2 \quad P_0 < P < P_1 \tag{4.1}$$

$$T = T_2 + \left(\frac{\ln(P/P_2)}{\alpha_2}\right)^2 \quad P_1 < P < P_3 \tag{4.2}$$

$$T = T_2 + \left(\frac{\ln(P_3/P_2)}{\alpha_2}\right)^2 \quad P > P_3 \tag{4.3}$$

A schematic of the profile is illustrated in Figure 1 of Madhusudhan and Seager (2009). The free parameters of the temperature profile are T_0, the temperature at the top of the atmosphere; α_1 and α_2, values responsible for gradients in the temperature profile; and P_1, P_2, and P_3 which define the distinct atmosphere layers and generally determine the presence of a thermal inversion. In the case of no thermal inversion the pressure parameters satisfy $P_2 \leq P_1 < P_3$, whereas those for thermally-inverted atmospheres obey $P_1 < P_2 < P_3$.[1] We partition our model atmosphere into 100 layers spaced equally in the logarithm of pressure between 10^{-6} bar and 10^2 bar. The upper pressure value of 10^{-6} bar represents the region where molecules become rarefied and thus no longer contribute appreciable opacity (Moses et al., 2011; Moses, 2014).

4.1.2 Gaseous Sources of Opacity

In addition to the temperature structure of the atmosphere, the general retrieval forward model contains a suite of chemical species in the atmosphere that absorb and scatter incident light. In the case of transmission spectra the light is from the star, while for emission spectra (i.e., for transiting planets in secondary eclipse as well as directly-imaged objects) the light is the thermal radiation of the object itself. Our model considers eight gaseous species: Na, K, H_2O, CO, CH_4, CO_2, HCN, and

[1] We note that the condition for Rayleigh-Taylor instability (i.e., fluid motion resulting from the gravitational force acting on an inverted density gradient) is $d\ln p > d\ln T$ by evaluating $d\rho/dr > 0$ (cf. equation (4.5)). The logarithmic nature of this condition means that an atmosphere would be unstable to Rayleigh-Taylor motion if the temperature changes drastically within a small region of atmosphere with a small drop in pressure; for example, a temperature drop from 3,000 to 1,000 K over a pressure range of only $10^{-2} - 10^{-2.5}$ bar could trigger instability. Strong thermal gradients produced by thermal inversions could in principle generate an such an instability, though in practice such retrieved profiles have not been observed using this parameterisation.

NH_3. We choose these species since they are shown to be significant contributors of opacity in the atmospheres of transiting planets and directly-imaged objects in the spectral range of observations between 0.3 and 5 μm (Madhusudhan, 2012; Moses et al., 2013; Venot and Agúndez, 2015). The volumetric mixing ratio of each species, $X_i = n_i/n_{\rm tot}$, is assumed uniform in the atmosphere and each is a free parameter in the retrieval framework. The volumetric mixing ratio of H_2 is calculated assuming a H_2-He dominated atmosphere with a solar composition $X_{\rm He}/X_{\rm H_2}$ ratio of 0.18 (derived from Asplund et al., 2009) and requiring the sum of relative abundances be unity, $X_{\rm H_2} = (1 - \Sigma_{i,i\neq{\rm He}} X_i)/(1 + X_{\rm He}/X_{\rm H_2})$, where i denotes one of the eight molecules above. The volumetric mixing ratios and masses of all the chemical species are used to compute the mean molecular mass of the atmosphere,

$$\mu_m = \sum_k m_k X_k. \tag{4.4}$$

This mean molecular mass and the atmospheric temperature profile provide the gas mass and number densities throughout the atmosphere under the assumption that the gas is ideal:

$$\rho(T) = \frac{P(T)\mu_m}{k_b T} \tag{4.5}$$

and

$$n_{\rm tot}(T) = \frac{\rho(T)}{\mu_m}. \tag{4.6}$$

We consider line absorption from the above chemical species and collision-induced absorption (CIA) from H_2-H_2 and H_2-He. The molecular cross-sections for CH_4, HCN, and NH_3 are computed from EXOMOL line data (Tennyson et al., 2016) and line data for H_2O, CO, and CO_2 are obtained from HITEMP (Rothman et al., 2010). The CIA line data are sourced from the HITRAN archive (Richard et al., 2012) (with the original CIA line data from Borysow et al. (1988) and Borysow (2002)). These line data are applied with a Voigt function to incorporate both temperature (Doppler) and pressure broadening. The computed molecular cross-sections are binned to a resolution of 0.01 $\rm cm^{-1}$ on a pre-defined temperature and pressure grid spanning

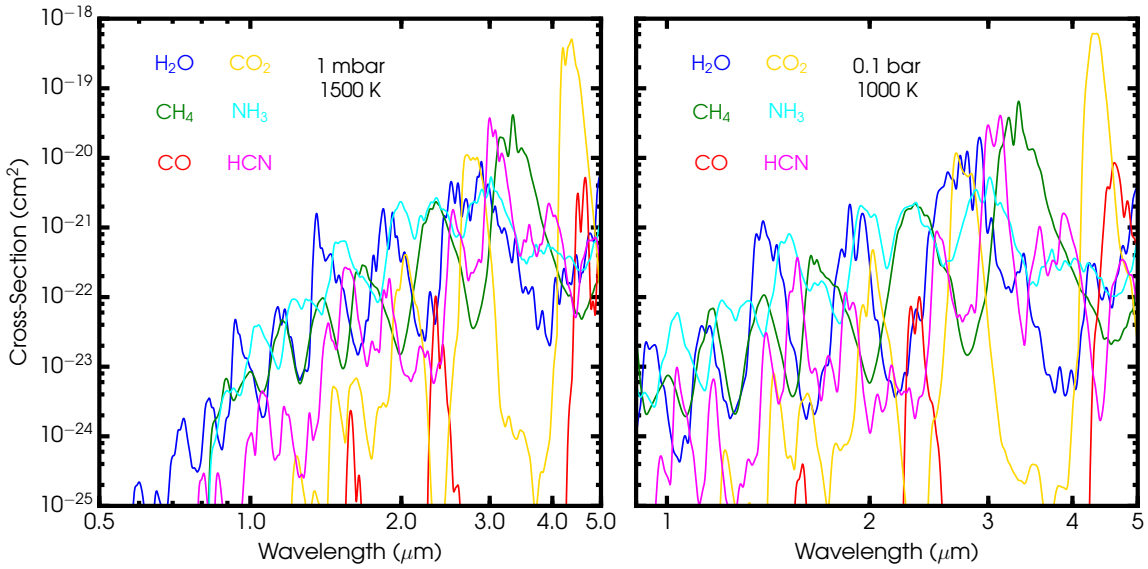

Figure 4.2: Cross-sections of molecular species. Left panel: Cross-sections of H_2O, CO, CH_4, CO_2, HCN, and NH_3 in the wavelength range relevant for transmission spectra. The temperature is typical of transiting hot Jupiters and the pressure indicates the region where the slant optical depth is about 1. Right panel: Cross-sections of H_2O, CO, CH_4, CO_2, HCN, and NH_3 in the wavelength range relevant for spectra of directly-imaged objects. The temperature is typical of imaged companions and the pressure indicates the region where the optical depth is about 1. In both cases the cross-sections are smoothed for clarity.

10^{-5} to 10^{2} bar and 300 – 3500 K. The established grid is interpolated to extract the cross-section for a general temperature, pressure and wavelength. A complete description of molecular cross-section calculations from the latest available line-list data as used in our work is presented in Gandhi and Madhusudhan (2017). Figure 4.2 shows the cross-sections for chemical species at 1500 K and 1 mbar as well as 1000 K and 0.1 bar. These temperatures represent typical regimes for transiting and directly-imaged planets, respectively. The pressures indicate the photospheric regions where the optical depths are $\sim$1.

The molecular cross-sections thus obtained are evaluated at each $p-T$ point of the atmosphere along the path of a light ray. The contributions from all species are summed at each point and weighted by their mixing ratios X_i to give the total extinction coefficient κ and differential optical depths $d\tau$ throughout the whole

atmosphere,

$$\kappa(p,T,\lambda) = \sum_i X_i n_{\rm tot}(p,T)\,\sigma_i(p,T,\lambda) + X_{\rm H_2} n_{\rm tot}(p,T)\sigma_{\rm H_2}(\lambda) + \sum_j X_{\rm H_2} X_j n_{\rm tot}^2 \sigma_{\rm H_2-j}(T,\lambda), \tag{4.7}$$

$$d\tau(p,T,\lambda) = -\frac{dp}{\rho g}\kappa(p,T,\lambda). \tag{4.8}$$

Here, the first term of equation (4.7) contributes extinction from molecular species and alkali metals, the second term represents H_2 Rayleigh scattering, and the third term serves for CIA extinction from interactions between H_2 and He such that $j \in \{H_2, He\}$. The CIA 'cross-section' σ_{H_2-j} has units of $[m^{-1}amagat^{-2}]$ or $[m^5]$. In the case of transmission spectra, $d\tau$ represents the differential optical depth to stellar light at each slant path in the atmosphere, while for emission spectra $d\tau$ is the differential optical depth to thermal planetary light along the path of a ray out from the atmosphere.

4.1.3 Cloud and Haze Opacity

Spectral observations of exoplanets have suggested clouds and hazes across a wide spectrum of planetary types (e.g., Kreidberg et al., 2014b; Knutson et al., 2014b; Sing et al., 2016; MacDonald and Madhusudhan, 2017a). The terms 'clouds' and 'hazes' are typically used in specific contexts in the literature. From a formation standpoint, 'hazes' imply particles formed through photochemical processes whereas a 'cloud' constitutes particles formed through condensation of vapour onto seed particles under suitable thermodynamic conditions (Marley et al., 2013). Hazes and clouds typically constitute small and large particles, respectively, where the distinction in particle size occurs at $\sim$0.1 μm (see Section 5.2.6 of West et al., 2004).

In the case of transmission spectra, these terms are also generally used in reference to the morphology of spectral features they produce, especially in parametric models used for atmospheric retrieval (e.g., Benneke and Seager, 2012; Kreidberg et al., 2014d; Sing et al., 2016; MacDonald and Madhusudhan, 2017a). A 'cloud' is generally used to mean a source of grey opacity from particle sizes greater than $\sim$1 μm present to a

certain height in an atmosphere, while a 'haze' is represented by a non-grey opacity in the optical wavelength region through a power-law dependence on wavelength and is present at higher altitudes (e.g., MacDonald and Madhusudhan, 2017a). In essence, hazes produce Rayleigh-like slopes in the visible spectral range and clouds produce a grey opacity throughout the spectrum.

The transmission retrieval model includes a parameterisation for inhomogeneous clouds and hazes according to their definitions in the above paragraph. The extinction coefficient which broadly incorporates these two spectral effects is given by (MacDonald and Madhusudhan, 2017a),

$$\kappa_{\rm cloud/haze}(p) = \begin{cases} n_{\rm H_2}(p) a \sigma_0 (\lambda/\lambda_0)^{\gamma} & \text{if } p < P_{\rm cloud} \\ \infty & \text{otherwise} \end{cases} \tag{4.9}$$

where the first relation represents a slope in the optical due to hazes and the second equality represents an opaque grey opacity across all wavelengths for clouds. Here, λ_0 is a reference wavelength (0.35 μm), σ_0 is the H_2 Rayleigh scattering cross-section at λ_0 ($5.31 \times 10^{-31} \mathrm{m}^2$), a is the 'Rayleigh-enhancement factor' and γ is the 'scattering slope'. The Rayleigh-enhancement factor determines the offset level of the optical transmission spectrum. Therefore three cloud/haze parameters in the retrieval model are a, γ, and $P_{\rm cloud}$. The fourth cloud/haze parameter $\bar{\phi}$ describes the cloud and haze contribution at the limb of a planet and enters into the transmission spectrum as

$$\Delta_{\rm planet}(\lambda) = \bar{\phi} \Delta_{\rm cloud/haze}(\lambda) + (1 - \bar{\phi}) \Delta_{\rm clear}(\lambda). \tag{4.10}$$

where $\Delta_{\rm cloud/haze}$ ($\Delta_{\rm clear}$) are the transit spectra computed with (without) incorporation of clouds and hazes. A terminator completely covered with clouds/hazes has $\bar{\phi} = 1$ while a clear atmosphere along the terminator has $\bar{\phi} = 0$. A terminator with $0 < \bar{\phi} < 1$ contains patchy or inhomogeneous clouds and hazes.

4.1.4 Radiative Transfer

4.1.4.1 Transmission Spectra

The final component of an atmospheric model for transiting planets is a way to calculate the transmission of stellar light through its atmosphere. As an exoplanet transits its host star, incident stellar light filters through the planetary atmosphere and experiences differential extinction across wavelength due to absorption and scattering from gas and solid particles. The observed transmission spectrum is modeled through consideration of pencil rays travelling through each layer in the atmosphere. The transit depth components in equation (4.10) are computed according to

$$\Delta_j(\lambda) = \frac{R_{\rm p}^2 + 2\int_{R_{\rm p}}^{R_{\rm p}+H_{\rm A}} b\,(1 - e^{-\tau_{s,j}(b,\lambda)})\,db - 2\int_0^{R_{\rm p}} be^{-\tau_{s,j}(b,\lambda)}db}{R_\star^2}. \tag{4.11}$$

This equation is adopted from the appendix of MacDonald and Madhusudhan (2017a). Here, $j \in \{\text{cloud/haze, clear}\}$ and denotes the component in equation (4.10), $R_\star$ is the stellar radius, $H_{\rm A}$ is the maximal atmospheric altitude (i.e., at 1 μbar), b is the impact parameter perpendicular to the line-of-sight, and $\tau_{s,j}$ is the total slant optical depth for component j at b. As such, $\tau_{s,j}(b,\lambda)$ is the integral of equation (4.8) over slant length s. The variable planetary radius with wavelength in equation (4.11) can be understood physically. The first term is achromatic absorption from an opaque planetary radius. The second term accounts for chromatic extinction of incident light rays above the fiducial $R_{\rm p}$, and the third term accounts for rays whose atmospheric optical depth becomes low below the assumed fiducial radius $R_{\rm p}$.

4.1.4.2 Emission Spectra

In contrast to transmission spectra, emission spectra represent the self-luminosity (i.e., thermal heat) of a planet. The observed spectrum is therefore the light energy originating from deep within an object and modulated by its overlying atmosphere.

We model the emergent thermal spectrum as follows. Thermal rays originating deep within an object are attenuated by molecular absorbers and enhanced by emis-

sion from each layer in the atmosphere. The spectrum of thermal rays that emanate from the top of the atmosphere is expressed succinctly as

$$I^{\rm top}_{\lambda,\mu} = I^{\rm bottom}_{\lambda,\mu} e^{-\tau/\mu} + \frac{1}{\mu}\int_0^\tau S_\lambda e^{-\tau/\mu} d\tau. \tag{4.12}$$

The first term represents absorption and scattering of light throughout the atmosphere and the second term represents a contribution to the intensity from emission in atmospheric layers. Here $I^{\rm bottom}_{\lambda,\mu}$ is the specific intensity at the atmosphere's bottom (10^2 bar), S_λ is the source function responsible for emission at each layer and is the Planck function assuming local thermodynamic equilibrium, $I^{\rm top}_{\lambda,\mu}$ is the emergent intensity at the top of the atmosphere (i.e., 10^{-6} bar), and $\mu = \cos\theta$ is the projection of an outgoing ray with angle θ onto the vector pointing towards the observer.

We discretise equation (4.12) for a numerical solution. Starting from a thermal Planck spectrum for $I^{\rm bottom}_{\lambda,\mu}$ with a temperature of the $p-T$ profile at 10^2 bar, we evolve the spectrum through each layer in the atmosphere for all wavelengths and a projected angle μ according to

$$\Delta I^{N\rightarrow N+1}_{\lambda,\mu} = (I^N_{\lambda,\mu} - B_\lambda)(e^{\Delta\tau/\mu} - 1). \tag{4.13}$$

Here, $I^N_{\lambda,\mu}$ is the specific intensity at the bottom boundary of layer N and $\Delta\tau = \tau_{N+1} - \tau_N$ and is the differential optical depth between the bottom boundaries of layers N and $N+1$. The specific intensity in layer N is modulated by $\Delta I^{N\rightarrow N+1}_{\lambda,\mu}$ to obtain the intensity in the next layer, $I^{N+1}_{\lambda,\mu}$. We iteratively apply equation (4.13) at each successive atmospheric layer to follow the spectral evolution of the ray until it exits the last layer at 1 μbar. The total emergent spectrum is a weighted sum over all projected rays μ and is

$$F^{\rm top}_\lambda = 2\pi\int_0^1 I^{\rm top}_{\lambda,\mu}\mu d\mu. \tag{4.14}$$

The method of Gaussian quadrature (Press et al., 1992, section 4.5) is applied to

Rays	Weights (w')	Projected Angles (μ')
One	$\{1\}$	$\left\{\frac{1}{2}\right\}$
Two	$\left\{\frac{1}{2}, \frac{1}{2}\right\}$	$\left\{\frac{1}{2}+\frac{1}{2\sqrt{3}}, \frac{1}{2}-\frac{1}{2\sqrt{3}}\right\}$
Three	$\left\{\frac{5}{18}, \frac{4}{9}, \frac{5}{18}\right\}$	$\left\{\frac{1}{2}-\frac{1}{2}\sqrt{\frac{3}{5}}, \frac{1}{2}, \frac{1}{2}+\frac{1}{2}\sqrt{\frac{3}{5}}\right\}$
Four	{0.56, 0.78, 0.56, 0.78}	{ 0.43, −0.43, 0.76, −0.76 }

Table 4.1: Modified weights and projected angles for various numbers of emergent thermal rays.

equation (4.14) for a numerical evaluation,

$$\int_0^1 I_\lambda^{\rm top}(\mu)\mu d\mu \approx \sum_i \frac{w_i}{2}\left(\frac{\mu_i}{2}+\frac{1}{2}\right) I_\lambda^{\rm top}(\mu_i/2+1/2) \tag{4.15}$$

$$\equiv \sum_i w_i' \mu_i' I_\lambda^{\rm top}(\mu_i') \tag{4.16}$$

where the modified weights and modified projected angles are defined as $w_i' \equiv w_i/2$ and $\mu_i' \equiv \mu_i/2 + 1/2$, respectively. The w_i' and μ_i' are listed in Table 4.1 for several ray values. Finally, the observed flux is the emergent flux at the object radius $R_{\rm obj}$ but spherically attenuated by the distance d to the observer,

$$F_\lambda^{\rm obs} = F_\lambda^{\rm top}\left(\frac{R_{\rm obj}}{d}\right)^2. \tag{4.17}$$

We emphasise that a retrieval of spectra for imaged objects involves additional model parameters compared to one for transiting planets and is thus generally more challenging. In addition to estimating atmospheric properties such as the temperature structure, the gaseous chemical abundances, and the bulk cloud properties, macroscopic properties including the radius $R_{\rm obj}$, the mass $M_{\rm obj}$, and the distance d to the imaged object are generally not known a priori. These three macroscopic parameters are therefore included in any retrieval of imaged spectra and introduce a greater challenge into a retrieval analysis.

4.1.5 Model-Data Comparison

With an atmospheric retrieval model established from components 4.1.1 − 4.1.4 for a set of free parameters, it is necessary to ascertain its degree of fit to observations. The statistical comparison of a high-resolution model to observations involves two steps. First, the high-resolution spectrum generated from a set of free parameters is convolved with the point-spread function (PSF) of each instrument, which degrades the model abstraction to the instrument's capability. The convolved model spectrum is then further degraded by binning it to the spectral resolution of the actual observations.

In practice, the transition of a high-resolution model $\mathcal{M}$ to a lower-resolution convolved spectrum is calculated from

$$\mathcal{M}_{\rm conv}(\lambda) = \int_{\lambda_{\rm min}}^{\lambda_{\rm max}} \mathcal{M}(\lambda')\mathrm{PSF}(\lambda - \lambda')d\lambda'. \tag{4.18}$$

The convolved spectrum is then discretised to the resolution of the data through weighting it by the instrument sensitivity function $s(\lambda)$,

$$\mathcal{M}_{{\rm binned},i} = \frac{\int_{\lambda_{{\rm min},i}}^{\lambda_{{\rm max},i}} \mathcal{M}_{\rm conv} s(\lambda)d\lambda}{\int_{\lambda_{{\rm min},i}}^{\lambda_{{\rm max},i}} s(\lambda)d\lambda}, \tag{4.19}$$

This calculation is performed for each data-point i where $\lambda_{{\rm min},i}$ ($\lambda_{{\rm max},i}$) is the minimum (maximum) wavelength value of the bin width for that data-point.

4.2 Bayesian Inference Method

The essence of the retrieval approach is to use spectra of exoplanets to infer various properties of their atmospheres. In addition to the estimation of planetary properties, it is beneficial to be able to compare the adequacy of models with different assumptions to an observed spectrum. We therefore adopt a Bayesian approach to the estimation of planetary properties and model comparison.

The Bayesian approach used in this work is the MultiNest multi-modal nested

sampling technique that enables parameter estimation as well as an efficient calculation of the Bayesian evidence (Skilling, 2004, 2006; Feroz and Hobson, 2008; Feroz et al., 2009, 2013). The MultiNest algorithm takes atmospheric spectra as input and samples the multi-dimensional space of atmospheric model parameters to compute the evidence $\mathcal{Z}$. In addition, the nested sampling approach allows for joint and marginalised posterior distributions of the retrieval model parameters and their statistical credibility intervals. We implement the MultiNest nested sampling algorithm through a Python interface, PyMultiNest (Buchner et al., 2014). Detailed discussions on the nested sampling method are available in Skilling (2004), Skilling (2006), Feroz et al. (2013), and Buchner et al. (2014).

4.2.1 Parameter Estimation

The heart of Bayesian parameter estimation lies in one relation known as Bayes' Theorem. Consider a parametric retrieval model $\mathcal{M}_i$ defined by a set of free parameters $\vec{\theta}$. The a priori values and probabilities of the parameters are described through the prior probability density function, $p_{\rm prior}(\vec{\theta}|\mathcal{M}_i)$. Consideration of observations allows for a formal modification on the probabilities of these prior parameters through Bayes' Theorem,

$$p_{\rm final}(\vec{\theta}|\mathcal{D}_{\rm obs}) = \frac{\mathcal{L}(\mathcal{D}_{\rm obs}|\vec{\theta},\mathcal{M}_i)\, p_{\rm prior}(\vec{\theta}|\mathcal{M}_i)}{\mathcal{Z}(\mathcal{D}_{\rm obs}|\mathcal{M}_i)}. \tag{4.20}$$

Here, the initial parameter plausabilities ($p_{\rm prior}(\vec{\theta}|\mathcal{M}_i)$) transform according to the plausability of the observations in light of the parameter values $\vec{\theta}$ ($\mathcal{L}(\mathcal{D}_{\rm obs}|\vec{\theta},\mathcal{M}_i)$) to give a final distribution of probabilities for each parameter ($p_{\rm final}(\vec{\theta}|\mathcal{D}_{\rm obs})$), called the posterior probability distribution. Normalisation of the posterior probability distribution is ensured through $\mathcal{Z}(\mathcal{D}_{\rm obs}|\mathcal{M}_i)$. The measure of fit between observations and model parameter values is given by the likelihood function according to

$$\mathcal{L}(\mathcal{D}_{\rm obs}|\vec{\theta},\mathcal{M}_i) = \prod_k^{N_{\rm obs}} (2\pi\sigma_k^2)^{-1/2} e^{-\frac{(\mathcal{D}_{{\rm obs},k}-\mathcal{M}_{i,k})^2}{2\sigma_k^2}}, \tag{4.21}$$

in which $\mathcal{M}_{i,k}$ is the k^{th} binned data-point of spectrum $\mathcal{M}_i$ as outlined in Section 4.1.5, and σ_k is the precision on the k^{th} datum. The estimation of parameter values through equation (4.20) does not in itself require a calculation of $\mathcal{Z}$ since the latter is simply a constant of normalisation. However, not considering $\mathcal{Z}$ assumes the model – among other putative models – is best suited to describe the data. Therefore, a calculation of $\mathcal{Z}$ is powerful when one aims to compare models with different assumptions (e.g., a clear versus cloudy atmosphere). The evidence $\mathcal{Z}$, so called for its utility in providing evidence for one model over another, is a weighted sum of the likelihood function over the prior space,

$$\mathcal{Z} = \int_{\vec{\theta}} \mathcal{L}(\mathcal{D}_{\rm obs}|\vec{\theta}, \mathcal{M}_i)\, p_{\rm prior}(\vec{\theta}|\mathcal{M}_i) d\vec{\theta}. \tag{4.22}$$

4.2.2 Model Comparison

In addition to the parameter estimation achieved through Bayes' Theorem, the nested sampling method allows for a direct calculation of $\mathcal{Z}$ which enables model comparisons. This is in contrast to Markov Chain Monte Carlo methods which have been designed to estimate parameters without providing $\mathcal{Z}$. The key to an efficient calculation of $\mathcal{Z}$ lies in collapsing the multi-dimensional integral in equation (4.22) to a sum over one dimension (Skilling, 2006). To obtain $\mathcal{Z}$ in this form, first we consider the 'cumulant prior mass' defined by

$$X(\beta) = \int_{\mathcal{L}(\vec{\theta})>\beta} p_{\rm prior}(\vec{\theta}|\mathcal{M}_i) d\vec{\theta} \tag{4.23}$$

and which considers all likelihood values greater than β. As β increases X decreases from 1 to 0, where for $\beta = \mathcal{L}_{\rm max}$, $X = 0$. Hence the evidence in equation (4.22) transforms to an integral across one dimension (Skilling, 2006),

$$\mathcal{Z} = \int_0^1 \mathcal{L}(X) dX, \tag{4.24}$$

which is computed numerically through a weighted sum over all sets of sampled priors,

$$\mathcal{Z} = \sum_{i}^{N_{\rm sampled}} \mathcal{L}_i w_i. \tag{4.25}$$

The nested sampling procedure runs with an evolving set of N 'live points' drawn from the prior mass where N can be large for accuracy or small for expedition (Skilling, 2006). At each sampling iteration one live point with the lowest likelihood value $\mathcal{L}_{\rm min}$ is substituted with another point of likelihood $\mathcal{L}_{\rm sub}$ drawn from the prior distribution such that $\mathcal{L}_{\rm sub} > \mathcal{L}_{\rm min}$. By induction, the live points are drawn from steadily increasing iso-likelihood contours with progressive iterations. The sampling process continues as above with $\mathcal{Z}$ calculated by equation (4.25) and is terminated once a pre-figured tolerance on $\Delta\mathcal{Z}$ is achieved, providing for a final value and error on $\mathcal{Z}$.

With the evidence thus acquired, a quantitative comparison of two models is given through the ratio of their evidences (Trotta, 2008),

$$\mathcal{B}_{ij} = \frac{\mathcal{Z}_i}{\mathcal{Z}_j} \tag{4.26}$$

where the sub-scripts i and j represent model i and j, respectively. A $\mathcal{B}_{ij} > 1$ represents a preference for model $\mathcal{M}_i$ over model $\mathcal{M}_j$. In particular, $\mathcal{B}_{ij}$ values of $1-3$, $3-20$, $20-150$, and >150 can be interpreted as 'weak', 'substantial', 'strong', and 'very strong' preferences of model $\mathcal{M}_i$ over model $\mathcal{M}_j$, respectively (Kass and Raftery, 1995). This enables direct model comparison for distinct model realisations (e.g., a model with H_2O versus a model without H_2O). The assumptions embedded in equation (4.26) are that the model components used in the interpretation of data are complete and correct, and that each model has an equal a priori plausibility. In practice, however, neither one of these assumptions is generally the case and an awareness of this should be kept in mind when interpreting data.

As discussed in Benneke and Seager (2013), the Bayes factor can be transformed into a detection significance (i.e., a σ significance) in the language of frequency statis-

tics and effectively quantifies the probability for model $\mathcal{M}_i$ against $\mathcal{M}_j$. We communicate both statistics in the presentation of our results to accommodate readers familiar with either area.

4.3 Outline of Retrieval Applications

The retrieval methods for transmission and emission spectra outlined in this chapter are applied to a suite of observations in Chapters $5-8$. In Chapter 5, we use the transmission retrieval framework to explore the chemical and thermal properties of ten hot giant exoplanets, with a particular focus on the water vapour abundances and bulk cloud/haze properties in their atmospheres. Chapter 6 extends the present transmission retrieval framework to incorporate effects from the host stars of planets. The new retrieval method allows the investigation of stellar and planetary properties simultaneously and is applied to nine hot giant exoplanets. The emission spectra of four iconic directly-imaged companions in the HR 8799 system are examined in Chapter 7. The clear presence of water vapour is confirmed in all four atmospheres. Finally, Chapter 8 presents two additional retrieval applications to the primary and secondary eclipse spectra of the transiting hot Jupiters XO-1b and WASP-18b, respectively.

Chapter 5

H_2O Abundances and Cloud Properties in Ten Hot Giant Exoplanets

The determination of chemical abundances is a major aspect in the characterisation of exoplanetary atmospheres. Nevertheless, chemical abundance estimates of gases is made challenging by the potential presence of atmospheric clouds and hazes which can contribute significantly to the optical depth of spectra (Fortney, 2005). In transmission spectra, the presence of a cloud deck in an atmosphere means that only the layers above the cloud deck contribute to the amplitude of a gas feature. The amplitude of a spectral feature can therefore be substantially diminished and challenge our ability to obtain reliable estimates of the corresponding molecular abundance since such small features could indicate either a significant presence of clouds and hazes (Deming et al., 2013; Sing et al., 2016) or inherently low abundances of a molecule (Madhusudhan et al., 2014b; Barstow et al., 2017).

Throughout the last decade, atmospheric observations of transiting exoplanets using the *Hubble Space Telescope (HST) Wide Field Camera 3 (WFC3)* spectrograph have revealed small absorption features of water vapour (H_2O) for almost all the observed hot giant exoplanets (i.e., hot Jupiters). Some of the earliest spectral observations (Deming et al., 2013; Pont et al., 2013) showed H_2O features which rep-

resent 1-2 scale heights instead of 5-7 scale heights expected for a saturated feature (Madhusudhan and Redfield, 2015). The former two studies attributed the small features to a significant presence of clouds and hazes as opposed to inherently low abundances of H_2O. Subsequently, Madhusudhan et al. (2014b) carried out a retrieval study of three hot Jupiter spectra with low-amplitude H_2O features but, contrary to the above studies, found inherently low H_2O abundances (i.e., sub-solar abundances) in their atmospheres. More recently, Sing et al. (2016) reported a collection of broad-band transmission spectra of ten hot giant exoplanets all of which have H_2O features characterised by small (i.e., $\sim$2) atmospheric scale heights. Sing et al. (2016) used theoretical transmission models to suggest the spectra could be explained by a prominence of clouds and hazes without sub-solar H_2O abundances. However, a subsequent retrieval study (Barstow et al., 2017) reported that nearly all of the planets in Sing et al. (2016) showed evidence for sub-solar H_2O abundances in their atmospheres, consistent with earlier retrieval interpretations of hot Jupiter spectra with low-amplitude H_2O features (e.g., Madhusudhan et al., 2014b).

Here we present a retrieval study of the atmospheric properties of the ten hot giant exoplanets contained in Sing et al. (2016). Our study represents the first time that detailed statistical estimates of atmospheric properties have been made for a size-able exoplanet sample with broadband data. The analysis confirms a significant trend of low H_2O abundances present in the atmospheres along the day-night terminator regions of the planets (Madhusudhan et al., 2014b; Barstow et al., 2017). The published form of this work is presented in Pinhas et al. (2019).

5.1 Background

A recent spectroscopic survey, Sing et al. (2016), investigated the atmospheric properties of ten hot giant exoplanets using transmission spectra in the $0.3 - 5.0$ μm range. The planets, all similar in size to Jupiter, range in equilibrium temperature between 900 K and 2600 K and in mass between 0.2 and 1.5 Jupiter masses. The spectra for the objects were obtained with multiple instruments including the *STIS* ($0.3 - 1.0$

μm) and *WFC3* ($0.8 - 1.8$ μm) spectrographs aboard the *HST* and the *Spitzer IRAC* photometric channels at 3.6 μm and 4.5 μm. The amplitudes of H_2O features across the sample were found to be low, below $\sim$2 atmospheric scale heights. Throughout the last decade, such low amplitudes were interpreted as either due to obscuration by clouds/hazes (e.g., Deming et al., 2013) or due to inherently low H_2O abundances (e.g., Madhusudhan et al., 2014b)

Sing et al. (2016) interpreted the observed atmospheric spectra using empirical metrics in an attempt to decipher the degree of clouds/hazes and the H_2O abundances in the atmospheres. The contribution of H_2O was represented by the amplitude of the H_2O feature at $\sim$1.4 μm, while the difference between the optical and infrared planetary radii was taken as representative of the cloud/haze contribution. These empirical metrics of the observations were evaluated with a grid of atmospheric models assuming chemical equilibrium to suggest that the atmospheres spanned a continuum from clear to cloudy without evidence for sub-solar H_2O abundances.

A complementary study of the Sing et al. (2016) survey, Barstow et al. (2017), suggested a general range of H_2O abundances indicating sub-solar abundances in most of the planetary atmospheres. Barstow et al. (2017) used the Non-linear Optimal Estimator for MultivariatE Spectral analySIS (NEMESIS) statistical algorithm to infer the properties of their atmospheres. They found the spectra are consistent with the presence of clouds and hazes but, contrary to the work of Sing et al. (2016), found that the planets have sub-solar H_2O abundances between $0.01\times$ solar and solar. The NEMESIS retrieval technique of Barstow et al. (2017) assumes Gaussian priors around a single best-fit solution and doesn't allow a full marginalisation of the parameter posterior distributions such that obtaining statistical estimates of model parameters as well as their significances is not possible.

In the present chapter we use the transmission retrieval method outlined in Chapter 4 to conduct a homogeneous analysis of the ten hot giant exoplanets contained in Sing et al. (2016) to determine statistical estimates of their atmospheric properties. The estimated atmospheric properties we report include the H_2O and other chemical abundances, the cloud/haze properties, and the temperature structures at the limbs

of the planets.

We present our results as follows. The atmospheric spectra which are used as inputs to the retrieval are outlined in Section 5.2 and we briefly highlight the importance of optical observations for reliable estimates of atmospheric properties in Section 5.2.1. In Section 5.3 we present results from our retrieval analysis, with a focus on the H_2O abundances. We then discuss our work in light of previous relevant studies (Sing et al., 2016; Barstow et al., 2017) and review the essential results of our analysis in Sections 5.4 and 5.5.

5.2 Observations

We use the transmission retrieval approach outlined in Chapter 4 to interpret the transmission observations of ten hot Jupiters included in Sing et al. (2016). Table 5.1 shows the properties of each planetary system along with details of the observations used as input to our retrievals. The transmission spectra are obtained from recent studies covering a broad wavelength range from $0.3 - 5.0$ μm using the *HST* and *Spitzer* facilities (Sing et al., 2016; Kreidberg et al., 2015; Line et al., 2013; Tsiaras et al., 2018). In particular, the data are products of eight observing modes: *HST STIS G430L*, *HST STIS G750L/M*, *HST ACS G800L*, *HST WFC3 G102*, *HST WFC3 G141*, and two *Spitzer IRAC* photometry bandpasses at $3.6\,\mu$m and $4.5\,\mu$m. All planets except for WASP-6b have data comprising at least *HST STIS G430L*, *HST STIS G750L/M*, *HST WFC3 G141*, and the two *Spitzer IRAC* channels. WASP-6b lacks *WFC3* spectroscopy while HD 189733b has additional spectroscopy in the $0.8 - 1.1$ μm range from *ACS G800L*.

We use the same data as in Sing et al. (2016) except in the cases of HAT-P-12b, WASP-12b, and WASP-39b, where other and/or additional data have been used in the near-infrared (Kreidberg et al., 2015; Line et al., 2013; Tsiaras et al., 2018). In addition, we have not used the *HST NICMOS* data for HD 189733b since its systematics cannot be reliably understood and corrected at the level needed to detect molecular absorption in hot Jupiters (Gibson et al., 2011). In the case of HAT-P-12b,

Planet	$T_{\rm eq}$ (K)	R_p (R_J)	M_p (M_J)	$R_\star$ ($R_\odot$)	Instrument/Sub-Instrument/Disperser or Detector
HAT-P-12b	960	0.96	0.21	0.720	*HST/STIS/G430L* *HST/STIS/G750L* *HST/WFC3 IR/G141* ♦ *Spitzer/IRAC/3.6 channel* *Spitzer/IRAC/4.5 channel*
WASP-39b	1,120	1.27	0.28	0.910	*HST/STIS/G430L* *HST/STIS/G750L* *HST/WFC3 IR/G141* ♦ *Spitzer/IRAC/3.6 channel* *Spitzer/IRAC/4.5 channel*
WASP-6b	1,150	1.22	0.50	0.864	*HST/STIS/G430L* *HST/STIS/G750L* *Spitzer/IRAC/3.6 channel* *Spitzer/IRAC/4.5 channel*
HD 189733b	1,200	1.14	1.14	0.751	*HST/STIS/G430L* *HST/STIS/G750M* *HST/ACS/G800L* *HST/WFC3 IR/G141* *Spitzer/IRAC/3.6 channel* *Spitzer/IRAC/4.5 channel*
HAT-P-1b	1,320	1.32	0.53	1.150	*HST/STIS/G430L* *HST/STIS/G750L* *HST/WFC3 IR/G141* *Spitzer/IRAC/3.6 channel* *Spitzer/IRAC/4.5 channel*
HD 209458b	1,450	1.359	0.69	1.155	*HST/STIS/G430L* *HST/STIS/G750L* *HST/WFC3 IR/G141* *Spitzer/IRAC/3.6 channel* *Spitzer/IRAC/4.5 channel*
WASP-31b	1,580	1.55	0.48	1.274	*HST/STIS/G430L* *HST/STIS/G750L* *HST/WFC3 IR/G141* *Spitzer/IRAC/3.6 channel* *Spitzer/IRAC/4.5 channel*
WASP-17b	1,740	1.89	0.51	1.578	*HST/STIS/G430L* *HST/STIS/G750L* *HST/WFC3 IR/G141* *Spitzer/IRAC/3.6 channel* *Spitzer/IRAC/4.5 channel*
WASP-19b	2,050	1.41	1.14	1.027	*HST/STIS/G430L* *HST/STIS/G750L* *HST/WFC3 IR/G141* *Spitzer/IRAC/3.6 channel* *Spitzer/IRAC/4.5 channel*
WASP-12b	2,510	1.73	1.40	1.506	*HST/STIS/G430L* *HST/STIS/G750L* *HST/WFC3 IR/G102* ♦ *HST/WFC3 IR/G141* ♦ *Spitzer/IRAC/3.6 channel* *Spitzer/IRAC/4.5 channel*

Table 5.1: Planetary system properties and observations. All data are from the spectral survey (Sing et al., 2016) except for *HST WFC3* data for HAT-P-12b (Line et al., 2013), WASP-12b (Kreidberg et al., 2015), and WASP-39b (Tsiaras et al., 2018), the latter three marked by ♦.

we use *HST WFC3 G141* spectra with 23 data points (Line et al., 2013) as compared with 11 *G141* data points in Sing et al. (2016). Different *G141* and additional *G102* observations were used for WASP-12b (Kreidberg et al., 2015). This was done for two reasons. First, the Kreidberg et al. (2015) WASP-12b *G141* data constitute a combination of six transits compared with one transit for the data in the spectral survey of Sing et al. (2016). The Kreidberg et al. (2015) data were also obtained in spatial scanning mode as opposed to staring mode, allowing for higher-precision transit depths. Both the increased transit count and spatial-scan observing mode result in a median precision of 51 parts per million (ppm) on the used data, while the best precision achieved by Sing et al. (2016) is 100 ppm. Retrieving the higher-precision data translates into tighter constraints on WASP-12b's average terminator H_2O abundance. Second, additional data with the *G102* grism are also used and have precisions similar to the *G141* grism spectroscopy (Kreidberg et al., 2015). The additional information content contained in the *G102* data between 0.78 and 1.07 μm provides for generally tighter constraints on the retrieved parameters. In the case of WASP-39b, additional *WFC3 G141* data (Tsiaras et al., 2018) are used to compensate for the lack of near-infrared data in Sing et al. (2016).

The average precisions on the observed spectra span a wide range from high precisions of $\sim$30 ppm (HD 209458b *G141* data) to low values of $\sim$400 ppm (WASP-12b *Spitzer* photometry). This suite of observations constitutes a baseline sample to study with retrieval techniques since the datasets have undergone a consonant reduction process for systematics (Sing et al., 2016), with the exception of the HAT-P-12b *G141* data (Line et al., 2013), WASP-12b *G102* and *G141* data (Kreidberg et al., 2015), and WASP-39b *G141* data (Tsiaras et al., 2018) included in our work.

5.2.1 Importance of Optical Data

The availability of optical data from *HST STIS* for the ten planets is essential in their interpretation, especially in the estimation of H_2O abundances. This is because the interpretation of *HST WFC3* data alone introduces a well known ambiguity between the water abundance X_{H_2O} and the reference pressure P_{ref} associated with the plan-

etary radius (Griffith, 2014; Heng and Kitzmann, 2017). The use of *HST STIS* data to infer a reliable constraint on the reference pressure and the water abundance is illustrated in Figure 5.1. In the retrieval of *HST WFC3* data alone the line of ambiguity between $P_{\rm ref}$ and $X_{\rm H_2O}$ spreads over two orders of magnitude and the inferred $X_{\rm H_2O}$ are mostly contained above 10^{-4}. The same degeneracy disappears when optical *HST STIS* data are included in the retrieval; the joint posterior between $P_{\rm ref}$ and $X_{\rm H_2O}$ shows a well-localised set of solutions with no correlative trend. Moreover, the $X_{\rm H_2O}$ values are constrained three times better and are contained below 10^{-4}. The juxtaposition in Figure 5.1 is a clear illustration that the broad ambiguity between $P_{\rm ref}$ and $X_{\rm H_2O}$ that exists for near-infrared *WFC3* data alone is reduced through the use of optical data, in this case *HST STIS* observations. Optical spectra thus allow reliable inferences of the H_2O abundance.

5.3 Results

In the present study we conduct a homogeneous Bayesian retrieval analysis on observations of ten hot giant planets (see Table 5.1) to determine statistical estimates of their atmospheric properties. The ensemble of hot Jupiters includes HAT-P-12b, WASP-39b, WASP-6b, HD 189733b, HAT-P-1b, HD 209458b, WASP-31b, WASP-17b, WASP-19b, and WASP-12b. The prior distributions and ranges of the retrieval model parameters are shown in Table 5.2. The estimated atmospheric properties include the H_2O and other chemical abundances, the temperature profiles, and bulk cloud/haze properties. We also calculate the detection significances for the chemical species. Each planet was sampled with about 5 million models, for a total of more than 60 million model runs. Using our framework, we derive marginalised posterior probability distributions and statistical estimates for each atmospheric parameter. A panorama of the retrieved model fits to the observations are shown in Figure 5.2, while the full set of our retrieval results including the posterior distributions, best-fit spectra, and $p-T$ profiles are available on the Open Science Framework[1] (OSF) and

[1] `https://osf.io/wtqjr/?view_only=8f70b80b5d834f3d8ef8be4ee7b77b27`

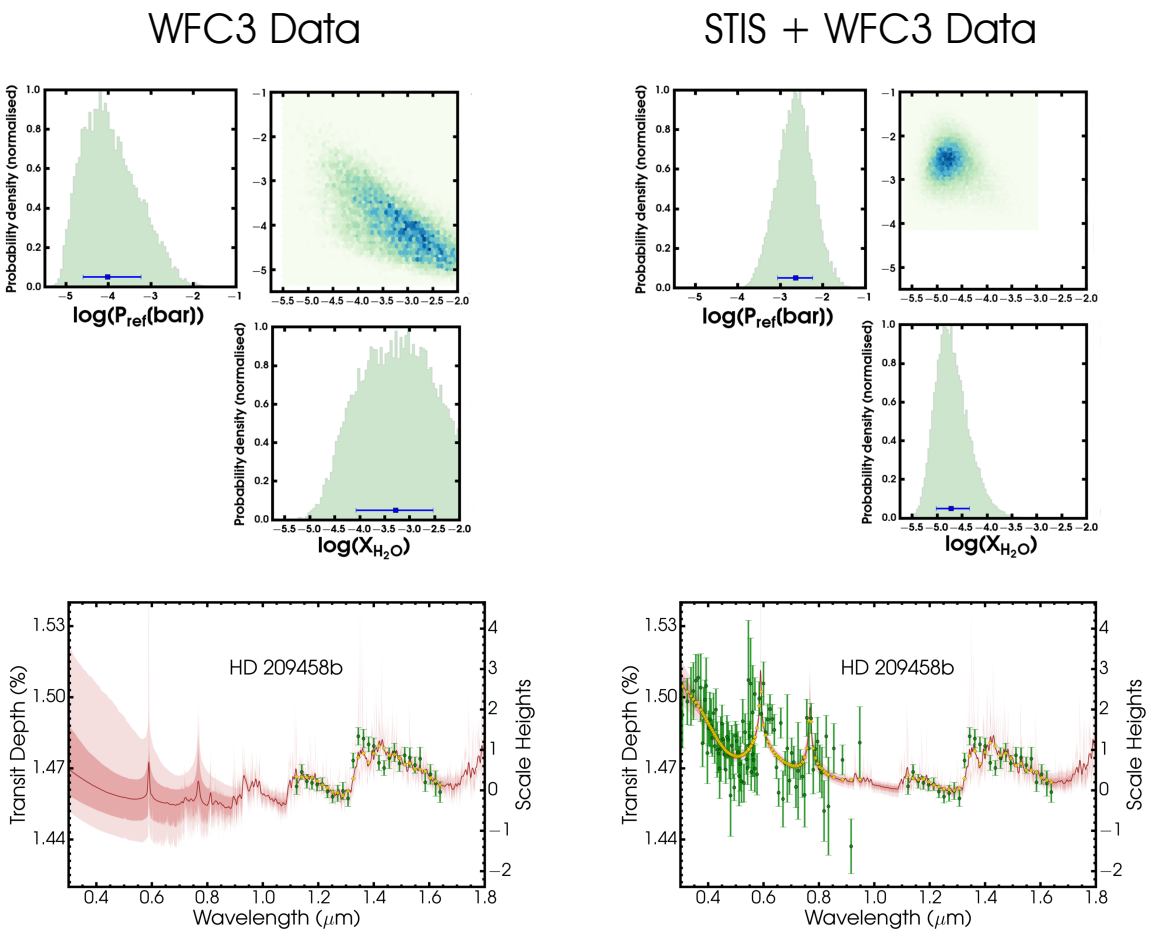

Figure 5.1: Demonstration of the use of optical data to precisely determine $P_{\rm ref}$ and $X_{\rm H_2O}$. HD 209458b is used for illustration. One retrieval (left column) inverts the *HST WFC3* data and another retrieval (right column) includes *HST STIS* data in the optical in addition to *WFC3* data. The juxtaposition demonstrates that data in the optical wavelength range break the degeneracy between $P_{\rm ref}$ and $X_{\rm H_2O}$.

Table 5.2: Prior information used in the retrieval analyses of ten hot giant exoplanets

Parameter	Prior Distribution	Prior Range
T_0	Uniform	$400 - T_{\rm eq} + 200$ K (for $T_{\rm eq} < 1200$ K) $800 - T_{\rm eq} + 200$ K (for $T_{\rm eq} > 1200$ K)
$\alpha_{1,2}$	Uniform	$0.02 - 1$ K$^{-1/2}$
$P_{1,2}$	Log-uniform	$10^{-6} - 10^{2}$ bar
P_3	Log-uniform	$10^{-2} - 10^{2}$ bar
X_i	Log-uniform	$10^{-12} - 10^{-2}$
a	Log-uniform	$10^{-4} - 10^{8}$
γ	Uniform	-20 − 2
$P_{\rm cloud}$	Log-uniform	$10^{-6} - 10^{2}$ bar
$\bar{\phi}$	Uniform	$0 - 1$

in Appendix Tables C.1−C.3. The properties of each planetary system along with details of observations used as input to our retrievals are listed in Table 5.1.

Our results are presented as follows. In Section 5.3.1.1, we first discuss the most constrained parameter given the data: the H_2O abundance. We then briefly consider other chemical species and their abundances in Section 5.3.1.2. Potential trends between the planetary parameters, H_2O abundances, and cloud/haze properties are explored in Section 5.3.2.

5.3.1 Chemistry

5.3.1.1 H_2O Abundances

The water vapour abundances are shown against planetary equilibrium temperature in Figure 5.3. The reference 'solar' H_2O, shown by the gold line in Figure 5.3, indicates the H_2O abundance as a function of temperature that is expected in hot Jupiter atmospheres with solar elemental abundances at a pressure of 1 bar (Asplund et al., 2009; Madhusudhan, 2012). For the majority of hot Jupiters considered in this work (i.e., those with equilibrium temperatures above ∼1,300 K), H_2O is expected to contain ∼50% of the total available oxygen (Madhusudhan, 2012) such that the solar water abundance is a constant and is $X^{\odot}_{\rm H_2O} = \frac{1}{2}\frac{\rm O}{\rm H_2}\big|_{\odot} X^{\odot}_{\rm H_2}$, where $\frac{\rm O}{\rm H_2}\big|_{\odot} = 2\frac{\rm O}{\rm H}\big|_{\odot}$

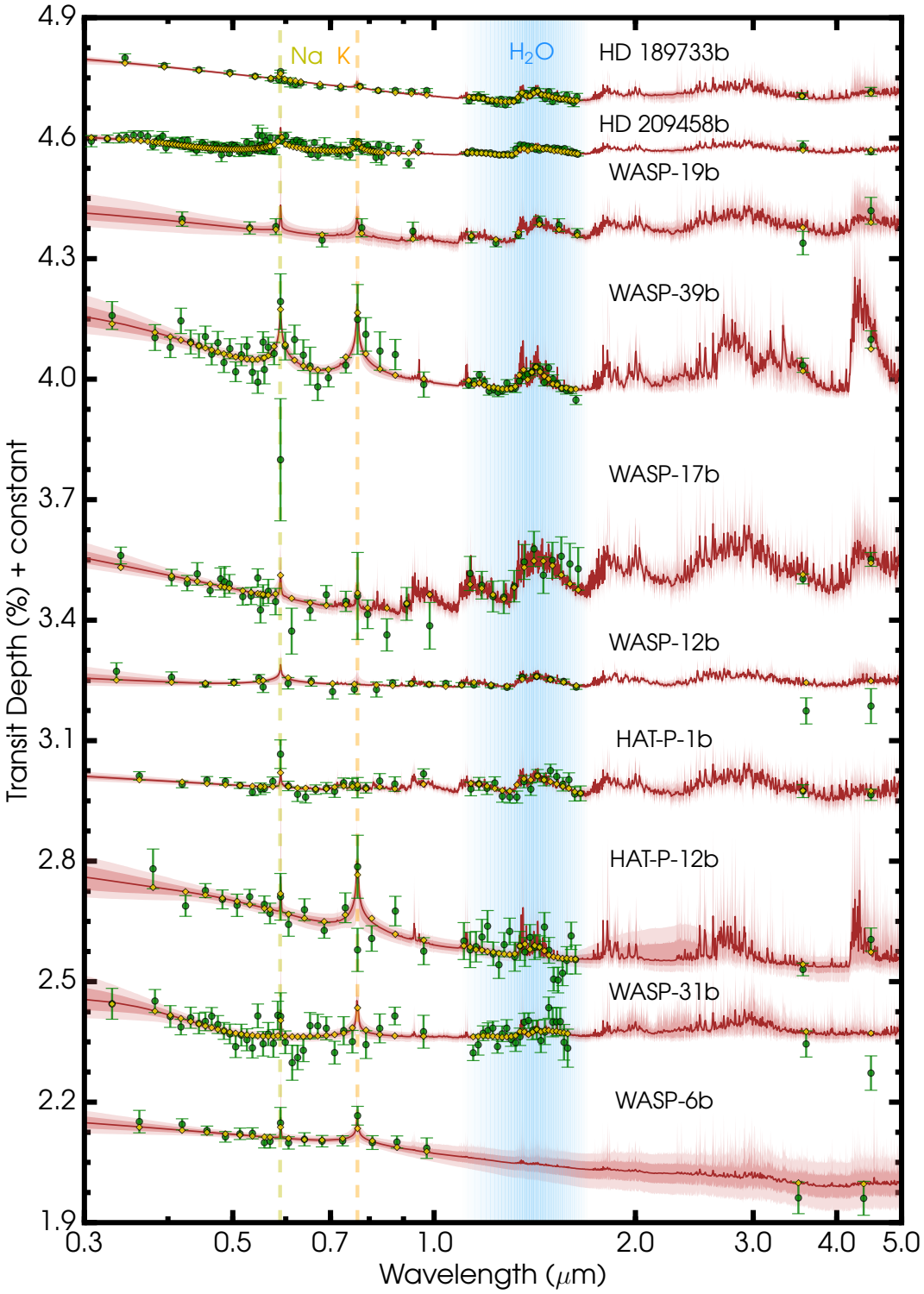

Figure 5.2: Retrieved model transmission spectra compared to observations for the ensemble of hot giant exoplanets. The data are shown in green and the retrieved median model is in dark red with associated 1σ and 2σ confidence contours. The yellow diamonds are the binned median model at the same resolution as the observations. The best-fit median model in dark red has been smoothed for clarity. The data are discussed in Section 5.2 and shown in Table 5.1.

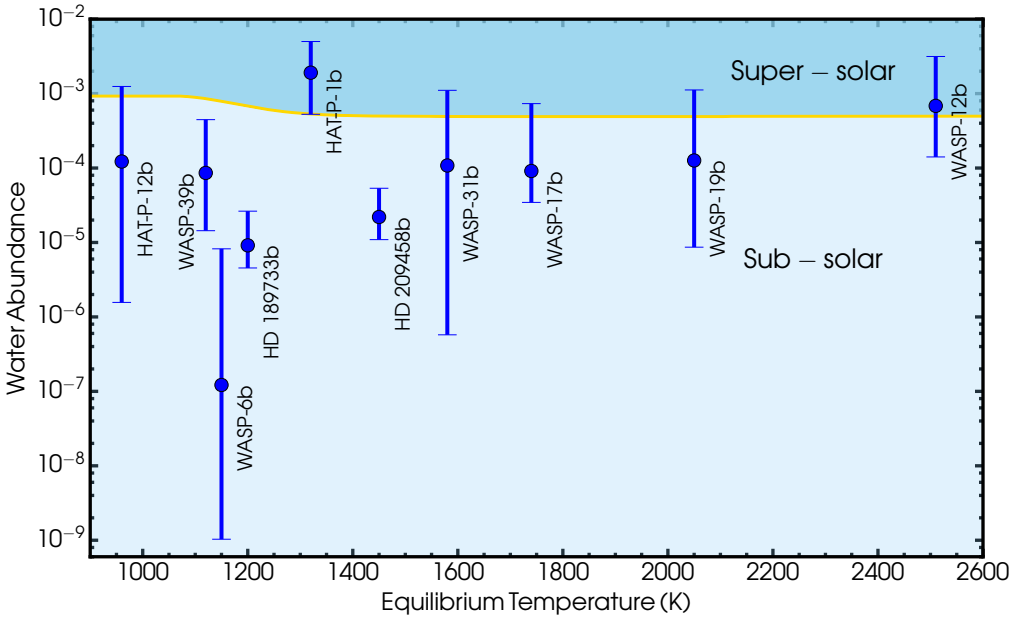

Figure 5.3: The retrieved H_2O volume mixing ratios and their associated 1σ ranges for the hot Jupiter sample. The planets are consistent with sub-solar H_2O abundances within 1σ with the exception of HAT-P-1b. The gold line shows the volume mixing ratio of water vapour calculated from solar elemental abundances in chemical equilibrium at 1 bar (Madhusudhan, 2012) and ranges from $\sim 10^{-3}$ at $T \lesssim 1{,}200$ K to 5×10^{-4} at higher temperatures.

and $\log(X^{\odot}_{\mathrm{H_2O}}) = -3.3$. The H_2O abundances, the solar-relative abundances, and the detection significances of water vapour are listed in Table 5.3.

The planets with the most precise observations in the *HST WFC3 G141* bandpass – HD 189733b, HD 209458b, and WASP-12b – have retrieved $\log(\mathrm{X_{H_2O}})$ abundances of $-5.04^{+0.46}_{-0.30}$, $-4.66^{+0.39}_{-0.30}$, and $-3.16^{+0.66}_{-0.69}$, respectively. The two hot Jupiters with the highest quality observations (HD 189733b and HD 209458b) show the most statistically significant H_2O depletion and are consistent with those of previous studies (Madhusudhan et al., 2014b; Barstow et al., 2017; MacDonald and Madhusudhan, 2017a). The inferred H_2O abundance of WASP-12b is consistent to 1σ with that of another study (Kreidberg et al., 2015). HAT-P-1b, WASP-31b, WASP-17b, WASP-19b, and WASP-12b contain relative abundances of $3.58^{+5.84}_{-2.60}\times$, $0.218^{+2.01}_{-0.217}\times$, $0.19^{+1.32}_{-0.12}\times$, $0.26^{+2.03}_{-0.24}\times$, $1.40^{+4.97}_{-1.11}\times$ solar which are consistent with super-solar to within 1σ. The retrieved water abundances for the planets with the lowest equilibrium temperatures, HAT-P-12b and WASP-39b, are $-3.91^{+1.01}_{-1.89}$ and $-4.07^{+0.72}_{-0.78}$, corresponding to $0.133^{+1.226}_{-0.131}\times$ and $0.10^{+0.42}_{-0.08}\times$ the solar abundance. The estimated water abundance for WASP-39b is inconsistent with that of another study (Wakeford et al., 2018) which used different *WFC3* data than in the present work. WASP-6b has the lowest derived abundance, consistent with a non-detection, owing largely to the lack of *WFC3* data. Finally, we find no clear correlation between the H_2O abundance and T_{eq}.

5.3.1.2 Other Species

We also constrain the presence and abundance of alkali absorbers, Na and K, in addition to H_2O. Table 5.4 lists cases which show clear modes in the retrieved posterior distributions with significances above 2σ. HD 189733b shows a confident detection of Na corresponding to a significance of 5.01σ (Bayes factor of 4.7×10^4) and a sub-solar value of $-7.77^{+1.64}_{-0.87}$. We detect potassium in WASP-6b at 2.67σ confidence with a constrained abundance of $-5.53^{+2.01}_{-1.85}$, consistent with the solar value. While there is a clear potassium signature in the spectrum of WASP-31b (see Figure 5.2), the fidelity of this data point has recently been called into question (Gibson et al., 2018) and therefore WASP-31b is not included in Table 5.4. In terms of other molecular species,

Planet	$\mathrm{Log}(X_{\mathrm{H_2O}}{}^{+1\sigma}_{-1\sigma})$	Normalised Abundance $(X^{\odot}_{\mathrm{H_2O}})^{+1\sigma}_{-1\sigma}$	Detection Significance
HAT-P-12b	$-3.91^{+1.01}_{-1.89}$	$0.133^{+1.226}_{-0.131}$	N/A
WASP-39b	$-4.07^{+0.72}_{-0.78}$	$0.10^{+0.42}_{-0.08}$	7.00σ
WASP-6b	$-6.91^{+1.83}_{-2.07}$	$0.000156^{+0.014}_{-0.000155}$	N/A
HD 189733b	$-5.04^{+0.46}_{-0.30}$	$0.018^{+0.035}_{-0.009}$	5.60σ
HAT-P-1b	$-2.72^{+0.42}_{-0.56}$	$3.58^{+5.84}_{-2.60}$	3.50σ
HD 209458b	$-4.66^{+0.39}_{-0.30}$	$0.04^{+0.06}_{-0.02}$	7.06σ
WASP-31b	$-3.97^{+1.01}_{-2.27}$	$0.218^{+2.01}_{-0.217}$	2.05σ
WASP-17b	$-4.04^{+0.91}_{-0.42}$	$0.19^{+1.32}_{-0.12}$	3.22σ
WASP-19b	$-3.90^{+0.95}_{-1.16}$	$0.26^{+2.03}_{-0.24}$	2.89σ
WASP-12b	$-3.16^{+0.66}_{-0.69}$	$1.40^{+4.99}_{-1.11}$	5.73σ

Table 5.3: Terminator H_2O abundances, solar-normalised H_2O abundances, and H_2O detection significances. The normalised H_2O abundances are relative to the solar values shown by the gold line in Figure 5.3. Detection significances are given for Bayes factors greater than 2.64 (i.e., 2σ).

Table 5.4: Retrieved atomic species with detection significances above 2σ.

Planet	Species	Detection Significance	Abundance
WASP-39b	Na	3.41σ	$-3.86^{+1.31}_{-1.36}$
	K	3.62σ	$-4.22^{+1.25}_{-1.12}$
WASP-6b	K	2.67σ	$-5.53^{+2.01}_{-1.85}$
HD 189733b	Na	5.01σ	$-7.77^{+1.64}_{-0.87}$
HAT-P-1b	Na	2.22σ	$-8.44^{+1.45}_{-2.12}$

the retrieved posteriors for WASP-39b show evidence for CH_4 and CO_2 and yet may be due to a possible systematic offset between the *HST* and *Spitzer* data. Evidence of nitrogen chemistry in these planetary spectra was examined in MacDonald and Madhusudhan (2017b), which found a weak detection of NH_3 in WASP-31b (2.2σ) and potential NH_3 in HD 209458b. Finally, we note that the retreived chemical abundances presented above rely on the assumption of our simplified cloud and haze model.

5.3.2 Exploring Trends with Planetary Parameters, H_2O Abundances, and Cloud/Haze Properties

We have carried out an extensive exploration of potential trends among planetary parameters, H_2O abundances, and cloud/haze properties. We have investigated 35 combinations of pairs and triplets over the parameters $T_{\rm eq}$, M_p, g, $X_{\rm H_2O}$, $\bar{\phi}$, and $P_{\rm cloud}$, resulting in no clear correlations. However, we present three parameter spaces and compare with analogous presentations in the literature (Sing et al., 2016; Barstow et al., 2017; Stevenson, 2016). An extensive comparison with the methodologies and results of Sing et al. (2016) and Barstow et al. (2017) is presented in Section 5.4.

The terminator cloud/haze fractions ($\bar{\phi}$) versus H_2O abundances with $T_{\rm eq}$ as a third dimension are shown in Figure 5.4. We do not find a clear trend between $\bar{\phi}$ and $X_{\rm H_2O}$, and the cloud fractions for the planetary sample do not follow the clear-to-cloudy/hazy trend suggested by Figure 1 of Sing et al. (2016). The median cloud/haze fractions for WASP-12b and WASP-6b imply fewer aerosols and those for HD 209458b, WASP-31b, and HAT-P-12b imply more aerosols compared to the order previously suggested in Sing et al. (2016).[2]

The derived grey cloud-top pressures ($P_{\rm cloud}$) versus $T_{\rm eq}$ are shown in Figure 5.5.

[2]We note however that this comparison is not fully consistent since the cloud/haze contribution in Sing et al. (2016) is discerned from the difference between the optical and infrared radii, while in our study the cloud/haze contribution basically discerns the fraction of the limb-averaged spectrum best fit simultaneously with a grey flat feature and a non-grey optical feature. In this light, larger cloud/haze contributions in Sing et al. (2016) represent an abundance of small ($\lesssim 0.1$ μm) haze/cloud particles and/or species with refractive index extinction properties productive of steep slopes in the optical wavelength region.

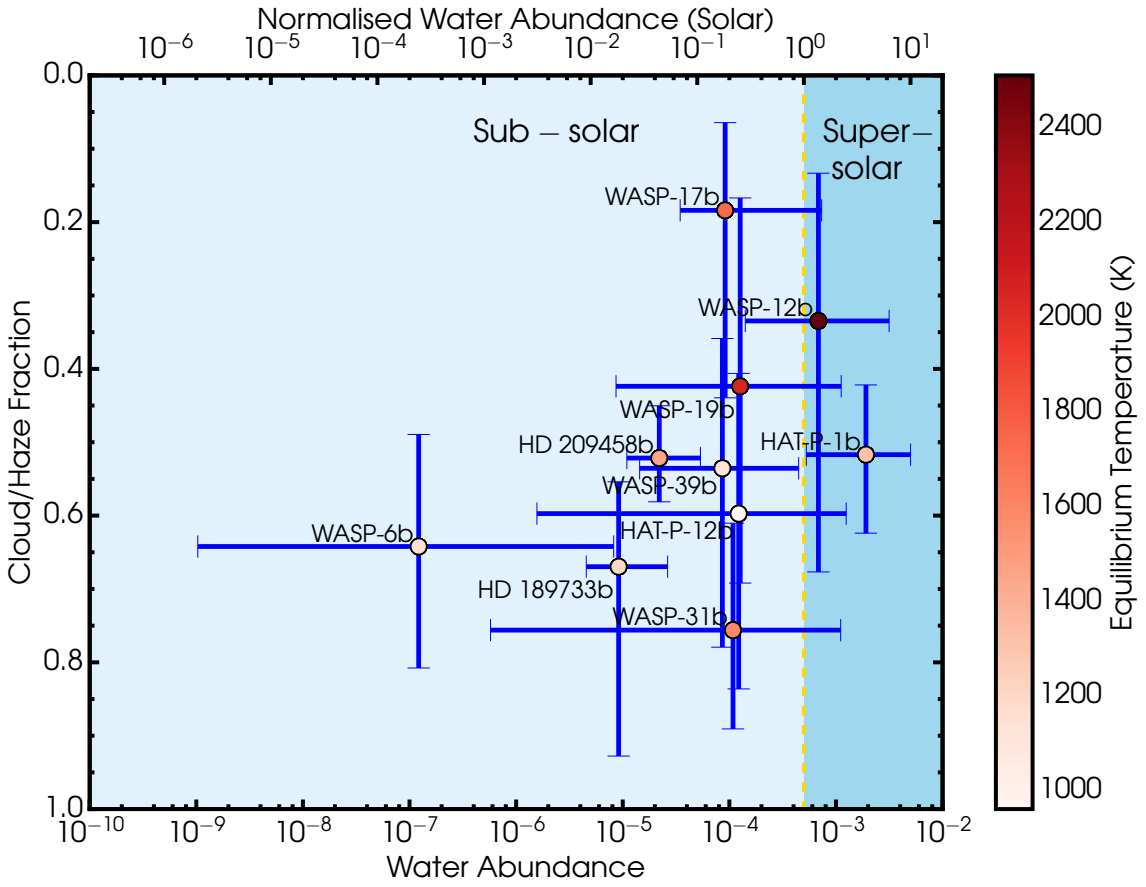

Figure 5.4: Terminator cloud/haze fractions, H_2O abundances, and equilibrium temperatures of the hot Jupiter sample. The dashed gold line represents the solar water abundance at high temperatures (i.e., 5×10^{-4}).

HD 189733b and WASP-6b likely have clouds composed of large particles deep in the atmospheres below $\sim 10^{-1}$ bar. On the other hand, opaque clouds with maximal cloud-top pressures of 0.1 mbar are found for HAT-P-12b, WASP-39b, HAT-P-1b, WASP-17b, WASP-19b, and WASP-12b but are relatively unconstrained. HD 209458b and WASP-31b have high-precision constraints of $\sim$0.5 dex on the cloud-top pressures and the cloud-tops lie above 1 mbar. Overall, we find no correlation between $T_{\rm eq}$ and $P_{\rm cloud}$. However, planets with low cloud-top pressures below $\sim$1 mbar span equilibrium temperatures of $1400 - 1600$ K.

Finally, the space of $T_{\rm eq}$, g, and $\bar{\phi}$ is shown in Figure 5.6. The lack of a clear correlation among these parameters is unlike previously suggested (Stevenson, 2016). For the equilibrium temperatures spanned in our work ($T_{\rm eq} > 700$ K), Stevenson

(2016) suggested that planets with $\log(g[\mathrm{cms}^{-2}])$ greater than 2.8 should be cloud-free while those with lower values should host a significant cloud/haze fraction. In contrast, we find no such division, consistent with a conclusion from a recent study (Barstow et al., 2017) of the spectra in Sing et al. (2016). This difference exists for at least two reasons. Firstly, some of the *G141* observations used in Stevenson (2016) are different than those we retrieve. Secondly, Stevenson (2016) explains the amplitude of an H_2O feature with reference to clouds alone, assuming no variations over the H_2O abundance. This assumption is too restrictive since a low-amplitude feature can imply peculiarly low water abundance with minimal cloud coverage and/or high P_{cloud} or a high water abundance with a significant cloud fraction and/or low P_{cloud}. On the other hand, the relatively clearer atmospheres of WASP-12b, WASP-19b, and WASP-17b shown in Figure 5.6 support suggestions of hotter ($T_{\mathrm{eq}} \gtrsim 1700\,\mathrm{K}$) close-in planets harbouring less cloudy atmospheres (Liang et al., 2004; Heng, 2016; Tsiaras et al., 2018).

5.3.2.1 Metallicity and Formation Conditions

The retrieved set of H_2O abundances provide initial clues on metal abundances in the exoplanetary atmospheres. Figure 5.7 shows the space of atmospheric metallicity versus planet mass for the hot Jupiter sample in addition to previously reported metallicities of WASP-43b (Kreidberg et al., 2014c), HAT-P-26b (Wakeford et al., 2017), and the solar system gas giants. The atmospheric metallicities are estimated from molecular species with well-determined abundances since knowledge of the full inventory of metals is limited by observational capabilities. The atmospheric metallicities for the hot Jupiter sample are calculated assuming that half of the oxygen is in the estimated H_2O and the remaining half is in CO, in accordance with chemical equilibrium expectations for a solar C/O ratio at high temperatures (Madhusudhan, 2012). The atmospheric metallicities of the four solar system gas giants are determined from the abundance of methane which contains most of the carbon at their low temperatures (Atreya et al., 2016). The abundance of oxygen in the atmospheres of solar system planets cannot be incorporated into a metallicity estimate since much

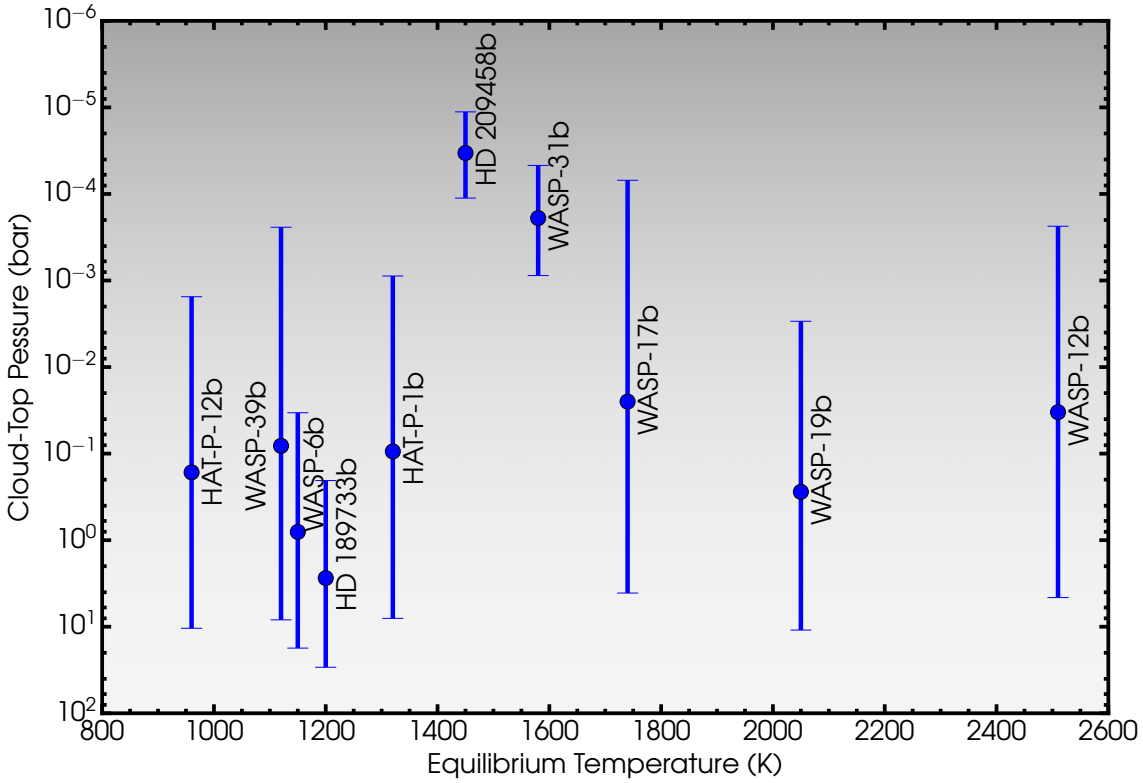

Figure 5.5: Top pressure of grey clouds versus planetary equilibrium temperature for the hot Jupiter ensemble.

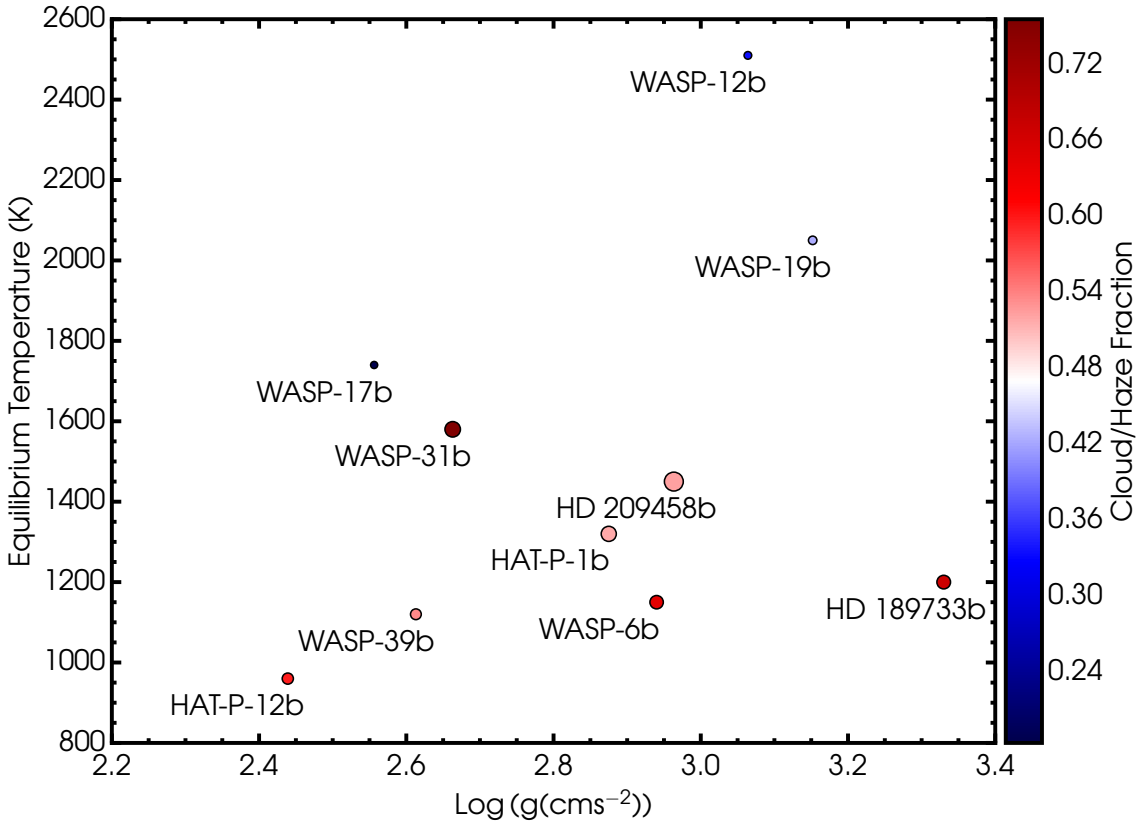

Figure 5.6: Cloud/haze fractions $\bar{\phi}$ as a function of $T_{\rm eq}$ and planetary gravity. The marker size is inversely proportional with the retrieved 1σ confidence on the cloud/haze fraction, such that more precise constraints are represented with larger circles.

of it is condensed in deep-lying water clouds.

We emphasize that there are limitations to the illustration in Figure 5.7 due to the different molecules used to represent the metallicities as well as using one molecular species as a metallicity descriptor. In principle, a high C/O ratio (e.g., C/O$\sim$1) can lead to significantly sub-solar H_2O. Therefore, the low H_2O abundances would indicate either a low metallicity and/or a high C/O ratio (Madhusudhan et al., 2014b). The metallicity proxy for solar system planets shows a decreasing trend with increasing planetary mass. The sub-solar hot Jupiter metallicities suggest a weak trend that is different from that of the solar system gas giants.

The inferred oxygen abundances provide initial clues into the formation and migration scenarios of these hot Jupiters when considering the metallicities of their host stars. The host stars of the majority of these hot Jupiters have O/H abundances in excess of the solar value (Teske et al., 2014; Brewer et al., 2017).[3] This implies that the O/H ratios in the majority of the planetary atmospheres are sub-stellar as well as being sub-solar. Hot Jupiter atmospheres are expected to possess super-stellar oxygen abundances if they are formed through core-accretion followed by migration within the disk (Madhusudhan et al., 2014a; Mordasini et al., 2016), as also suggested for Jupiter based on its super-solar abundances in several elements (Owen et al., 1999; Atreya and Wong, 2005; Mousis et al., 2012).

On the other hand, the generally sub-solar and sub-stellar oxygen abundances found in these atmospheric spectra suggest a general scenario in which the hot Jupiters form far from their stars with efficient gas accretion and relatively inefficient solid planetesimal accretion (Madhusudhan et al., 2014b, 2016a) since the gaseous O/H abundance is low in outer regions of protoplanetary disks due to successive condensation fronts of O-rich species (Öberg et al., 2011). Subsequent impulse inwards through gravitational interactions with other bodies in the system by disk-free migration may have brought many of these hot Jupiters to their present locations (Rasio and Ford, 1996). Such disk-free migration could lead to low oxygen abundances ir-

[3]Brewer et al. (2017) measured super-solar O/H ratios for HD 189733, HD 209458, WASP-31, WASP-17, WASP-19, and WASP-12, and Teske et al. (2014) measured a super-solar O/H ratio for HAT-P-1. The O/H ratios of HAT-P-12, WASP-39, and WASP-6 have not been determined.

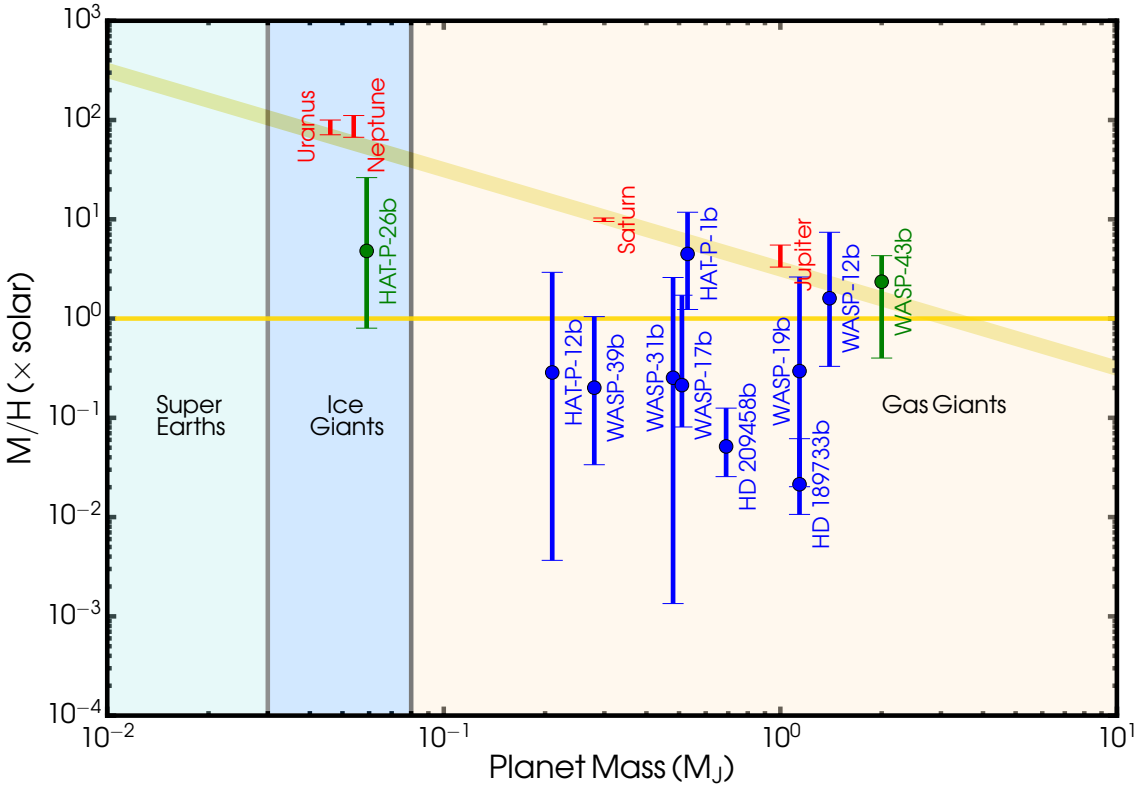

Figure 5.7: Atmospheric metal abundances as a function of planetary mass for the hot Jupiter ensemble. The planets in the current study are shown in blue, along with WASP-43b (Kreidberg et al., 2014c) and HAT-P-26b (Wakeford et al., 2017) from previous studies shown in green. The solar system giant planets are shown in red. The solar metallicity reference is shown by the horizontal gold line. WASP-6b is excluded due to lack of *WFC3* observations. The exoplanetary atmosphere metallicities M/H of the giant exoplanets in our sample are derived from the H_2O volume mixing ratio, such that M represents O, and assuming that half of the oxygen is in H_2O as expected for a solar C/O ratio at high temperatures (Madhusudhan, 2012). The metallicities of solar system planets are derived from the CH_4 abundances, such that M represents C.

respective of formation mechanisms, either core-accretion or gravitational instability (Madhusudhan et al., 2014a). Alternatively, it has been suggested that hot Jupiters with sub-solar oxygen abundances may form through pebble accretion and migrate inward with or without the disk but without significant erosion of the core (Madhusudhan et al., 2017; Booth et al., 2017). In all, disk-free migration is suggested to be of considerable importance for such planets. The suggested importance of disk-free migration implied from the general trend of low oxygen abundances is consistent with proposals in other studies of the prevalence of disk-free migration based on dynamical properties of hot Jupiters and their environments (e.g., Brucalassi et al., 2016; Nelson et al., 2017).

5.4 Comparison to Previous Studies

Here we compare our work with two previous studies: the spectral survey of Sing et al. (2016) that first reported the ten hot Jupiter observations and Barstow et al. (2017) that conducted initial retrievals on those datasets. The differences between our work and these previous studies lie in both the modeling and retrieval approaches, as well as the results. At the outset, the key aspect of our present work is the ability to derive statistical constraints (i.e., estimates with non-Gaussian error bars), along with full posterior distributions, for all the atmospheric parameters concerned. This allows one to pursue comparative exoplanetology for a sizeable exoplanet sample. We note that our retrieval forward model has also been validated against results from radiative transfer codes of other groups (Fortney et al., 2010; Deming et al., 2013; Line et al., 2013; Heng and Marley, 2017), with which we find good agreement.

The differences in H_2O abundances and cloud/haze properties between our findings and those of Sing et al. (2016) can be attributed to several crucial factors. Firstly, the conclusions of the latter study were reached through a comparison of the data with chemical equilibrium models of hot Jupiter atmospheres computed over a predetermined grid in metallicity and temperature[4], as opposed to a full retrieval as in

[4]In these models, the abundances of the considered chemical species are determined by minimizing

the present study. Given the limited number of models in the grid and the equilibrium assumption, it was not possible to explore the model space adequately (e.g., there was no exploration of cloudy/hazy models with sub-solar water abundances (see their Figure 3)) nor could the atmospheric properties be estimated statistically. This meant that it was necessary to invoke empirical metrics to qualitatively assess the contributions of the H_2O abundance and clouds/hazes in the atmospheres. For example, the amplitude of the H_2O feature at $\sim$1.4 μm was suggested to correlate with the difference between the planetary radius in the optical and infrared (Sing et al., 2016). However, this correlation was based on cloudy/hazy models which assumed solar and super-solar H_2O abundances, without an exploration of cloudy/hazy atmospheres with sub-solar water abundances as well as sub-solar cloudy/hazy opacities (see their Figure 3). As such, their conclusions were unable to reflect the full range of possible solutions, as confirmed in a follow-up study by Barstow et al. (2017) (discussed below) which found predominantly sub-solar H_2O solutions. Our study instead uses a comprehensive retrieval of all the datasets using a Bayesian nested sampling approach, enabling a detailed exploration of the entire multi-dimensional space of atmospheric parameters. We thereby assume no a priori values for the H_2O abundances and cloud/haze properties.

There are also several differences between our study and that of Barstow et al. (2017). The differences are of three kinds: model parameterisations, statistical sampling algorithms, and reported estimates. Here we discuss each of these in turn.

There are several important differences in the model parameterisations. The main aspect of the Barstow et al. (2017) study is that it is effectively a grid-based retrieval, in the sense that a separate retrieval is conducted for each assumption of a cloud prescription. Importantly, the study treats two kinds of cloud models separately: a model with Rayleigh-like slopes (i.e., our hazes) and one with grey opacity (i.e., our clouds). On the other hand, our cloud/haze model simultaneously accounts for small and large particle sizes (see equation (4.9) in Chapter 4). An important distinction

the Gibbs free energy of the system for a given temperature, pressure, and elemental abundances using the CONDOR code (Lodders and Fegley, 2002).

also lies in the aerosol parameterisation. Our study includes a grey cloud overlain by a haze such that both types of aerosols are retrieved for a planet, although the retrieved parameters could indicate no hazes (i.e., $a = 1$ and $\gamma = -4$) and/or no grey clouds (i.e., $P_{\rm cloud} \gtrsim 10$ bar). On the other hand, Barstow et al. (2017) allows for the presence of a vertically-finite cloud or haze deck at variable locations in the atmosphere. In some cases (e.g., HD 189733b) where our study retrieves a deep cloud layer with an extensive overlying haze layer, Barstow et al. (2017) retrieve a decade-confined haze layer at low pressures. These two different interpretations, however, produce similar fits to the spectrum.

An additional crucial difference in the aerosol models is that the present study accounts for inhomogeneous clouds and hazes along the planetary limb. The inclusion of patchy clouds is important since the shape of the H_2O feature in the *WFC3* band-pass is sensitive to the degree of cloud contribution (e.g., see Line and Parmentier, 2016). These differences in modeling are likely another principal element responsible for discrepancies in the cloud and haze properties between the present work and that of Barstow et al. (2017). Second, Barstow et al. (2017) assumes an isotherm for the observable region of the atmosphere (i.e., pressures below 0.1 bar) whereas we allow a fully general temperature profile that allows for any temperature gradient. Third, the cloud properties and temperature profiles in Barstow et al. (2017) were pre-defined on a grid, whereas the atmospheric parameters in our study are sampled continuously over the entire parameter space.

There are also important differences in the statistical inference methods. Barstow et al. (2017) uses an optimal estimation (OE) sampler (Rodgers, 2000; Lee et al., 2012) whereas our analysis uses a Bayesian nested sampling algorithm, MultiNest (Skilling, 2006; Feroz et al., 2013; Buchner et al., 2014). First, while OE has been shown to be accurate for very high resolution data, its accuracy has been shown to be limited for low resolution spectrophotometry (Line et al., 2013) as is relevant in the present case. On the other hand, the MultiNest Bayesian analysis approach has been shown to be more accurate for the quality of hot Jupiter data considered here since it is able to explore parameter spaces with multi-modal solutions (Feroz and

Hobson, 2008; Feroz et al., 2013). Second, the OE sampler in Barstow et al. (2017) requires assuming Gaussian-distributed priors on the model parameters whereas no such assumption is required in the present Bayesian approach. This is significant since the retrieved parameter posteriors in our study indeed show mostly non-Gaussian distributions. Third, given the efficiency of our modeling and retrieval approach a much larger volume of the high-dimensional model parameter space is explored for each planet (i.e., ∼5,000,000 models) while the approach in Barstow et al. (2017) was limited to 3,600 model evaluations per planet.

Finally, there are important differences regarding the nature of reported parameter estimates. First, Barstow et al. (2017) does not provide statistical estimates on the abundances and other atmospheric properties but instead provides parameter values of a select set of model fits to the data based on chi-square values below a certain threshold. On the other hand, our analysis provides statistical limits, along with full posteriors, for all the atmospheric parameters through a consideration of all model evaluations. Hence, our estimated median values and 1σ uncertainties are obtained through marginalization over the full posteriors. Second, the cloud/haze properties and temperatures profiles in Barstow et al. (2017) were pre-defined on a grid and hence joint constraints on these properties and chemistry are not possible. Our approach allows for complete marginalization over all parameters and hence provides joint statistical correlations between all atmospheric parameters, thereby enabling a more extensive illumination of the atmospheres.

The considerations above naturally lead to differences between our results and those of the Barstow et al. (2017) study, particularly on the nature of clouds/hazes. Barstow et al. (2017) find three planets – WASP-39b, HD 209458b, and WASP-31b – are best fit by grey opacity clouds with top pressures of 10^{-5} bar, 0.01 bar, and 0.1 bar, respectively. Figure 5.5 shows the retrieved median cloud-top pressures for HD 209458b and WASP-31b are smaller by ∼2 dex, whereas the cloud-top pressure for WASP-39b is larger by ∼4 dex. A comparison with other planets in the sample is not possible since the cloud-top pressures in Barstow et al. (2017) are quoted for pure Rayleigh clouds (i.e., only for particles of small sizes).

In addition, a trend is suggested in the analysis of Barstow et al. (2017) such that planets with equilibrium temperatures spanning 1300 K to 1700 K possess grey clouds that are confined deep in their atmospheres below ∼10 mbar. On the other hand, our analysis finds that HAT-P-1b ($T_{\rm eq}$ = 1320 K), HD 209458b ($T_{\rm eq}$ = 1450 K), and WASP-31b ($T_{\rm eq}$ = 1580 K) are consistent with high-altitude grey cloud-top pressures (see Figure 5.5). WASP-17b and WASP-12b, with equilibrium temperatures above 1700 K, have also been suggested to have small-particle aerosols at high atmospheric altitudes (Barstow et al., 2017). We find that a model without hazes or clouds composed of small particles provides statistically comparable fits to the spectra of WASP-17b and WASP-12b, and is therefore suggestive of weak evidence for small-particle aerosols in their atmospheres.

The discussion above illustrates there are differences in the retrieved cloud properties between our analysis and that of Barstow et al. (2017) which may be attributed to the different approaches of cloud/haze modelling. In spite of these differences, we emphasize that the estimated water abundances in the hot Jupiter atmospheres are generally in good agreement and show a trend towards sub-solar values. Planets for which similar *WFC3* data are used (HD 189733b, HD 209458b, WASP-31b, WASP-17b, and WASP-19b) illustrate that the H_2O abundances can be robust to different aerosol treatments in retrieval studies.

Beyond the key advancements in the modelling approach, the Bayesian inference method, and the results, the major contribution of our work is to provide detailed statistical estimates of important atmospheric properties for a sizable sample of hot Jupiters. All in all, these estimates will prove invaluable for comparative planetology, across both exoplanetary and solar system giant planets and for understanding their formation pathways.

5.5 Summary

We have carried out a comprehensive atmospheric study of transmission spectra of ten hot giant exoplanets contained in Sing et al. (2016). Through a homogeneous

Bayesian retrieval analysis of the planetary spectra, we determine statistically robust estimates of various atmospheric parameters including the H_2O abundances, cloud/haze properties, other chemical abundances, and the temperature structures. In particular, we find that all the planetary atmospheres are consistent in harbouring sub-solar H_2O abundances within 1σ with the exception of HAT-P-1b. This is consistent with results from previous retrieval studies (Madhusudhan et al., 2014b; Barstow et al., 2017). The planets with the most precise observations in the *HST WFC3 G141* bandpass – HD 189733b, HD 209458b, and WASP-12b – are constrained to have H_2O abundances of $0.018^{+0.035}_{-0.009}\times$, $0.04^{+0.06}_{-0.02}\times$, and $1.40^{+4.97}_{-1.11}\times$ solar, respectively. We find a continuum over cloud and haze contributions as suggested in recent studies (Sing et al., 2016; Barstow et al., 2017), although the details are different than suggested therein.

The lack of a clear correlation among various properties of the atmospheres and macroscopic properties of the planets may imply a unique and detailed evolutionary history for each giant exoplanet and/or point to the simplicity of the underlying atmospheric retrieval model. Nevertheless, in light of the host stars' solar or super-solar O/H metallicities and the generally sub-solar O/H abundances, the majority of the hot giant exoplanets are suggested to form beyond the H_2O ice-line with subsequent dynamical interaction and disk-free migration to their present environments.

Chapter 6

Retrieving the Stellar and Planetary Influence on a Transmission Spectrum

6.1 A Changing Stellar Radius

The retrieval model in Chapter 5 assumes one value for the radius of the star when calculating the transmission spectrum of each planet. By the Stefan-Boltzmann equation, a constant stellar radius corresponds to one stellar temperature for a given bolometric luminosity (i.e., one stellar spectrum). Therefore the retrieval model assumes the star has a homogeneous photosphere characterised by one spectrum. However, stellar photospheres are in reality not perfectly homogeneous. The disk of a star can be made of differential areas each with a unique spectrum that can differ from one representative average spectrum (Chapman, 1987; Shapiro et al., 2014).

Active regions of the stellar surface, in the form of cool spots and hot faculae, are among the primary features of stars responsible for heterogeneity of the photosphere and variability in a star's brightness over time. Such features on active stars may induce significant modifications to an otherwise pristine planetary transmission spectrum and hence also the retrieved atmospheric properties (Pont et al., 2013; Oshagh

et al., 2014; McCullough et al., 2014; Barstow et al., 2015; Rackham et al., 2017). For example, the slope of a transmission spectrum in the visible wavelength region is usually interpreted as due to extinction from hazes and/or clouds that are composed of small particles, but such slopes can also be caused by cool star spots which are unocculted by the transiting planet. Consequently, the steep optical slope of HD 189733b's transmission spectrum has been interpreted as opacity from haze particles in the planetary atmosphere (Pont et al., 2013) as well as possible contamination from activity features in the photosphere of its variable host star, either unocculted star spots (McCullough et al., 2014) or occulted stellar plages (i.e., bright chromospheric regions, Oshagh et al., 2014).

On the other hand, hot faculae and plages, when not occulted by the transiting planet, decrease the observed optical transit spectrum due to an increasing stellar radius at shorter wavelengths. The optical transmission spectrum of GJ 1214b, which displays a significant decline towards shorter wavelengths and shallower transit depths than observed in the near-infrared (Kreidberg et al., 2014b), has recently suggested a heterogeneous stellar photosphere dominated by hot faculae (Rackham et al., 2017). Unocculted faculae have also been suggested to affect the transmission spectrum of GJ 1132b, which displays a significant decrease in transit depth at optical wavelengths (Dittmann et al., 2017) and, like GJ 1214b, orbits a mid-M dwarf star (Berta-Thompson et al., 2015). The various effects caused by active stars conveys the importance for a method capable of differentiating properties of the planetary atmosphere and heterogeneous stellar photosphere from an observed spectrum.

In this chapter we present a new retrieval framework, Aura, that enables simultaneous inference of exoplanetary and stellar properties from a transmission spectrum. In addition to the usual properties explored for exoplanetary atmospheres (i.e., chemical abundances, clouds/hazes, and temperature structures), we incorporate a model that accounts for an active stellar photosphere into the transmission retrieval method outlined in Chapter 4. The stellar photosphere model allows inferences on the fraction of the stellar disk that is covered by heterogeneity features, their average temperature, and the temperature of the stellar photosphere. Our retrieval method ushers

in the first instance of a simultaneous inference of stellar and planetary properties in the literature. The retrieval method is an adapted version of the retrieval method in Gandhi and Madhusudhan (2018). We have made several adaptations including the creation of a model to calculate the transfer of radiation in the primary eclipse geometry as well as the integration of a stellar heterogeneity model which has been developed separately by Rackham et al. (2017).

Our work is presented as follows. In Section 6.2 we detail the stellar heterogeneity model that is incorporated into the transmission retrieval method described in Chapter 4. We then apply our new method to nine hot giant exoplanets in Section 6.3 to determine the significance of stellar heterogeneity and clouds/hazes in their observed transmission spectra. Limitations of our approach and future model considerations are discussed in Section 6.4. We discuss future observing prospects and summarise in Section 6.5. The published form of this work is presented in Pinhas et al. (2018).

6.2 Model of Heterogeneous Stellar Photospheres

The photospheres of stars display heterogeneity in the form of magnetic active regions. Beyond observations of the Sun, the most straightforward evidence for this comes from observed periodic brightness variations (e.g., McQuillan et al., 2014; Newton et al., 2016), which correspond to active regions rotating into and out of the projected stellar disk. The types of stellar activity we consider here are cool spots and hot faculae, respectively dimmer and brighter areas of a star that evolve on timescales of days to weeks (see Hathaway, 2015, and references therein). A model for heterogeneous stellar photospheres (Rackham et al., 2017) is combined with the transmission retrieval method outlined in Chapter 4 to study the stellar and planetary nature of transmission spectra.

We use the *Composite Photosphere and Atmospheric Transmission (CPAT)* model to account for inhomogeneities in the stellar photosphere (Rackham et al., 2017). This model was developed previously and used to interpret the optical transmission spectrum of GJ 1214b (Rackham et al., 2017). The model divides the stellar surface

into two components, called the 'unocculted' and 'occulted' components, defined so by the region of the star occulted by the planet during transit. The occulted component of the stellar disk has an average spectral energy distribution $\mathcal{S}_o(\lambda)$ and contains the planetary transit chord. The unocculted component accounts for heterogeneity features (cool spots and/or hot faculae) outside of the transit chord in aggregate and has an average spectral energy distribution $\mathcal{S}_u(\lambda)$. A schematic of the model is shown in Figure 6.1. We use PHOENIX atmospheric models (Husser et al., 2013) to construct the two spectral components of the star. The spectral energy distributions are interpolated from the grid of PHOENIX models through specification of three stellar parameters: the photospheric temperature, the stellar metallicity, and the stellar gravity. Here we fix the stellar metallicity and gravity to literature values for each host star and parameterise the two spectral components by the temperature.

The family of PHOENIX stellar models are limited to effective temperatures of ∼2300 K and hence we have incorporated the DRIFT-PHOENIX grid of atmospheric models (Witte et al., 2011) which allows consideration of lower temperatures to 1,000 K. While both model grids are based on the PHOENIX stellar atmosphere code (Hauschildt and Baron, 1999), the DRIFT-PHOENIX models include additional physics applicable to cooler atmospheres, including the growth and settling of dust grains (Woitke and Helling, 2003, 2004; Helling and Woitke, 2006; Helling et al., 2008a,b; Witte et al., 2009). While the host stars considered in this work have effective temperatures above 4,500 K, DRIFT-PHOENIX can be used to study present and future transmission spectra of planets orbiting cooler active stars.

The observed transmission spectrum accounting for a heterogeneous stellar photosphere is then,

$$\underbrace{\left(\frac{\mathcal{R}_p(\lambda)}{\mathcal{R}_\star(\lambda)}\right)^2}_{\substack{\text{Observed}\\ \text{Spectrum}}} = \underbrace{\left(\frac{R_p(\lambda)}{R_\star}\right)^2}_{\substack{\text{Planetary}\\ \text{Spectrum}}} \underbrace{\left(1-\delta\left(1-\frac{\mathcal{S}_u(\lambda)}{\mathcal{S}_o(\lambda)}\right)\right)^{-1}}_{\substack{\text{Stellar}\\ \text{Contamination}}} \tag{6.1}$$

or succinctly,

$$\Delta_{\rm obs} = \Delta_{\rm planet}\mathcal{E}_{\rm het}. \tag{6.2}$$

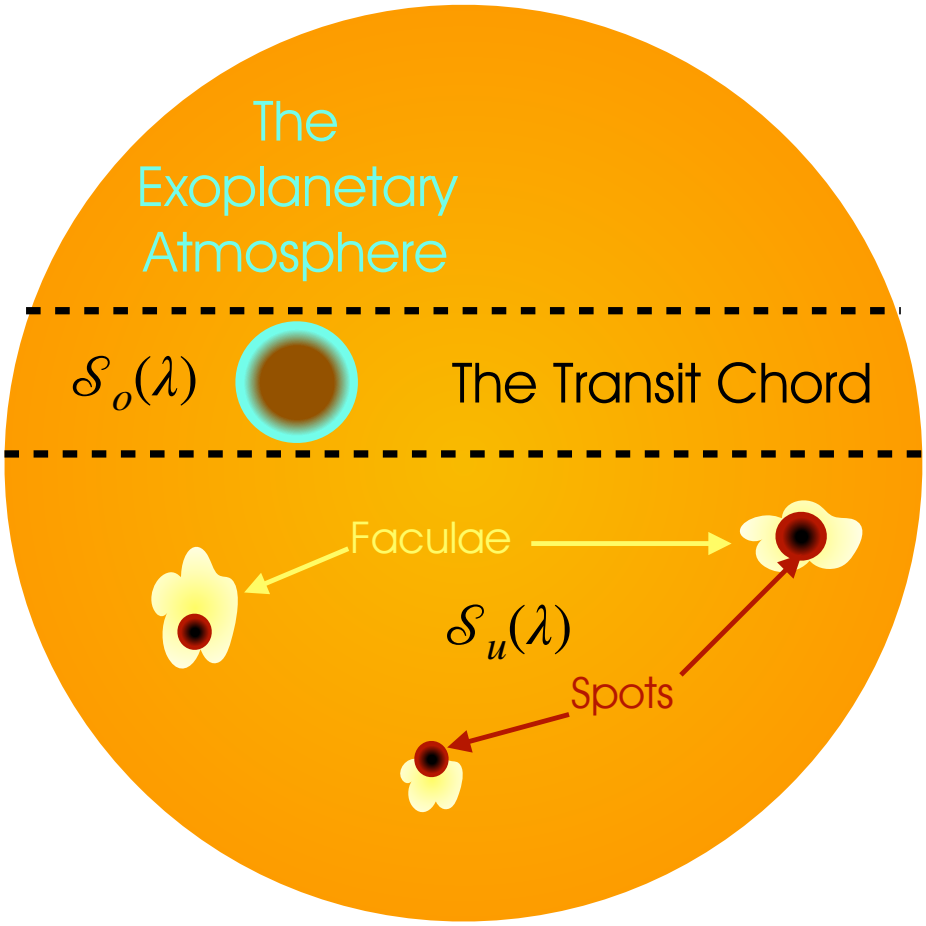

Figure 6.1: The AURA retrieval method explores the transmission spectrum that is produced by the combination of the exoplanetary atmosphere and the stellar photosphere. In the stellar heterogeneity model, the stellar photosphere consists of two components with different spectra: an occulted component that includes the transit path of the exoplanet and another unocculted component that contains cool spots and/or hot faculae.

Here, δ is the areal fraction of the projected stellar disk covered with heterogeneities (cool spots and/or hot faculae), $\mathcal{S}_u(\lambda)$ is the representative spectrum of the heterogeneities, and $\mathcal{S}_o(\lambda)$ is the spectrum of the occulted stellar surface and which we assume to be the immaculate photosphere. Equation (6.1) can be understood plainly. The first term on the right is the 'pristine' transit spectrum which alone considers effects from the planetary atmosphere (i.e., equation (4.10)). The second is a perturbative term that incorporates heterogeneity of the stellar disk and is the 'contamination spectrum' $\mathcal{E}_{\rm het}$. The observed spectrum is the product of these two terms. In the case of cool spots, Figure 6.2 shows that $\mathcal{S}_u/\mathcal{S}_o$ decreases with bluer wavelengths. This causes a decrease in the apparent radius of the star $R_\star$ and thereby increases the observed transit depth $\Delta_{\rm obs}$. On the other hand, hot faculae increase $\mathcal{S}_u/\mathcal{S}_o$ with bluer wavelengths, thereby increasing the apparent radius of the star and decreasing $\Delta_{\rm obs}$. We note that both cool spots and hot faculae may be present simultaneously in the unocculted component of the stellar disk and thus both affect the transmission spectrum. However, as shown in the right panel of Figure 6.2, these features produce opposing effects on the transmission spectrum, and in practice, one effect will dominate the observed spectrum. In this light, δ broadly represents the relative overabundance of the dominant heterogeneity in the unocculted portion of the disk. Nevertheless, it is important to emphasise that equation (6.1) can be easily expanded to incorporate effects from spots and faculae separately as is expressed in equation (3) of Rackham et al. (2018a).

Figure 6.3 shows the effects of the three stellar parameters (δ, $T_{\rm het}$, and $T_{\rm phot}$) on transmission spectra. Stellar heterogeneity is most pronounced in the $0.2 - 1.0$ μm spectral range. An increase in the heterogeneity covering fraction δ amplifies the ratio of spectral energy distributions, $\mathcal{S}_u/\mathcal{S}_o$, and therefore increasingly portrays the fine spectral details from the two stellar components. For a covering fraction dominated by cool spots, an increased δ amounts to a decreased apparent stellar radius and leads to increased transit depths. The increase in transit depth is not uniform, with the visible spectral range affected much more than the near- and mid-infrared ranges. In addition, an increase in the heterogeneity temperature $T_{\rm het}$ modifies the fine

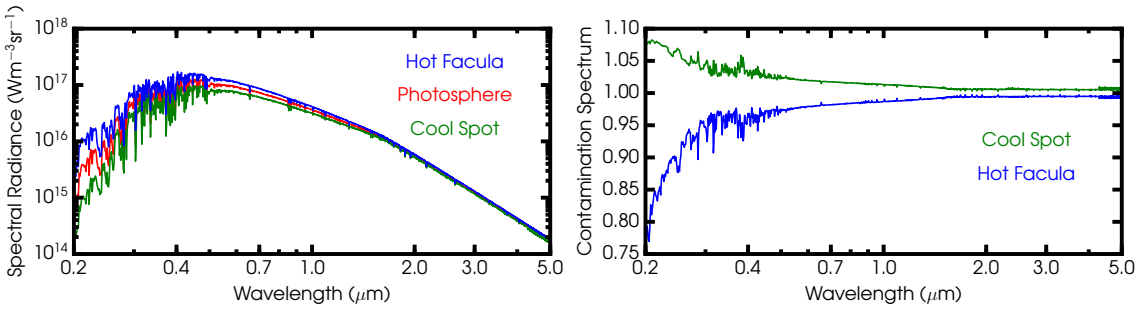

Figure 6.2: Spectral influence of stellar heterogeneity features. Left panel: Spectral radiances of a hot facula, the photosphere, and a cool spot. It is clear that $\mathcal{S}_u/\mathcal{S}_o$ increases (decreases) for a hot facula (cool spot) with bluer wavelengths. The spectrum of the photosphere was produced assuming properties of HAT-P-1 and adding (subtracting) 300 K for the hot facula (cool spot) spectrum. Right panel: Stellar contamination spectrum $\mathcal{E}_{\rm het}$. A cool spot (hot facula) displays an increase (decrease) in the contamination spectrum (and hence ultimately the observed spectrum) with smaller wavelengths. In both cases a covering fraction of ten percent is assumed.

spectral features apparent in the spectrum and is representative of different stellar types, as seen in the middle panel of Figure 6.3. For $T_{\rm het}$ greater than $T_{\rm phot}$, the optical spectrum curves downward due to an increasing $\mathcal{S}_u/\mathcal{S}_o$ with bluer wavelengths, increasing the apparent radius of the star. As shown in the bottom panel, increasing the representative photospheric temperature $T_{\rm phot}$ dampens spectral features peculiar to the unocculted component and results in higher transit depths throughout the whole spectral range.

6.3 Application to Transmission Observations

We use our retrieval framework, Aura, to study the stellar and planetary properties in the spectra of nine hot giant exoplanets. We apply our joint retrieval method to the ensemble of planets presented in Sing et al. (2016) with the exception of HD 189733b. We do not analyse HD 189733b since a transmission spectrum that is uncorrected for potential imprints of stellar heterogeneity is not available. Specifically, we focus on determining whether the transmission spectra demonstrate imprints of stellar heterogeneity and clouds/hazes in the planetary atmosphere, with these information deriving especially from the $0.3 - 1.0$ μm range.

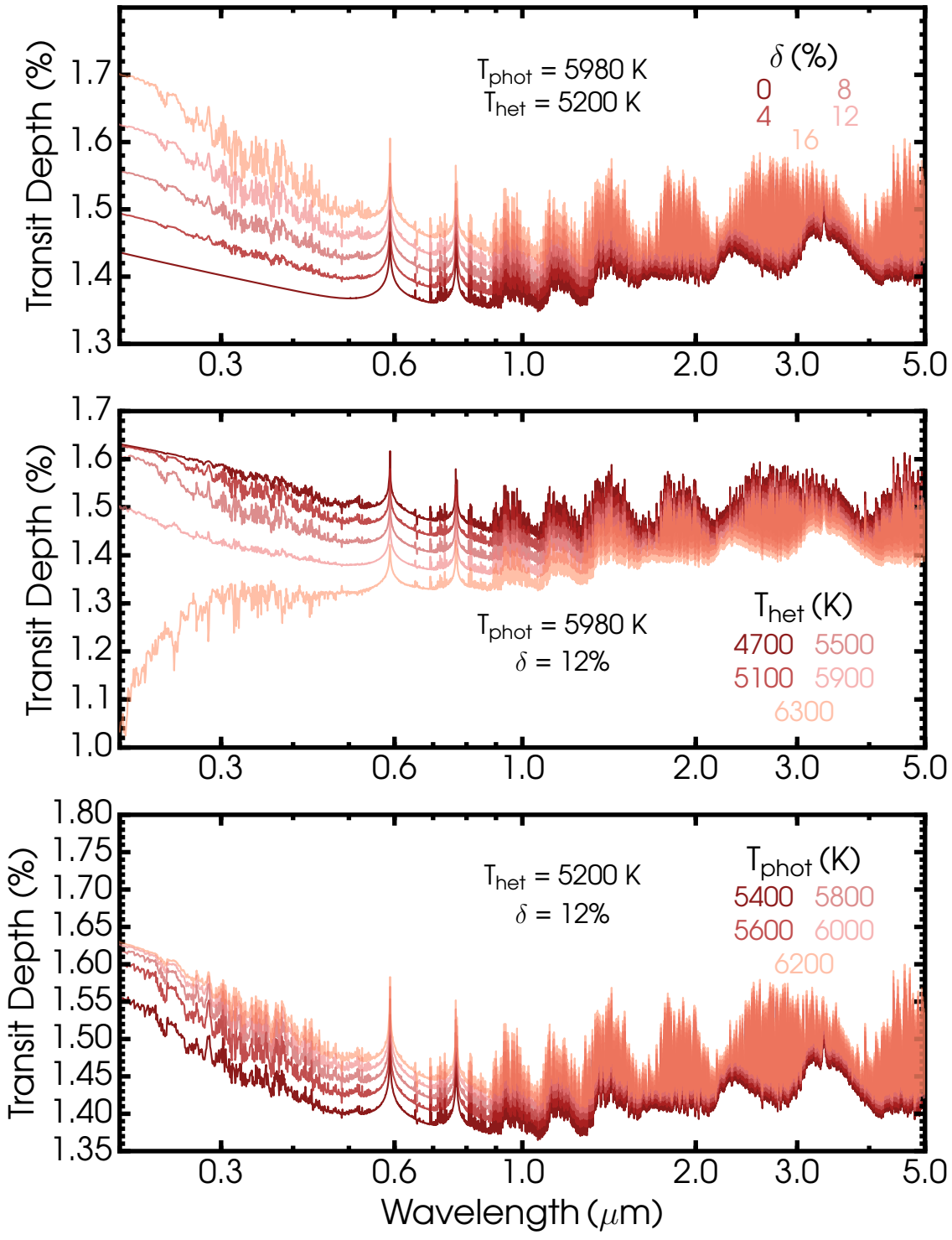

Figure 6.3: Effects of stellar properties on observed transmission spectra. The upper, middle, and bottom panels illustrate variations in the covering fraction, heterogeneity temperature, and photospheric temperature, respectively. Lighter colours represent larger values in the considered parameters. The transmission spectra are calculated according to equation (6.1) for underlying properties representative of HAT-P-1b.

Retrieval of the transmission spectra requires that the data have not been processed or corrected for stellar activity features. Therefore, we first outline the pre-corrected data used as inputs to Aura. We then present our retrieval analyses on these pre-corrected observations to illuminate the relative significance of stellar heterogeneity and clouds/hazes in the ensemble of hot Jupiter spectra.

6.3.1 Data Uncorrected for Stellar Heterogeneity

A portion of the hot Jupiter transmission observations presented in Sing et al. (2016) have been processed and corrected for unocculted and occulted stellar heterogeneity features. We therefore remove any applied heterogeneity corrections to the spectra before a retrieval application is carried out on the ensemble. Table 6.1 lists the data components as well as system properties for each planet. In what follows, we briefly describe the pre-processed data used for the planets.

6.3.1.1 WASP-19b

The uncorrected transmission spectrum of WASP-19b in the optical is obtained by reversing the correction to the four *HST STIS* data points as detailed by Huitson et al. (2013). We note that Sing et al. (2016) present two more data points in the blue wavelength region that are not present in the optical data of Huitson et al. (2013). However, sufficient information is not present in Sing et al. (2016) to determine the applied corrections to these points. We therefore do not use these two additional data and consider only the optical observations from Huitson et al. (2013). In addition to these optical data, we use *HST WFC3 G141* observations and two *Spitzer* data presented in Sing et al. (2016), to which no stellar correction was applied.

6.3.1.2 WASP-6b

To produce the WASP-6b transit spectrum uncorrected for heterogeneity of its star, we start with the data presented in Nikolov et al. (2015) and subtract the additional uncertainty applied in their Section 2.3. The typical uncertainty is now $\Delta R_p/R_\star$

Planet	log $R^{'}_{\rm HK}$	Spectral Type	$T_{\rm phot}$ (K)	Data	References
WASP-19b	−4.660	G8	5500 ± 100	*HST/STIS/G430L, G750L* *HST/WFC3/G141* *Spitzer/IRAC/3.6, 4.5 channel*	Huitson et al. (2013) Sing et al. (2016)
WASP-6b	−4.741	G8	5375 ± 65	*HST/STIS/G430L, G750L* *Spitzer/IRAC/3.6, 4.5 channel*	Nikolov et al. (2015)
HD 209458b	−4.970	G0	6092 ± 103	*HST/STIS/G430L, G750L* *HST/WFC3/G141* *Spitzer/IRAC/3.6, 4.5 channel*	Sing et al. (2016)
HAT-P-1b	−4.984	G0	5980 ± 8	*HST/STIS/G430L, G750L* *HST/WFC3/G141* *Spitzer/IRAC/3.6, 4.5 channel*	Sing et al. (2016)
WASP-39b	−4.994	G8	5400 ± 150	*HST/STIS/G430L, G750L* *HST/WFC3/G141* *Spitzer/IRAC/3.6, 4.5 channel*	Tsiaras et al. (2018) Sing et al. (2016)
HAT-P-12b	−5.104	K5	4650 ± 60	*HST/STIS/G430L, G750L* *HST/WFC3/G141* *Spitzer/IRAC/3.6, 4.5 channel*	Line et al. (2013) Sing et al. (2016)
WASP-31b	−5.225	F	6300 ± 100	*HST/STIS/G430L, G750L* *HST/WFC3/G141* *Spitzer/IRAC/3.6, 4.5 channel*	Sing et al. (2016)
WASP-12b	−5.500	G0	6400 ± 190	*HST/STIS/G430L, G750L* *HST/WFC3/G102, G141* *Spitzer/IRAC/3.6, 4.5 channel*	Kreidberg et al. (2015) Sing et al. (2016)
WASP-17b	−5.531	F4	6650 ± 80	*HST/STIS/G430L, G750L* *HST/WFC3/G141* *Spitzer/IRAC/3.6, 4.5 channel*	Sing et al. (2016)

Table 6.1: Planetary system properties and observations. Columns two to four list properties of the stellar host. The disk-integrated chromospheric Ca II log $R^{'}_{\rm HK}$ index is proportional to the ratio of the flux in the Ca II H and K line cores and the flux in the nearby continuum (see Noyes et al., 1984) and correlates with the photospheric activity level (Lockwood et al., 2007). The observations used for each planet and and which are uncorrected for stellar activity effects are shown in the fifth column, with relevant references for the uncorrected data in the last column. Planetary equilibrium temperatures and radii are listed in Table 5.1 of Chapter 5.

∼220 ppm smaller, in agreement with the change described in Nikolov et al. (2015). This change is significant for most wavelength bins, representing a ∼40% reduction in the error on the measurement.

6.3.1.3 Other Hot Jupiters

The transmission spectra for the remaining seven planets experienced no corrections. Therefore we use the data as presented in Sing et al. (2016) for HD 209458b, HAT-P-1b, WASP-39b, HAT-P-12b, WASP-31b, WASP-12b, and WASP-17b. Additional *HST WFC3* data for WASP-39b (Tsiaras et al., 2018), HAT-P-12b (Line et al., 2013), and WASP-12b (Kreidberg et al., 2015) complement the data from Sing et al. (2016).

6.3.2 Retrieval of Uncorrected Data

We conduct five independent retrievals for each planet to examine the roles of stellar heterogeneity and clouds/hazes contained in the spectral ensemble. The roles of stellar heterogeneity and clouds/hazes in the hot Jupiter spectra are summarised in Table 6.2. Appendix Table D.1 provides the detailed statistical results for the five retrieval types used to arrive at the conclusions in Table 6.2 for each planet. The full retrieval results including posterior distributions, spectral fits, and $p-T$ profiles are available on the Open Science Framework[1] (OSF). Representative spectral fits for the planetary ensemble are displayed in Figure 6.4. All retrieval types include parameters of the $p-T$ profile and mixing ratios of eight molecules and alkali metals and are distinct as follows:

1. **Heterogeneity + Molecules + Clouds/Hazes (hereafter, HMch)**: Three stellar parameters, eight molecular and elemental abundances, and four cloud and haze parameters (grey and non-grey opacities, respectively).

2. **Heterogeneity + Molecules + Clouds (hereafter, HMc)**: Three stellar parameters, eight molecular and elemental abundances, and two cloud parameters (grey opacity only). This model excludes non-grey opacity from hazes.

[1] `https://osf.io/6gwtm/?view_only=46c6e5ece1264da598dc461948873055`

Group	Planet	Stellar Heterogeneity	Clouds/Hazes
I	WASP-6b	Strong	Weak - Substantial
	WASP-39b	Substantial	Weak - Strong
II	HD 209458b	Weak	Substantial - Very Strong
	HAT-P-12b	Weak	Weak (against) - Very Strong
III	HAT-P-1b	Weak (against)	Weak (against) - Substantial
	WASP-31b	Weak (against)	Weak
IV	WASP-19b	Substantial (against)	Weak - Substantial
	WASP-17b	Substantial (against)	Weak (against)
	WASP-12b	Substantial (against)	Weak (against) - Weak

Table 6.2: Roles of stellar heterogeneity and clouds/hazes in the spectral ensemble. The qualitative descriptions in the two categories are based on the Bayes factor results listed in Appendix Table D.1 and the Bayes factor nomenclature scale of Kass and Raftery (1995). Instances of '(against)' following the qualitative descriptions signify that the category is not favoured to the degree of the description. Thus, for example, the spectrum of WASP-31b is best interpreted through a weak suggestion against stellar heterogeneity and weak evidence for hazes and/or clouds. The results for WASP-6b represent the full set of data. In summary, four groups of planets are distinguished through the role in which stellar heterogeneity and clouds/hazes explain their spectra. Group I is best characterised by imprints of stellar heterogeneity and clouds/hazes. Group II comprises HD 209458b and HAT-P-12b and shows weak evidence for stellar heterogeneity but beyond substantial suggestions of clouds and/or hazes. HAT-P-1b and WASP-31b constitute Group III and show weak evidence against stellar heterogeneity but weak to substantial indications of clouds and/or hazes. The fourth group – WASP-19b, WASP-17b, and WASP-12b – can be explained best without stellar heterogeneity and weak to no evidence for clouds/hazes.

3. **Heterogeneity + Molecules (hereafter, HM)**: Three stellar parameters and eight molecular and elemental abundances. This model excludes haze and cloud opacities.

4. **Molecules + Clouds/Hazes (hereafter, Mch)**: Eight molecular and elemental abundances and four cloud and haze parameters (both non-grey and grey opacities). This model excludes stellar heterogeneity.

5. **Molecules (hereafter, M)**: Eight molecular and elemental abundances. This model excludes both stellar heterogeneity and clouds/hazes.

The retrieval analyses reveal four groups of planets distinguished through the

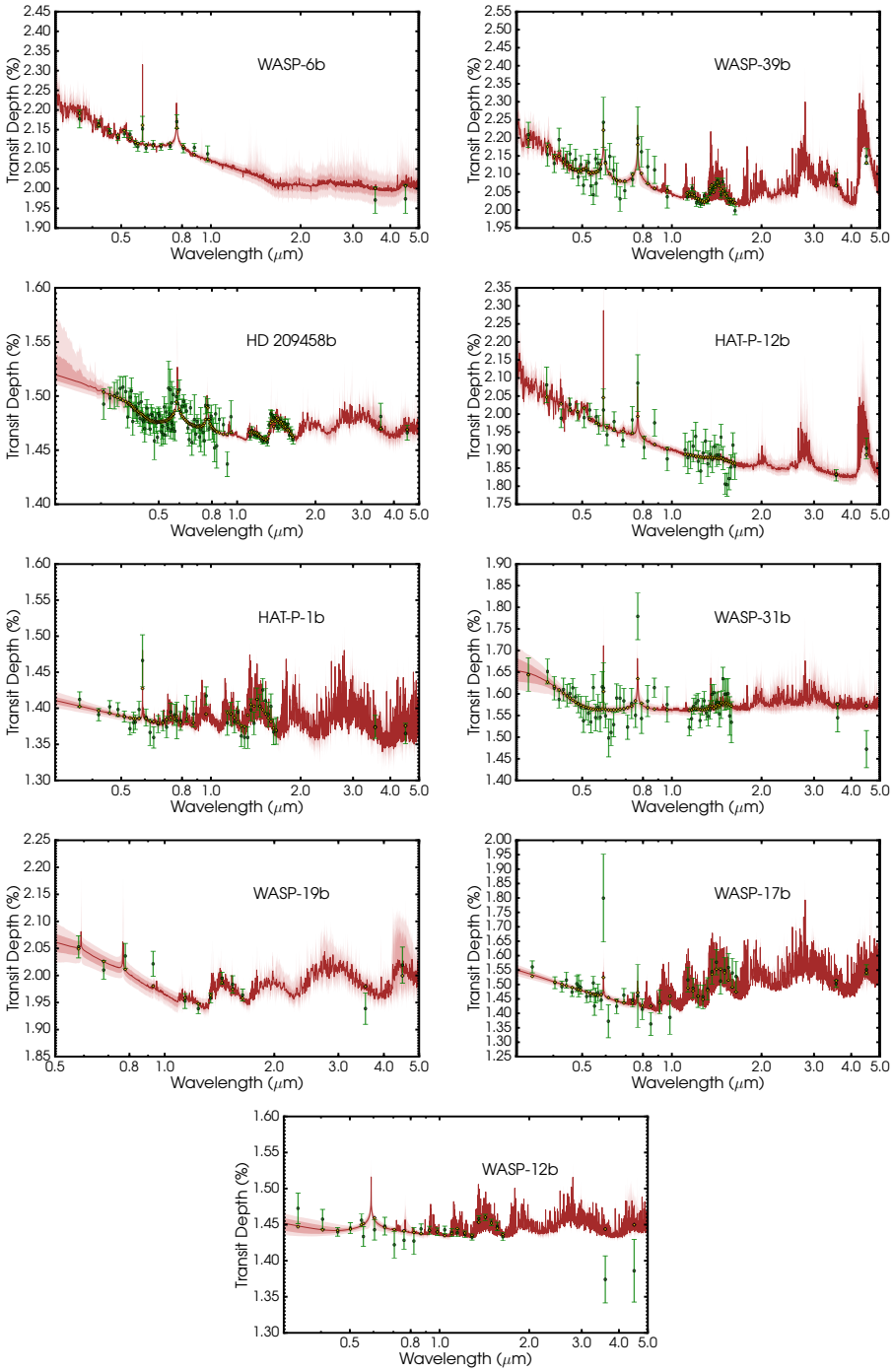

Figure 6.4: Retrieved model transmission spectra compared to observations for the ensemble of hot Jupiters. The data are shown in green and the retrieved median model is in dark red with associated 1σ and 2σ confidence contours. The yellow diamonds are the binned median model at the same resolution as the observations. Model type HMch is shown for WASP-6b, WASP-39b, and HD 209458b; model type HMc is shown for HAT-P-12b; model type Mch is shown for HAT-P-1b, WASP-31b, and WASP-19b; and model type M is shown for WASP-17b and WASP-12b.

role in which stellar heterogeneity and clouds/hazes explain the spectra. This is summarised in Table 6.2. The first group comprises WASP-39b and WASP-6b. Their spectra are best characterised by imprints of stellar heterogeneity and clouds and/or hazes. HD 209458b and HAT-P-12b comprise the second group for which there is high importance of hazes and/or clouds and weak evidence for stellar heterogeneity. The third group constitutes HAT-P-1b and WASP-31b and shows weak evidence against stellar heterogeneity but weak to substantial indications of clouds and/or hazes. The fourth group – WASP-19b, WASP-17b, and WASP-12b – are fit best by alkali and molecular absorbers with H_2 scattering without stellar heterogeneity and weak to no evidence for clouds/hazes. Here we discuss the detailed role of stellar heterogeneity and clouds/hazes for the planets in each group.

6.3.2.1 Group I: Stellar Heterogeneity + Clouds/Hazes

Table 6.2 shows the spectra of WASP-6b and WASP-39b are best explained in light of stellar heterogeneity as well as clouds and hazes. The full observations of WASP-6b show the greatest suggestion for stellar heterogeneity imprints among the planetary sample. The significance of stellar heterogeneity in the spectrum is 3.13σ through a comparison of the evidences for HMch and Mch model types. The Bayes factor of HMch to HMc models is 1.22 (1.37σ), indicating weak evidence for hazes in addition to stellar heterogeneity. The combined evidence for hazes and clouds is 2.48σ (Bayes factor of 6.48) and is thus substantial. Therefore stellar heterogeneity and planetary hazes/clouds are complementary in best interpreting the full spectrum.

The retrieved results of the HMch model suggest an active star with a covering fraction of $12.1^{+2.2}_{-1.9}$%. This substantial active area is dominated by cool spots with temperatures of 4556^{+242}_{-213} K, indicating large temperature contrasts of ∼800 K between the photosphere (∼5375 K) and regions of unocculted cool spots.[2] This

[2]It is here appropriate to gauge the reasonableness of the retrieved heterogeneity temperatures and coverage fractions with values obtained from Doppler Imaging measurements (Vogt and Penrod, 1983; Donati et al., 1997). In reality starspots are composed of cool penumbrae and still cooler umbrae, but our model essentially describes such spots with one temperature and therefore amounts to averaging over the umbral and penumbral temperatures as well as their individual temperature ranges. The retrieved heterogeneity temperatures in the present study have uncertainties of ∼200 K,

evidence for widespread unocculted cool spots is intriguing as photometric monitoring suggests that the flux of the star does not vary by more than 1% in V band (Nikolov et al., 2015). However, photometric monitoring places only a lower limit on the heterogeneity, as longitudinally symmetric active regions do not contribute to the observed variability (Rackham et al., 2018a). Furthermore, the Ca II H and K stellar activity index for WASP-6, $\log R'_{\rm HK} = -4.741$, which is higher than all in this sample except WASP-19, points to a high level of chromospheric activity, which in turn correlates to higher photospheric activity (Lockwood et al., 2007).

To investigate the influence of the *Spitzer* data on the above suggestions, we have carried out another set of five retrievals which includes one of each model type described above but with the *Spitzer* data excluded. In this case, a heterogeneity explanation is not statistically strong since the Bayes factor of HMch to Mch models is 1.28 (1.43σ). Moreover, the *STIS* data indicate weak evidence against hazes (Bayes factor of 0.89). The existence of grey opacity clouds is favoured in both scenarios given the increase in significances between HMc and HM models. In all, it is clear that a definitive (non)detection of heterogeneity from the transmission spectrum of WASP-6b will need to await future high quality observations, specifically high-resolution and high-precision observations in the $0.3 - 1.0$ μm range where heterogeneity effects are most pronounced. Observations in the *HST WFC3* bandpass could also detail the degree to which molecular absorption features from the planetary atmosphere are muted by the presence of clouds/hazes or enhanced by cool star spots.

The full observations of WASP-39b show a second suggestion of stellar heterogeneity imprinted in a transmission spectrum. The Bayes factor of HMch to Mch models is 6.26, indicative of a substantial heterogeneity signal at 2.47σ. The retrieved covering fraction of heterogeneity features is $10.3^{+5.9}_{-3.7}$%. The coverage area is dominated by

while the temperature variations of umbra and penumbra inferred from Doppler Imaging of stars are ∼200-300 K (e.g., Strassmeier, 1999; Berdyugina, 2005; Rosén and Kochukhov, 2012; Kővári et al., 2013; Hackman et al., 2018). Stellar surfaces may also contain faculae, and being brighter, may be better detected in atomic lines and should provide smaller inferred uncertainties than for spots. Taken together, these points suggest that the retrieved temperature uncertainties are reasonable given the model assumptions and typical measured values. The retrieved spot covering fractions are also consistent with determined precisions of spot filling factors from Doppler Imaging (e.g., Petit et al., 2004).

cool spots with temperatures of 4936^{+240}_{-309} K and photospheric temperature contrasts of ∼500 K. The general presence of clouds and hazes is evident at 4.22σ (Bayes factor of 1430) and the spectral component arising from hazes is suggested to be weak at 1.45σ (Bayes factor of 1.30).

6.3.2.2 Group II: Weak Stellar Heterogeneity + Clouds/Hazes

Table 6.2 shows the spectra of HD 209458b and HAT-P-12b are best explained in light of hazes and/or clouds with weak evidence for stellar heterogeneity. HD 209458b and HAT-P-12b display slender hints of heterogeneity considering Bayes factors of 1.44 and 1.20 (respectively, 1.55σ and 1.35σ) between HMch and Mch models. The retrieved covering fraction of heterogeneity features for HD 209458 (HAT-P-12) is $3^{+2}_{-1}\%$ ($18^{+3}_{-2}\%$). Cool spots with temperatures of 4167^{+119}_{-157} K dominate the coverage area for HAT-P-12, giving a photosphere-spot temperature contrast of ∼500 K. On the other hand, the spots on HD 209458 have retrieved temperatures of ∼3500 K and/or ∼5700 K. Spot temperatures between 4900 and 5500 K have been inferred for HD 209458 based on spot crossing events in observed lightcurves (Silva, 2003), albeit this conclusion is for data from 2001 for which the stellar activity (and therefore its signatures) is different than in the data analysed here. No focused analysis of HD 209458 spot temperatures has been attempted in recent times as HD 209458 is a relatively quiet star.

The general presence of clouds and hazes in HD 209458b is evident at 5.34σ (Bayes factor of 2.4×10^5) and the spectral component arising from hazes is suggested to be substantial at 2.14σ (Bayes factor of 3.31). In the case of HAT-P-12b, a Bayesian interpretation weakly favours a model without hazes since the Bayes factor of HMch to HMc models is 0.92 but illustrates a very strong suggestion for clouds at more than 6σ.

6.3.2.3 Group III: Weak Evidence Against Stellar Heterogeneity + Weak to No Clouds/Hazes

Table 6.2 shows the spectra of HAT-P-1b and WASP-31b are best explained through a weak suggestion against stellar heterogeneity and weak to no evidence for clouds/hazes. HAT-P-1b and WASP-31b constitute spectral interpretations with a weak suggestion against a heterogeneity component since the Bayes factors of HMch to Mch models are below one. The Bayes factors in Appendix Table D.1 imply the importance of clouds over hazes in the spectrum of HAT-P-1b, while hazes are weakly favoured in WASP-31b.

6.3.2.4 Group IV: Substantial Evidence Against Stellar Heterogeneity + Weak to No Clouds/Hazes

Table 6.2 shows the spectra of three planets – WASP-19b, WASP-17b, and WASP-12b – are best explained through substantial evidence against stellar heterogeneity and weak or no evidence for cloud/haze coverage. In the case of WASP-19b, the model with the largest Bayesian evidence is Mch, such that stellar heterogeneity is not substantially preferred. Clouds and hazes are suggested to a weak degree through comparison of models HMc and HM with HMch. On the other hand, features in the spectra of WASP-17b and WASP-12b are sufficiently explained through molecular and alkali absorption as well as H_2 Rayleigh scattering (i.e., model type M). We emphasise that although the finding of relatively clear atmospheres for WASP-12b, WASP-19b, and WASP-17b are consistent with suggestions of hotter ($T_{\rm eq} \gtrsim 1700$ K) close-in planets having less cloudy atmospheres (e.g., Heng, 2016), it would be prudent to test these results using a detailed physical cloud model (e.g., using a 3D formalism similar to Helling et al., 2019).

The result for WASP-19b is surprising as WASP-19 displays the highest stellar activity index of the host stars in the current sample (see Table 6.1), suggesting a high level of chromospheric activity. Corresponding photospheric activity has been observed in the form of V-band rotational variability (Huitson et al., 2013) and spot-

crossing events during transit (Mancini et al., 2013; Huitson et al., 2013; Sedaghati et al., 2017). However, the stellar contribution to transmission spectra depends on a variety of parameters, including active region temperature contrasts, covering fractions, and locations within the projected stellar disk at the time of the observation. Nevertheless, we have explored whether the unexpected lack of evidence for stellar contamination for WASP-19b is a result of the two-component stellar heterogeneity model of equation (6.1) which assumes the prominence of either cool spots or hot faculae. We have conducted two additional retrievals that use a modified model that treats spots and faculae as separate components following equation (3) of Rackham et al. (2018a). The two retrievals are made available on the OSF[1] under 'WASP-19b/Three-component photosphere'.

In the case of the HMch model with spots and faculae treated independently, we find that the Bayes factor of Mch to HMch models is above 3. This lack of evidence for heterogeneity is also supported by the fact that the retrieved covering fractions of faculae and spots in the HMch model are consistent with zero. Clouds and hazes are suggested at 2.5σ (Bayes factor of 6.75) by comparing the HMch and HM models and the cloud/haze properties are also not significantly different than those of the two-component heterogeneity model. The results from a three-component heterogeneity model validate the suggestion that the WASP-19b data show a lack of evidence for stellar heterogeneity.

The case of WASP-19b illustrates that the relationship between stellar activity and contamination of transmission spectra might not correlate in all cases. Still, given that WASP-19b possesses the least constraining optical spectrum of the current sample, consisting of only four points between 0.5 and 1.0 μm, higher-resolution optical observations uncorrected for stellar effects can elucidate this relationship further. We emphasize that the suggestion against stellar heterogeneity for WASP-19b might be driven by the low data quality of the available spectrum in addition to multiple limiting facets discussed in the next section.

6.4 Atmospheric-Photospheric Retrieval: Limitations and Future Steps

Our joint retrieval methodology and its first applications provide a novel insight into how stellar contamination can affect some of the published transmission spectra. It also shows encouraging results in disentangling stellar contamination from genuine planetary signatures. Here we explore several assumptions and limitations of our methodology as well as constructive future developments in joint retrievals for better elucidation of stellar and exoplanetary properties.

6.4.1 Model Components: Hazes and Starspots

Our Bayesian approach is based on the assumptions that the model components used are complete (i.e., no significant component is missing) and correct (i.e., the models and its components rightly capture the key properties of the real system). Although our retrieval model components and therefore these underlying assumptions are supported by state-of-the-art knowledge on exoplanets and stars and are also widely used (e.g., Lockwood et al., 2007; Line et al., 2013; Jackson and Jeffries, 2013; Moses, 2014; Waldmann et al., 2015b; Kreidberg et al., 2015; Line and Parmentier, 2016; Apai et al., 2018a; Rackham et al., 2018b), it is important to point out that they are still assumptions. It is thus prudent to briefly review the uncertainties implicit to our assumptions and, especially, place them in the context of stellar contamination, which is explored in this study.

It is important to recognise that we do not have a complete and correct model for stellar contamination yet: the spatial distribution of temperature/spectral variations across stellar disks and its temporal evolution as a function of stellar parameters is very poorly understood (for recent summaries see Rackham et al. 2018a and Apai et al. 2018b). For now, we do not have a good handle on basic parameters such as starspot covering fractions and typical temperature distributions of spots and faculae in stars other than the Sun.

The stellar contamination model chosen in this study is state-of-the-art (Lockwood et al., 2007; Jackson and Jeffries, 2013; Apai et al., 2018a; Rackham et al., 2018b); nevertheless, the spectral components that we use for the heterogeneities are simply stellar photospheric model spectra, not starspot/facular spectra (e.g., Norris et al., 2017). Observational efforts are being made to study the spatial distribution and properties of stellar magnetic activity (e.g., Metcalfe et al., 2013; Haywood et al., 2014; Mengel et al., 2017; Giles et al., 2017; Fares et al., 2017; Şenavci et al., 2018), but no such endeavors have been made simultaneously during periods in which exoplanetary spectra were taken. Future efforts should be directed to gain contemporaneous stellar magnetic activity measurements. This will allow testing our stellar heterogeneity model component on the starspot/facular properties, thereby allowing better interpretation of the spectral contribution from the planetary atmospheres.

The limitations of our model for stellar contamination are especially significant due to its potential to resemble hazes, which have been invoked in exoplanetary atmospheres and also included in our models. We note that these unidentified particles are represented by featureless spectra, where the extinction coefficient of the assumed particles is free to vary by four or more orders of magnitude relative to that of H_2 scattering. As the putative haze particles do not have any other detectable features in the optical, their existence is only inferred from residual spectral slopes that are not otherwise explained by planetary atmosphere models.

However, as recognized in the literature (McCullough et al., 2014; Rackham et al., 2017) and also shown by our results (see Table 6.2), some transit spectra can be better reproduced by stellar contamination as well. The distinction of hazes and stellar contamination on the basis of the Bayesian evidence is necessarily based on the assumption that we have complete and correct models for both: future efforts should focus on testing and verifying these assumptions, as hazes and stellar contamination can have degenerate spectral signatures.

6.4.2 Stellar Variability

Our methodology represents an important step forward in disentangling stellar contamination and genuine planetary features but still only focuses on the transmission spectra. It does not yet incorporate the evidence provided by focused stellar variability observations. Stellar heterogeneity can be, to some level, constrained by stellar variability measurements (e.g., Sing et al., 2011; Aigrain et al., 2012; Zellem et al., 2017) and by absorption and emission line measurements (e.g., Boisse et al., 2009). It is important to note that neither these nor other methods yet allow precise measurements of spot/facular covering fractions or temperature distributions over the stellar disk; variability measurements can only place a lower limit on these parameters (Jackson and Jeffries, 2013; Rackham et al., 2018a).

Perhaps the most important information provided by stellar activity indicators is that stellar disks are heterogeneous and that stellar contamination, to some level, must occur. Therefore, in principle, uniform priors on the models (as in the present work) should not be assumed, though the weight that should be assigned to models is challenging to quantify in practice. Future studies should attempt to integrate an improved understanding of an individual stellar disk's heterogeneity (spatial distribution of regions with unique temperatures/spectra) through priors informed by the combined knowledge from spectroscopic and photometric activity indicators.

6.4.3 Multi-epoch Observations

Due to the limited wavelength range of any single spectrograph or imager, most exoplanetary transmission spectra have been obtained with multiple instruments and at multiple epochs, often separated by months or years. Stellar heterogeneity, however, varies in time. Therefore, the stellar contamination imprinted in a spectrum can vary between epochs. By necessity our study has analysed the planetary spectra as if the observations occurred in a single epoch. A multi-epoch study is currently beyond the information content of the available datasets; nevertheless, future observations should ensure that data are collected in a fashion that facilitates retrieval of multi-

epoch data. Stellar contamination, if significant, will be time-variable. Assuming an average, representative contamination (as in our study) will likely not be satisfactory for objects where some datasets have been collected at times of greater stellar activity.

6.4.4 Analysis Restricted to Lower-activity Stars

It is important to note that our current analysis excludes exoplanets for which the most significant stellar contamination is expected. Some published high-quality datasets could not be included since stellar activity corrections were so significant that the data could not be reasonably 'un-corrected'.

A good example for this limitation is HD 189733b for which *HST* datasets using multiple *STIS*, *ACS*, and *WFC3* modes have been published, representing data collected over 22 different epochs (Pont et al., 2013; Sing et al., 2016). The host star HD 189733 is clearly active: significant photometric variations at the 3% level have been observed between different epochs (Sing et al., 2011).

Pont et al. (2013) and subsequent studies of these HD 189733b data are based on a stellar contamination correction that applies a multiplicative and wavelength-dependent correction to each dataset. The correction is derived from an estimated starspot covering fraction (determined for each epoch) and a starspot temperature (constant in time, and derived on the basis of a single starspot occultation by HD 189733b). Although the Pont et al. (2013) study certainly represented a state-of-the-art analysis, the stellar correction method used was based on optimistic assumptions and had several significant limitations, some of which were also acknowledged in that work (see their Section 3.3).

As assumptions similar to those in Pont et al. (2013) are often used in the literature to combine multi-epoch data, it is instructive to review their limitations here. First, the systematic uncertainties introduced by the starspot corrections are not in all cases analyzed fully or folded into the uncertainties on the data. Second, the corrections optimistically assume the lowest possible starspot covering fraction and stellar contamination, because the starspot areal covering fractions are derived from photometric variability assuming a linear relation between the amplitude of photo-

metric variation and the spot covering fraction. However, this linear relation is valid only in the most optimistic cases, a finding later quantified independently for general cases by Jackson and Jeffries (2013) and Rackham et al. (2018a). Third, the stellar contamination correction applied by Pont et al. (2013) is constrained by spot-crossing events collected for very large spots. It is very likely that due to strong observational selection biases, very large spots are not representative of the size population of starspots/faculae that exist on HD 189733 and other stars. Fourth, no photometric data existed for some of the epochs in which data were taken and Pont et al. (2013) were forced to interpolate spot covering fractions between neighboring epochs, which is unlikely to provide a correct value. Finally, Pont et al. (2013) use a common assumption that planetary transmission spectra must be continuous across different instruments and applies an offset to ensure this. However, this step, intended to compensate for stellar brightness variations, does not account for the color terms intrinsic to the stellar heterogeneity.

The HD 189733b data – used in a significant number of follow-up studies – effectively demonstrate the challenges in correcting for stellar contamination in moderately active stars and highlight potentially unreliable assumptions in the corrections that are introducing poorly understood and possibly significant systematic errors in such datasets.

In all, our study did not include data from significantly active stars whose stellar luminosities have changed by more than a few per cent between epochs. Our sample of planets therefore does not represent the full range of stellar contamination that should be expected in transmission spectra.

6.4.5 Future Observing Prospects

The substantial and yet indefinite suggestions of stellar heterogeneity in the spectra of WASP-6b and WASP-39b offer observational strategies to increase the significance of inferred stellar heterogeneity effects and planetary properties with our retrieval methodology. While the effects of stellar heterogeneity can be significant at wavelengths as long as 2 μm (see Figure 6.3), they are most pronounced between 0.3 and

1 μm and observations should thus focus on this spectral range to probe the activity of stellar photospheres. The corollary is that observations in the infrared essentially ascertain atmospheric properties of the exoplanet alone.

Joint studies of exoplanetary atmosphere compositions and heterogeneous stellar photospheres would benefit from precision observations in the Na and K absorption bands achievable with multiple *HST* orbits using the *STIS 430L* and *STIS 750L* grisms. Cool spots can masquerade as Na and K absorption features for a variety of stellar temperatures, metallicities, and gravities (Rackham et al., 2018b). In such cases and for observations of limited precisions (i.e., $\lesssim$ 100 ppm), degenerate explanations arise between Na and K abundances and stellar activity influence. Higher-precision observations in the Na and K bands can break this degeneracy, in turn enabling more precise estimates of heterogeneity covering fractions, alkali abundances, and haze properties. In addition, joint inferences will also benefit from high-resolution, broadband observations in the 0.3 to 1.0 μm window. This aspiration is already achievable through intelligent use of the *VLT FORS2* spectrograph (e.g., Sedaghati et al., 2017). Such finely-sampled observations can serve as a microscope into the heterogeneous coverage fraction since δ amplifies features of the spot/faculae spectra (see Figure 6.3, upper panel). The positive correlation between the coverage fraction and heterogeneity temperature seen in Figure 6.3 would also mean better constraints on the heterogeneity temperature with such *VLT* observations.

The *JWST* can also contribute much to the joint retrieval of stellar and exoplanetary properties. The multi-wavelength capabilities facilitated by *JWST* can help separate stellar and planetary spectral imprints as the contrast between heterogeneous features and the pristine stellar photosphere decreases with longer wavelengths as shown in Figure 6.2. Thus, for example, spectra across 5 to 28 μm obtained with observing modes of the *MIRI* instrument will essentially reflect properties of the exoplanetary atmosphere alone. Simultaneous study of stellar and exoplanetary properties will also be possible. The time-series observing mode of the *NIRCam* instrument will permit stellar activity monitoring in the 0.6 to 5.0 μm range. The amplitude of time-series photometry can reveal lower limits on heterogeneous covering fractions

(Rackham et al., 2018a) which can in turn be used as retrieval constraints using spectroscopy in the 0.6 to 5.0 μm range from *NIRISS* and *NIRSpec* spectroscopy.

6.5 Summary

The four groups of planets identified in Table 6.2 are approximately arranged by increasing chromospheric activity index (log $R'_{\rm HK}$), as seen by a comparison of Tables 6.1 and 6.2. The evident exceptions to this arrangement are WASP-19b and WASP-39b. Highly active stars (i.e., WASP-6) are found in the first group with evidence for stellar heterogeneity while low activity stars (i.e., WASP-12 and WASP-17) settle into the fourth group with substantial evidence against heterogeneity. The remaining planets (excepting WASP-19b and WASP-39b) are essentially ordered into the second and third groups, with weak evidence for or against heterogeneity. The observational consequences of this rough ordering of planets based on log $R'_{\rm HK}$ is noteworthy, for it suggests that the popular chromospheric activity indicator offers some predictive power as to whether an exoplanet transmission spectrum will be affected by stellar heterogeneity.

In summary, we have presented a new retrieval methodology, Aura, that enables simultaneous inference of the properties of exoplanetary atmospheres and their host stars in the transiting configuration. The developed framework permits the inference of general inhomogeneous properties of the star including the stellar disk fraction covered by heterogeneity features, the average temperature of the heterogeneous fraction, and the temperature of the stellar photosphere. Jointly with the three stellar properties, the methodology permits the retrieval of a host of exoplanet atmosphere properties including the chemical compositions and abundances, attributes of clouds and hazes, and the temperature profiles throughout the atmosphere. Our methodology is the first joint retrieval framework suited for the extraction of properties of exoplanetary atmospheres and their host stars. As such it sets a precedence for more detailed analysis techniques of exoplanets and their stars in the future.

We have applied our methodology to the transmission spectra of a sample of hot

giant exoplanets to ascertain the influence of stellar heterogeneity and clouds/hazes in their spectra. The analysis distinguishes four groups of planets defined by the components needed to best explain their spectra. These four groups are illustrated in Table 6.2. In the first case, we find that the spectra of WASP-6b and WASP-39b are best fit with stellar heterogeneity as well as hazes and/or clouds. In the second case, there is marginal evidence for stellar heterogeneity effects and beyond substantial evidence for hazes and/or clouds in the spectra of HD 209458b and HAT-P-12b. The third group constitutes HAT-P-1b and WASP-31b and shows weak evidence against stellar heterogeneity but weak to substantial indications of clouds/hazes. In the fourth group three planets – WASP-19b, WASP-17b, and WASP-12b – are fit best by alkali and molecular absorbers with H_2 scattering without stellar heterogeneity and weak to no evidence of cloud/haze coverage. We therefore emphasize that the suggestion against heterogeneity for WASP-19b is potentially due to the low data quality of the spectrum, and thus future studies of WASP-19b may suggest differently.

We note that joint retrievals of the stellar photosphere and exoplanetary atmosphere rely on the assumptions that the model components are reasonably correct and reasonably complete. Presently, however, even state-of-the-art models for stellar heterogeneity are based on very limited knowledge; furthermore, the hypothesized haze particles can provide similar spectral signatures in the optical and the retrieved results depend on the included chemical species. Future efforts must be aimed towards collecting better data as well as enhancing the model components to break the degeneracy between stellar contamination and possible atmospheric aerosols.

Ultimately, upcoming observatories will provide improved spectral resolutions and precisions useful for more definite and detailed joint analyses of transmission spectra. The simultaneous information on stellar and planetary properties facilitated through Aura can serve as a helpful tool in the analysis of present high-precision spectra and future high fidelity observations from the *JWST* and powerful ground-based facilities.

Chapter 7

Retrieving the Spectra of the Directly-Imaged HR 8799 Companions

Direct imaging refers to the detection of an exoplanet or brown dwarf as a point source of light through the object's own thermal emission. The first detection via direct imaging was of a massive, wide-orbit brown dwarf in 1995 (Nakajima et al., 1995). The NASA Exoplanet Archive (Exoplanetarchive.ipac.caltech.edu, 2019) lists 44 direct-imaging discoveries to date including a quadruple of companions around HR 8799 (Marois et al., 2008, 2010), Fomalhaut b (Kalas et al., 2008), β Pictoris b (Lagrange et al., 2009), 51 Eri b (Macintosh et al., 2015), and the LkCa 15 system composed of two planets which are still in the stages of formation (Sallum et al., 2015). Of these, the HR 8799 system is exceptionally unique.

HR 8799 is the first system with multiple companions to be imaged directly. Coronographic observations of the HR 8799 system were initially made with the *Keck* and *Gemini North* telescopes and revealed the presence of three massive objects at projected separations of 24, 38, and 68 AU (named HR 8799d, HR 8799c, and HR 8799b, respectively; Marois et al., 2008). Over the next two years, further observations with the *Keck* telescopes revealed a fourth companion object interior to the first three at a projected separation of 15 AU (named HR 8799e; Marois et al., 2010). These four

companions were subsequently confirmed with the *Large Binocular Telescope (LBT)* at 1.6 and 3.3 μm (Skemer et al., 2012). The architecture of the HR 8799 system is analogous to the outer configuration of our solar system. Observations have revealed the presence of two disks of warm ($T\sim$150 K) and cold ($T\sim$45 K) material bounding the inner and outer companions (Su et al., 2009; Marois et al., 2010), respectively, in an arrangement similar to the asteroid belt, giant planets, and Kuiper belt in our solar system.

Spectrophotometry of directly-imaged objects offers a way to characterise their atmospheres. At present there are various state-of-the-art instruments capable of obtaining thermal emission spectra of imaged planets and brown dwarfs including the *Spectro-Polarimetric High-contrast Exoplanet REsearch (SPHERE)* at the *VLT*, the *Gemini Planet Imager (GPI)* at *Gemini South*, and *OH-Suppressing Infra-Red Imaging Spectrograph (OSIRIS)* at *Keck*. While the number of objects discovered through direct imaging is fewer than for transiting systems, the spectra of imaged objects can be of higher resolutions and precisions owing to the use of large-aperture ground-based facilities (e.g., Konopacky et al., 2013).

These spectra have traditionally been studied through evolutionary models (e.g., Burrows et al., 1997; Baraffe et al., 2003). Theoretical evolutionary tracks use the infrared bolometric luminosity of an imaged object along with an age estimate of its star to estimate its mass. This mass estimate can then be used in self-consistent atmospheric models over a coarse grid in parameter space to estimate the radius and other atmospheric properties from χ^2 model fits (e.g., Bonnefoy et al., 2016). Nevertheless, several issues limit the characterisation of imaged systems with such models. The models are limited to exploring a high-dimensional parameter space over a coarse grid. In addition, the majority of studies do not account for processes of non-equilibrium chemistry and assume chemical equilibrium for solar elemental abundances (e.g., Madhusudhan et al., 2011a; Baudino et al., 2015), even though advective quenching of molecular species that leads to departures from equilibrium chemistry has been emphasized for imaged objects (e.g., Bowler et al., 2010; Hinz et al., 2010; Janson et al., 2013; Zahnle and Marley, 2014). Finally, the masses are

sensitive to the assumed age of the system, and stellar chronology is in many cases challenging (Soderblom, 2010). For example, Marois et al. (2008) estimated the age of the HR 8799 companions to be $30 - 160$ Myr based on four indirect arguments, placing their masses between $5 - 13$ M_J and below the nominal deuterium-burning limit distinguishing planets from brown dwarfs. On the other hand, Moya et al. (2010) carried out an astroseismological investigation of HR 8799, suggesting the possibility of ages up to 1 Gyr for the HR 8799 companions and implying brown dwarf masses rather than planetary masses. The limitations of conventional modelling outlined above can therefore be benefited by a complimentary retrieval technique.

Already, the generally higher resolutions and/or precisions of directly-imaged spectra make it possible to obtain detections of chemical species using atmospheric retrieval methods. For example, clear detections of H_2O have been made in the atmospheres of the giant planet κ Andromedae b (Todorov et al., 2016), the four HR 8799 companions (Lavie et al., 2017), and numerous brown dwarfs (Burningham et al., 2017; Madhusudhan et al., 2017; Line et al., 2017). Evidence for CO has been found in HR 8799b and HR 8799b (Lavie et al., 2017), and several detections of NH_3 and CH_4 have been made in various brown dwarf classes (Madhusudhan et al., 2017; Line et al., 2017).

On the other hand, retrievals of imaged objects are more challenging than for transiting planets due to several more unknown parameters and degeneracies. The planetary radius and mass as well as the distance to the imaged object are usually not known a priori and therefore must be included as free parameters in direct-imaging retrievals. In addition, the mass and radius of an object are degenerate with the chemical abundances of species such as H_2O and CH_4 (see Section 7.2.3).

Here we apply the direct-imaging retrieval method described in Chapter 4 to the emission spectra of four companion objects in the iconic HR 8799 system. We describe the atmospheric observations in Section 7.1. Sections 7.2.1 through 7.2.3 present a range of results including the retrieved molecular abundances, atomic abundances of O and C, and macroscopic properties of the four HR 8799 companions. The evident challenges in retrievals of directly-imaged spectra are discussed in Section 7.3. We

summarise and provide a future outlook in Section 7.4. We emphasise that this study has not been published and is still a work in progress.

7.1 Observations

Bonnefoy et al. (2016) presented a comprehensive catalogue of previous spectroscopic and photometric observations of the HR 8799 companions sourced from ten literature studies. We use this eclectic set of ground-based data to retrieve the atmospheric properties of the four companions. We do not provide a detailed description of the data components here but use the spectro-photometric observations as in Figure 4 of Bonnefoy et al. (2016) with the exception of Project 1640 near-infrared spectroscopy for HR 8799c. The Project 1640 data are excluded since its spectral bandpass contains strong water vapour bands for which telluric absorption could not be reliably calibrated (Pueyo et al., 2015). We refer the reader to Tables $1-4$ and Section 2 of Bonnefoy et al. (2016) for the tabulated photometric observations and details on the spectroscopy, respectively.

7.2 Results

We retrieve the atmospheric properties of the four HR 8799 companions. We report estimates of a select set of molecular abundances, the temperature structures, the macroscopic parameters, and the derived abundances of O and C. The retrieved spectra and temperature structures of the companions are shown in Figure 7.1. The full retrieval results including spectral fits, $p-T$ profiles, and parameter posteriors are made available on the Open Science Framework[1] (OSF). The Bayesian model comparison and estimated parameter statistics are provided in Appendix Tables E.1−E.5. Table 7.1 shows the prior information used for the retrievals, where the prior on the distance is derived from using parallax data from Gaia Data Release 1[2].

[1] `https://osf.io/c6nva/?view_only=f162c5e476dd4bd384e0d4f963017102`
[2] `https://gea.esac.esa.int/archive/`

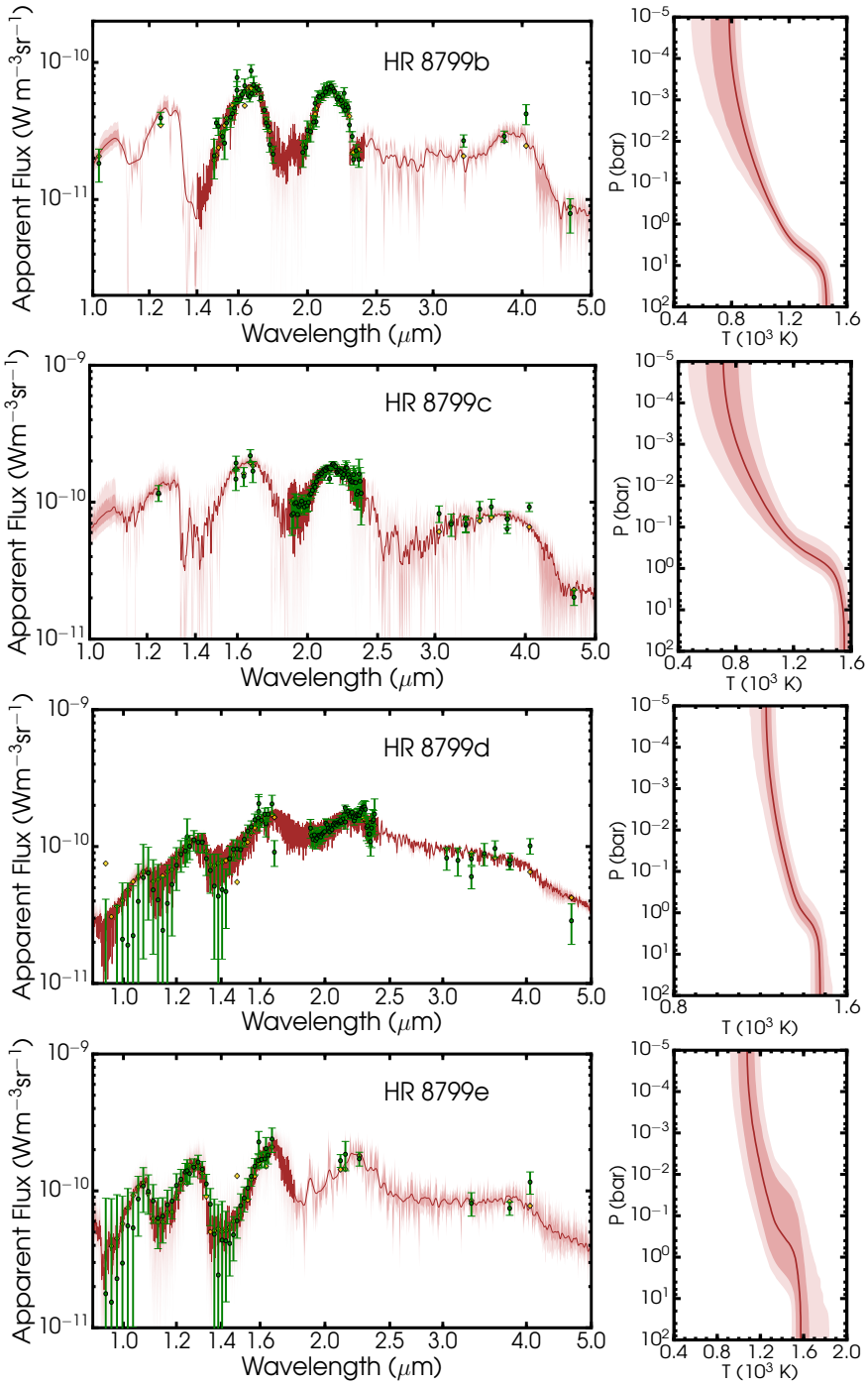

Figure 7.1: Retrieved model spectra compared to observations of the HR 8799 companion objects. The data are shown in green and the retrieved median models are in dark red with associated 1σ and 2σ confidence contours. The yellow diamonds are the binned median model at the same resolution as the data. The median model spectra have been smoothed for clarity. To the right are the retrieved median temperature structures in dark red with 1σ and 2σ contours of confidence.

Parameter	Prior Distribution	Prior Range
T_0	Uniform	$400 - 2000$ K
$\alpha_{1,2}$	Uniform	$0.02 - 1$ K$^{-1/2}$
$P_{1,2}$	Log-uniform	$10^{-6} - 10^{2}$ bar
P_3	Log-uniform	$10^{-2} - 10^{2}$ bar
X_i	Log-uniform	$10^{-14} - 1$
$R_{\rm obj}$	Uniform	$0.5 - 2.0$ R_J
d	Gaussian	40.39 ± 1 pc
$M_{\rm obj}$	Log-uniform	$1 - 80$ M_J

Table 7.1: Retrieval prior information used for spectrophotometry of the HR 8799 companions.

Given the generally low signal-to-noise ratios of the data (i.e., less than 10) we find that the abundance estimates are somewhat dependent on the assumed wavelength resolution of the model, specifically in regions containing medium-resolution spectroscopic data ($R \approx 250$). We found that 5,000 wavelength points in these spectroscopic regions provides a nominal value in that estimated parameters do not change significantly for higher resolutions. Thus the retrieval models were run with 5,000 wavelengths in the spectroscopic regions for all four HR 8799 companions in Figure 7.1. The isothermal upper atmospheres in Figure 7.1 agree with expectations for atmospheres heated from within at $\tau \lesssim 1$ (see equation (9.42) of Seager (2010)). However, the isothermal structures at high pressures are inconsistent with expectations from self-consistent models (e.g., see Figure 3 of Gandhi and Madhusudhan (2017)) and are an issue which we are currently investigating.

7.2.1 Molecular Abundances

The atmospheric observations of the HR 8799 companions indicate several molecular compositions. The retrieved posterior probability distributions of the molecular abundances are shown in Figure 7.2.

Water vapour is detected at high confidence in the atmospheres of all four companions. The significances of these detections are 23.8σ (HR 8799b), 7.30σ (HR

8799c), 5.82σ (HR 8799d), and 8.36σ (HR 8799e). The corresponding retrieved $\log(X_{\mathrm{H_2O}})$ abundances from the outer (HR 8799b) to inner (HR 8799e) companions are $-2.08^{+0.30}_{-0.22}$, $-2.67^{+0.32}_{-0.29}$, $-2.09^{+0.39}_{-0.31}$, and $-1.43^{+1.03}_{-1.02}$. The second most common detected molecule is CO. HR 8799b and HR 8799c show strong evidence of CO with statistical significance levels of 12.48σ and 3.34σ and $\log(X_{\mathrm{CO}})$ abundances of $-0.68^{+0.31}_{-0.24}$ and $-2.43^{+0.44}_{-0.40}$, respectively. There is weak evidence of CO in HR 8799d (2σ) with a mixing ratio of $-2.82^{+1.42}_{-6.91}$ and a 'tail' that extends to low concentrations. There is no suggestion of CO for HR 8799e since it has no flux measurements in the K band and 4.5 μm where CO has prominent band-heads. Hence, the lack of evidence for CO in HR 8799e may change in light of available data in these spectral regions.

The atmosphere of HR 8799b potentially hosts CH_4 (at 2.78σ) with a Gaussian constraint on the abundance of $-3.74^{+0.33}_{-0.30}$. On the other hand, Bayes factors from model comparisons suggest weak to no evidence for methane in the other atmospheres. There are marginal suggestions of CO_2 in HR 8799b, HR 8799c, and HR 8799d. The potential presence of nitrogen chemistry is not evident except for a weak signature of NH_3 at -4.5 dex for HR 8799b. The tails in the distributions of the above molecules arise from the low precisions of the data. We emphasise that though the signatures H_2O are clear in all four atmospheres, their exact abundances can be considered preliminary as they depend on an object's radius and mass (see Section 7.2.3 for further discussion).

7.2.2 Elemental Abundances

The abundances of O and C in the four companion atmospheres – and hence the C/O ratios – can be derived from the retrieved molecular mixing ratios. Comparing these to those of the host star HR 8799 can also provide insights into possible formation scenarios. HR 8799 is a member of the λ Bootis stellar class (Gray and Kaye, 1999; Paunzen et al., 2002; Baines et al., 2012) characterised by solar abundances of C, N, and O. Indeed, Sadakane (2006) determined the O and C metallicities of HR 8799 and found they are consistent with solar-composition values. We thus take the metallicities to be $\mathrm{C/H} = 2.7 \times 10^{-4}$ and $\mathrm{O/H} = 4.9 \times 10^{-4}$ (Asplund et al., 2009)

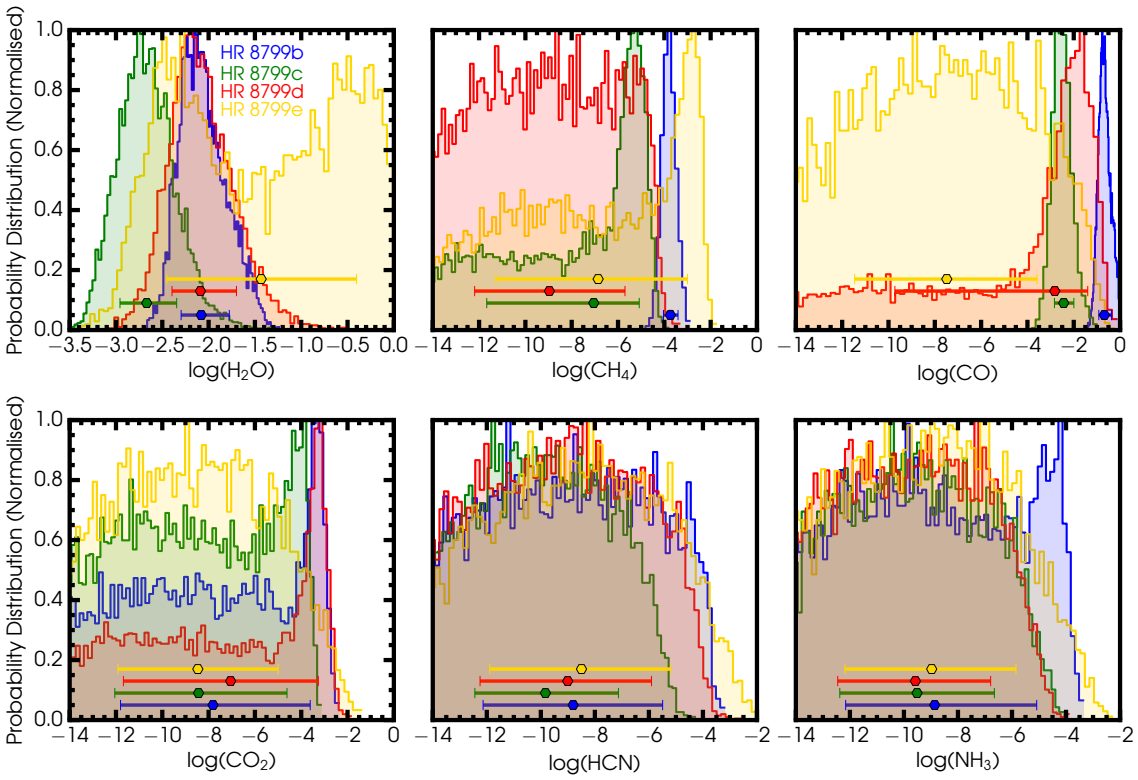

Figure 7.2: Retrieved molecular abundances of the HR 8799 companions. Each panel presents estimated abundances of one molecule across the four atmospheres. The points and errors represent the median abundance and 1σ ranges.

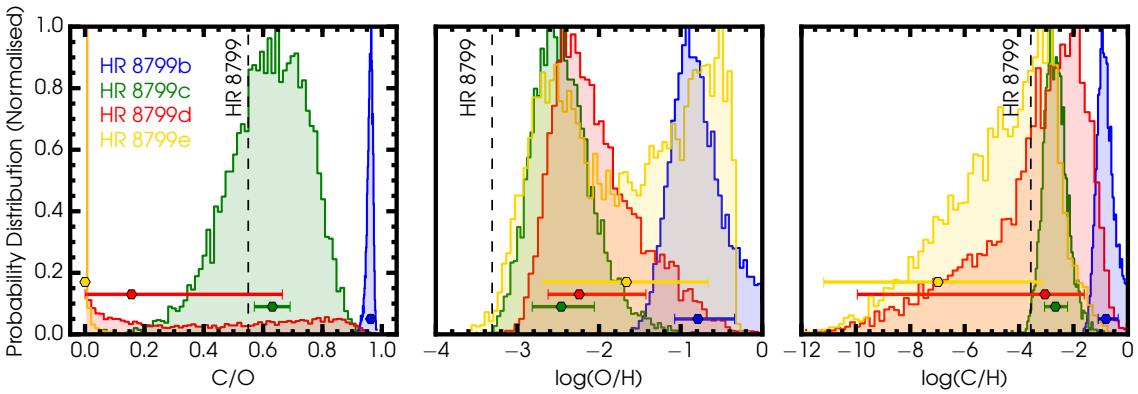

Figure 7.3: Derived posterior distributions of O/H, C/H, and C/O ratios for the HR 8799 companions. The points and error bars represent the median values and 1σ ranges, respectively. Vertical dashed lines show values of the host star for reference.

such that C/O = 0.55.

The retrieved C/H, O/H, and C/O ratios of the companions are shown in Figure 7.3. The atmospheric C/O ratios are obtained from the amount of C and O present in the retrieved molecular mixing ratios as

$$\mathrm{C/O} \equiv \frac{X_\mathrm{C}}{X_\mathrm{O}} = \frac{X_{\mathrm{CH_4}} + X_\mathrm{CO} + X_{\mathrm{CO_2}} + X_\mathrm{HCN}}{X_{\mathrm{H_2O}} + X_\mathrm{CO} + 2X_{\mathrm{CO_2}}}, \tag{7.1}$$

and assumes that the considered molecules are the main C and O carriers in the companion atmospheres. The metallicities of oxygen and carbon are

$$\mathrm{O/H} \equiv \frac{X_\mathrm{O}}{X_\mathrm{H}} = \frac{X_{\mathrm{H_2O}} + X_\mathrm{CO} + 2X_{\mathrm{CO_2}}}{2X_{\mathrm{H_2}} + 2X_{\mathrm{H_2O}} + 4X_{\mathrm{CH_4}} + X_\mathrm{HCN} + 3X_{\mathrm{NH_3}}}, \tag{7.2}$$

$$\mathrm{C/H} \equiv \frac{X_\mathrm{C}}{X_\mathrm{H}} = \frac{X_{\mathrm{CH_4}} + X_\mathrm{CO} + X_{\mathrm{CO_2}} + X_\mathrm{HCN}}{2X_{\mathrm{H_2}} + 2X_{\mathrm{H_2O}} + 4X_{\mathrm{CH_4}} + X_\mathrm{HCN} + 3X_{\mathrm{NH_3}}}. \tag{7.3}$$

Figure 7.3 shows the companion atmospheres are highly super-solar in oxygen. The derived O/H values are $-0.79^{+0.45}_{-0.28}$ (HR 8799b), $-2.46^{+0.40}_{-0.36}$ (HR 8799c), $-2.24^{+0.82}_{-0.38}$ (HR 8799d), and $-1.66^{+1.00}_{-1.02}$ (HR 8799e), which compared to solar-composition abundances correspond to $331^{+602}_{-157}\times$, $7^{+11}_{-4}\times$, $12^{+66}_{-7}\times$, and $45^{+401}_{-41}\times$ solar. These super-solar oxygen abundances arise from high H_2O concentrations in the companion atmospheres (all $\gtrsim 5\times$ solar) in addition to abundant CO in HR 8799b and HR 8799c. On the other hand, the carbon abundances are consistent with a wide range from $\sim 500\times$

super-solar to very depleted values. The atmospheres of HR 8799b and HR 8799c harbour super-stellar C/H of $-0.81^{+0.45}_{-0.29}$ ($574^{+1043}_{-280}\times$ solar) and $-2.66^{+0.44}_{-0.40}$ ($8^{+16}_{-5}\times$ solar), respectively. HR 8799d and HR 8799e are consistent to 1σ with sub-stellar and super-stellar C metallicities with values of $-3.05^{+1.45}_{-6.90}$ and $-6.98^{+3.83}_{-4.20}$, respectively. However, the C/H value for HR 8799e is likely unrepresentative of its actual metallicity given the lack of data in the K band and at 4.5 μm, regions host to prominent CH_4 and CO band heads. The super-stellar O/H and varied C/H in the atmospheres provide for C/O ratios spanning the range from 0 to 1. HR 8799b and HR 8799c have super-stellar C/O ratios whereas the innermost companions favour depleted C/O ratios. However, the estimated C/O values for HR 8799e may again be unrepresentative of the real composition due to the lack of K band spectroscopy and photometry at 4.5 μm.

7.2.2.1 Formation Conditions

In general, atmospheric metallicities of O and C as well as C/O ratios have the potential to provide information on possible formation environments and conditions (e.g., Öberg et al., 2011; Helling et al., 2014; Madhusudhan et al., 2014b; Piso et al., 2016; Cridland et al., 2016; Mordasini et al., 2016; Ilee et al., 2017; Booth et al., 2017; Madhusudhan et al., 2017; Ali-Dib, 2017; Lammer and Blanc, 2018; Pudritz et al., 2018). Figure 7.4 shows the space of atmospheric metallicity versus object mass for the four HR 8799 companions in addition to previous metallicity determinations for an ensemble of ten hot giant exoplanets (Chapter 5), WASP-18b (Sheppard et al., 2017), WASP-43b (Kreidberg et al., 2014c), HAT-P-26b (Wakeford et al., 2017), and the solar system gas giants. The C/H trend in the solar system, where C metallicities decrease with increasing object mass, does not hold for the C/H of the three outer companions assuming retrieved median masses.

The super-stellar O metallicities of the companions suggest a trend different than that of C abundances in the solar system giants. The addition of the HR 8799 system suggests that more massive giant planets may accrete higher amounts of O-rich material. This is a viable interpretation only if the HR 8799 companions have

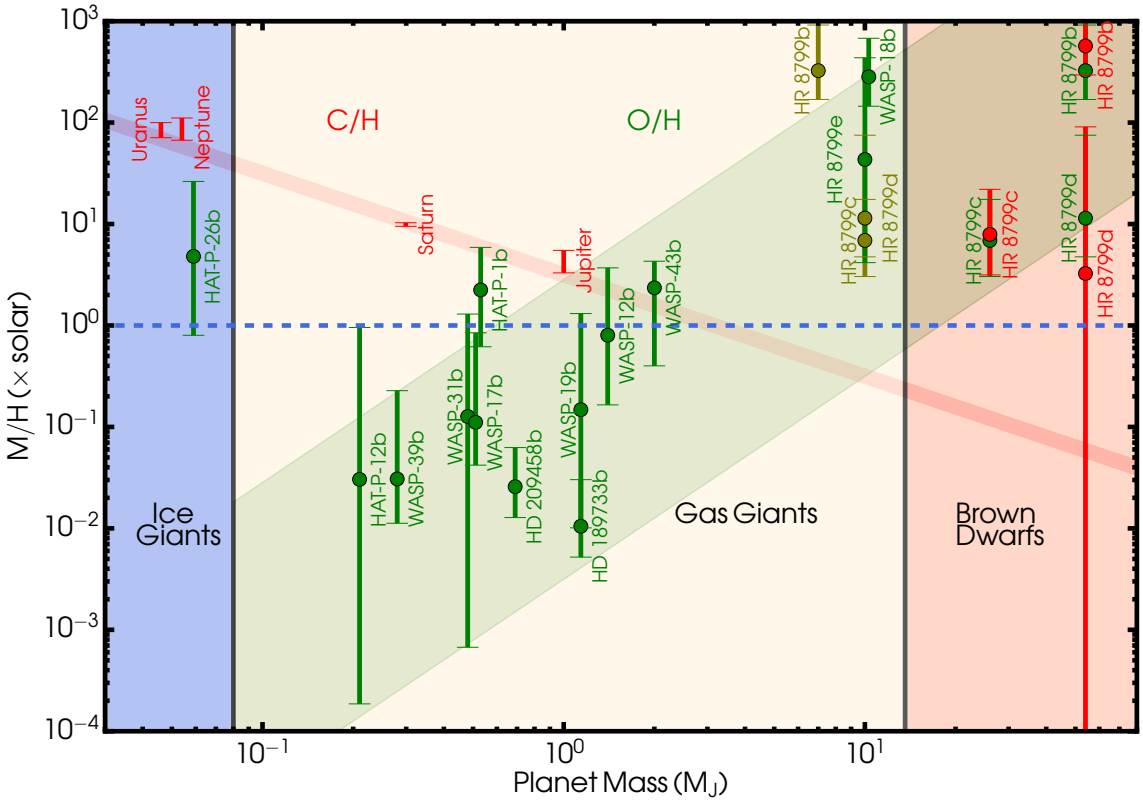

Figure 7.4: Atmospheric metal abundances as a function of object mass. Red (green) constraints indicate C/H (O/H) abundances. C/H values of solar system giant planets and three outer HR 8799 companions are shown in red. O/H values are shown for the four HR 8799 companions as well as an ensemble of hot giant exoplanets (Chapter 5), WASP-18b (Sheppard et al., 2017), WASP-43b (Kreidberg et al., 2014c), and HAT-P-26b (Wakeford et al., 2017). The masses of the four companions in green are the median O/H estimates from the retrievals. The olive points represent the O/H estimates but for planetary masses assuming 60 Myr (Marois et al., 2008, 2010). The O/H and C/H metallicities of the HR 8799 objects are derived from the full set of retrieved molecules (H_2O, CH_4, CO, CO_2, HCN, and NH_3) through equations (7.2) and (7.3), whereas the O/H metallicities of the other giant exoplanets are obtained from the H_2O abundances. The C/H of solar system planets are derived from the CH_4 abundances.

masses in the planetary domain since sub-solar metallicities of O, C, and N have been found for several brown dwarfs (e.g., Madhusudhan et al., 2016b). The O/H and C/H values illustrate the HR 8799 system to be different than the outer planets of our solar system and hints at varied formation and evolutionary processes for these companions.

A coherent explanation of companion formation scenarios is challenging even in light of the present retrieved chemistry. The estimated C/O ratios in principle reveal information about the companions' formation locations since the gaseous C/O ratio increases with the distance from the star (Öberg et al., 2011). The gas C/O ratios range from 0.85 to 1 between the H_2O and CO snow lines (Öberg et al., 2011). In this context and assuming an in-situ core accretion model of formation, the atmosphere of HR 8799b could have formed between the H_2O and CO ice lines and accumulated its atmosphere from disk gas as well as being potentially enriched by evaporating C- and O-rich planetesimals. The closer companion, HR 8799c, could have formed similarly but with substantial atmospheric contamination from H_2O- and CO_2-rich bodies. However, such a scenario is unlikely to assimilate with HR 8799d whose C/O ratio is mainly sub-solar. The lack of K band spectroscopy for HR 8799e implies its C/O ratio is unreliable as a basis for a formation discussion.

Nevertheless, core accretion presents a viability issue; the timescale for in-situ core accretion is substantial at radii above 10 AU (Pollack et al., 1996) and increases with orbital distance. HR 8799c would require $\sim$200 Myr to grow to the proposed planetary mass of Marois et al. (2008) at 38 AU – palpably long after the gaseous depletion of the disk – and would require even longer assuming potentially higher object masses as hinted in this work. HR 8799b would require a much longer time (many times the stellar age) to have formed in-situ by core accretion (Close, 2010).

The large orbital separations of the companions may therefore be more conducive towards formation by gravitational instabilities in the disk (Mayer et al., 2004). Helled and Bodenheimer (2010) modelled the capture of solids by giant protoplanets at the corresponding distances of the three outer HR 8799 companions. Their crucial finding is that massive protoplanets have relatively short collapse stages, and thus limited

time for planetesimal capture. This leads to the prediction that the metallicities of the companion atmospheres should be similar to that of the host star.

Our retrieved O/H for the four companions and C/H for the outer two companions are inconsistent with this suggestion (see Figure 7.3). This inconsistency might arise from at least two considerations. First, the study of Helled and Bodenheimer (2010) assumed planetary masses for the HR 8799 companions in estimating the mass of accreted heavy elements during the collapse stage. However, the possibility remains of higher companion masses which might facilitate more considerable heavy-element accretion leading to super-stellar O/H and C/H. A second caveat acknowledged by Helled and Bodenheimer (2010) is that proto-companions could form at the center of spiral structures which are themselves enhanced in metals relative to the surrounding proto-planetary disk (Haghighipour and Boss, 2003; Rice et al., 2004; Durisen et al., 2008; Helled and Bodenheimer, 2010; Boley and Durisen, 2010) and/or involved late-stage planetesimal accretion. Solids with stopping distances comparable to the widths of spiral arms in proto-planetary disks should be efficiently collected in the arms before fragmentation through gravitational instability. Subsequent fragmentation of these arms would produce companions with super-stellar metallicities.

Dodson-Robinson et al. (2009) simulated three formation mechanisms – core accretion (with or without migration), scattering from the inner disk, and gravitational instability – in an effort to ascertain the efficient formation mode of long-period companions like those of HR 8799. Spiral instability structures arose naturally in high-mass disks of A stars such as HR 8799 and they concluded that massive objects on stable orbits beyond $\sim$30 AU form by gravitational instability in the disk. The abundances of heavy metal contents of the star have also been used to suggest formation through gravitational instability for the HR 8799 companions (Meru and Bate, 2010). In all, the companions seem more physically consistent with a formation by disk instability considering the caveats are more easily overcome. Future studies of this iconic system will test this hypothesis further.

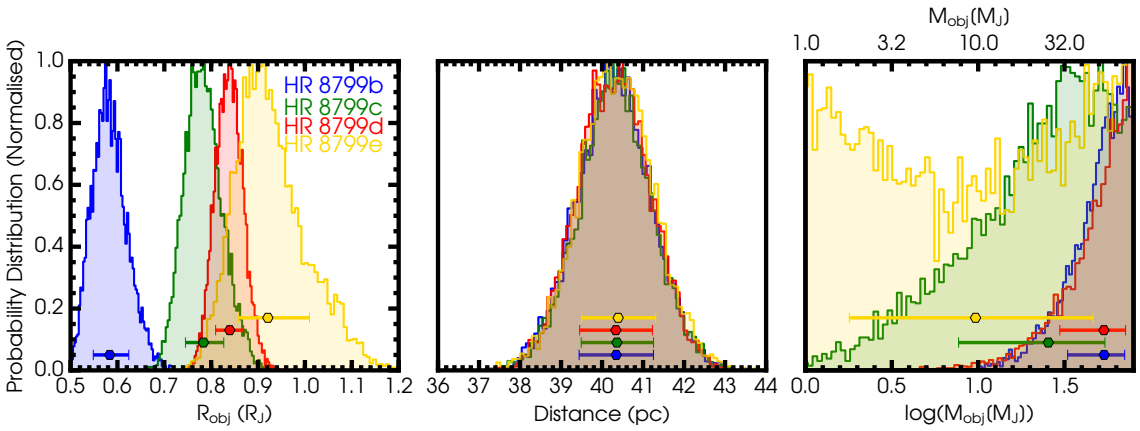

Figure 7.5: Retrieved posterior distributions of macroscopic parameters for the HR 8799 companions. Each panel presents values for one macroscopic parameter across the four objects. The points and error bars represent the median and 1σ ranges.

7.2.3 Macroscopic Parameters

Figure 7.5 shows the retrieved posterior distributions of macroscopic parameters for the HR 8799 companions. The estimated radii all lie below 1 Jovian radius and the retrieved masses span the range from those of planets to brown dwarfs.

The estimated radii of the three inner companions are $0.78^{+0.04}_{-0.04}$ R_J (HR 8799c), $0.84^{+0.03}_{-0.03}$ R_J (HR 8799d), and $0.92^{+0.09}_{-0.06}$ R_J (HR 8799e). The masses of the three outer companions are higher than the deuterium-burning mass threshold for brown dwarfs but the estimates aggregate at the upper edge of the prior. HR 8799e is the only companion for which the inferred mass is consistent with planetary values, though its posterior is relatively uniform and is rather uninformative. HR 8799b is peculiar in that both the radius and mass concentrate on the lower and upper prior limits, respectively. These HR 8799b estimates are likely inconsistent with theoretical mass-radius relations for sub-stellar objects (Chabrier et al., 2009) and the masses of HR 8799c and HR 8799d (which pile at 80 M_J) are also suspect. The estimates are not in accord with the planetary masses and radii inferred for the traditional age of the HR 8799 system (Marois et al., 2008, 2010).

In light of the questionable estimates on some of the masses and radii, we quantify the effect these macroscopic parameters have on the retrieved abundances. Figure 7.6

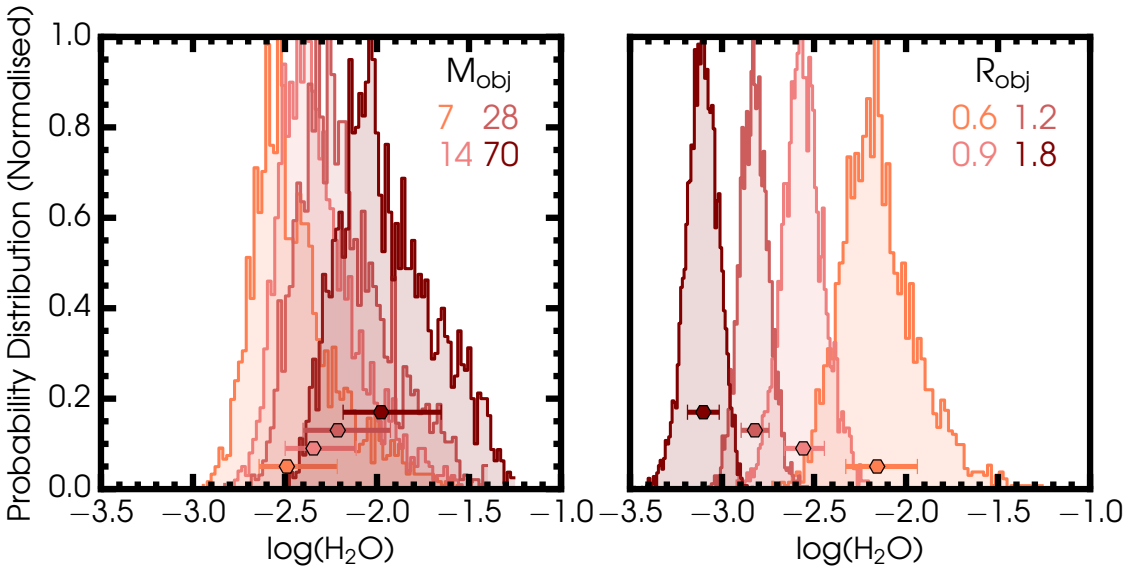

Figure 7.6: Effects of M_{obj} and R_{obj} on the retrieved water abundance. Left panel: Posterior distributions of the H_2O abundance for companion masses of 7, 14, 28, and 70 M_J. Right panel: Posterior distributions of the H_2O abundance for companion radii of 1.8, 1.2, 0.9, and 0.6 R_J.

shows the effect of different masses and radii on the estimated H_2O abundances. Similar effects occur for other molecules with significant abundances and thus the present discussion of H_2O abundances is applicable to molecules generally. The left panel of Figure 7.6 shows the changes in X_{H_2O} induced by companion masses, showing that higher water abundances occur for high companion masses. The positive correlation between mass and abundance arises from equation (4.8), which shows that the optical depth is proportional to the chemical abundance and inversely proportional to the mass. High-mass objects harbour small atmospheric scale heights, and thus high chemical abundances are needed to fit a given spectrum. A similar spectral fit can be achieved with lower abundances for less massive objects with more extended atmospheres. The abundances in the left panel are generally consistent to 1σ across the mass range. The exception occurs for the mass extremes of 7 and 70 M_J which have respective abundances of $-2.49^{+0.27}_{-0.15}$ and $-1.98^{+0.33}_{-0.21}$. Abundances therefore increase by $\sim$0.5 dex for a 1 dex increase in M_{obj}. This means that abundances can only change by a maximum of 0.5 dex if the mass is uncertain.

The right panel of Figure 7.6 shows the dependence of the H_2O abundance on the radius. It is clear that the abundances are more sensitive to changes in the radius than in the mass. For example, a change in the parameters by a factor of 2 (i.e., $R_{\rm obj} = \{0.9, 1.8\}$ and $M_{\rm obj} = \{14, 28\}$) changes the median H_2O concentrations by 0.6 dex (0.1 dex) for radius (mass) adjustments. Indeed, the absolute difference in $X_{\rm H_2O}$ associated with a radial increase of 50% (i.e., from 0.6 to 0.9 $R_{\rm J}$) is similar to that from a 900% increase (i.e., from 7 to 70 $M_{\rm J}$) in mass. However, whereas the correlation between abundance and mass is positive, the correlation between abundance and radius is negative. The latter also arises from equation (4.8), which shows that the optical depth is proportional to both the chemical abundance and the square of the radius. The greater sensitivity of abundances to the radius is due to this square dependence of the atmospheric scale height on $R_{\rm obj}$ (as opposed to a reciprocal linear dependence on mass). In all, the effect of larger radii or masses would respectively decrease or increase the oxygen abundances in Figure 7.4, with radial differences affecting the oxygen abundances more. We conclude that knowledge of $R_{\rm obj}$ is more important for the accuracy of retrieved abundances than is knowledge of $M_{\rm obj}$.

7.3 Highlighted Challenges

A key observation arising from this work is that estimated masses and radii from a retrieval approach (Figure 7.5) can differ significantly from those inferred through an assumed age and evolutionary models (Marois et al., 2008, 2010). The retrieved companion masses span the planetary and brown dwarf domain, though the estimated masses of HR 8799b and HR 8799c aggregate on the upper edge of the prior and are therefore an issue. Marois et al. (2008, 2010) inferred planetary masses spanning $5 - 13$ M_J for the companions assuming an age estimate for the system of $30 - 160$ Myr. All the retrieved companion radii also lie below 1 Jovian radius, while the masses derived through an age estimate and evolutionary models imply companion radii of $1.1 - 1.3$ R_J (Marois et al., 2008, 2010). The reason for the discrepancy

in macroscopic parameters between the modeling approaches remains unclear (see also Section 4.1 and 5.1 of Lavie et al., 2017), although potentially contributing factors include our present lack of a cloud treatment, additional chemical species with considerable opacity in the infrared, the use of solar abundances in the self-consistent PHOENIX models used in Marois et al. (2008), and the uncertain stellar chronology of HR 8799.

There is yet to be decisive conclusion as to the true nature of the HR 8799 companion masses though the majority of literature studies favour planetary masses. Marois et al. (2008, 2010) used four indirect lines of argument to estimate a young age of $30 - 160$ Myr for the HR 8799 system and thus companion masses ranging from 5 to 13 M_J. Additionally, N-body simulations of the HR 8799 companions suggest a strong preference for masses $\lesssim 13$ M_J; it is argued that otherwise they should have become dynamically unstable by $\sim$100 Myr (Goździewski and Migaszewski, 2009; Fabrycky and Murray-Clay, 2010; Sudol and Haghighipour, 2012; Goździewski and Migaszewski, 2014). On the other hand, Moya et al. (2010) carried out an astroseismological study which implies a system many times older ($\sim$1 Gyr) and implies brown dwarf masses rather than planetary masses for the companions. However, the older age estimate depends on the uncertain inclination of the stellar rotation axis (Moya et al., 2010). Nevertheless, Moya et al. (2010) raise important reservations on the four methods of age estimation of Marois et al. (2008) which are discussed in Section 2 of their work.

HR 8799b best highlights the remaining challenges in understanding the atmospheres and formation of the HR 8799 companions. For example, the retrieved mass and radius estimates of HR 8799b are likely physically implausible. In light of these issues and the added challenge of modeling clouds, it is important to remember that the abundance estimates retrieved in this work are not sacred and might change with future studies. A few progressive paths certainly include a reliable and accurate retrieval cloud model component and appropriate corrections for multi-epoch spectra since influences of atmospheric variability might be present in the used datasets.

7.4 Summary

This decade is a dynamic era in the exploration of objects at large orbital separations from their stars. Observational facilities of the near future will increase the number of directly-imaged systems and extend the discovery domain to masses of 1 M_J and inner working angles equal to $\sim$5 AU (Lagrange, 2014). The promise of more imaged objects motivates the need for an architecture capable of characterising their atmospheres and bulk properties with minimal assumptions. Our work aims to meet this need. We have presented an application of a state-of-the-art Bayesian atmospheric retrieval method for spectrophotometry of imaged exoplanets and brown dwarfs. The retrieval facilitates comprehensive statistical inferences of atmospheric and macroscopic properties including chemical compositions and abundances, radii and masses, and temperature profiles throughout the atmosphere.

We have applied our retrieval methodology to spectrophotometry of the iconic HR 8799 system comprised of four companions. The analysis reveals the clear presence ($>5.8\sigma$) of H_2O gas in all four companion atmospheres. The retrieved $\log(X_{H_2O})$ abundances from the outer (HR 8799b) to inner (HR 8799e) companions are $-2.08^{+0.30}_{-0.22}$, $-2.67^{+0.32}_{-0.29}$, $-2.09^{+0.39}_{-0.31}$, and $-1.43^{+1.03}_{-1.02}$. There is strong evidence ($>3.3\sigma$) of CO gas in the atmospheres of HR 8799b and HR 8799c with corresponding abundances of $-0.68^{+0.31}_{-0.24}$ and $-2.43^{+0.44}_{-0.40}$, respectively. There is also weak evidence (2σ) of CO in HR 8799d with a mixing ratio of $-2.82^{+1.42}_{-6.91}$. Finally, evidence for CH_4 is substantial (2.78σ) in the atmosphere of HR 8799b with a Gaussian abundance constraint of $3.74^{+0.33}_{-0.30}$.

The four atmospheres are chemically rich compared to the photosphere of HR 8799. The atmospheric O/H of all companions are enhanced over the solar/stellar value. The retrieved O/H values are $-0.79^{+0.45}_{-0.28}$ (HR 8799b), $-2.46^{+0.40}_{-0.36}$ (HR 8799c), $-2.24^{+0.82}_{-0.38}$ (HR 8799d), and $-1.66^{+1.00}_{-1.02}$ (HR 8799e), which compared to solar-composition abundances are $331^{+602}_{-157}\times$, $7^{+11}_{-4}\times$, $12^{+66}_{-7}\times$, and $45^{+401}_{-41}\times$ solar. The median C/H abundances of the outer three companions are super-solar. The C/H of HR 8799b and HR 8799c are $-0.81^{+0.45}_{-0.29}$ ($574^{+1043}_{-280}\times$ solar) and $-2.66^{+0.44}_{-0.40}$ ($8^{+16}_{-5}\times$ solar), respectively.

Carbon metallicities for HR 8799d span the range from sub-stellar to super-stellar (common log abundance of $-3.05^{+1.45}_{-6.90}$). The resulting C/O ratios of HR 8799b and HR 8799c are distinctly super-solar with values of $0.96^{+0.0002}_{-0.002}$ and $0.63^{+0.06}_{-0.06}$. On the other hand, HR 8799d favours depleted C/O ratios relative to solar, though is still consistent with super-solar values to within 1σ. The retrieved abundances depend on the retrieved mass and radius of the companions, with abundances more sensitive to uncertainties in the radius. Knowledge of the radius is therefore more important for accurate abundance inferences than is knowledge of the mass.

Future observing facilities will provide improved spectral resolutions and precisions useful for more detailed and decisive studies of directly-imaged objects. Though the *James Webb Space Telescope (JWST)* was not designed for high-contrast direct imaging, coronographs of the *Near-Infrared Camera (NIRCam)* and *Mid-Infrared Camera (MIRI)* have their own wavelength filters and will provide a crucial broadband spectrum from $1 - 28$ μm, affording vital information on chemical bands and cloud properties (Perryman, 2011).

The next generation of extremely large ground observatories have instruments which are specifically designed for imaging of super-Earths in the the habitable zones of their stars (e.g., Kasper et al., 2010; Wright et al., 2014). These facilities will enable unparalleled abundance and mass/radius estimates and may afford greater potential for illuminating the potential formation histories of imaged companions. Specifically, the *Exoplanet Imaging Camera and Spectrograph (EPICS)* instrument on the *E-ELT* (Kasper et al., 2010) and the *Infrared Imaging Spectrograph (IRIS)* IFS on the *TMT* (Wright et al., 2014) should be invaluable. Currie (2016) notes the latter will cover $0.8 - 2.5$ μm and provide high-precision flux measurements for all four companions at $R = 4000 - 8000$, improving on the current observations in the H and K bands with $R \approx 250$ (Bonnefoy et al., 2016). The degeneracy between the object mass and chemical abundances suggests the need for informative mass priors for more accurate chemical abundance estimates; one path to informative mass measurements is to use stellar radial velocity or astrometric observations (Apai et al., 2017a). The suite of future efforts promises great revelations ahead.

Chapter 8

WASP-18b and XO-1b

The retrieval methods outlined in Chapter 4 have also been applied to several observations as part of external collaborations. Here we present two applications of these methods which include the characterisation of WASP-18b's secondary eclipse spectrum and XO-1b's primary eclipse spectrum. These collaborative studies have been published and are presented in Sheppard et al. (2017) and Southworth et al. (2018), respectively. The day-side atmosphere of the highly irradiated hot Jupiter WASP-18b is found to have a strong thermal inversion and an atmosphere with a super-solar metallicity and C/O ratio due to a high abundance of carbon monoxide. The most complete transmission spectrum of the giant planet XO-1b spanning the optical to infrared is best explained by an atmosphere composed of inhomogeneous clouds and a low H_2O abundance compared to the solar expectation. The details of these retrieval applications are presented here.

8.1 Secondary Eclipse Spectrum of WASP-18b

A fellow PhD student (Siddharth Gandhi) and I have characterised the secondary eclipse spectrum of WASP-18b, an extremely hot (T∼2,400 K) and massive ($M = 10.3\,M_J$) giant exoplanet which orbits its star in less than one day. The secondary eclipse spectrum comprises *HST WFC3* data, K band photometry at 2.15 μm, and *Spitzer IRAC* photometry in the 3.6, 4.5, 5.8, and 8 μm channels. We use the HyDRA

retrieval code of Gandhi and Madhusudhan (2018) to analyse these data.

The retrieved model spectrum and posterior distributions of the molecular abundances are shown in Figures 8.1 and 8.2, respectively. Our retrieved model spectrum requires a strong thermal inversion in the dayside atmosphere of WASP-18b. The bottom inset of Figure 8.1 shows the retrieved $p-T$ profile indicating a temperature increase between 1 and 10^{-3} bar in the atmosphere. The requirement of a thermal inversion is guided by the strong emission feature in the 4.5 μm *Spitzer* band, with a brightness temperature of 3100 ± 50 K, which is significantly higher than the rest of the data. This can be explained by the presence of a thermal inversion in the atmosphere along with the presence of either CO or CO_2, which both exhibit pronounced spectral features in the 4.5 μm band. We break this degeneracy by requiring that CO_2 be less than H_2O as expected for hot Jupiter atmospheres (Madhusudhan, 2012; Heng and Lyons, 2016). Another subtlety is the apparent minor trough near $\sim$1.6 μm, which we attribute to CO absorption below the inversion layer (i.e., $\sim 1-10$ bar), where temperature decreases outward. Emission in the 4.5 μm band is due to CO in the $10^{-3}-10^{-1}$ bar range, which contains the thermal inversion.

As part of the nested sampling analysis we compute the Bayesian evidence value for our retrieved spectrum. By comparing this value with that obtained for a model without a thermal inversion, we conclude that a thermal inversion is favored at the 6.3σ significance level. Similarly, comparison of the Bayesian evidence to that of a model lacking CO implies that the presence of CO is favored at the 6.1σ level. The transition point of the inversion occurs at $\sim$0.1 bar which also happens to be a characteristic level at which inversions occur in the atmospheres of solar system planets as well as models of hot Jupiters (Madhusudhan and Seager, 2009; Robinson and Catling, 2014).

Figure 8.2 shows the posterior probability distributions of all of the chemical species. The data require a CO volume mixing ratio of 19^{+18}_{-8}% in the atmosphere, which is 380^{+360}_{-160} times the amount expected for a solar-abundance atmosphere in chemical equilibrium at WASP-18b's temperature. The high CO abundance is primarily constrained by the emission required to explain the 4.5 μm *IRAC* point as

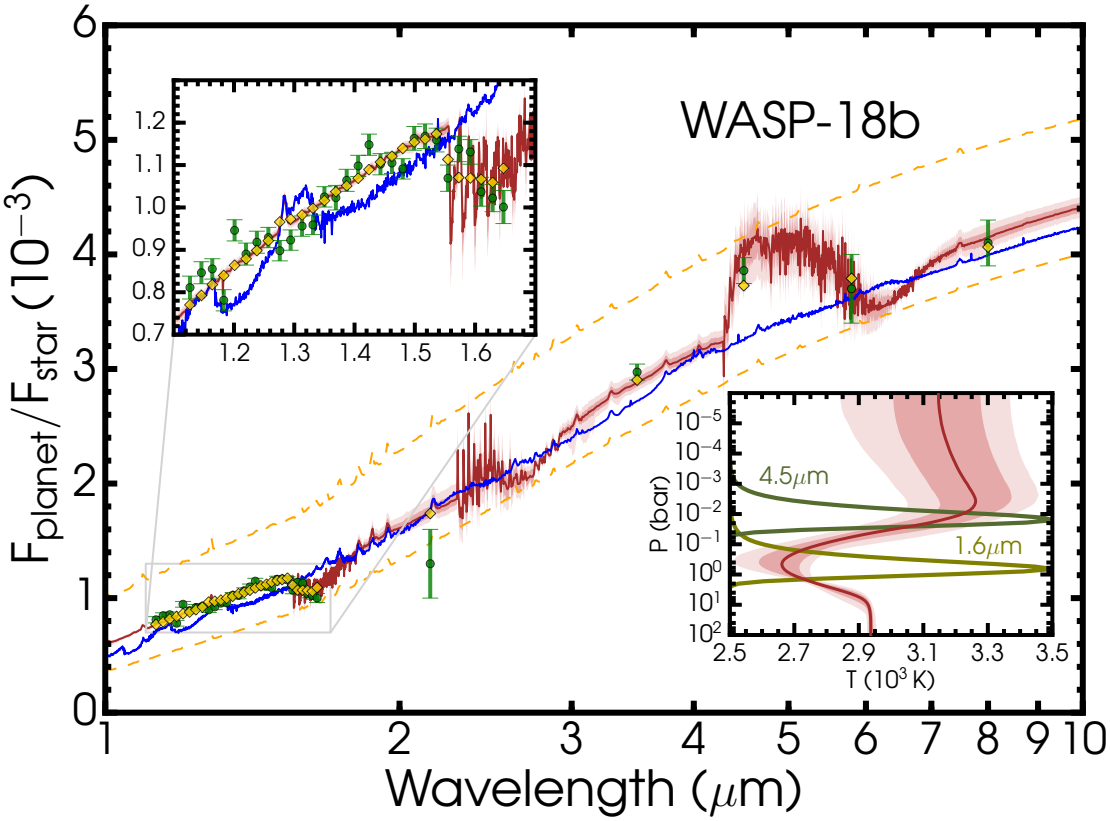

Figure 8.1: Observed spectrum and retrieved solutions. The data are shown in green. The median retrieved spectrum with the 1σ and 2σ uncertainty envelopes is shown in red. The binned median model, in yellow, has a reduced chi-square of 3.67 and is an unambiguously better fit than a blackbody ($\chi^2_{\rm red} = 15.2$). A reference model with a solar-abundance of H_2O is shown in blue to demonstrate the lack of an H_2O absorption feature in the data. The results favor a thermal inversion, and the only spectral features detected are those of CO at 1.6 and 4.5 μm. The retrieved $p-T$ profile with 1σ and 2σ uncertainty contours is shown in the lower right inset along with the contribution functions of CO at 1.6 and 4.5 μm.

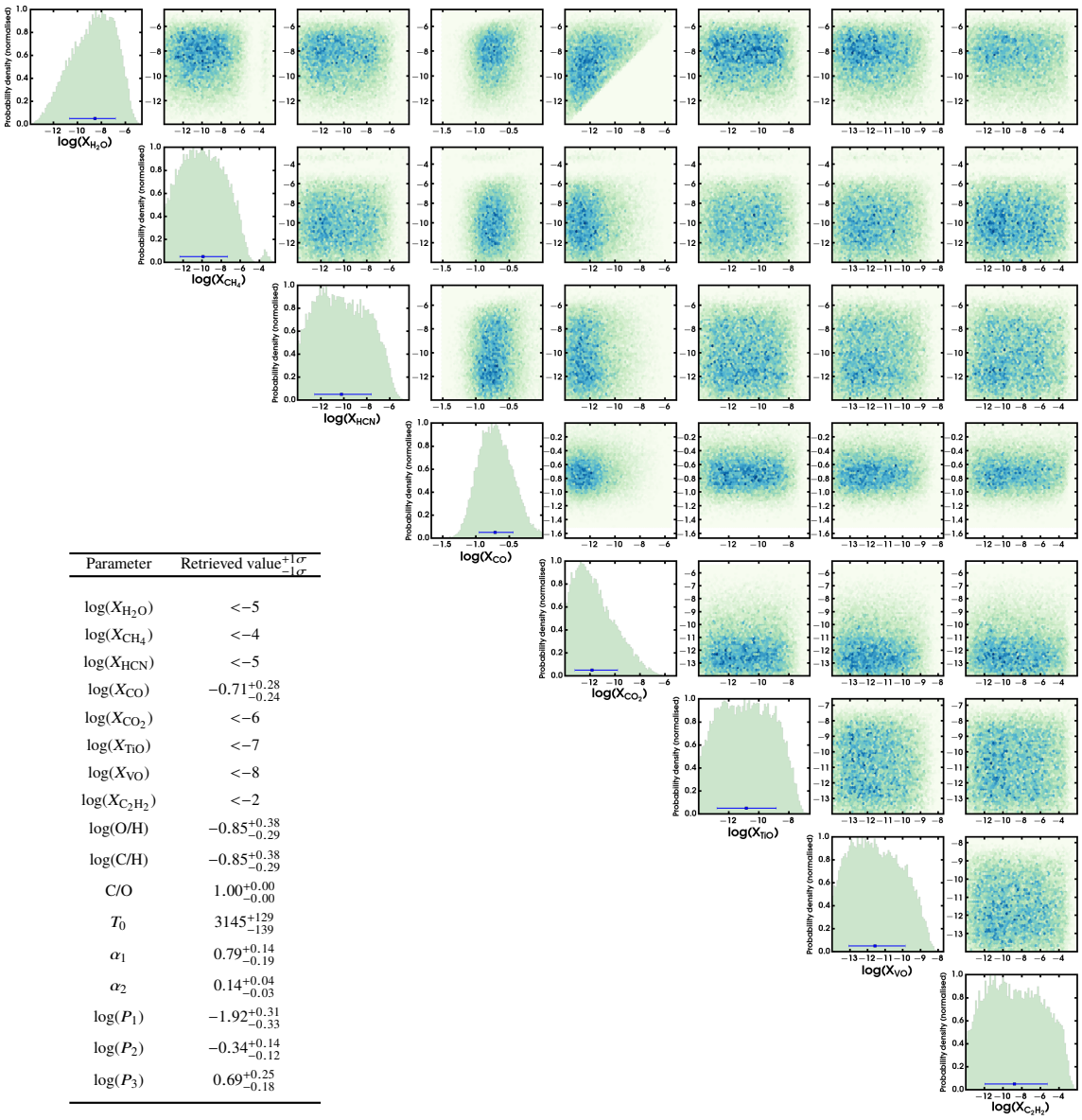

Parameter	Retrieved value$^{+1\sigma}_{-1\sigma}$
$\log(X_{\mathrm{H_2O}})$	<-5
$\log(X_{\mathrm{CH_4}})$	<-4
$\log(X_{\mathrm{HCN}})$	<-5
$\log(X_{\mathrm{CO}})$	$-0.71^{+0.28}_{-0.24}$
$\log(X_{\mathrm{CO_2}})$	<-6
$\log(X_{\mathrm{TiO}})$	<-7
$\log(X_{\mathrm{VO}})$	<-8
$\log(X_{\mathrm{C_2H_2}})$	<-2
log(O/H)	$-0.85^{+0.38}_{-0.29}$
log(C/H)	$-0.85^{+0.38}_{-0.29}$
C/O	$1.00^{+0.00}_{-0.00}$
T_0	3145^{+129}_{-139}
α_1	$0.79^{+0.14}_{-0.19}$
α_2	$0.14^{+0.04}_{-0.03}$
$\log(P_1)$	$-1.92^{+0.31}_{-0.33}$
$\log(P_2)$	$-0.34^{+0.14}_{-0.12}$
$\log(P_3)$	$0.69^{+0.25}_{-0.18}$

Figure 8.2: Retrieved posterior distributions for the chemical abundances. The high CO abundance implies a high metallicity and high C/O ratio. The mixing ratios are in units of the common logarithm.

well as the absorption trough in the *WFC3* band at $1.6 - 1.7$ μm. Besides CO we detect no other chemical species (see Figure 8.2). In particular, the non-detection of H_2O at both 1.4 and 6 μm provides a 3σ upper-limit of 10^{-6} on the volume mixing ratio. The constraints on the chemical species lead to a super-solar metallicity in the planetary atmosphere (C/H = O/H = $283^{+395}_{-138}\times$ solar O/H) and a C/O ratio of $\sim$1. We also conducted a retrieval without the restriction that $X_{CO_2} < X_{H_2O}$. In both cases, the data require a strong thermal inversion, a C/O ratio of $\sim$1, and a super-solar metallicity.

8.1.1 Discussion

The inference of an extraordinarily high CO abundance in the dayside atmosphere of WASP-18b is inconsistent with expectations for an atmosphere with a high C/O ratio and high temperatures where chemical equilibrium is expected to be satisfied (Madhusudhan, 2012; Moses et al., 2013). In particular, the retrieved CO volume mixing ratio is 380^{+360}_{-160} times the amount expected from chemical equilibrium at high temperatures. In contrast, the low abundance of H_2O that is retrieved is consistent with chemical equilibrium expectations for a C/O$\sim$1 at high temperatures. The constraints on all of the other species are also consistent with this scenario. While we cannot rule out a contribution from CO_2 emission in the 4.5 μm *Spitzer* band, the high abundance of CO_2 needed would be chemically inconsistent with the non-detection of H_2O and is therefore exceedingly unlikely.

Our inferences for this planet indicate an unusual atmosphere in several respects. While the inference of a temperature inversion is no longer surprising for strongly irradiated planets (Haynes et al., 2015; Evans et al., 2017), both the very high metallicity and C/O$\sim$1 have less precedent. The high C/O ratio is governed by the lack of observed water features in the *WFC3* and *Spitzer* bandpasses, by the slight decrease at the long end of the *WFC3* band, and by the *Spitzer* photometry point at 4.5 μm. We reiterate that the inference of a thermal inversion hinges critically on the single *Spitzer* photometric point at 4.5 μm. Previously, Nymeyer et al. (2011) postulated a temperature inversion for exactly that reason. Nevertheless, the photometry does

not reveal the resolved band structure of the 4.5 μm CO band in emission that would lead to an unequivocal detection of molecular emission. However, given the data we have and the many checks on our data analysis procedures, the unusual atmosphere of WASP-18b is a compelling conclusion.

The observations also reveal the first instance where both absorption and emission features are seen in the spectrum of an exoplanet, both due to CO. The absorption at $\sim$1.6 μm is caused by a weaker CO band compared to the emission in a stronger CO band in the 4.5 μm region. As shown by the contribution functions in the $p-T$ profile inset in Figure 8.1, the 1.6 μm region of the spectrum probes the lower atmosphere while the 4.5 μm band probes the upper atmosphere. The only other atmosphere where simultaneous absorption and emission in the same molecule are observed is in the Earth's infrared spectrum, specifically in the 15 μm band of CO_2, due to the temperature structure at the tropopause and stratosphere (Hanel et al., 1972).

If confirmed, the atmospheric properties of WASP-18b open a new regime in the diversity of hot Jupiters. Classically, thermal inversions in hot Jupiters were suggested to be caused by TiO and VO in very high temperature atmospheres (Hubeny et al., 2003; Fortney et al., 2008). All studies so far have focused on the plausibility of TiO/VO as a function of various parameters and processes such as gravitational settling (Spiegel et al., 2009), stellar chromospheric emission (Knutson et al., 2010), C/O ratio (Madhusudhan et al., 2011b), and dynamics (Menou, 2012; Parmentier et al., 2013). For TiO or VO to be abundant enough to cause thermal inversions, the C/O ratio must be $\sim$0.5 or lower (Madhusudhan et al., 2011b). Planets with high C/O ratios were not predicted to host thermal inversions since their TiO/VO abundances would be severely depleted (Madhusudhan, 2012); however, recent work suggests other processes, such as inefficient atmospheric cooling, could lead to a temperature inversion (Mollière et al., 2015). Alternatively, oxygen-poor absorbers may play a similar role to TiO and VO (Zahnle et al., 2009). The two hot Jupiters for which thermal inversions have been detected have both shown signatures of TiO/VO in their atmospheres: WASP- 33b (Haynes et al., 2015) and WASP-121 (Evans et al., 2017). WASP-18b is the first system that shows a thermal inversion along with a high C/O

ratio of ∼1 with no evidence for TiO/VO, and hence provides a new test case for theories of thermal inversions in hot Jupiters.

The unique atmospheric composition of WASP-18b implies an interesting constraint for planetary formation theories. Its metal enrichment is consistent with a possible trend in mass-metallicity parameter space for a 10 M_J planet (see Chapter 7). High metallicity and a C/O ratio of 1 are plausibly explained by formation from extremely CO-rich gas beyond the H_2O condensation line (Öberg et al., 2011) or upper atmospheric enrichment in carbon and oxygen due to ablation of icy planetesimals during late-stage accretion (see Chapter 2). Future eclipse observations with *JWST* and improved modeling of giant planet accretion processes could help clarify the details of WASP-18b's formation history.

8.2 Primary Eclipse Spectrum of XO-1b

We use the transmission retrieval method presented in Chapter 4 to analyse the transmission spectrum of XO-1b across the optical and infrared wavelengths. XO-1b is a moderately hot (T∼1,200 K) planet with a mass similar to Jupiter ($M = 0.92\,M_J$) and orbits a Sun-like star every 4 days. The observations in the optical wavelength range were obtained with the u (0.366 μm), g (0.478 μm), r (0.663 μm), Hα (0.687 μm), I (0.810 μm), and z (0.910 μm) photometric filters on several large-aperture ground telescopes. These optical measurements are augmented with published *HST WFC3* observations (Deming et al., 2013) to construct the transmission spectrum of XO-1b covering $0.37 - 1.65$ μm.

Figure 8.3 shows the best-fit model to the observations. The model represents an atmosphere with patchy clouds and hazes and a cloud/haze fraction of 54 percent along the planetary limb. The patchy cloud model is weakly preferred to a clear-atmosphere model at the 1.3σ level. Water vapour is present at 3.05σ confidence to fit the *HST WFC3* data, signifying H_2O is present with a certainty of 99.87 percent. Evidence for nitrogen chemistry in the form of either NH_3 or HCN is marginal at 1.5σ. The optical data do not provide evidence for the presence of either Na or K.

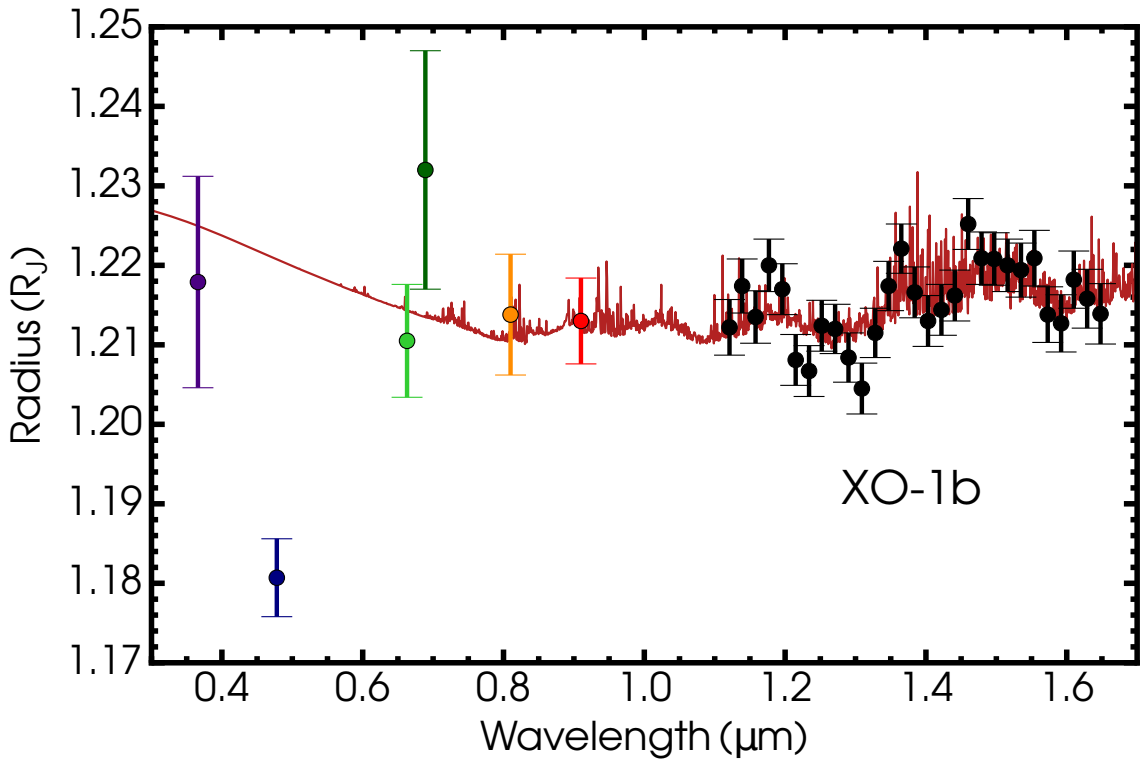

Figure 8.3: Best-fitting model transmission spectrum of XO-1b (dark red line). The observed transmission spectrum is shown using coloured points for the optical data and black points for the *HST WFC3* data.

Our model fits the optical transmission spectrum in the u, r, I, and z bands to within 0.5σ.

The best-fitting model is unable to explain the measured planetary radius in the g band, which lies 8σ below the model transmission spectrum and well below all other radius measurements. The reason for this discrepancy is not clear. It is a challenge to understand observationally, as the two light curves in this passband have high precisions and show mutual agreement, and such an effect has not been seen in this band in previous observations.[1] Temporal variability of the planetary atmosphere or heterogeneity of the stellar photosphere are unlikely because both g-band light curves were obtained simultaneously with z-band and either u-band or r-band measurements.

We conclude that the transmission spectrum of XO-1b is best reproduced by a

[1]For example, WASP-57 (Southworth et al., 2015), HAT-P-23 and WASP-48 (Ciceri et al., 2015), Qatar-2 (Mancini et al., 2014), and HAT-P-32 (Tregloan-Reed et al., 2018).

H_2/He-rich atmosphere containing H_2O with low confidence levels of patchy clouds and nitrogen-bearing molecules (NH3 and HCN). An anomalously small planet radius in the g band is difficult to explain either observationally or theoretically and should be investigated by obtaining new observations in this wavelength region at higher resolutions (e.g., with *VLT FORS2*).

8.2.1 Impact of the Optical Data

The motivation for obtaining ground-based observations in the optical wavelength range was to improve knowledge of XO-1b's atmospheric properties beyond what can be inferred from the *HST WFC3* data. We investigated this by modelling both the full transmission spectrum as well as only the *HST WFC3* data. We find that the addition of the optical data to the near-infrared observations introduces an alternative H_2O abundance.

Figure 8.4 shows the retrieved H_2O abundances for the case of the full transmission spectrum and the *HST WFC3* data alone. In the latter case, the modal $\log(X_{\mathrm{H_2O}})$ abundance is approximately -1 dex with a median and 1σ uncertainty of $-1.45^{+0.50}_{-2.19}$. The slight tail of the posterior distribution arises from a weak degeneracy with HCN. The adjoined observations in the optical range offer an alternative interpretation of XO-1b's atmosphere, adding a second mode to the H_2O mixing ratio at -4 dex and thus altering the median abundance by ~ -2 dex.

The two interpretations of XO-1b's atmospheric H_2O concentration emerge from two possible cloud condensate configurations. The water abundance mode at -4 dex that is introduced by the optical data suggests an atmosphere with condensate clouds composed of ~ 1 μm particles with cloud-top pressures between 10^{-2} and 10^{-1} mbar. The formation efficiency of condensate particles decreases with atmospheric height (Parmentier et al., 2013), and therefore, clouds extending to such low pressures require strong vertical mixing processes that could advect material upwards. On the other hand, the second mode constituting a high water abundance of about -1 dex proposes cloud-top pressures greater than 1 mbar. Ultimately, elucidating the atmosphere of XO-1b from these two distinct possibilities (low water abundance/high-

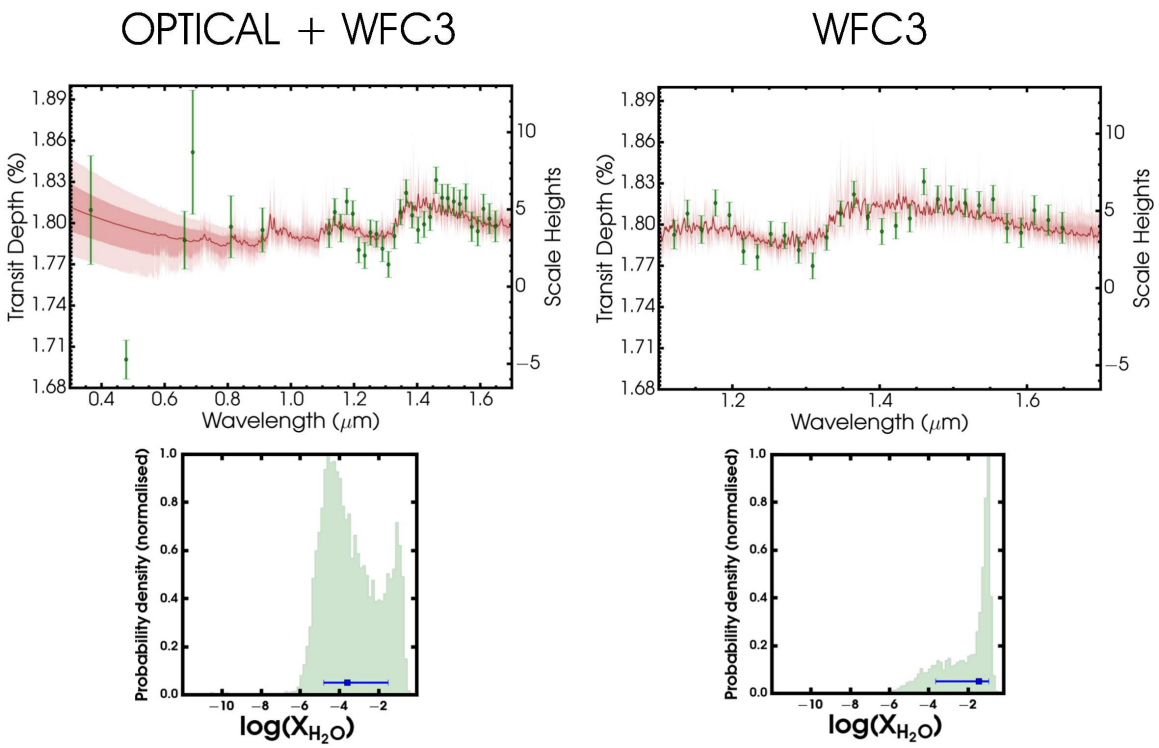

Figure 8.4: Retrieved model transmission spectra of XO-1b observations for the optical and near-infrared (left) and near-infrared only (right). The observations are shown in green and the retrieved median model is in dark red with associated 1σ and 2σ confidence contours. The median model in dark red has been smoothed for clarity. The probability density functions of the H_2O abundances are shown in the lower panels, where the points and errors represent the median abundance and 1σ intervals, respectively.

extending clouds, and high water abundance/low-extending clouds) will have to await more precise observations in the optical wavelength range.

8.3 Summary

We have used the retrieval methods described in Chapter 4 to characterise the atmospheres of two transiting exoplanets, WASP-18b and XO-1b. The secondary eclipse spectrum of WASP-18b displays an emission feature at 4.5 μm which signifies a thermal inversion in its dayside atmosphere at the 6.3σ significance level. The thermal inversion is likely not due to heating from TiO or VO since no signatures are detected in the near-infrared, but the atmosphere contains a significantly high abundance of

CO gas. We have also analysed the optical and near-infrared transmission spectrum of XO-1b. The atmosphere is likely host to patchy clouds extending to high altitudes and a sub-solar abundance of H_2O. However, an alternative interpretation of the atmosphere is of a super-solar H_2O abundance and a grey deck of clouds at pressures below 1 mbar.

Chapter 9

Conclusions

Extra-solar planets and their atmospheres exhibit a great variety which stems from the infinite personality of Nature. In reality there are an untold number of processes which influence the state and evolution of exoplanetary atmospheres. In this thesis I explored effective descriptions for several prominent physical processes which influence the character of these atmospheres as well as surveyed various observations to see what information they contain. The former was approached through detailed theoretical models while for the latter I used several new retrieval methods.

In Chapter 2 I studied the ways in which solid bodies evaporate and enrich the atmospheres of gas giant exoplanets with their chemistry. The chemical composition of an atmosphere as observed today is the end product of a long history of formation and evolution. The formation history of a planet involves the accretion of gases and solid bodies which contribute to the planet's total composition, both to the interior portions which are not observable to us and to the observable regions of the atmosphere. Although the observable atmosphere can be regarded as a bulk representation of the accreted gas throughout a planet's life, the case is not as clear for the solids. The efficiency with which solids ablate in fluid envelopes determines the extent to which an atmosphere mirrors the compositions of accreted solids. Therefore, an atmosphere observed today to have low water abundances may either be due small amounts of accreted icy bodies or inefficient ablation of icy bodies in the upper regions of the planet. Our study of solid ablation in gas giant systems reveals

that chemical enrichment of exoplanetary atmospheres is efficient, and means that the chemical composition of an observable atmosphere should reflect both the solid and gas components accreted throughout time. This efficiency of solid evaporation nevertheless makes studying the formation histories of giant planets more challenging than if an atmosphere were only expected to reflect the accreted gases.

The gas-rich atmospheres of giant exoplanets also host liquid and solid material in the form of clouds. Chapter 3 investigates the effects which condensed gases have on observations of large planets which transit their host stars. Investigating the ways in which clouds affect observations is crucial, for they influence interpretations of the gas chemistry in an atmosphere and hence also the formation conditions of planets. We thus explore three metrics that can be used to interpret atmospheric observations of transiting planets. The first metric is the slope of a spectrum at the blue end of the optical wavelength range from 0.3 to 0.56 μm. The slopes in this range provide hints about multiple cloud properties including the cloud species, the dominant particle sizes composing the clouds, and the vertical extent of clouds. The degree of uniformity of the optical slope acts as a second tool for deciphering cloud properties, particularly the cloud species. Clouds also efficiently absorb near-infrared light as seen on Earth by the Greenhouse effect. The third metric therefore involves the absorption features of clouds in the near- and mid-infrared regions. The increased quality of observations from future facilities means that these three metrics should become common ways through which to better characterise cloud condensates and therefore exoplanets and their atmospheres more generally.

Transitioning to retrievals, Chapter 4 details the inverse approach towards estimating atmospheric properties from transmission and emission spectra. The methods represent elegant ways of inferring the most likely attributes of an atmosphere given the observations and our general prior ignorance about the nature of a certain atmosphere. Chapter 5 uses the transmission retrieval method of Chapter 4 to gain statistical estimates of the atmospheric properties of ten hot giant exoplanets which have the broadest observational wavelength coverage. Indeed, the availability of observations in the optical wavelength region allow us to achieve a reliable assessment

of the amount of water vapour along the limb of the planets. The spectroscopic measurements confirm that the majority of these planets harbour low water abundances (i.e., sub-solar) along their limbs. Since this finding is representative of a size-able sample of planets, it may well be that the majority of close-in giant planets in our galaxy contain sub-solar amounts of water in their atmospheres. The lack of any other oxygen-carrying molecules suggests that the abundances of oxygen are also mostly below the solar value, and imply that most of these planets likely migrated to their present locations through gravitational interactions with other planets in their systems.

The spectrum of a transiting planet is not necessarily representative of physics in its atmosphere alone. Chapter 6 presents a new retrieval method which considers the influence of stellar processes on a planet's transit spectrum. Stars are active and dynamic, varying in brightness on timescales of days to weeks due in large part to cool spots and hot faculae in their photospheres. These forms of activity modulate the radius of the star as a function of wavelength and create a source of contamination for the planetary spectrum. The new retrieval method is capable of distinguishing the stellar activity from the chemical and thermal properties intrinsic to the planet. The application of this method to the spectra of nine hot giant exoplanets reveals the relative importance of clouds and hazes compared with stellar spectral imprints. Our analysis finds that the spectra of four planets likely display considerable contamination from their host stars. The observational push towards the discovery and characterisation of Earth-sized planets in the next decade will benefit greatly from this new method, as most searches of small planets will occur around M stars which display the highest activity among all stellar types.

The discovery and characterisation of planets is also achieved by directly suppressing the influence of the star. In Chapter 7 I apply a retrieval method for directly-imaged objects to the thermal spectra of four imaged companions in orbit around HR 8799. Imaged spectra are typically analysed through models that depend on an assumption of the system's age as well as equilibrium chemistry in the atmospheres. The retrieval method aids in moving beyond these assumptions. The four companion

atmospheres all display high abundances of water vapour, with detection significances well beyond the 5σ threshold. The outermost companions, HR 8799b and HR 8799c, carry additional oxygen in the form of high abundances of carbon monoxide. The relatively low temperatures of these objects ($\sim$1000 K) and the detected chemistry implies that their atmospheres are significantly out of chemical equilibrium. Future spectral measurements using the *JWST* and the *ELTs* will provide an information cache to test whether these companions formed through gravitational instabilities.

I have used the above set of retrieval methods to characterise the atmospheres of two other transiting exoplanets, WASP-18b and XO-1b. In Chapter 8, a fellow PhD student and I have shown that the super-hot Jupiter WASP-18b displays an extensive thermal inversion in its dayside atmosphere which is likely not due to feedback heating from titanium oxide or vanadium oxide. The inference of a thermal inversion arises from the high amount of emission in the 4.5 μm region and is due to excited states of the carbon monoxide molecule, which constitutes about 20 percent of the atmosphere by number. WASP-18b serves as an outstanding case of a super-hot Jupiter atmosphere that is rich in metals and with an extreme temperature increase with height. In addition, I have analysed the optical and near-infrared spectrum of XO-1b's atmosphere. The atmosphere likely hosts patchy clouds extending to high altitudes and a sub-solar abundance of water vapour.

The studies presented in this thesis accentuate the variety and complexity of planets and their atmospheres. Ultimately, exploring the diversity of exoplanets and their atmospheres using more able facilities of the future such as the *JWST* and the *ELTs* will continue to prompt questions about their compositions and formation histories. Nature will continue to evolve its mysteries forward in time.

Appendix A

Chapter 3: Calculation of Mie Coefficients

The Mie coefficients a_n and b_n are the primary variables needed to calculate the scattering and extinction cross-sections of cloud particles in equations (3.8) and (3.9). Traditionally these are calculated using expressions in either Deirmendjian (1969) or Bohren and Huffman (1983). The expressions for these coefficients in Deirmendjian (1969) are

$$\begin{aligned} a_n(m,x) =& \{\Theta_1 J_{n+1/2}(x) - J_{n-1/2}(x)\} \times \{\Theta_1 [J_{n+1/2}(x) \\ & + i(-1)^n J_{-n-1/2}(x)] - [J_{n-1/2} - i(-1)^n \\ & \times J_{-n+1/2}(x)]\}^{-1}, \end{aligned} \tag{A.1}$$

$$\begin{aligned} b_n(m,x) =& \{\Theta_2 J_{n+1/2}(x) - J_{n-1/2}(x)\} \times \{\Theta_2 [J_{n+1/2}(x) \\ & + i(-1)^n J_{-n-1/2}(x)] - [J_{n-1/2} - i(-1)^n \\ & \times J_{-n+1/2}(x)]\}^{-1}. \end{aligned} \tag{A.2}$$

Here $J_{\pm n \pm 1/2}$ are Bessel functions of the first kind with fractional orders. The coefficients are nearly identical except for the differences in Θ_1 and Θ_2 which are $\Theta_1 = A_n(mx)/m + n/x$ and $\Theta_2 = mA_n(mx) + n/x$, with $A_n(mx) = J_{n-1/2}(mx)/J_{n+1/2}(mx) - n/(mx)$.

We find that the representation of these coefficients in this form is not best suited for computations (see also page 127 of Bohren and Huffman, 1983). For some small volumes of the $\{a, \lambda, n(\lambda), \kappa(\lambda)\}$ parameter space the above expressions break down giving 'NaN's. This mainly occurs for large parameter sizes x. As noted in Section 3.1.2, a large x translates into a greater number of terms n in the sum of the scattering and extinction coefficients. The 'NaN's arise due to the numerical round-off error associated with a finite representation of the Bessel functions which accumulates for large n.

We therefore calculate the Mie coefficient expressions as in Bohren and Huffman (1983),

$$a_n(m,x) = \frac{\{D_n(mx)/m + n/x\}\psi_n(x) - \psi_{n-1}(x)}{\{D_n(mx)/m + n/x\}\xi_n(x) - \xi_{n-1}(x)}, \tag{A.3}$$

$$b_n(m,x) = \frac{\{mD_n(mx) + n/x\}\psi_n(x) - \psi_{n-1}(x)}{\{mD_n(mx) + n/x\}\xi_n(x) - \xi_{n-1}(x)}, \tag{A.4}$$

where $D_n = \frac{d\ln\psi_n}{dx}$ and satisfies the backward recurrence relation $D_{n-1} = n/(mx) - (D_n + n/(mx))^{-1}$. This recurrence relation is stable when computed from the maximal value of the series $n_{\max}$ downward. Further, the Ricatti-Bessel functions, ψ_n and ξ_n, are

$$\psi_n(x) = \sqrt{\frac{\pi x}{2}} J_{n+1/2}(x), \tag{A.5}$$

$$\xi_n(x) = \sqrt{\frac{\pi x}{2}} \{J_{n+1/2}(x) - iY_{n+1/2}(x)\} = \psi_n(x) - i\chi_n(x), \tag{A.6}$$

where $J_{n+1/2}$ and $Y_{n+1/2}$ are Bessel functions of the first and second kind with fractional orders, respectively. The Ricatti-Bessel functions satisfy the following recurrence relations computed in ascending fashion (Bohren and Huffman, 1983)

$$\psi_{n+1}(x) = \frac{2n+1}{x}\psi_n(x) - \psi_{n-1}(x) \tag{A.7}$$

$$\xi_{n+1}(x) = \frac{2n+1}{x}\xi_n(x) - \xi_{n-1}(x) \tag{A.8}$$

and with initial values of

$$\begin{aligned} \psi_{-1} &= \cos x \\ \psi_0 &= \sin x \end{aligned} \quad \text{and} \quad \begin{aligned} \chi_{-1} &= -\sin x \\ \chi_0 &= \cos x. \end{aligned} \tag{A.9}$$

Appendix B

Chapter 3: Mixing Ratio of Cloud Particles

Here we present a derivation of the cloud particle abundance $X_{\rm cloud}$ for condensate particles composed of a single chemical species. The abundance of cloud particles assuming an H_2-rich atmosphere is

$$X_{\rm cloud} \approx \frac{\text{Number of cloud particles per volume}}{\text{Number of } H_2 \text{ particles per volume}} = \frac{n_{\rm cloud}}{n_{\rm H_2}}. \tag{B.1}$$

The number of cloud particles in a unit volume is limited by the atom in the cloud species which has the lowest abundance of all the atoms. Therefore the number of cloud particles in unit a volume is

$$n_{\rm cloud} = \frac{\text{Number of limiting atom type per volume}}{\text{Number of limiting atom type per cloud particle}} = \frac{n_{\rm lim}}{N_{\rm lim}} \tag{B.2}$$

The number density of the limiting type of atom is

$$n_{\rm lim} = X_{\rm lim} \times \text{Number of atoms per unit volume} \approx X_{\rm lim} \times 2n_{\rm H_2} \tag{B.3}$$

Now since each cloud particle is composed of one type of condensate species, we may write

$$N_{\rm lim} = \frac{M_{\rm cloud}}{\mu_{\rm cloud}} \tilde{N}_{\rm lim} \tag{B.4}$$

where $\tilde{N}_{\rm lim}$ is the number of the limiting atom type per molecule of a cloud species. With these assumptions, the volumetric number density of the cloud particles is

$$n_{\rm cloud} = \frac{2 n_{\rm H_2} \mu_{\rm cloud} X_{\rm lim}}{M_{\rm cloud} \tilde{N}_{\rm lim}}. \tag{B.5}$$

Finally, a spherical grain implies $M_{\rm cloud} = 4\pi a^3 \rho_{\rm cloud}/3$ and therefore the cloud particle abundance is

$$X_{\rm cloud} = \frac{3 X_{\rm lim} \mu_{\rm cloud}}{2 \rho_{\rm cloud} \pi a^3 \tilde{N}_{\rm lim}}. \tag{B.6}$$

Appendix C

Chapter 5: Retrieved Atmospheric Properties for the Ensemble of Ten Hot Giant Exoplanets

Table C.1: Retrieved chemical abundances of the hot giant exoplanet ensemble.

Planet	M_p (M_J)	$X_{\mathrm{Na}}{}^{\dagger}$	$X_{\mathrm{K}}{}^{\dagger}$	$X_{\mathrm{H_2O}}{}^{\dagger}$	$X_{\mathrm{CH_4}}{}^{\dagger}$	$X_{\mathrm{NH_3}}{}^{\dagger}$	$X_{\mathrm{HCN}}{}^{\dagger}$	$X_{\mathrm{CO}}{}^{\dagger}$	$X_{\mathrm{CO_2}}{}^{\dagger}$
HAT-P-12b	$0.21^{+0.01}_{-0.01}$	$-8.75^{+2.92}_{-2.16}$	$-3.24^{+0.89}_{-4.25}$	$\mathbf{-3.91^{+1.01}_{-1.89}}$	$-9.14^{+2.00}_{-1.82}$	$-8.98^{+2.10}_{-1.94}$	$-8.43^{+2.64}_{-2.28}$	$-5.65^{+2.77}_{-4.02}$	$-6.16^{+2.21}_{-3.39}$
WASP-39b	$0.28^{+0.03}_{-0.03}$	$-3.86^{+1.31}_{-1.36}$	$-4.22^{+1.25}_{-1.12}$	$\mathbf{-4.07^{+0.72}_{-0.78}}$	$-5.65^{+0.78}_{-1.02}$	$-8.65^{+2.28}_{-2.16}$	$-8.24^{+2.53}_{-2.43}$	$-7.02^{+3.08}_{-3.22}$	$-4.31^{+0.91}_{-1.04}$
WASP-6b	$0.50^{+0.02}_{-0.04}$	$-9.18^{+2.14}_{-1.82}$	$-5.53^{+2.01}_{-1.85}$	$\mathbf{-6.91^{+1.83}_{-2.07}}$	$-9.15^{+1.97}_{-1.83}$	$-8.62^{+2.20}_{-2.17}$	$-8.60^{+2.25}_{-2.18}$	$-7.77^{+2.93}_{-2.69}$	$-10.08^{+1.76}_{-1.29}$
HD 189733b	$1.14^{+0.03}_{-0.03}$	$-7.77^{+1.64}_{-0.87}$	$-8.87^{+1.38}_{-1.52}$	$\mathbf{-5.04^{+0.46}_{-0.30}}$	$-9.18^{+1.86}_{-1.84}$	$-9.09^{+1.99}_{-1.91}$	$-8.13^{+2.38}_{-2.55}$	$-6.93^{+2.97}_{-3.33}$	$-9.02^{+1.84}_{-1.96}$
HAT-P-1b	$0.53^{+0.02}_{-0.02}$	$-8.44^{+1.45}_{-2.12}$	$-9.10^{+1.92}_{-1.84}$	$\mathbf{-2.72^{+0.42}_{-0.56}}$	$-8.39^{+2.37}_{-2.29}$	$-7.85^{+2.66}_{-2.64}$	$-7.65^{+2.78}_{-2.79}$	$-7.29^{+3.15}_{-3.05}$	$-8.93^{+2.11}_{-1.96}$
HD 209458b	$0.69^{+0.02}_{-0.02}$	$-4.92^{+0.83}_{-0.57}$	$-6.46^{+0.84}_{-0.64}$	$\mathbf{-4.66^{+0.39}_{-0.30}}$	$-8.60^{+2.20}_{-2.22}$	$-8.56^{+2.22}_{-2.28}$	$-8.66^{+2.25}_{-2.21}$	$-8.37^{+2.57}_{-2.38}$	$-9.80^{+1.57}_{-1.45}$
WASP-31b	$0.48^{+0.03}_{-0.03}$	$-7.66^{+2.76}_{-2.68}$	$-3.43^{+0.95}_{-1.62}$	$\mathbf{-3.97^{+1.01}_{-2.27}}$	$-8.30^{+2.42}_{-2.34}$	$-5.01^{+1.52}_{-4.45}$	$-7.92^{+2.64}_{-2.59}$	$-7.32^{+3.15}_{-3.01}$	$-9.20^{+2.09}_{-1.83}$
WASP-17b	$0.49^{+0.03}_{-0.03}$	$-8.71^{+1.55}_{-1.76}$	$-9.77^{+1.55}_{-1.38}$	$\mathbf{-4.04^{+0.91}_{-0.42}}$	$-9.26^{+1.76}_{-1.73}$	$-8.33^{+2.34}_{-2.32}$	$-8.70^{+2.25}_{-2.10}$	$-5.41^{+2.46}_{-4.13}$	$-7.04^{+1.86}_{-2.77}$
WASP-19b	$1.11^{+0.04}_{-0.04}$	$-7.51^{+2.75}_{-2.80}$	$-7.10^{+2.48}_{-2.63}$	$\mathbf{-3.90^{+0.95}_{-1.16}}$	$-8.76^{+2.16}_{-2.05}$	$-8.44^{+2.40}_{-2.23}$	$-8.03^{+2.71}_{-2.48}$	$-6.45^{+3.04}_{-3.48}$	$-7.03^{+2.28}_{-2.97}$
WASP-12b	$1.40^{+0.10}_{-0.10}$	$-4.11^{+1.30}_{-1.75}$	$-8.88^{+2.29}_{-2.00}$	$\mathbf{-3.16^{+0.66}_{-0.69}}$	$-8.84^{+2.09}_{-1.99}$	$-8.47^{+2.28}_{-2.19}$	$-8.17^{+2.47}_{-2.41}$	$-7.18^{+3.10}_{-3.00}$	$-8.34^{+2.43}_{-2.32}$

† All values are in $\log_{10}(X_i)$.

Table C.2: Retrieved cloud/haze properties of the hot giant exoplanet ensemble.

Planet	M_p (M_J)	$\log_{10}(a)$	γ	$\log_{10}(P_{\rm cloud})$	$\bar{\phi}$
HAT-P-12b	$0.21^{+0.01}_{-0.01}$	$4.70^{+1.66}_{-1.74}$	$-9.04^{+4.62}_{-7.78}$	$-0.78^{+1.80}_{-2.03}$	$0.60^{+0.24}_{-0.19}$
WASP-39b	$0.28^{+0.03}_{-0.03}$	$3.83^{+1.22}_{-1.10}$	$-13.27^{+4.29}_{-4.24}$	$-1.09^{+2.01}_{-2.53}$	$0.54^{+0.24}_{-0.18}$
WASP-6b	$0.50^{+0.02}_{-0.04}$	$4.92^{+2.04}_{-1.41}$	$-6.06^{+1.99}_{-2.63}$	$-0.10^{+1.34}_{-1.38}$	$0.64^{+0.17}_{0.15}$
HD 189733b	$1.14^{+0.03}_{-0.03}$	$3.64^{+0.79}_{-1.01}$	$-7.75^{+1.29}_{-1.43}$	$0.44^{+1.03}_{-1.13}$	$0.67^{+0.26}_{-0.12}$
HAT-P-1b	$0.53^{+0.02}_{-0.02}$	$5.68^{+1.52}_{-1.49}$	$-5.77^{+2.49}_{-3.09}$	$-1.02^{+1.93}_{-2.03}$	$0.52^{+0.11}_{-0.10}$
HD 209458b	$0.69^{+0.02}_{-0.02}$	$4.57^{+0.58}_{-0.74}$	$-14.82^{+4.79}_{-3.45}$	$-4.47^{+0.52}_{-0.48}$	$0.52^{+0.06}_{-0.07}$
WASP-31b	$0.48^{+0.03}_{-0.03}$	$4.00^{+0.95}_{-0.98}$	$-14.08^{+4.07}_{-3.69}$	$-3.72^{+0.66}_{-0.61}$	$0.76^{+0.13}_{-0.15}$
WASP-17b	$0.49^{+0.03}_{-0.03}$	$2.33^{+2.20}_{-2.53}$	$-10.55^{+5.66}_{-5.84}$	$-1.60^{+2.21}_{-2.56}$	$0.18^{+0.26}_{-0.12}$
WASP-19b	$1.11^{+0.04}_{-0.04}$	$3.95^{+2.00}_{-2.22}$	$-11.52^{+5.29}_{-5.11}$	$-0.56^{+1.60}_{-1.97}$	$0.42^{+0.27}_{-0.26}$
WASP-12b	$1.40^{+0.10}_{-0.10}$	$2.07^{+2.64}_{-2.87}$	$-10.47^{+7.11}_{-6.47}$	$-1.48^{+2.14}_{-2.15}$	$0.33^{+0.34}_{-0.20}$

Table C.3: Retrieved temperature profile parameters of the hot giant exoplanet ensemble.

Planet	T_0	α_1	α_2	P_1†	P_2†	P_3†	$P_{\rm ref}$†
HAT-P-12b	456^{+70}_{-40}	$0.81^{+0.13}_{-0.17}$	$0.63^{+0.24}_{-0.28}$	$-1.54^{+1.63}_{-1.74}$	$-3.97^{+1.74}_{-1.34}$	$0.61^{+0.94}_{-1.32}$	$-2.68^{+0.84}_{-0.40}$
WASP-39b	775^{+282}_{-166}	$0.66^{+0.22}_{-0.21}$	$0.59^{+0.27}_{-0.26}$	$-1.50^{+1.64}_{-1.77}$	$-3.99^{+1.92}_{-1.35}$	$0.60^{+0.95}_{-1.37}$	$-2.55^{+0.52}_{-0.39}$
WASP-6b	1057^{+198}_{-290}	$0.57^{+0.26}_{-0.22}$	$0.60^{+0.26}_{-0.25}$	$-1.70^{+1.61}_{-1.65}$	$-4.06^{+1.79}_{-1.30}$	$0.49^{+1.00}_{-1.33}$	$-3.55^{+0.60}_{-0.74}$
HD 189733b	1159^{+146}_{-157}	$0.76^{+0.16}_{-0.22}$	$0.67^{+0.22}_{-0.27}$	$-1.70^{+1.75}_{-1.83}$	$-3.98^{+1.85}_{-1.35}$	$0.48^{+1.05}_{-1.42}$	$-2.07^{+0.23}_{-0.43}$
HAT-P-1b	1114^{+251}_{-205}	$0.65^{+0.22}_{-0.22}$	$0.59^{+0.26}_{-0.25}$	$-1.58^{+1.61}_{-1.72}$	$-4.04^{+1.83}_{-1.31}$	$0.57^{+0.95}_{-1.30}$	$-3.63^{+0.42}_{-0.41}$
HD 209458b	949^{+252}_{-109}	$0.59^{+0.27}_{-0.20}$	$0.35^{+0.38}_{-0.17}$	$-1.85^{+1.66}_{-1.28}$	$-4.22^{+1.80}_{-1.22}$	$0.05^{+1.29}_{-1.07}$	$-2.65^{+0.39}_{-0.43}$
WASP-31b	1043^{+287}_{-172}	$0.69^{+0.21}_{-0.23}$	$0.61^{+0.25}_{-0.26}$	$-1.64^{+1.65}_{-1.75}$	$-4.04^{+1.84}_{-1.32}$	$0.54^{+0.98}_{-1.37}$	$-3.43^{+0.61}_{-0.53}$
WASP-17b	1147^{+259}_{-305}	$0.58^{+0.26}_{-0.21}$	$0.58^{+0.26}_{-0.24}$	$-1.52^{+1.51}_{-1.68}$	$-3.99^{+1.82}_{-1.33}$	$0.55^{+0.95}_{-1.26}$	$-2.38^{+0.32}_{-0.66}$
WASP-19b	1386^{+370}_{-337}	$0.66^{+0.22}_{-0.22}$	$0.61^{+0.24}_{-0.24}$	$-1.69^{+1.64}_{-1.66}$	$-3.99^{+1.74}_{-1.33}$	$0.49^{+0.98}_{-1.33}$	$-2.83^{+0.89}_{-0.76}$
WASP-12b	990^{+169}_{-122}	$0.77^{+0.15}_{-0.18}$	$0.66^{+0.22}_{-0.26}$	$-1.55^{+1.65}_{-1.71}$	$-3.92^{+1.79}_{-1.35}$	$0.60^{+0.93}_{-1.38}$	$0.16^{+0.64}_{-0.63}$

† All values are in $\log_{10}(P_i[\text{bar}])$.

Appendix D

Chapter 6: Bayesian Model Comparison of the Nine Hot Giant Exoplanets

Table D.1: Bayesian model comparisons of the hot Jupiter ensemble in Chapter 6. Listed are the evaluated model types, natural logarithms of the evidences $\mathcal{Z}$, and Bayes factors with their associated significance levels. The reference model ('Ref.') includes a formalism for the heterogeneity of the stellar disk, opacity contributions from H_2O, CH_4, CO, CO_2, HCN, NH_3, Na, K, H_2-H_2 and H_2-He, and a cloud and haze parameterisation. The Bayes factor $\mathcal{B}_{0i}$ represents the preference for the reference model over model i. The detection significance signifies the degree of inclination of the reference model over the alternative model. Detection significance calculations are valid for Bayes factors above one, hence the instances of 'N/A'.

WASP-6b (Full Data)			
Model Type	Evidence ($\ln(\mathcal{Z})$)	Bayes Factor $\mathcal{B}_{0i}$	Detection Sig.
HMch	134.25	Ref.	Ref.
HMc	134.06	1.22	1.37σ
HM	132.39	6.48	2.48σ
Mch	130.76	32.94	3.13σ
M	119.20	3.46×10^6	5.83σ

WASP-6b (Without Spitzer Data)			
Model Type	Evidence ($\ln(\mathcal{Z})$)	Bayes Factor $\mathcal{B}_{0i}$	Detection Sig.
HMch	124.16	Ref	Ref.
HMc	124.28	0.89	N/A
HM	123.79	1.45	1.56σ
Mch	124.06	1.11	1.23σ
M	124.47	0.74	N/A

WASP-39b			
Model Type	Evidence ($\ln(\mathcal{Z})$)	Bayes Factor $\mathcal{B}_{0i}$	Detection Sig.
HMch	401.44	Ref.	Ref.
HMc	401.17	1.30	1.45σ
HM	394.17	1430	4.22σ
Mch	399.60	6.26	2.47σ
M	393.16	3923	4.47σ

HD 209458b			
Model Type	Evidence ($\ln(\mathcal{Z})$)	Bayes Factor $\mathcal{B}_{0i}$	Detection Sig.
HMch	957.83	Ref.	Ref.
HMc	956.64	3.31	2.14σ
HM	945.45	2.38×10^5	5.34σ
Mch	957.47	1.44	1.55σ
M	947.01	5×10^4	5.02σ

HAT-P-12b			
Model Type	Evidence ($\ln(\mathcal{Z})$)	Bayes Factor $\mathcal{B}_{0i}$	Detection Sig.
HMch	264.74	Ref.	Ref.
HMc	264.83	0.92	N/A
HM	245.84	1.62×10^8	6.47σ
Mch	264.56	1.20	1.35σ
M	245.67	1.9×10^8	6.50σ

HAT-P-1b

Model Type	Evidence ($\ln(\mathcal{Z})$)	Bayes Factor $\mathcal{B}_{0i}$	Detection Sig.
HMch	302.16	Ref.	Ref.
HMc	302.23	0.93	N/A
HM	299.98	8.90	2.62σ
Mch	302.57	0.69	N/A
M	296.07	443.86	3.92σ

WASP-31b

Model Type	Evidence ($\ln(\mathcal{Z})$)	Bayes Factor $\mathcal{B}_{0i}$	Detection Sig.
HMch	395.54	Ref.	Ref.
HMc	394.98	1.75	1.72σ
HM	395.17	1.45	1.56σ
Mch	395.98	0.64	N/A
M	392.00	34.51	3.14σ

WASP-19b

Model Type	Evidence ($\ln(\mathcal{Z})$)	Bayes Factor $\mathcal{B}_{0i}$	Detection Sig.
HMch	76.00	Ref.	Ref.
HMc	74.89	3.06	2.09σ
HM	75.71	1.34	1.48σ
Mch	77.27	0.28	N/A
M	72.59	30.53	3.10σ

WASP-17b

Model Type	Evidence ($\ln(\mathcal{Z})$)	Bayes Factor $\mathcal{B}_{0i}$	Detection Sig.
HMch	249.31	Ref.	Ref.
HMc	249.98	0.51	N/A
HM	250.08	0.47	N/A
Mch	250.52	0.30	N/A
M	251.02	0.18	N/A

WASP-12b

Model Type	Evidence ($\ln(\mathcal{Z})$)	Bayes Factor $\mathcal{B}_{0i}$	Detection Sig.
HMch	195.33	Ref.	Ref.
HMc	196.38	0.35	N/A
HM	195.20	1.14	1.28σ
Mch	197.34	0.13	N/A
M	196.79	0.23	N/A

Appendix E

Chapter 7: Bayesian Model Comparison and Retrieved Parameters for the HR 8799 Companions

Table E.1: Bayesian model comparisons of the HR 8799 companions. Listed are the evaluated model types, natural logarithms of the evidences $\mathcal{Z}$ and Bayes factors with their associated significance levels. The reference model ('Ref.') includes opacity contributions from H_2O, CH_4, CO, CO_2, HCN, NH_3, H_2-H_2 and H_2-He. The Bayes factor $\mathcal{B}_{0i}$ represents the preference for the reference model over model i. The detection significance signifies the degree to which the reference model is preferred over the alternative model in the frequentest statistics approach. Detection significance calculations are valid for Bayes factors above one, hence the 'N/A' values.

HR 8799b

Model Type	Evidence ($\ln(\mathcal{Z})$)	Bayes Factor $\mathcal{B}_{0i}$	Detection Sig.
Full	1630.90	Ref.	Ref.
No H_2O	1350.75	10^{121}	23.80σ
No CH_4	1628.35	12.82	2.78σ
No CO	1555.61	5×10^{32}	12.48σ
No CO_2	1630.77	1.13	1.27σ
No HCN	1631.37	0.62	N/A
No NH_3	1630.73	1.19	1.34σ

HR 8799c

Model Type	Evidence ($\ln(\mathcal{Z})$)	Bayes Factor $\mathcal{B}_{0i}$	Detection Sig.
Full	1777.99	Ref.	Ref.
No H_2O	1753.50	4.33×10^{10}	7.30σ
No CH_4	1778.02	0.97	N/A
No CO	1773.88	61.13	3.34σ
No CO_2	1777.73	1.30	1.45σ
No HCN	1778.42	0.65	N/A
No NH_3	1778.20	0.81	N/A

HR 8799d

Model Type	Evidence ($\ln(\mathcal{Z})$)	Bayes Factor $\mathcal{B}_{0i}$	Detection Sig.
Full	2666.56	Ref.	Ref.
No H_2O	2651.57	3.22×10^{6}	5.82σ
No CH_4	2666.55	1.00	0.96σ
No CO	2665.59	2.63	2σ
No CO_2	2666.20	1.43	1.54σ
No HCN	2666.65	0.91	N/A
No NH_3	2666.98	0.65	N/A

HR 8799e

Model Type	Evidence ($\ln(\mathcal{Z})$)	Bayes Factor $\mathcal{B}_{0i}$	Detection Sig.
Full	1110.99	Ref.	Ref.
No H_2O	1078.34	1.52×10^{14}	8.36σ
No CH_4	1110.96	1.03	1.08σ
No CO	1111.04	0.95	N/A
No CO_2	1111.09	0.90	N/A
No HCN	1111.31	0.73	N/A
No NH_3	1111.16	0.85	N/A

Table E.2: Retrieved molecular abundances of the HR 8799 companions.

Companion	$\log(X_{H_2O})$	$\log(X_{CH_4})$	$\log(X_{CO})$	$\log(X_{CO_2})$	$\log(X_{HCN})$	$\log(X_{NH_3})$
HR 8799b	$-2.08^{+0.30}_{-0.22}$	$-3.74^{+0.33}_{-0.30}$	$-0.68^{+0.31}_{-0.24}$	$-7.81^{+4.20}_{-3.99}$	$-8.80^{+3.31}_{-3.33}$	$-8.86^{+3.78}_{-3.29}$
HR 8799c	$-2.67^{+0.32}_{-0.29}$	$-7.05^{+1.96}_{-4.62}$	$-2.43^{+0.44}_{-0.40}$	$-8.44^{+3.82}_{-3.62}$	$-9.83^{+2.70}_{-2.61}$	$-9.51^{+2.86}_{-2.86}$
HR 8799d	$-2.09^{+0.39}_{-0.31}$	$-8.96^{+3.27}_{-3.23}$	$-2.82^{+1.42}_{-6.91}$	$-7.05^{+3.79}_{-4.63}$	$-9.01^{+3.10}_{-3.24}$	$-9.58^{+2.79}_{-2.88}$
HR 8799e	$-1.43^{+1.03}_{-1.02}$	$-6.86^{+3.86}_{-4.42}$	$-7.48^{+3.90}_{-3.98}$	$-8.47^{+3.47}_{-3.45}$	$-8.49^{+3.29}_{-3.40}$	$-8.97^{+3.12}_{-3.22}$

Table E.3: Derived C/H, O/H, and C/O ratios of the HR 8799 companions.

Companion	X_C/X_O	$\log(X_O/X_H)$	$\log(X_C/X_H)$
HR 8799b	$0.96^{+0.0002}_{-0.002}$	$-0.79^{+0.45}_{-0.28}$	$-0.81^{+0.45}_{-0.29}$
HR 8799c	$0.63^{+0.06}_{-0.06}$	$-2.46^{+0.40}_{-0.36}$	$-2.66^{+0.44}_{-0.40}$
HR 8799d	$0.16^{+0.51}_{-0.16}$	$-2.24^{+0.82}_{-0.38}$	$-3.05^{+1.45}_{-6.90}$
HR 8799e	$0.00^{+0.00}_{-0.00}$	$-1.66^{+1.00}_{-1.02}$	$-6.98^{+3.83}_{-4.20}$

Table E.4: Retrieved macroscopic parameters of the HR 8799 companions.

Companion	Object Radius (R_J)	Distance (pc)	$\log(M_{obj}(M_J))$
HR 8799b	$0.58^{+0.04}_{-0.04}$	$40.35^{+0.91}_{-0.90}$	$1.73^{+0.12}_{-0.21}$
HR 8799c	$0.78^{+0.04}_{-0.04}$	$40.36^{+0.89}_{-0.87}$	$1.41^{+0.33}_{-0.52}$
HR 8799d	$0.84^{+0.03}_{-0.03}$	$40.34^{+0.89}_{-0.88}$	$1.73^{+0.13}_{-0.26}$
HR 8799e	$0.92^{+0.09}_{-0.06}$	$40.39^{+0.92}_{-0.89}$	$0.99^{+0.68}_{-0.73}$

Table E.5: Retrieved temperature profile parameters of the HR 8799 companions.

Companion	T_0	α_1	α_2	$\log(P_1)$	$\log(P_2)$	$\log(P_3)$
HR 8799b	782^{+39}_{-112}	$0.62^{+0.05}_{-0.03}$	$0.64^{+0.24}_{-0.20}$	$0.65^{+0.17}_{-3.11}$	$-2.77^{+2.72}_{-2.15}$	$1.31^{+0.39}_{-0.29}$
HR 8799c	706^{+109}_{-121}	$0.47^{+0.05}_{-0.04}$	$0.70^{+0.19}_{-0.18}$	$-0.31^{+0.27}_{-0.30}$	$-2.52^{+2.01}_{-2.09}$	$0.96^{+0.65}_{-0.65}$
HR 8799d	1226^{+23}_{-26}	$0.93^{+0.04}_{-0.05}$	$0.74^{+0.17}_{-0.23}$	$0.14^{+0.21}_{-0.27}$	$-1.18^{+1.60}_{-2.61}$	$0.70^{+0.78}_{-0.40}$
HR 8799e	1077^{+66}_{-79}	$0.59^{+0.11}_{-0.10}$	$0.67^{+0.21}_{-0.24}$	$-0.58^{+0.94}_{-1.12}$	$-2.59^{+2.08}_{-2.01}$	$0.78^{+0.74}_{-0.94}$

Bibliography

Ackerman, A. S. and Marley, M. S. (2001). Precipitating Condensation Clouds in Substellar Atmospheres. *ApJ*, 556:872–884.

Agol, E. and Fabrycky, D. C. (2017). *Transit-Timing and Duration Variations for the Discovery and Characterization of Exoplanets*, page 7.

Aigrain, S., Pont, F., and Zucker, S. (2012). A simple method to estimate radial velocity variations due to stellar activity using photometry. *MNRAS*, 419:3147–3158.

Ali-Dib, M. (2017). Disentangling hot Jupiters formation location from their chemical composition. *MNRAS*, 467:2845–2854.

Apai, D., Cowan, N., Kopparapu, R., Kasper, M., Hu, R., Morley, C., Fujii, Y., Kane, S., Maley, M., del Genio, A., Karalidi, T., Komacek, T., Mamajek, E., Mandell, A., Domagal-Goldman, S., Barman, T., Boss, A., Breckinridge, J., Crossfield, I., Danchi, W., Ford, E., Iro, N., Kasting, J., Lowrance, P., Madhusudhan, N., McElwain, M., Moore, W., Pascucci, I., Plavchan, P., Roberge, A., Schneider, G., Showman, A., and Turnbull, M. (2017a). Exploring Other Worlds: Science Questions for Future Direct Imaging Missions (EXOPAG SAG15 Report). *ArXiv e-prints*.

Apai, D., Karalidi, T., Marley, M. S., Yang, H., Flateau, D., Metchev, S., Cowan, N. B., Buenzli, E., Burgasser, A. J., Radigan, J., Artigau, E., and Lowrance, P. (2017b). Zones, spots, and planetary-scale waves beating in brown dwarf atmospheres. *Science*, 357:683–687.

Apai, D., Rackham, B. V., Giampapa, M. S., Angerhausen, D., Teske, J., Barstow, J., Carone, L., Cegla, H., Domagal-Goldman, S. D., Espinoza, N., Giles, H., Gully-Santiago, M., Haywood, R., Hu, R., Jordan, A., Kreidberg, L., Line, M., Llama, J., López-Morales, M., Marley, M. S., and de Wit, J. (2018a). Understanding Stellar Contamination in Exoplanet Transmission Spectra as an Essential Step in Small Planet Characterization. *arXiv e-prints*.

Apai, D., Rackham, B. V., Giampapa, M. S., Angerhausen, D., Teske, J., Barstow, J., Carone, L., Cegla, H., Domagal-Goldman, S. D., Espinoza, N., Giles, H., Gully-Santiago, M., Haywood, R., Hu, R., Jordan, A., Kreidberg, L., Line, M., Llama, J., López-Morales, M., Marley, M. S., and de Wit, J. (2018b). Understanding Stellar

Contamination in Exoplanet Transmission Spectra as an Essential Step in Small Planet Characterization. *ArXiv e-prints*.

Artemieva, N. A. and Shuvalov, V. V. (2001). Motion of a fragmented meteoroid through the planetary atmosphere. *J. Geophys. Res.*, 106:3297–3310.

Asplund, M., Grevesse, N., Sauval, A. J., and Scott, P. (2009). The Chemical Composition of the Sun. *ARA&A*, 47:481–522.

Atreya, S. K., Crida, A., Guillot, T., Lunine, J. I., Madhusudhan, N., and Mousis, O. (2016). The Origin and Evolution of Saturn, with Exoplanet Perspective. *ArXiv e-prints*.

Atreya, S. K. and Wong, A.-S. (2005). Coupled Clouds and Chemistry of the Giant Planets- A Case for Multiprobes. *Space Sci. Rev.*, 116:121–136.

Baines, E. K., White, R. J., Huber, D., Jones, J., Boyajian, T., McAlister, H. A., ten Brummelaar, T. A., Turner, N. H., Sturmann, J., Sturmann, L., Goldfinger, P. J., Farrington, C. D., Riedel, A. R., Ireland, M., von Braun, K., and Ridgway, S. T. (2012). The CHARA Array Angular Diameter of HR 8799 Favors Planetary Masses for its Imaged Companions. *ApJ*, 761:57.

Baraffe, I., Chabrier, G., Barman, T. S., Allard, F., and Hauschildt, P. H. (2003). Evolutionary models for cool brown dwarfs and extrasolar giant planets. The case of HD 209458. *A&A*, 402:701–712.

Barman, T. (2007). Identification of Absorption Features in an Extrasolar Planet Atmosphere. *ApJ*, 661:L191–L194.

Barman, T. S., Hauschildt, P. H., and Allard, F. (2001). Irradiated Planets. *ApJ*, 556:885–895.

Barstow, J. K., Aigrain, S., Irwin, P. G. J., Kendrew, S., and Fletcher, L. N. (2015). Transit spectroscopy with James Webb Space Telescope: systematics, starspots and stitching. *MNRAS*, 448:2546–2561.

Barstow, J. K., Aigrain, S., Irwin, P. G. J., and Sing, D. K. (2017). A Consistent Retrieval Analysis of 10 Hot Jupiters Observed in Transmission. *ApJ*, 834:50.

Baudino, J.-L., Bézard, B., Boccaletti, A., Bonnefoy, M., Lagrange, A.-M., and Galicher, R. (2015). Interpreting the photometry and spectroscopy of directly imaged planets: a new atmospheric model applied to β Pictoris b and SPHERE observations. *A&A*, 582:A83.

Becker, A., Lorenzen, W., Fortney, J. J., Nettelmann, N., Schöttler, M., and Redmer, R. (2014). Ab Initio Equations of State for Hydrogen (H-REOS.3) and Helium (He-REOS.3) and their Implications for the Interior of Brown Dwarfs. *ApJS*, 215:21.

Becker , A.and Nettelmann, N., Holst, B., and Redmer, R. (2013). Isentropic compression of hydrogen: Probing conditions deep in planetary interiors. *Phys. Rev. B*, 88(4):045122.

Benneke, B. and Seager, S. (2012). Atmospheric Retrieval for Super-Earths: Uniquely Constraining the Atmospheric Composition with Transmission Spectroscopy. *ApJ*, 753:100.

Benneke, B. and Seager, S. (2013). How to Distinguish between Cloudy Mini-Neptunes and Water/Volatile-dominated Super-Earths. *ApJ*, 778:153.

Berdyugina, S. V. (2005). Starspots: A Key to the Stellar Dynamo. *Living Reviews in Solar Physics*, 2:8.

Berta-Thompson, Z. K., Irwin, J., Charbonneau, D., Newton, E. R., Dittmann, J. A., Astudillo-Defru, N., Bonfils, X., Gillon, M., Jehin, E., Stark, A. A., Stalder, B., Bouchy, F., Delfosse, X., Forveille, T., Lovis, C., Mayor, M., Neves, V., Pepe, F., Santos, N. C., Udry, S., and Wünsche, A. (2015). A rocky planet transiting a nearby low-mass star. *Nature*, 527:204–207.

Blecic, J. (2016). Observations, Thermochemical Calculations, and Modeling of Exoplanetary Atmospheres. *ArXiv e-prints*.

Blecic, J., Harrington, J., and Bowman, M. O. (2016). TEA: A Code Calculating Thermochemical Equilibrium Abundances. *ApJS*, 225:4.

Bohren, C. F. and Huffman, D. R. (1983). *Absorption and scattering of light by small particles*. Wiley-VCH.

Boisse, I., Moutou, C., Vidal-Madjar, A., Bouchy, F., Pont, F., Hébrard, G., Bonfils, X., Croll, B., Delfosse, X., Desort, M., Forveille, T., Lagrange, A.-M., Loeillet, B., Lovis, C., Matthews, J. M., Mayor, M., Pepe, F., Perrier, C., Queloz, D., Rowe, J. F., Santos, N. C., Ségransan, D., and Udry, S. (2009). Stellar activity of planetary host star HD 189 733. *A&A*, 495:959–966.

Boley, A. C. and Durisen, R. H. (2010). On the Possibility of Enrichment and Differentiation in Gas Giants During Birth by Disk Instability. *ApJ*, 724:618–639.

Bonnefoy, M., Zurlo, A., Baudino, J. L., Lucas, P., Mesa, D., Maire, A.-L., Vigan, A., Galicher, R., Homeier, D., Marocco, F., Gratton, R., Chauvin, G., Allard, F., Desidera, S., Kasper, M., Moutou, C., Lagrange, A.-M., Antichi, J., Baruffolo, A., Baudrand, J., Beuzit, J.-L., Boccaletti, A., Cantalloube, F., Carbillet, M., Charton, J., Claudi, R. U., Costille, A., Dohlen, K., Dominik, C., Fantinel, D., Feautrier, P., Feldt, M., Fusco, T., Gigan, P., Girard, J. H., Gluck, L., Gry, C., Henning, T., Janson, M., Langlois, M., Madec, F., Magnard, Y., Maurel, D., Mawet, D., Meyer, M. R., Milli, J., Moeller-Nilsson, O., Mouillet, D., Pavlov, A., Perret, D., Pujet, P., Quanz, S. P., Rochat, S., Rousset, G., Roux, A., Salasnich, B., Salter, G., Sauvage, J.-F., Schmid, H. M., Sevin, A., Soenke, C., Stadler, E., Turatto,

M., Udry, S., Vakili, F., Wahhaj, Z., and Wildi, F. (2016). First light of the VLT planet finder SPHERE. IV. Physical and chemical properties of the planets around HR8799. *A&A*, 587:A58.

Booth, R. A. and Clarke, C. J. (2018). Chemical enrichment of the planet-forming region as probed by accretion. *MNRAS*, 473:757–764.

Booth, R. A., Clarke, C. J., Madhusudhan, N., and Ilee, J. D. (2017). Chemical enrichment of giant planets and discs due to pebble drift. *MNRAS*, 469:3994–4011.

Borysow, A. (2002). Collision-induced absorption coefficients of H_2 pairs at temperatures from 60 K to 1000 K. *A&A*, 390:779–782.

Borysow, J., Frommhold, L., and Birnbaum, G. (1988). Collison-induced rototranslational absorption spectra of H2-He pairs at temperatures from 40 to 3000 K. *ApJ*, 326:509–515.

Bowler, B. P., Liu, M. C., Dupuy, T. J., and Cushing, M. C. (2010). Near-infrared Spectroscopy of the Extrasolar Planet HR 8799 b. *ApJ*, 723:850–868.

Brewer, J. M., Fischer, D. A., and Madhusudhan, N. (2017). C/O and O/H Ratios Suggest Some Hot Jupiters Originate Beyond the Snow Line. *AJ*, 153:83.

Brooke, T. Y., Knacke, R. F., Encrenaz, T., Drossart, P., Crisp, D., and Feuchtgruber, H. (1998). Models of the ISO 3-μm Reflection Spectrum of Jupiter. *Icarus*, 136:1–13.

Brown, T. M. (2001). Transmission Spectra as Diagnostics of Extrasolar Giant Planet Atmospheres. *ApJ*, 553:1006–1026.

Brucalassi, A., Pasquini, L., Saglia, R., Ruiz, M. T., Bonifacio, P., Leão, I., Canto Martins, B. L., de Medeiros, J. R., Bedin, L. R., Biazzo, K., Melo, C., Lovis, C., and Randich, S. (2016). Search for giant planets in M67. III. Excess of hot Jupiters in dense open clusters. *A&A*, 592:L1.

Buchner, J., Georgakakis, A., Nandra, K., Hsu, L., Rangel, C., Brightman, M., Merloni, A., Salvato, M., Donley, J., and Kocevski, D. (2014). X-ray spectral modelling of the AGN obscuring region in the CDFS: Bayesian model selection and catalogue. *A&A*, 564:A125.

Budaj, J., Kocifaj, M., Salmeron, R., and Hubeny, I. (2015). Tables of phase functions, opacities, albedos, equilibrium temperatures, and radiative accelerations of dust grains in exoplanets. *MNRAS*, 454:2–27.

Burningham, B., Marley, M. S., Line, M. R., Lupu, R., Visscher, C., Morley, C. V., Saumon, D., and Freedman, R. (2017). Retrieval of atmospheric properties of cloudy L dwarfs. *MNRAS*, 470:1177–1197.

Burrows, A., Budaj, J., and Hubeny, I. (2008). Theoretical Spectra and Light Curves of Close-in Extrasolar Giant Planets and Comparison with Data. *ApJ*, 678:1436–1457.

Burrows, A., Marley, M., Hubbard, W. B., Lunine, J. I., Guillot, T., Saumon, D., Freedman, R., Sudarsky, D., and Sharp, C. (1997). A Nongray Theory of Extrasolar Giant Planets and Brown Dwarfs. *ApJ*, 491:856–875.

Burrows, A. and Sharp, C. M. (1999). Chemical Equilibrium Abundances in Brown Dwarf and Extrasolar Giant Planet Atmospheres. *ApJ*, 512:843–863.

Butler, R. P., Marcy, G. W., Fischer, D. A., Brown, T. M., Contos, A. R., Korzennik, S. G., Nisenson, P., and Noyes, R. W. (1999). Evidence for Multiple Companions to Upsilon Andromedae. *ApJ*, 526:916–927.

Şenavci, H. V., Bahar, E., Montes, D., Zola, S., Hussain, G. A. J., Frasca, A., Işık, E., and Yörükoğlu, O. (2018). Star-spot distributions and chromospheric activity on the RS CVn type eclipsing binary SV Cam. *MNRAS*, 479:875–889.

Cabrera, J., Csizmadia, S., Lehmann, H., Dvorak, R., Gandolfi, D., Rauer, H., Erikson, A., Dreyer, C., Eigmüller, P., and Hatzes, A. (2014). The Planetary System to KIC 11442793: A Compact Analogue to the Solar System. *ApJ*, 781:18.

Campbell, B., Walker, G. A. H., and Yang, S. (1988). A search for substellar companions to solar-type stars. *ApJ*, 331:902–921.

Carlson, B. E., Lacis, A. A., and Rossow, W. B. (1994). Belt-zone variations in the Jovian cloud structure. *J. Geophys. Res.*, 99:14.

Cassan, A., Kubas, D., Beaulieu, J.-P., Dominik, M., Horne, K., Greenhill, J., Wambsganss, J., Menzies, J., Williams, A., Jørgensen, U. G., Udalski, A., Bennett, D. P., Albrow, M. D., Batista, V., Brillant, S., Caldwell, J. A. R., Cole, A., Coutures, C., Cook, K. H., Dieters, S., Dominis Prester, D., Donatowicz, J., Fouqué, P., Hill, K., Kains, N., Kane, S., Marquette, J.-B., Martin, R., Pollard, K. R., Sahu, K. C., Vinter, C., Warren, D., Watson, B., Zub, M., Sumi, T., Szymański, M. K., Kubiak, M., Poleski, R., Soszynski, I., Ulaczyk, K., Pietrzyński, G., and Wyrzykowski, Ł. (2012). One or more bound planets per Milky Way star from microlensing observations. *Nature*, 481:167–169.

Chabrier, G., Baraffe, I., Leconte, J., Gallardo, J., and Barman, T. (2009). The mass-radius relationship from solar-type stars to terrestrial planets: a review. In Stempels, E., editor, *15th Cambridge Workshop on Cool Stars, Stellar Systems, and the Sun*, volume 1094 of *American Institute of Physics Conference Series*, pages 102–111.

Chapman, G. A. (1987). Solar variability due to sunspots and faculae. *J. Geophys. Res.*, 92:809–812.

Charbonneau, D., Brown, T. M., Latham, D. W., and Mayor, M. (2000). Detection of Planetary Transits Across a Sun-like Star. *ApJ*, 529:L45–L48.

Charbonneau, D., Brown, T. M., Noyes, R. W., and Gilliland, R. L. (2002). Detection of an Extrasolar Planet Atmosphere. *ApJ*, 568:377–384.

Chyba, C. F., Thomas, P. J., Brookshaw, L., and Sagan, C. (1990). Cometary Delivery of Organic Molecules to the Early Earth. *Science*, 249:366–373.

Chyba, C. F., Thomas, P. J., and Zahnle, K. J. (1993). The 1908 Tunguska explosion - Atmospheric disruption of a stony asteroid. *Nature*, 361:40–44.

Chylek, P., Grams, G. W., and Pinnick, R. G. (1976). Light scattering by irregular randomly oriented particles. *Science*, 193:480–482.

Ciceri, S., Mancini, L., Southworth, J., Bruni, I., Nikolov, N., D'Ago, G., Schröder, T., Bozza, V., Tregloan-Reed, J., and Henning, T. (2015). Physical properties of the HAT-P-23 and WASP-48 planetary systems from multi-colour photometry. *A&A*, 577:A54.

Clampin, M. (2009). Comparative Planetology: Transiting Exoplanet Science with JWST. In *astro2010: The Astronomy and Astrophysics Decadal Survey*, volume 2010 of *Astronomy*.

Close, L. (2010). Extrasolar planets: A giant surprise. *Nature*, 468:1048–1049.

Crampton, D., Simard, L., and Silva, D. (2009). TMT Science and Instruments. *Astrophysics and Space Science Proceedings*, 9:279.

Cridland, A. J., Pudritz, R. E., and Alessi, M. (2016). Composition of early planetary atmospheres - I. Connecting disc astrochemistry to the formation of planetary atmospheres. *MNRAS*, 461:3274–3295.

Curiel, S., Cantó, J., Georgiev, L., Chávez, C. E., and Poveda, A. (2011). A fourth planet orbiting Upsilon Andromedae. *A&A*, 525:A78.

Currie, T. (2016). HR 8799: The Benchmark Directly-Imaged Planetary System. *ArXiv e-prints*.

Dalcanton, J., Seager, S., Aigrain, S., Battel, S., Brandt, N., Conroy, C., Feinberg, L., Gezari, S., Guyon, O., Harris, W., Hirata, C., Mather, J., Postman, M., Redding, D., Schiminovich, D., Stahl, H. P., and Tumlinson, J. (2015). From Cosmic Birth to Living Earths: The Future of UVOIR Space Astronomy. *ArXiv e-prints*.

de Wit, J., Gillon, M., Demory, B.-O., and Seager, S. (2012). Towards consistent mapping of distant worlds: secondary-eclipse scanning of the exoplanet HD 189733b. *A&A*, 548:A128.

de Wit, J. and Seager, S. (2013). Constraining Exoplanet Mass from Transmission Spectroscopy. *Science*, 342:1473–1477.

de Wit, J., Wakeford, H. R., Gillon, M., Lewis, N. K., Valenti, J. A., Demory, B.-O., Burgasser, A. J., Burdanov, A., Delrez, L., Jehin, E., Lederer, S. M., Queloz, D., Triaud, A. H. M. J., and Van Grootel, V. (2016). A combined transmission spectrum of the Earth-sized exoplanets TRAPPIST-1 b and c. *Nature*, 537:69–72.

de Wit, J., Wakeford, H. R., Lewis, N. K., Delrez, L., Gillon, M., Selsis, F., Leconte, J., Demory, B.-O., Bolmont, E., Bourrier, V., Burgasser, A. J., Grimm, S., Jehin, E., Lederer, S. M., Owen, J. E., Stamenković, V., and Triaud, A. H. M. J. (2018). Atmospheric reconnaissance of the habitable-zone Earth-sized planets orbiting TRAPPIST-1. *Nature Astronomy*, 2:214–219.

Deirmendjian, D. (1964). Scattering and polarization properties of water clouds and hazes in the visible and infrared. *Appl. Opt.*, 3:187.

Deirmendjian, D. (1969). *Electromagnetic scattering on spherical polydispersions.* Elsevier.

Deming, D., Harrington, J., Laughlin, G., Seager, S., Navarro, S. B., Bowman, W. C., and Horning, K. (2007). Spitzer Transit and Secondary Eclipse Photometry of GJ 436b. *ApJ*, 667:L199–L202.

Deming, D., Seager, S., Richardson, L. J., and Harrington, J. (2005). Infrared radiation from an extrasolar planet. *Nature*, 434:740–743.

Deming, D., Wilkins, A., McCullough, P., Burrows, A., Fortney, J. J., Agol, E., Dobbs-Dixon, I., Madhusudhan, N., Crouzet, N., Desert, J.-M., Gilliland, R. L., Haynes, K., Knutson, H. A., Line, M., Magic, Z., Mandell, A. M., Ranjan, S., Charbonneau, D., Clampin, M., Seager, S., and Showman, A. P. (2013). Infrared Transmission Spectroscopy of the Exoplanets HD 209458b and XO-1b Using the Wide Field Camera-3 on the Hubble Space Telescope. *ApJ*, 774:95.

Demory, B.-O., Gillon, M., de Wit, J., Madhusudhan, N., Bolmont, E., Heng, K., Kataria, T., Lewis, N., Hu, R., Krick, J., Stamenković, V., Benneke, B., Kane, S., and Queloz, D. (2016). A map of the large day-night temperature gradient of a super-Earth exoplanet. *Nature*, 532:207–209.

Dittmann, J. A., Irwin, J. M., Charbonneau, D., Berta-Thompson, Z. K., and Newton, E. R. (2017). A Search for Additional Bodies in the GJ 1132 Planetary System from 21 Ground-based Transits and a 100-hr Spitzer Campaign. *AJ*, 154:142.

Dobbs-Dixon, I. and Agol, E. (2013). Three-dimensional radiative-hydrodynamical simulations of the highly irradiated short-period exoplanet HD 189733b. *MNRAS*, 435:3159–3168.

Dobbs-Dixon, I. and Lin, D. N. C. (2008). Atmospheric Dynamics of Short-Period Extrasolar Gas Giant Planets. I. Dependence of Nightside Temperature on Opacity. *ApJ*, 673:513–525.

Dodson-Robinson, S. E., Veras, D., Ford, E. B., and Beichman, C. A. (2009). The Formation Mechanism of Gas Giants on Wide Orbits. *ApJ*, 707:79–88.

Donati, J.-F., Semel, M., Carter, B. D., Rees, D. E., and Collier Cameron, A. (1997). Spectropolarimetric observations of active stars. *MNRAS*, 291:658.

Durisen, R. H., Hartquist, T. W., and Pickett, M. K. (2008). The formation of fragments at corotation in isothermal protoplanetary disks. *Ap&SS*, 317:3–8.

Ehrenreich, D., Bonfils, X., Lovis, C., Delfosse, X., Forveille, T., Mayor, M., Neves, V., Santos, N. C., Udry, S., and Ségransan, D. (2014). Near-infrared transmission spectrum of the warm-Uranus GJ 3470b with the Wide Field Camera-3 on the Hubble Space Telescope. *A&A*, 570:A89.

Eistrup, C., Walsh, C., and van Dishoeck, E. F. (2018). Molecular abundances and C/O ratios in chemically evolving planet-forming disk midplanes. *A&A*, 613:A14.

Evans, T. M., Sing, D. K., Kataria, T., Goyal, J., Nikolov, N., Wakeford, H. R., Deming, D., Marley, M. S., Amundsen, D. S., Ballester, G. E., Barstow, J. K., Ben-Jaffel, L., Bourrier, V., Buchhave, L. A., Cohen, O., Ehrenreich, D., García Muñoz, A., Henry, G. W., Knutson, H., Lavvas, P., Lecavelier Des Etangs, A., Lewis, N. K., López-Morales, M., Mandell, A. M., Sanz-Forcada, J., Tremblin, P., and Lupu, R. (2017). An ultrahot gas-giant exoplanet with a stratosphere. *Nature*, 548:58–61.

Fabrycky, D. C. and Murray-Clay, R. A. (2010). Stability of the Directly Imaged Multiplanet System HR 8799: Resonance and Masses. *ApJ*, 710:1408–1421.

Fares, R., Bourrier, V., Vidotto, A. A., Moutou, C., Jardine, M. M., Zarka, P., Helling, C., Lecavelier des Etangs, A., Llama, J., Louden, T., Wheatley, P. J., and Ehrenreich, D. (2017). MOVES - I. The evolving magnetic field of the planet-hosting star HD189733. *MNRAS*, 471:1246–1257.

Feroz, F. and Hobson, M. P. (2008). Multimodal nested sampling: an efficient and robust alternative to Markov Chain Monte Carlo methods for astronomical data analyses. *MNRAS*, 384:449–463.

Feroz, F., Hobson, M. P., and Bridges, M. (2009). MULTINEST: an efficient and robust Bayesian inference tool for cosmology and particle physics. *MNRAS*, 398:1601–1614.

Feroz, F., Hobson, M. P., Cameron, E., and Pettitt, A. N. (2013). Importance Nested Sampling and the MultiNest Algorithm. *ArXiv e-prints*.

Field, G. B. and Ferrara, A. (1995). The behavior of fragments of comet Shoemaker-Levy 9 in the atmosphere of Jupiter. *ApJ*, 438:957–967.

Fischer, D. A., Marcy, G. W., Butler, R. P., Vogt, S. S., Laughlin, G., Henry, G. W., Abouav, D., Peek, K. M. G., Wright, J. T., Johnson, J. A., McCarthy, C., and Isaacson, H. (2008). Five Planets Orbiting 55 Cancri. *ApJ*, 675:790–801.

Fischer, P. D., Knutson, H. A., Sing, D. K., Henry, G. W., Williamson, M. W., Fortney, J. J., Burrows, A. S., Kataria, T., Nikolov, N., Showman, A. P., Ballester, G. E., Désert, J.-M., Aigrain, S., Deming, D., Lecavelier des Etangs, A., and Vidal-Madjar, A. (2016). HST Hot-Jupiter Transmission Spectral Survey: Clear Skies for Cool Saturn WASP-39b. *ApJ*, 827:19.

Fortney, J. J. (2005). The effect of condensates on the characterization of transiting planet atmospheres with transmission spectroscopy. *MNRAS*, 364:649–653.

Fortney, J. J., Lodders, K., Marley, M. S., and Freedman, R. S. (2008). A Unified Theory for the Atmospheres of the Hot and Very Hot Jupiters: Two Classes of Irradiated Atmospheres. *ApJ*, 678:1419–1435.

Fortney, J. J., Shabram, M., Showman, A. P., Lian, Y., Freedman, R. S., Marley, M. S., and Lewis, N. K. (2010). Transmission Spectra of Three-Dimensional Hot Jupiter Model Atmospheres. *ApJ*, 709:1396–1406.

French, M., Becker, A., Lorenzen, W., Nettelmann, N., Bethkenhagen, M., Wicht, J., and Redmer, R. (2012). Ab Initio Simulations for Material Properties along the Jupiter Adiabat. *ApJS*, 202:5.

Gandhi, S. and Madhusudhan, N. (2017). GENESIS: new self-consistent models of exoplanetary spectra. *MNRAS*, 472:2334–2355.

Gandhi, S. and Madhusudhan, N. (2018). Retrieval of exoplanet emission spectra with HyDRA. *MNRAS*, 474:271–288.

Geballe, T. R., Kulkarni, S. R., Woodward, C. E., and Sloan, G. C. (1996). The Near-Infrared Spectrum of the Brown Dwarf Gliese 229B. *ApJ*, 467:L101.

Gibson, N. P., de Mooij, E. J. W., Evans, T. M., Merritt, S., Nikolov, N., Sing, D. K., and Watson, C. (2018). Revisiting the potassium feature of WASP-31b at high-resolution. *ArXiv e-prints*.

Gibson, N. P., Pont, F., and Aigrain, S. (2011). A new look at NICMOS transmission spectroscopy of HD 189733, GJ-436 and XO-1: no conclusive evidence for molecular features. *MNRAS*, 411:2199–2213.

Giles, H. A. C., Collier Cameron, A., and Haywood, R. D. (2017). A Kepler study of starspot lifetimes with respect to light-curve amplitude and spectral type. *MNRAS*, 472:1618–1627.

Gillon et al., M. (2017). Seven temperate terrestrial planets around the nearby ultra-cool dwarf star TRAPPIST-1. *Nature*, 542:456–460.

Goldreich, P. and Tremaine, S. (1980). Disk-satellite interactions. *ApJ*, 241:425–441.

Goukenleuque, C., Bézard, B., Joguet, B., Lellouch, E., and Freedman, R. (2000). A Radiative Equilibrium Model of 51 Peg b. *Icarus*, 143:308–323.

Goyal, J. M., Mayne, N., Sing, D. K., Drummond, B., Tremblin, P., Amundsen, D. S., Evans, T., Carter, A. L., Spake, J., Baraffe, I., Nikolov, N., Manners, J., Chabrier, G., and Hebrard, E. (2018). A library of ATMO forward model transmission spectra for hot Jupiter exoplanets. *MNRAS*, 474:5158–5185.

Goździewski, K. and Migaszewski, C. (2009). Is the HR8799 extrasolar system destined for planetary scattering? *MNRAS*, 397:L16–L20.

Goździewski, K. and Migaszewski, C. (2014). Multiple mean motion resonances in the HR 8799 planetary system. *MNRAS*, 440:3140–3171.

Graaff, R., Aarnoudse, J. G., Zijp, J. R., Sloot, P. M. A., de Mul, F. F. M., Greve, J., and Koelink, M. H. (1992). Reduced light-scattering properties for mixtures of spherical particles: a simple approximation derived from Mie calculations. *Appl. Opt.*, 31:1370–1376.

Gray, R. O. and Kaye, A. B. (1999). HR 8799: A Link between γ Doradus Variables and λ Bootis Stars. *AJ*, 118:2993–2996.

Greene, T. P., Line, M. R., Montero, C., Fortney, J. J., Lustig-Yaeger, J., and Luther, K. (2016). Characterizing Transiting Exoplanet Atmospheres with JWST. *ApJ*, 817:17.

Griffith, C. A. (2014). Disentangling degenerate solutions from primary transit and secondary eclipse spectroscopy of exoplanets. *Philosophical Transactions of the Royal Society of London Series A*, 372:20130086–20130086.

Guyon, O., Pluzhnik, E. A., Kuchner, M. J., Collins, B., and Ridgway, S. T. (2006). Theoretical Limits on Extrasolar Terrestrial Planet Detection with Coronagraphs. *ApJS*, 167:81–99.

Hackman, T., Ilyin, I., Lehtinen, J. J., Kochukhov, O., Käpylä, M. J., Piskunov, N., and Willamo, T. (2018). Starspot activity of HD 199178 - Doppler images from 1994–2017. *arXiv e-prints*.

Haghighipour, N. and Boss, A. P. (2003). On Gas Drag-Induced Rapid Migration of Solids in a Nonuniform Solar Nebula. *ApJ*, 598:1301–1311.

Hanel, R. A., Conrath, B. J., Jennings, D. E., and Samuelson, R. E. (1992). *Exploration of the solar system by infrared remote sensing*.

Hanel, R. A., Conrath, B. J., Kunde, V. G., Prabhakara, C., Revah, I., Salomonson, V. V., and Wolford, G. (1972). The Nimbus 4 infrared spectroscopy experiment: 1. Calibrated thermal emission spectra. *J. Geophys. Res.*, 77:2629–2641.

Harrington, J., de Pater, I., Brecht, S. H., Deming, D., Meadows, V., Zahnle, K., and Nicholson, P. D. (2004). *Lessons from Shoemaker-Levy 9 about Jupiter and planetary impacts*, pages 159–184. Cambridge University Press.

Hathaway, D. H. (2015). The Solar Cycle. *Living Reviews in Solar Physics*, 12:4.

Hatzes, A. P. and Cochran, W. D. (1993). Long-period radial velocity variations in three K giants. *ApJ*, 413:339–348.

Hauschildt, P. H. and Baron, E. (1999). Numerical solution of the expanding stellar atmosphere problem. *Journal of Computational and Applied Mathematics*, 109:41–63.

Haynes, K., Mandell, A. M., Madhusudhan, N., Deming, D., and Knutson, H. (2015). Spectroscopic Evidence for a Temperature Inversion in the Dayside Atmosphere of Hot Jupiter WASP-33b. *ApJ*, 806:146.

Haywood, R. D., Collier Cameron, A., Queloz, D., Barros, S. C. C., Deleuil, M., Fares, R., Gillon, M., Lanza, A. F., Lovis, C., Moutou, C., Pepe, F., Pollacco, D., Santerne, A., Ségransan, D., and Unruh, Y. C. (2014). Planets and stellar activity: hide and seek in the CoRoT-7 system. *MNRAS*, 443:2517–2531.

Helled, R. and Bodenheimer, P. (2010). Metallicity of the massive protoplanets around HR 8799 If formed by gravitational instability. *Icarus*, 207:503–508.

Helling, C. (2018). Exoplanet Clouds. *arXiv e-prints*.

Helling, C., Dehn, M., Woitke, P., and Hauschildt, P. H. (2008a). Consistent Simulations of Substellar Atmospheres and Nonequilibrium Dust Cloud Formation. *ApJ*, 675:L105.

Helling, C., Gourbin, P., Woitke, P., and Parmentier, V. (2019). Sparkling nights and very hot days on WASP-18b: the formation of clouds and the emergence of an ionosphere. *arXiv e-prints*.

Helling, C., Lee, G., Dobbs-Dixon, I., Mayne, N., Amundsen, D. S., Khaimova, J., Unger, A. A., Manners, J., Acreman, D., and Smith, C. (2016). The mineral clouds on HD 209458b and HD 189733b. *MNRAS*, 460:855–883.

Helling, C. and Woitke, P. (2006). Dust in brown dwarfs. V. Growth and evaporation of dirty dust grains. *A&A*, 455:325–338.

Helling, C., Woitke, P., Rimmer, P. B., Kamp, I., Thi, W.-F., and Meijerink, R. (2014). Disk Evolution, Element Abundances and Cloud Properties of Young Gas Giant Planets. *Life*, 4.

Helling, C., Woitke, P., and Thi, W.-F. (2008b). Dust in brown dwarfs and extra-solar planets. I. Chemical composition and spectral appearance of quasi-static cloud layers. *A&A*, 485:547–560.

Heng, K. (2016). A Cloudiness Index for Transiting Exoplanets Based on the Sodium and Potassium Lines: Tentative Evidence for Hotter Atmospheres Being Less Cloudy at Visible Wavelengths. *ApJ*, 826:L16.

Heng, K. and Kitzmann, D. (2017). The theory of transmission spectra revisited: a semi-analytical method for interpreting WFC3 data and an unresolved challenge. *MNRAS*, 470:2972–2981.

Heng, K. and Lyons, J. R. (2016). Carbon Dioxide in Exoplanetary Atmospheres: Rarely Dominant Compared to Carbon Monoxide and Water in Hot, Hydrogen-dominated Atmospheres. *ApJ*, 817:149.

Heng, K. and Marley, M. S. (2017). *Radiative Transfer for Exoplanet Atmospheres*, page 102.

Heng, K. and Tsai, S.-M. (2016). Analytical Models of Exoplanetary Atmospheres. III. Gaseous C-H-O-N Chemistry with Nine Molecules. *ApJ*, 829:104.

Henry, G. W., Marcy, G., Butler, R. P., and Vogt, S. S. (1999). HD 209458. *IAU Circ.*, 7307.

Henry, G. W., Marcy, G. W., Butler, R. P., and Vogt, S. S. (2000). A Transiting "51 Peg-like" Planet. *ApJ*, 529:L41–L44.

Hill, J. M., Green, R. F., Ashby, D. S., Brynnel, J. G., Cushing, N. J., Little, J., Slagle, J. H., and Wagner, R. M. (2010). The Large Binocular Telescope. In *Ground-based and Airborne Telescopes III*, volume 7733 of *Proc. SPIE*, page 77330C.

Hinz, P. M., Rodigas, T. J., Kenworthy, M. A., Sivanandam, S., Heinze, A. N., Mamajek, E. E., and Meyer, M. R. (2010). Thermal Infrared MMTAO Observations of the HR 8799 Planetary System. *ApJ*, 716:417–426.

Houghton, J. T., Taylor, F. W., and Rodgers, C. D. (1984). *Remote sounding of atmospheres*.

Hubbard, W. B., Fortney, J. J., Lunine, J. I., Burrows, A., Sudarsky, D., and Pinto, P. (2001). Theory of Extrasolar Giant Planet Transits. *ApJ*, 560:413–419.

Hubeny, I., Burrows, A., and Sudarsky, D. (2003). A Possible Bifurcation in Atmospheres of Strongly Irradiated Stars and Planets. *ApJ*, 594:1011–1018.

Huitson, C. M., Sing, D. K., Pont, F., Fortney, J. J., Burrows, A. S., Wilson, P. A., Ballester, G. E., Nikolov, N., Gibson, N. P., Deming, D., Aigrain, S., Evans, T. M., Henry, G. W., Lecavelier des Etangs, A., Showman, A. P., Vidal-Madjar, A., and Zahnle, K. (2013). An HST optical-to-near-IR transmission spectrum of the hot Jupiter WASP-19b: detection of atmospheric water and likely absence of TiO. *MNRAS*, 434:3252–3274.

Huitson, C. M., Sing, D. K., Vidal-Madjar, A., Ballester, G. E., Lecavelier des Etangs, A., Désert, J.-M., and Pont, F. (2012). Temperature-pressure profile of the hot Jupiter HD 189733b from HST sodium observations: detection of upper atmospheric heating. *MNRAS*, 422:2477–2488.

Husser, T.-O., Wende-von Berg, S., Dreizler, S., Homeier, D., Reiners, A., Barman, T., and Hauschildt, P. H. (2013). A new extensive library of PHOENIX stellar atmospheres and synthetic spectra. *A&A*, 553:A6.

Ilee, J. D., Forgan, D. H., Evans, M. G., Hall, C., Booth, R., Clarke, C. J., Rice, W. K. M., Boley, A. C., Caselli, P., Hartquist, T. W., and Rawlings, J. M. C. (2017). The chemistry of protoplanetary fragments formed via gravitational instabilities. *MNRAS*, 472:189–204.

Irwin, P. G. J., Teanby, N. A., de Kok, R., Fletcher, L. N., Howett, C. J. A., Tsang, C. C. C., Wilson, C. F., Calcutt, S. B., Nixon, C. A., and Parrish, P. D. (2008). The NEMESIS planetary atmosphere radiative transfer and retrieval tool. *J. Quant. Spec. Radiat. Transf.*, 109:1136–1150.

Jackson, R. J. and Jeffries, R. D. (2013). On the relationship between the size and surface coverage of starspots on magnetically active low-mass stars. *MNRAS*, 431:1883–1890.

Janson, M., Brandt, T. D., Kuzuhara, M., Spiegel, D. S., Thalmann, C., Currie, T., Bonnefoy, M., Zimmerman, N., Sorahana, S., Kotani, T., Schlieder, J., Hashimoto, J., Kudo, T., Kusakabe, N., Abe, L., Brandner, W., Carson, J. C., Egner, S., Feldt, M., Goto, M., Grady, C. A., Guyon, O., Hayano, Y., Hayashi, M., Hayashi, S., Henning, T., Hodapp, K. W., Ishii, M., Iye, M., Kandori, R., Knapp, G. R., Kwon, J., Matsuo, T., McElwain, M. W., Mede, K., Miyama, S., Morino, J.-I., Moro-Martín, A., Nakagawa, T., Nishimura, T., Pyo, T.-S., Serabyn, E., Suenaga, T., Suto, H., Suzuki, R., Takahashi, Y., Takami, M., Takato, N., Terada, H., Tomono, D., Turner, E. L., Watanabe, M., Wisniewski, J., Yamada, T., Takami, H., Usuda, T., and Tamura, M. (2013). Direct Imaging Detection of Methane in the Atmosphere of GJ 504 b. *ApJ*, 778:L4.

Janson, M., Carson, J., Thalmann, C., McElwain, M. W., Goto, M., Crepp, J., Wisniewski, J., Abe, L., Brandner, W., Burrows, A., Egner, S., Feldt, M., Grady, C. A., Golota, T., Guyon, O., Hashimoto, J., Hayano, Y., Hayashi, M., Hayashi, S., Henning, T., Hodapp, K. W., Ishii, M., Iye, M., Kandori, R., Knapp, G. R., Kudo, T., Kusakabe, N., Kuzuhara, M., Matsuo, T., Mayama, S., Miyama, S., Morino, J.-I., Moro-Martín, A., Nishimura, T., Pyo, T.-S., Serabyn, E., Suto, H., Suzuki, R., Takami, M., Takato, N., Terada, H., Tofflemire, B., Tomono, D., Turner, E. L., Watanabe, M., Yamada, T., Takami, H., Usuda, T., and Tamura, M. (2011). Near-infrared Multi-band Photometry of the Substellar Companion GJ 758 B. *ApJ*, 728:85.

Johns, M. (2008). The Giant Magellan Telescope (GMT). In *Extremely Large Telescopes: Which Wavelengths? Retirement Symposium for Arne Ardeberg*, volume 6986 of *Proc. SPIE*, page 698603.

Kalas, P., Graham, J. R., Chiang, E., Fitzgerald, M. P., Clampin, M., Kite, E. S., Stapelfeldt, K., Marois, C., and Krist, J. (2008). Optical Images of an Exosolar Planet 25 Light-Years from Earth. *Science*, 322:1345.

Kasper, M., Beuzit, J.-L., Verinaud, C., Gratton, R. G., Kerber, F., Yaitskova, N., Boccaletti, A., Thatte, N., Schmid, H. M., Keller, C., Baudoz, P., Abe, L., Aller-Carpentier, E., Antichi, J., Bonavita, M., Dohlen, K., Fedrigo, E., Hanenburg, H., Hubin, N., Jager, R., Korkiakoski, V., Martinez, P., Mesa, D., Preis, O., Rabou, P., Roelfsema, R., Salter, G., Tecza, M., and Venema, L. (2010). EPICS: direct imaging of exoplanets with the E-ELT. In *Ground-based and Airborne Instrumentation for Astronomy III*, volume 7735 of *Proc. SPIE*, pages 77352E–77352E–9.

Kass, R. E. and Raftery, A. E. (1995). Bayes Factors. *Journal of the American Statistical Association*, 90:773.

Kővári, Z., Korhonen, H., Strassmeier, K. G., Weber, M., Kriskovics, L., and Savanov, I. (2013). Doppler imaging of stellar surface structure. XXIV. The lithium-rich single K-giants DP Canum Venaticorum and DI Piscium. *A&A*, 551:A2.

Knutson, H. A., Benneke, B., Deming, D., and Homeier, D. (2014a). A featureless transmission spectrum for the Neptune-mass exoplanet GJ436b. *Nature*, 505:66–68.

Knutson, H. A., Benneke, B., Deming, D., and Homeier, D. (2014b). A featureless transmission spectrum for the Neptune-mass exoplanet GJ436b. *Nature*, 505:66–68.

Knutson, H. A., Charbonneau, D., Allen, L. E., Fortney, J. J., Agol, E., Cowan, N. B., Showman, A. P., Cooper, C. S., and Megeath, S. T. (2007). A map of the day-night contrast of the extrasolar planet HD 189733b. *Nature*, 447:183–186.

Knutson, H. A., Dragomir, D., Kreidberg, L., Kempton, E. M.-R., McCullough, P. R., Fortney, J. J., Bean, J. L., Gillon, M., Homeier, D., and Howard, A. W. (2014c). Hubble Space Telescope Near-IR Transmission Spectroscopy of the Super-Earth HD 97658b. *ApJ*, 794:155.

Knutson, H. A., Howard, A. W., and Isaacson, H. (2010). A Correlation Between Stellar Activity and Hot Jupiter Emission Spectra. *ApJ*, 720:1569–1576.

Konopacky, Q. M., Barman, T. S., Macintosh, B. A., and Marois, C. (2013). Detection of Carbon Monoxide and Water Absorption Lines in an Exoplanet Atmosphere. *Science*, 339:1398–1401.

Korycansky, D. G., Harrington, J., Deming, D., and Kulick, M. E. (2006). Shoemaker-Levy 9 Impact Modeling. I. High-Resolution Three-dimensional Bolides. *ApJ*, 646:642–652.

Korycansky, D. G. and Zahnle, K. J. (2005). Modeling crater populations on Venus and Titan. *Planet. Space Sci.*, 53:695–710.

Korycansky, D. G., Zahnle, K. J., and Law, M.-M. M. (2000). High-Resolution Calculations of Asteroid Impacts into the Venusian Atmosphere. *Icarus*, 146:387–403.

Kreidberg, L., Bean, J. L., Désert, J.-M., Benneke, B., Deming, D., Stevenson, K. B., Seager, S., Berta-Thompson, Z., Seifahrt, A., and Homeier, D. (2014a). Clouds in the atmosphere of the super-Earth exoplanet GJ1214b. *Nature*, 505:69–72.

Kreidberg, L., Bean, J. L., Désert, J.-M., Benneke, B., Deming, D., Stevenson, K. B., Seager, S., Berta-Thompson, Z., Seifahrt, A., and Homeier, D. (2014b). Clouds in the atmosphere of the super-Earth exoplanet GJ1214b. *Nature*, 505:69–72.

Kreidberg, L., Bean, J. L., Désert, J.-M., Line, M. R., Fortney, J. J., Madhusudhan, N., Stevenson, K. B., Showman, A. P., Charbonneau, D., McCullough, P. R., Seager, S., Burrows, A., Henry, G. W., Williamson, M., Kataria, T., and Homeier, D. (2014c). A Precise Water Abundance Measurement for the Hot Jupiter WASP-43b. *ApJ*, 793:L27.

Kreidberg, L., Bean, J. L., Désert, J.-M., Line, M. R., Fortney, J. J., Madhusudhan, N., Stevenson, K. B., Showman, A. P., Charbonneau, D., McCullough, P. R., Seager, S., Burrows, A., Henry, G. W., Williamson, M., Kataria, T., and Homeier, D. (2014d). A Precise Water Abundance Measurement for the Hot Jupiter WASP-43b. *ApJ*, 793:L27.

Kreidberg, L., Line, M. R., Bean, J. L., Stevenson, K. B., Désert, J.-M., Madhusudhan, N., Fortney, J. J., Barstow, J. K., Henry, G. W., Williamson, M. H., and Showman, A. P. (2015). A Detection of Water in the Transmission Spectrum of the Hot Jupiter WASP-12b and Implications for Its Atmospheric Composition. *ApJ*, 814:66.

Lagrange, A.-M. (2014). Direct imaging of exoplanets. *Philosophical Transactions of the Royal Society of London Series A*, 372:20130090–20130090.

Lagrange, A.-M., Gratadour, D., Chauvin, G., Fusco, T., Ehrenreich, D., Mouillet, D., Rousset, G., Rouan, D., Allard, F., Gendron, É., Charton, J., Mugnier, L., Rabou, P., Montri, J., and Lacombe, F. (2009). A probable giant planet imaged in the β Pictoris disk. VLT/NaCo deep L'-band imaging. *A&A*, 493:L21–L25.

Lammer, H. and Blanc, M. (2018). From Disks to Planets: The Making of Planets and Their Early Atmospheres. An Introduction. *Space Sci. Rev.*, 214:60.

Latham, D. W., Mazeh, T., Stefanik, R. P., Mayor, M., and Burki, G. (1989). The unseen companion of HD114762 - A probable brown dwarf. *Nature*, 339:38–40.

Lavie, B., Mendonça, J. M., Mordasini, C., Malik, M., Bonnefoy, M., Demory, B.-O., Oreshenko, M., Grimm, S. L., Ehrenreich, D., and Heng, K. (2017). HELIOS-RETRIEVAL: An Open-source, Nested Sampling Atmospheric Retrieval Code; Application to the HR 8799 Exoplanets and Inferred Constraints for Planet Formation. *AJ*, 154:91.

Lecavelier Des Etangs, A., Pont, F., Vidal-Madjar, A., and Sing, D. (2008). Rayleigh scattering in the transit spectrum of HD 189733b. *A&A*, 481:L83–L86.

Lee, G., Dobbs-Dixon, I., Helling, C., Bognar, K., and Woitke, P. (2016). Dynamic mineral clouds on HD 189733b. I. 3D RHD with kinetic, non-equilibrium cloud formation. *A&A*, 594:A48.

Lee, J.-M., Fletcher, L. N., and Irwin, P. G. J. (2012). Optimal estimation retrievals of the atmospheric structure and composition of HD 189733b from secondary eclipse spectroscopy. *MNRAS*, 420:170–182.

Lew, B. W. P., Apai, D., Zhou, Y., Schneider, G., Burgasser, A. J., Karalidi, T., Yang, H., Marley, M. S., Cowan, N. B., Bedin, L. R., Metchev, S. A., Radigan, J., and Lowrance, P. J. (2016). Cloud Atlas: Discovery of Patchy Clouds and High-amplitude Rotational Modulations in a Young, Extremely Red L-type Brown Dwarf. *ApJ*, 829:L32.

Liang, M.-C., Seager, S., Parkinson, C. D., Lee, A. Y.-T., and Yung, Y. L. (2004). On the Insignificance of Photochemical Hydrocarbon Aerosols in the Atmospheres of Close-in Extrasolar Giant Planets. *ApJ*, 605:L61–L64.

Line, M. R., Knutson, H., Wolf, A. S., and Yung, Y. L. (2014). A Systematic Retrieval Analysis of Secondary Eclipse Spectra. II. A Uniform Analysis of Nine Planets and their C to O Ratios. *ApJ*, 783:70.

Line, M. R., Marley, M. S., Liu, M. C., Burningham, B., Morley, C. V., Hinkel, N. R., Teske, J., Fortney, J. J., Freedman, R., and Lupu, R. (2017). Uniform Atmospheric Retrieval Analysis of Ultracool Dwarfs. II. Properties of 11 T dwarfs. *ApJ*, 848:83.

Line, M. R. and Parmentier, V. (2016). The Influence of Nonuniform Cloud Cover on Transit Transmission Spectra. *ApJ*, 820:78.

Line, M. R., Teske, J., Burningham, B., Fortney, J. J., and Marley, M. S. (2015). Uniform Atmospheric Retrieval Analysis of Ultracool Dwarfs. I. Characterizing Benchmarks, Gl 570D and HD 3651B. *ApJ*, 807:183.

Line, M. R., Wolf, A. S., Zhang, X., Knutson, H., Kammer, J. A., Ellison, E., Deroo, P., Crisp, D., and Yung, Y. L. (2013). A Systematic Retrieval Analysis of Secondary Eclipse Spectra. I. A Comparison of Atmospheric Retrieval Techniques. *ApJ*, 775:137.

Lines, S., Mayne, N. J., Boutle, I. A., Manners, J., Lee, G. K. H., Helling, C., Drummond, B., Amundsen, D. S., Goyal, J., Acreman, D. M., Tremblin, P., and Kerslake, M. (2018). Simulating the cloudy atmospheres of HD 209458 b and HD 189733 b with the 3D Met Office Unified Model. *A&A*, 615:A97.

Linsky, J. L., Yang, H., France, K., Froning, C. S., Green, J. C., Stocke, J. T., and Osterman, S. N. (2010). Observations of Mass Loss from the Transiting Exoplanet HD 209458b. *ApJ*, 717:1291–1299.

Lockwood, G. W., Skiff, B. A., Henry, G. W., Henry, S., Radick, R. R., Baliunas, S. L., Donahue, R. A., and Soon, W. (2007). Patterns of Photometric and Chromospheric Variation among Sun-like Stars: A 20 Year Perspective. *ApJS*, 171:260–303.

Lodders, K. and Fegley, B. (2002). Atmospheric Chemistry in Giant Planets, Brown Dwarfs, and Low-Mass Dwarf Stars. I. Carbon, Nitrogen, and Oxygen. *Icarus*, 155:393–424.

Lovis, C., Ségransan, D., Mayor, M., Udry, S., Benz, W., Bertaux, J.-L., Bouchy, F., Correia, A. C. M., Laskar, J., Lo Curto, G., Mordasini, C., Pepe, F., Queloz, D., and Santos, N. C. (2011). The HARPS search for southern extra-solar planets. XXVIII. Up to seven planets orbiting HD 10180: probing the architecture of low-mass planetary systems. *A&A*, 528:A112.

Lyot, B. (1939). The study of the solar corona and prominences without eclipses (George Darwin Lecture, 1939). *MNRAS*, 99:580.

Mac Low, M.-M. and Zahnle, K. (1994). Explosion of comet Shoemaker-Levy 9 on entry into the Jovian atmosphere. *ApJ*, 434:L33–L36.

MacDonald, R. J. and Madhusudhan, N. (2017a). Signatures of Nitrogen Chemistry in Hot Jupiter Atmospheres. *ApJ*, 850:L15.

MacDonald, R. J. and Madhusudhan, N. (2017b). Signatures of Nitrogen Chemistry in Hot Jupiter Atmospheres. *ApJ*, 850:L15.

Machalek, P., McCullough, P. R., Burke, C. J., Valenti, J. A., Burrows, A., and Hora, J. L. (2008). Thermal Emission of Exoplanet XO-1b. *ApJ*, 684:1427–1432.

Macintosh, B., Graham, J. R., Barman, T., De Rosa, R. J., Konopacky, Q., Marley, M. S., Marois, C., Nielsen, E. L., Pueyo, L., Rajan, A., Rameau, J., Saumon, D., Wang, J. J., Patience, J., Ammons, M., Arriaga, P., Artigau, E., Beckwith, S., Brewster, J., Bruzzone, S., Bulger, J., Burningham, B., Burrows, A. S., Chen, C., Chiang, E., Chilcote, J. K., Dawson, R. I., Dong, R., Doyon, R., Draper, Z. H., Duchêne, G., Esposito, T. M., Fabrycky, D., Fitzgerald, M. P., Follette, K. B., Fortney, J. J., Gerard, B., Goodsell, S., Greenbaum, A. Z., Hibon, P., Hinkley, S., Cotten, T. H., Hung, L.-W., Ingraham, P., Johnson-Groh, M., Kalas, P., Lafreniere, D., Larkin, J. E., Lee, J., Line, M., Long, D., Maire, J., Marchis, F., Matthews, B. C., Max, C. E., Metchev, S., Millar-Blanchaer, M. A., Mittal, T., Morley, C. V.,

Morzinski, K. M., Murray-Clay, R., Oppenheimer, R., Palmer, D. W., Patel, R., Perrin, M. D., Poyneer, L. A., Rafikov, R. R., Rantakyrö, F. T., Rice, E. L., Rojo, P., Rudy, A. R., Ruffio, J.-B., Ruiz, M. T., Sadakuni, N., Saddlemyer, L., Salama, M., Savransky, D., Schneider, A. C., Sivaramakrishnan, A., Song, I., Soummer, R., Thomas, S., Vasisht, G., Wallace, J. K., Ward-Duong, K., Wiktorowicz, S. J., Wolff, S. G., and Zuckerman, B. (2015). Discovery and spectroscopy of the young jovian planet 51 Eri b with the Gemini Planet Imager. *Science*, 350:64–67.

Madhusudhan, N. (2012). C/O Ratio as a Dimension for Characterizing Exoplanetary Atmospheres. *ApJ*, 758:36.

Madhusudhan, N. (2018). Atmospheric Retrieval of Exoplanets. *ArXiv e-prints*.

Madhusudhan, N., Agúndez, M., Moses, J. I., and Hu, Y. (2016a). Exoplanetary Atmospheres-Chemistry, Formation Conditions, and Habitability. *Space Sci. Rev.*.

Madhusudhan, N., Amin, M. A., and Kennedy, G. M. (2014a). Toward Chemical Constraints on Hot Jupiter Migration. *ApJ*, 794:L12.

Madhusudhan, N., Apai, D., and Gandhi, S. (2016b). Atmospheric Compositions of Three Brown Dwarfs and Implications for their Formation Conditions. *ArXiv e-prints*.

Madhusudhan, N., Bitsch, B., Johansen, A., and Eriksson, L. (2017). Atmospheric signatures of giant exoplanet formation by pebble accretion. *MNRAS*, 469:4102–4115.

Madhusudhan, N., Burrows, A., and Currie, T. (2011a). Model Atmospheres for Massive Gas Giants with Thick Clouds: Application to the HR 8799 Planets and Predictions for Future Detections. *ApJ*, 737:34.

Madhusudhan, N., Crouzet, N., McCullough, P. R., Deming, D., and Hedges, C. (2014b). H_2O Abundances in the Atmospheres of Three Hot Jupiters. *ApJ*, 791:L9.

Madhusudhan, N., Harrington, J., Stevenson, K. B., Nymeyer, S., Campo, C. J., Wheatley, P. J., Deming, D., Blecic, J., Hardy, R. A., Lust, N. B., Anderson, D. R., Collier-Cameron, A., Britt, C. B. T., Bowman, W. C., Hebb, L., Hellier, C., Maxted, P. F. L., Pollacco, D., and West, R. G. (2011b). A high C/O ratio and weak thermal inversion in the atmosphere of exoplanet WASP-12b. *Nature*, 469:64–67.

Madhusudhan, N. and Redfield, S. (2015). Optimal measures for characterizing water-rich super-Earths. *International Journal of Astrobiology*, 14:177–189.

Madhusudhan, N. and Seager, S. (2009). A Temperature and Abundance Retrieval Method for Exoplanet Atmospheres. *ApJ*, 707:24–39.

Madhusudhan, N. and Seager, S. (2011). High Metallicity and Non-equilibrium Chemistry in the Dayside Atmosphere of hot-Neptune GJ 436b. *ApJ*, 729:41.

Majeau, C., Agol, E., and Cowan, N. B. (2012). A Two-dimensional Infrared Map of the Extrasolar Planet HD 189733b. *ApJ*, 747:L20.

Mancini, L., Ciceri, S., Chen, G., Tregloan-Reed, J., Fortney, J. J., Southworth, J., Tan, T. G., Burgdorf, M., Calchi Novati, S., Dominik, M., Fang, X.-S., Finet, F., Gerner, T., Hardis, S., Hinse, T. C., Jørgensen, U. G., Liebig, C., Nikolov, N., Ricci, D., Schäfer, S., Schönebeck, F., Skottfelt, J., Wertz, O., Alsubai, K. A., Bozza, V., Browne, P., Dodds, P., Gu, S.-H., Harpsøe, K., Henning, T., Hundertmark, M., Jessen-Hansen, J., Kains, N., Kerins, E., Kjeldsen, H., Lund, M. N., Lundkvist, M., Madhusudhan, N., Mathiasen, M., Penny, M. T., Prof, S., Rahvar, S., Sahu, K., Scarpetta, G., Snodgrass, C., and Surdej, J. (2013). Physical properties, transmission and emission spectra of the WASP-19 planetary system from multi-colour photometry. *MNRAS*, 436:2–18.

Mancini, L., Southworth, J., Ciceri, S., Tregloan-Reed, J., Crossfield, I., Nikolov, N., Bruni, I., Zambelli, R., and Henning, T. (2014). Physical properties, starspot activity, orbital obliquity and transmission spectrum of the Qatar-2 planetary system from multicolour photometry. *MNRAS*, 443:2391–2409.

Manjavacas, E., Apai, D., Zhou, Y., Karalidi, T., Lew, B. W. P., Schneider, G., Cowan, N., Metchev, S., Miles-Páez, P. A., Burgasser, A. J., Radigan, J., Bedin, L. R., Lowrance, P. J., and Marley, M. S. (2018). Cloud Atlas: Discovery of Rotational Spectral Modulations in a Low-mass, L-type Brown Dwarf Companion to a Star. *AJ*, 155:11.

Marley, M. S., Ackerman, A. S., Cuzzi, J. N., and Kitzmann, D. (2013). *Clouds and Hazes in Exoplanet Atmospheres*, pages 367–391. University of Arizona Press.

Marley, M. S., Gelino, C., Stephens, D., Lunine, J. I., and Freedman, R. (1999). Reflected Spectra and Albedos of Extrasolar Giant Planets. I. Clear and Cloudy Atmospheres. *ApJ*, 513:879–893.

Marois, C., Lafrenière, D., Doyon, R., Macintosh, B., and Nadeau, D. (2006). Angular Differential Imaging: A Powerful High-Contrast Imaging Technique. *ApJ*, 641:556–564.

Marois, C., Macintosh, B., Barman, T., Zuckerman, B., Song, I., Patience, J., Lafrenière, D., and Doyon, R. (2008). Direct Imaging of Multiple Planets Orbiting the Star HR 8799. *Science*, 322:1348.

Marois, C., Zuckerman, B., Konopacky, Q. M., Macintosh, B., and Barman, T. (2010). Images of a fourth planet orbiting HR 8799. *Nature*, 468:1080–1083.

Mayer, L., Quinn, T., Wadsley, J., and Stadel, J. (2004). The Evolution of Gravitationally Unstable Protoplanetary Disks: Fragmentation and Possible Giant Planet Formation. *ApJ*, 609:1045–1064.

Mayne, N. J., Baraffe, I., Acreman, D. M., Smith, C., Browning, M. K., Skålid Amundsen, D., Wood, N., Thuburn, J., and Jackson, D. R. (2014). The unified model, a fully-compressible, non-hydrostatic, deep atmosphere global circulation model, applied to hot Jupiters. ENDGame for a HD 209458b test case. *A&A*, 561:A1.

Mayor, M. and Queloz, D. (1995). A Jupiter-mass companion to a solar-type star. *Nature*, 378:355–359.

McCullough, P. R., Crouzet, N., Deming, D., and Madhusudhan, N. (2014). Water Vapor in the Spectrum of the Extrasolar Planet HD 189733b. I. The Transit. *ApJ*, 791:55.

McQuillan, A., Mazeh, T., and Aigrain, S. (2014). Rotation Periods of 34,030 Kepler Main-sequence Stars: The Full Autocorrelation Sample. *ApJS*, 211:24.

Mengel, M. W., Marsden, S. C., Carter, B. D., Horner, J., King, R., Fares, R., Jeffers, S. V., Petit, P., Vidotto, A. A., Morin, J., and BCool Collaboration (2017). A BCool survey of the magnetic fields of planet-hosting solar-type stars. *MNRAS*, 465:2734–2747.

Menou, K. (2012). Thermo-resistive Instability of Hot Planetary Atmospheres. *ApJ*, 754:L9.

Meru, F. and Bate, M. R. (2010). Exploring the conditions required to form giant planets via gravitational instability in massive protoplanetary discs. *MNRAS*, 406:2279–2288.

Metcalfe, T. S., Buccino, A. P., Brown, B. P., Mathur, S., Soderblom, D. R., Henry, T. J., Mauas, P. J. D., Petrucci, R., Hall, J. C., and Basu, S. (2013). Magnetic Activity Cycles in the Exoplanet Host Star epsilon Eridani. *ApJ*, 763:L26.

Miguel, Y. and Kaltenegger, L. (2014). Exploring Atmospheres of Hot Mini-Neptunes and Extrasolar Giant Planets Orbiting Different Stars with Application to HD 97658b, WASP-12b, CoRoT-2b, XO-1b, and HD 189733b. *ApJ*, 780:166.

MIT Dynamics Lecture (2018). Other Coordinate Systems. `https://ocw.mit.edu/courses/aeronautics-and-astronautics/16-07-dynamics-fall-2009/lecture-notes/MIT16_07F09_Lec05.pdf`.

Mollière, P., van Boekel, R., Bouwman, J., Henning, T., Lagage, P.-O., and Min, M. (2017). Observing transiting planets with JWST. Prime targets and their synthetic spectral observations. *A&A*, 600:A10.

Mollière, P., van Boekel, R., Dullemond, C., Henning, T., and Mordasini, C. (2015). Model Atmospheres of Irradiated Exoplanets: The Influence of Stellar Parameters, Metallicity, and the C/O Ratio. *ApJ*, 813:47.

Mordasini, C., Mollière, P., Dittkrist, K.-M., Jin, S., and Alibert, Y. (2015). Global models of planet formation and evolution. *International Journal of Astrobiology*, 14:201–232.

Mordasini, C., van Boekel, R., Mollière, P., Henning, T., and Benneke, B. (2016). The Imprint of Exoplanet Formation History on Observable Present-day Spectra of Hot Jupiters. *ApJ*, 832:41.

Moses, J. I. (2014). Chemical kinetics on extrasolar planets. *Philosophical Transactions of the Royal Society of London Series A*, 372:20130073–20130073.

Moses, J. I., Madhusudhan, N., Visscher, C., and Freedman, R. S. (2013). Chemical Consequences of the C/O Ratio on Hot Jupiters: Examples from WASP-12b, CoRoT-2b, XO-1b, and HD 189733b. *ApJ*, 763:25.

Moses, J. I., Visscher, C., Fortney, J. J., Showman, A. P., Lewis, N. K., Griffith, C. A., Klippenstein, S. J., Shabram, M., Friedson, A. J., Marley, M. S., and Freedman, R. S. (2011). Disequilibrium Carbon, Oxygen, and Nitrogen Chemistry in the Atmospheres of HD 189733b and HD 209458b. *ApJ*, 737:15.

Mousis, O., Lunine, J. I., Madhusudhan, N., and Johnson, T. V. (2012). Nebular Water Depletion as the Cause of Jupiter's Low Oxygen Abundance. *ApJ*, 751:L7.

Moya, A., Amado, P. J., Barrado, D., García Hernández, A., Aberasturi, M., Montesinos, B., and Aceituno, F. (2010). Age determination of the HR8799 planetary system using asteroseismology. *MNRAS*, 405:L81–L85.

Nakajima, T., Oppenheimer, B. R., Kulkarni, S. R., Golimowski, D. A., Matthews, K., and Durrance, S. T. (1995). Discovery of a cool brown dwarf. *Nature*, 378:463–465.

Nelson, B. E., Ford, E. B., and Rasio, F. A. (2017). Evidence for Two Hot-Jupiter Formation Paths. *AJ*, 154:106.

Nettelmann, N., Becker, A., Holst, B., and Redmer, R. (2012). Jupiter Models with Improved Ab Initio Hydrogen Equation of State (H-REOS.2). *ApJ*, 750:52.

Newton, E. R., Irwin, J., Charbonneau, D., Berta-Thompson, Z. K., Dittmann, J. A., and West, A. A. (2016). The Rotation and Galactic Kinematics of Mid M Dwarfs in the Solar Neighborhood. *ApJ*, 821:93.

Nikolov, N., Sing, D. K., Burrows, A. S., Fortney, J. J., Henry, G. W., Pont, F., Ballester, G. E., Aigrain, S., Wilson, P. A., Huitson, C. M., Gibson, N. P., Désert, J.-M., Lecavelier Des Etangs, A., Showman, A. P., Vidal-Madjar, A., Wakeford, H. R., and Zahnle, K. (2015). HST hot-Jupiter transmission spectral survey: haze in the atmosphere of WASP-6b. *MNRAS*, 447:463–478.

Nikolov, N., Sing, D. K., Fortney, J. J., Goyal, J. M., Drummond, B., Evans, T. M., Gibson, N. P., De Mooij, E. J. W., Rustamkulov, Z., Wakeford, H. R., Smalley, B., Burgasser, A. J., Hellier, C., Helling, C., Mayne, N. J., Madhusudhan, N., Kataria, T., Baines, J., Carter, A. L., Ballester, G. E., Barstow, J. K., McCleery, J., and Spake, J. J. (2018). An absolute sodium abundance for a cloud-free 'hot Saturn' exoplanet. *Nature*, 557:526–529.

Nikolov, N., Sing, D. K., Pont, F., Burrows, A. S., Fortney, J. J., Ballester, G. E., Evans, T. M., Huitson, C. M., Wakeford, H. R., Wilson, P. A., Aigrain, S., Deming, D., Gibson, N. P., Henry, G. W., Knutson, H., Lecavelier des Etangs, A., Showman, A. P., Vidal-Madjar, A., and Zahnle, K. (2014). Hubble Space Telescope hot Jupiter transmission spectral survey: a detection of Na and strong optical absorption in HAT-P-1b. *MNRAS*, 437:46–66.

Norris, C. M., Beeck, B., Unruh, Y. C., Solanki, S. K., Krivova, N. A., and Yeo, K. L. (2017). Spectral variability of photospheric radiation due to faculae. I. The Sun and Sun-like stars. *A&A*, 605:A45.

Noyes, R. W., Hartmann, L. W., Baliunas, S. L., Duncan, D. K., and Vaughan, A. H. (1984). Rotation, convection, and magnetic activity in lower main-sequence stars. *ApJ*, 279:763–777.

Nymeyer, S., Harrington, J., Hardy, R. A., Stevenson, K. B., Campo, C. J., Madhusudhan, N., Collier-Cameron, A., Loredo, T. J., Blecic, J., Bowman, W. C., Britt, C. B. T., Cubillos, P., Hellier, C., Gillon, M., Maxted, P. F. L., Hebb, L., Wheatley, P. J., Pollacco, D., and Anderson, D. R. (2011). Spitzer Secondary Eclipses of WASP-18b. *ApJ*, 742:35.

Öberg, K. I., Murray-Clay, R., and Bergin, E. A. (2011). The Effects of Snowlines on C/O in Planetary Atmospheres. *ApJ*, 743:L16.

Opik, E. J. (1958). *Physics of meteor flight in the atmosphere.* John Wiley & Sons Inc.

Oppenheimer, B. R., Kulkarni, S. R., Matthews, K., and Nakajima, T. (1995). Infrared Spectrum of the Cool Brown Dwarf Gl 229B. *Science*, 270:1478–1479.

Oreshenko, M., Lavie, B., Grimm, S. L., Tsai, S.-M., Malik, M., Demory, B.-O., Mordasini, C., Alibert, Y., Benz, W., Quanz, S. P., Trotta, R., and Heng, K. (2017). Retrieval Analysis of the Emission Spectrum of WASP-12b: Sensitivity of Outcomes to Prior Assumptions and Implications for Formation History. *ApJ*, 847:L3.

Oshagh, M., Santos, N. C., Ehrenreich, D., Haghighipour, N., Figueira, P., Santerne, A., and Montalto, M. (2014). Impact of occultations of stellar active regions on transmission spectra. Can occultation of a plage mimic the signature of a blue sky? *A&A*, 568:A99.

Owen, T., Mahaffy, P., Niemann, H. B., Atreya, S., Donahue, T., Bar-Nun, A., and de Pater, I. (1999). A low-temperature origin for the planetesimals that formed Jupiter. *Nature*, 402:269–270.

Parmentier, V., Showman, A. P., and Lian, Y. (2013). 3D mixing in hot Jupiters atmospheres. I. Application to the day/night cold trap in HD 209458b. *A&A*, 558:A91.

Paunzen, E., Iliev, I. K., Kamp, I., and Barzova, I. S. (2002). The status of Galactic field λ Bootis stars in the post-Hipparcos era. *MNRAS*, 336:1030–1042.

Perryman, M. (2011). *The Exoplanet Handbook*. Cambridge University Press.

Petit, P., Donati, J.-F., Wade, G. A., Landstreet, J. D., Bagnulo, S., Lüftinger, T., Sigut, T. A. A., Shorlin, S. L. S., Strasser, S., Aurière, M., and Oliveira, J. M. (2004). Magnetic topology and surface differential rotation on the K1 subgiant of the RS CVn system HR 1099. *MNRAS*, 348:1175–1190.

Petrovic, S. T., Markovic, S., and Pavlovic, Z. A. (2003). Mechanical properties of ice and snow. *Journal of Materials Science*, 38:3263–3268.

Pinhas, A. and Madhusudhan, N. (2017). On signatures of clouds in exoplanetary transit spectra. *MNRAS*, 471:4355–4373.

Pinhas, A., Madhusudhan, N., and Clarke, C. (2016). Efficiency of planetesimal ablation in giant planetary envelopes. *MNRAS*, 463:4516–4532.

Pinhas, A., Madhusudhan, N., Gandhi, S., and MacDonald, R. (2019). H_2O abundances and cloud properties in ten hot giant exoplanets. *MNRAS*, 482:1485–1498.

Pinhas, A., Rackham, B. V., Madhusudhan, N., and Apai, D. (2018). Retrieval of planetary and stellar properties in transmission spectroscopy with AURA. *MNRAS*, 480:5314–5331.

Piso, A.-M. A., Pegues, J., and Öberg, K. I. (2016). The Role of Ice Compositions for Snowlines and the C/N/O Ratios in Active Disks. *ApJ*, 833:203.

Podolak, M., Pollack, J. B., and Reynolds, R. T. (1988). Interactions of planetesimals with protoplanetary atmospheres. *Icarus*, 73:163–179.

Pollack, J. B., Hubickyj, O., Bodenheimer, P., Lissauer, J. J., Podolak, M., and Greenzweig, Y. (1996). Formation of the Giant Planets by Concurrent Accretion of Solids and Gas. *Icarus*, 124:62–85.

Pond, J. W. T., Palotai, C., Gabriel, T., Korycansky, D. G., Harrington, J., and Rebeli, N. (2012). Numerical Modeling of the 2009 Impact Event on Jupiter. *ApJ*, 745:113.

Pont, F., Knutson, H., Gilliland, R. L., Moutou, C., and Charbonneau, D. (2008). Detection of atmospheric haze on an extrasolar planet: the 0.55-1.05 μm transmission spectrum of HD 189733b with the HubbleSpaceTelescope. *MNRAS*, 385:109–118.

Pont, F., Sing, D. K., Gibson, N. P., Aigrain, S., Henry, G., and Husnoo, N. (2013). The prevalence of dust on the exoplanet HD 189733b from Hubble and Spitzer observations. *MNRAS*, 432:2917–2944.

Press, W. H., Teukolsky, S. A., Vetterling, W. T., and Flannery, B. P. (1992). *Numerical recipes in C. The art of scientific computing*.

Pudritz, R. E., Cridland, A. J., and Alessi, M. (2018). *Connecting Planetary Composition with Formation*, page 144.

Pueyo, L., Soummer, R., Hoffmann, J., Oppenheimer, R., Graham, J. R., Zimmerman, N., Zhai, C., Wallace, J. K., Vescelus, F., Veicht, A., Vasisht, G., Truong, T., Sivaramakrishnan, A., Shao, M., Roberts, Jr., L. C., Roberts, J. E., Rice, E., Parry, I. R., Nilsson, R., Lockhart, T., Ligon, E. R., King, D., Hinkley, S., Hillenbrand, L., Hale, D., Dekany, R., Crepp, J. R., Cady, E., Burruss, R., Brenner, D., Beichman, C., and Baranec, C. (2015). Reconnaissance of the HR 8799 Exosolar System. II. Astrometry and Orbital Motion. *ApJ*, 803:31.

Rackham, B., Espinoza, N., Apai, D., López-Morales, M., Jordán, A., Osip, D. J., Lewis, N. K., Rodler, F., Fraine, J. D., Morley, C. V., and Fortney, J. J. (2017). ACCESS I: An Optical Transmission Spectrum of GJ 1214b Reveals a Heterogeneous Stellar Photosphere. *ApJ*, 834:151.

Rackham, B. V., Apai, D., and Giampapa, M. S. (2018a). The Transit Light Source Effect: False Spectral Features and Incorrect Densities for M-dwarf Transiting Planets. *ApJ*, 853:122.

Rackham, B. V., Apai, D., and Giampapa, M. S. (2018b). The Transit Light Source Effect II: The Impact of Stellar Heterogeneity on Transmission Spectra of Planets Orbiting Broadly Sun-like Stars. *arXiv e-prints*.

Rasio, F. A. and Ford, E. B. (1996). Dynamical instabilities and the formation of extrasolar planetary systems. *Science*, 274:954–956.

Recktenwald, G. W. (2011). Finite-difference approximations to the diffusion equation. [Online; posted 6-March-2011].

Rice, W. K. M., Lodato, G., Pringle, J. E., Armitage, P. J., and Bonnell, I. A. (2004). Accelerated planetesimal growth in self-gravitating protoplanetary discs. *MNRAS*, 355:543–552.

Richard, C., Gordon, I. E., Rothman, L. S., Abel, M., Frommhold, L., Gustafsson, M., Hartmann, J.-M., Hermans, C., Lafferty, W. J., Orton, G. S., Smith, K. M., and Tran, H. (2012). New section of the HITRAN database: Collision-induced absorption (CIA). *J. Quant. Spec. Radiat. Transf.*, 113:1276–1285.

Robinson, T. D. and Catling, D. C. (2014). Common 0.1bar tropopause in thick atmospheres set by pressure-dependent infrared transparency. *Nature Geoscience*, 7:12–15.

Rodgers, C. D. (2000). *Inverse Methods for Atmospheric Sounding: Theory and Practice*. World Scientific Publishing Co.

Rosén, L. and Kochukhov, O. (2012). How reliable is Zeeman Doppler imaging without simultaneous temperature reconstruction? *A&A*, 548:A8.

Rothman, L. S., Gordon, I. E., Barber, R. J., Dothe, H., Gamache, R. R., Goldman, A., Perevalov, V. I., Tashkun, S. A., and Tennyson, J. (2010). HITEMP, the high-temperature molecular spectroscopic database. *J. Quant. Spec. Radiat. Transf.*, 111:2139–2150.

Sachs, A. (1974). Babylonian Observational Astronomy. *Philosophical Transactions of the Royal Society of London Series A*, 276:43–50.

Sadakane, K. (2006). λ Bootis-Like Abundances in the Vega-Like, γ Doradus Type-Pulsator HD 218396. *PASJ*, 58:1023–1032.

Sallum, S., Follette, K. B., Eisner, J. A., Close, L. M., Hinz, P., Kratter, K., Males, J., Skemer, A., Macintosh, B., Tuthill, P., Bailey, V., Defrère, D., Morzinski, K., Rodigas, T., Spalding, E., Vaz, A., and Weinberger, A. J. (2015). Accreting protoplanets in the LkCa 15 transition disk. *Nature*, 527:342–344.

Salpeter, E. E. (1973). On Convection and Gravitational Layering in Jupiter and in Stars of Low Mass. *ApJ*, 181:L83.

Sánchez-Lavega, A., Pérez-Hoyos, S., and Hueso, R. (2004). Clouds in planetary atmospheres: A useful application of the Clausius-Clapeyron equation. *American Journal of Physics*, 72:767–774.

Schuerman, D. W. (1980). *Light scattering by irregularly shaped particles. Conference held at Albany, N.Y., USA, 5 - 7 June 1979.* Springer US.

Seager, S. (2010). *Exoplanet Atmospheres: Physical Processes*. Princeton University Press.

Seager, S., Deming, D., and Valenti, J. A. (2009). Transiting Exoplanets with JWST. *Astrophysics and Space Science Proceedings*, 10:123.

Seager, S., Richardson, L. J., Hansen, B. M. S., Menou, K., Cho, J. Y.-K., and Deming, D. (2005). On the Dayside Thermal Emission of Hot Jupiters. *ApJ*, 632:1122–1131.

Seager, S. and Sasselov, D. D. (2000). Theoretical Transmission Spectra during Extrasolar Giant Planet Transits. *ApJ*, 537:916–921.

Sedaghati, E., Boffin, H. M. J., MacDonald, R. J., Gandhi, S., Madhusudhan, N., Gibson, N. P., Oshagh, M., Claret, A., and Rauer, H. (2017). Detection of titanium oxide in the atmosphere of a hot Jupiter. *Nature*, 549:238–241.

Seiff, A. and Kirk, D. B. (1982). Structure of the Venus mesosphere and lower thermosphere from measurements during entry of the Pioneer Venus probes. *Icarus*, 49:49–70.

Seiff, A., Kirk, D. B., Knight, T. C. D., Young, R. E., Mihalov, J. D., Young, L. A., Milos, F. S., Schubert, G., Blanchard, R. C., and Atkinson, D. (1998). Thermal structure of Jupiter's atmosphere near the edge of a 5-μm hot spot in the north equatorial belt. *J. Geophys. Res.*, 103:22857–22890.

Shallue, C. J. and Vanderburg, A. (2018). Identifying Exoplanets with Deep Learning: A Five-planet Resonant Chain around Kepler-80 and an Eighth Planet around Kepler-90. *AJ*, 155:94.

Shapiro, A. I., Solanki, S. K., Krivova, N. A., Schmutz, W. K., Ball, W. T., Knaack, R., Rozanov, E. V., and Unruh, Y. C. (2014). Variability of Sun-like stars: reproducing observed photometric trends. *A&A*, 569:A38.

Sharp, C. M. and Huebner, W. F. (1990). Molecular equilibrium with condensation. *ApJS*, 72:417–431.

Sheppard, K. B., Mandell, A. M., Tamburo, P., Gandhi, S., Pinhas, A., Madhusudhan, N., and Deming, D. (2017). Evidence for a Dayside Thermal Inversion and High Metallicity for the Hot Jupiter WASP-18b. *ApJ*, 850:L32.

Showman, A. P., Fortney, J. J., Lian, Y., Marley, M. S., Freedman, R. S., Knutson, H. A., and Charbonneau, D. (2009). Atmospheric Circulation of Hot Jupiters: Coupled Radiative-Dynamical General Circulation Model Simulations of HD 189733b and HD 209458b. *ApJ*, 699:564–584.

Silva, A. V. R. (2003). Method for Spot Detection on Solar-like Stars. *ApJ*, 585:L147–L150.

Sing, D. K., Fortney, J. J., Nikolov, N., Wakeford, H. R., Kataria, T., Evans, T. M., Aigrain, S., Ballester, G. E., Burrows, A. S., Deming, D., Désert, J.-M., Gibson, N. P., Henry, G. W., Huitson, C. M., Knutson, H. A., Lecavelier Des Etangs, A., Pont, F., Showman, A. P., Vidal-Madjar, A., Williamson, M. H., and Wilson, P. A. (2016). A continuum from clear to cloudy hot-Jupiter exoplanets without primordial water depletion. *Nature*, 529:59–62.

Sing, D. K., Huitson, C. M., Lopez-Morales, M., Pont, F., Désert, J.-M., Ehrenreich, D., Wilson, P. A., Ballester, G. E., Fortney, J. J., Lecavelier des Etangs, A., and Vidal-Madjar, A. (2012). GTC OSIRIS transiting exoplanet atmospheric survey: detection of sodium in XO-2b from differential long-slit spectroscopy. *MNRAS*, 426:1663–1670.

Sing, D. K., Lecavelier des Etangs, A., Fortney, J. J., Burrows, A. S., Pont, F., Wakeford, H. R., Ballester, G. E., Nikolov, N., Henry, G. W., Aigrain, S., Deming, D., Evans, T. M., Gibson, N. P., Huitson, C. M., Knutson, H., Showman, A. P., Vidal-Madjar, A., Wilson, P. A., Williamson, M. H., and Zahnle, K. (2013). HST hot-Jupiter transmission spectral survey: evidence for aerosols and lack of TiO in the atmosphere of WASP-12b. *MNRAS*, 436:2956–2973.

Sing, D. K., Pont, F., Aigrain, S., Charbonneau, D., Désert, J.-M., Gibson, N., Gilliland, R., Hayek, W., Henry, G., Knutson, H., Lecavelier Des Etangs, A., Mazeh, T., and Shporer, A. (2011). Hubble Space Telescope transmission spectroscopy of the exoplanet HD 189733b: high-altitude atmospheric haze in the optical and near-ultraviolet with STIS. *MNRAS*, 416:1443–1455.

Skemer, A. J., Hinz, P. M., Esposito, S., Burrows, A., Leisenring, J., Skrutskie, M., Desidera, S., Mesa, D., Arcidiacono, C., Mannucci, F., Rodigas, T. J., Close, L., McCarthy, D., Kulesa, C., Agapito, G., Apai, D., Argomedo, J., Bailey, V., Boutsia, K., Briguglio, R., Brusa, G., Busoni, L., Claudi, R., Eisner, J., Fini, L., Follette, K. B., Garnavich, P., Gratton, R., Guerra, J. C., Hill, J. M., Hoffmann, W. F., Jones, T., Krejny, M., Males, J., Masciadri, E., Meyer, M. R., Miller, D. L., Morzinski, K., Nelson, M., Pinna, E., Puglisi, A., Quanz, S. P., Quiros-Pacheco, F., Riccardi, A., Stefanini, P., Vaitheeswaran, V., Wilson, J. C., and Xompero, M. (2012). First Light LBT AO Images of HR 8799 bcde at 1.6 and 3.3 μm: New Discrepancies between Young Planets and Old Brown Dwarfs. *ApJ*, 753:14.

Skilling, J. (2004). Nested Sampling. In Fischer, R., Preuss, R., and Toussaint, U. V., editors, *American Institute of Physics Conference Series*, volume 735 of *American Institute of Physics Conference Series*, pages 395–405.

Skilling, J. (2006). Nested sampling for general Bayesian computation. *Bayesian Anal.*

Soderblom, D. R. (2010). The Ages of Stars. *ARA&A*, 48:581–629.

Southworth, J., Mancini, L., Tregloan-Reed, J., Calchi Novati, S., Ciceri, S., D'Ago, G., Delrez, L., Dominik, M., Evans, D. F., Gillon, M., Jehin, E., Jørgensen, U. G., Haugbølle, T., Lendl, M., Arena, C., Barbieri, L., Barbieri, M., Corfini, G., Lopresti, C., Marchini, A., Marino, G., Alsubai, K. A., Bozza, V., Bramich, D. M., Jaimes, R. F., Hinse, T. C., Henning, T., Hundertmark, M., Juncher, D., Korhonen, H., Popovas, A., Rabus, M., Rahvar, S., Schmidt, R. W., Skottfelt, J., Snodgrass, C., Starkey, D., Surdej, J., and Wertz, O. (2015). Larger and faster: revised properties and a shorter orbital period for the WASP-57 planetary system from a pro-am collaboration. *MNRAS*, 454:3094–3107.

Southworth, J., Tregloan-Reed, J., Pinhas, A., Madhusudhan, N., Mancini, L., and Smith, A. (2018). Physical properties and optical-infrared transmission spectrum of the giant planet XO-1b. *MNRAS*, 481:4261.

Spiegel, D. S., Silverio, K., and Burrows, A. (2009). Can TiO Explain Thermal Inversions in the Upper Atmospheres of Irradiated Giant Planets? *ApJ*, 699:1487–1500.

Stevenson, K. B. (2016). Quantifying and Predicting the Presence of Clouds in Exoplanet Atmospheres. *ApJ*, 817:L16.

Strassmeier, K. G. (1999). Doppler imaging of stellar surface structure. XI. The super starspots on the K0 giant HD 12545: larger than the entire Sun. *A&A*, 347:225–234.

Su, K. Y. L., Rieke, G. H., Stapelfeldt, K. R., Malhotra, R., Bryden, G., Smith, P. S., Misselt, K. A., Moro-Martin, A., and Williams, J. P. (2009). The Debris Disk Around HR 8799. *ApJ*, 705:314–327.

Sudarsky, D., Burrows, A., and Pinto, P. (2000). Albedo and Reflection Spectra of Extrasolar Giant Planets. *ApJ*, 538:885–903.

Sudol, J. J. and Haghighipour, N. (2012). High-mass, Four-planet Configurations for HR 8799: Constraining the Orbital Inclination and Age of the System. *ApJ*, 755:38.

Svetsov, V. V., Nemtchinov, I. V., and Teterev, A. V. (1995). Disintegration of large meteoroids in Earth's atmosphere: Theoretical models. *Icarus*, 116:131–153.

Tennyson, J., Yurchenko, S. N., Al-Refaie, A. F., Barton, E. J., Chubb, K. L., Coles, P. A., Diamantopoulou, S., Gorman, M. N., Hill, C., Lam, A. Z., Lodi, L., McKemmish, L. K., Na, Y., Owens, A., Polyansky, O. L., Rivlin, T., Sousa-Silva, C., Underwood, D. S., Yachmenev, A., and Zak, E. (2016). The ExoMol database: Molecular line lists for exoplanet and other hot atmospheres. *Journal of Molecular Spectroscopy*, 327:73–94.

Teske, J. K., Cunha, K., Smith, V. V., Schuler, S. C., and Griffith, C. A. (2014). C/O Ratios of Stars with Transiting Hot Jupiter Exoplanets. *ApJ*, 788:39.

Todorov, K. O., Line, M. R., Pineda, J. E., Meyer, M. R., Quanz, S. P., Hinkley, S., and Fortney, J. J. (2016). The Water Abundance of the Directly Imaged Substellar Companion κ And b Retrieved from a Near Infrared Spectrum. *ApJ*, 823:14.

Traub, W. A. and Oppenheimer, B. R. (2010). *Direct Imaging of Exoplanets*, pages 111–156. University of Arizona Press.

Tregloan-Reed, J., Southworth, J., Mancini, L., Mollière, P., Ciceri, S., Bruni, I., Ricci, D., Ayala-Loera, C., and Henning, T. (2018). Possible detection of a bimodal cloud distribution in the atmosphere of HAT-P-32 A b from multiband photometry. *MNRAS*, 474:5485–5499.

Triaud, A. H. M. J. (2017). *The Rossiter-McLaughlin Effect in Exoplanet Research*, page 2.

Trotta, R. (2008). Bayes in the sky: Bayesian inference and model selection in cosmology. *Contemporary Physics*, 49:71–104.

Tsiaras, A., Waldmann, I. P., Zingales, T., Rocchetto, M., Morello, G., Damiano, M., Karpouzas, K., Tinetti, G., McKemmish, L. K., Tennyson, J., and Yurchenko, S. N. (2018). A Population Study of Gaseous Exoplanets. *AJ*, 155:156.

Turrini, D., Nelson, R. P., and Barbieri, M. (2015). The role of planetary formation and evolution in shaping the composition of exoplanetary atmospheres. *Experimental Astronomy*, 40:501–522.

Vahidinia, S., Cuzzi, J. N., Marley, M., and Fortney, J. (2014). Cloud Base Signature in Transmission Spectra of Exoplanet Atmospheres. *ApJ*, 789:L11.

Valletta, C. and Helled, R. (2018). The distribution of heavy-elements in giant protoplanetary atmospheres: the importance of planetesimal-envelope interactions. *arXiv e-prints*.

van Dam, M. A., Bouchez, A. H., Le Mignant, D., Johansson, E. M., Wizinowich, P. L., Campbell, R. D., Chin, J. C. Y., Hartman, S. K., Lafon, R. E., Stomski, Jr., P. J., and Summers, D. M. (2006). The W. M. Keck Observatory Laser Guide Star Adaptive Optics System: Performance Characterization. *PASP*, 118:310–318.

Van de Hulst, H. C. (2003). *Light Scattering by Small Particles*. Dover Publications Inc.

Vanderburg, A., Johnson, J. A., Rappaport, S., Bieryla, A., Irwin, J., Lewis, J. A., Kipping, D., Brown, W. R., Dufour, P., Ciardi, D. R., Angus, R., Schaefer, L., Latham, D. W., Charbonneau, D., Beichman, C., Eastman, J., McCrady, N., Wittenmyer, R. A., and Wright, J. T. (2015). A disintegrating minor planet transiting a white dwarf. *Nature*, 526:546–549.

Venot, O. and Agúndez, M. (2015). Chemical modeling of exoplanet atmospheres. *Experimental Astronomy*, 40:469–480.

Vidal-Madjar, A., Désert, J.-M., Lecavelier des Etangs, A., Hébrard, G., Ballester, G. E., Ehrenreich, D., Ferlet, R., McConnell, J. C., Mayor, M., and Parkinson, C. D. (2004). Detection of Oxygen and Carbon in the Hydrodynamically Escaping Atmosphere of the Extrasolar Planet HD 209458b. *ApJ*, 604:L69–L72.

Vogt, S. S. and Penrod, G. D. (1983). Doppler Imaging of spotted stars - Application to the RS Canum Venaticorum star HR 1099. *PASP*, 95:565–576.

von Zahn, U. and Hunten, D. M. (1996). The Helium Mass Fraction in Jupiter's Atmosphere. *Science*, 272:849–851.

Wakeford, H. R. and Sing, D. K. (2015). Transmission spectral properties of clouds for hot Jupiter exoplanets. *A&A*, 573:A122.

Wakeford, H. R., Sing, D. K., Deming, D., Gibson, N. P., Fortney, J. J., Burrows, A. S., Ballester, G., Nikolov, N., Aigrain, S., Henry, G., Knutson, H., Lecavelier des Etangs, A., Pont, F., Showman, A. P., Vidal-Madjar, A., and Zahnle, K. (2013). HST hot Jupiter transmission spectral survey: detection of water in HAT-P-1b from WFC3 near-IR spatial scan observations. *MNRAS*, 435:3481–3493.

Wakeford, H. R., Sing, D. K., Deming, D., Lewis, N. K., Goyal, J., Wilson, T. J., Barstow, J., Kataria, T., Drummond, B., Evans, T. M., Carter, A. L., Nikolov, N., Knutson, H. A., Ballester, G. E., and Mandell, A. M. (2018). The Complete Transmission Spectrum of WASP-39b with a Precise Water Constraint. *AJ*, 155:29.

Wakeford, H. R., Sing, D. K., Kataria, T., Deming, D., Nikolov, N., Lopez, E. D., Tremblin, P., Amundsen, D. S., Lewis, N. K., Mandell, A. M., Fortney, J. J., Knutson, H., Benneke, B., and Evans, T. M. (2017). HAT-P-26b: A Neptune-mass exoplanet with a well-constrained heavy element abundance. *Science*, 356:628–631.

Waldmann, I. P., Rocchetto, M., Tinetti, G., Barton, E. J., Yurchenko, S. N., and Tennyson, J. (2015a). Tau-REx II: Retrieval of Emission Spectra. *ApJ*, 813:13.

Waldmann, I. P., Tinetti, G., Rocchetto, M., Barton, E. J., Yurchenko, S. N., and Tennyson, J. (2015b). Tau-REx I: A Next Generation Retrieval Code for Exoplanetary Atmospheres. *ApJ*, 802:107.

Watanabe, M., Takami, H., Takato, N., Colley, S., Eldred, M., Kane, T., Guyon, O., Hattori, M., Goto, M., Iye, M., Hayano, Y., Kamata, Y., Arimoto, N., Kobayashi, N., and Minowa, Y. (2004). Design of the Subaru laser guide star adaptive optics module. In Bonaccini Calia, D., Ellerbroek, B. L., and Ragazzoni, R., editors, *Advancements in Adaptive Optics*, volume 5490 of *Proc. SPIE*, pages 1096–1104.

West, R. A., Baines, K. H., Friedson, A. J., Banfield, D., Ragent, B., and Taylor, F. W. (2004). *Jovian clouds and haze*, pages 79–104.

Williams, P. K. G., Charbonneau, D., Cooper, C. S., Showman, A. P., and Fortney, J. J. (2006). Resolving the Surfaces of Extrasolar Planets with Secondary Eclipse Light Curves. *ApJ*, 649:1020–1027.

Witte, S., Helling, C., Barman, T., Heidrich, N., and Hauschildt, P. H. (2011). Dust in brown dwarfs and extra-solar planets. III. Testing synthetic spectra on observations. *A&A*, 529:A44.

Witte, S., Helling, C., and Hauschildt, P. H. (2009). Dust in brown dwarfs and extra-solar planets. II. Cloud formation for cosmologically evolving abundances. *A&A*, 506:1367–1380.

Woitke, P. and Helling, C. (2003). Dust in brown dwarfs. II. The coupled problem of dust formation and sedimentation. *A&A*, 399:297–313.

Woitke, P. and Helling, C. (2004). Dust in brown dwarfs. III. Formation and structure of quasi-static cloud layers. *A&A*, 414:335–350.

Wolszczan, A. and Frail, D. A. (1992). A planetary system around the millisecond pulsar PSR1257 + 12. *Nature*, 355:145–147.

Wolszczan, A. and Kuchner, M. (2010). *Planets Around Pulsars and Other Evolved Stars: The Fates of Planetary Systems*, pages 175–190.

Wong, I., Knutson, H. A., Kataria, T., Lewis, N. K., Burrows, A., Fortney, J. J., Schwartz, J., Shporer, A., Agol, E., Cowan, N. B., Deming, D., Désert, J.-M., Fulton, B. J., Howard, A. W., Langton, J., Laughlin, G., Showman, A. P., and Todorov, K. (2016). 3.6 and 4.5 μm Spitzer Phase Curves of the Highly Irradiated Hot Jupiters WASP-19b and HAT-P-7b. *ApJ*, 823:122.

Wong, M. H., Mahaffy, P. R., Atreya, S. K., Niemann, H. B., and Owen, T. C. (2004). Updated Galileo probe mass spectrometer measurements of carbon, oxygen, nitrogen, and sulfur on Jupiter. *Icarus*, 171:153–170.

Wood, P. L., Maxted, P. F. L., Smalley, B., and Iro, N. (2011). Transmission spectroscopy of the sodium 'D' doublet in WASP-17b with the VLT. *MNRAS*, 412:2376–2382.

Wright, S. A., Larkin, J. E., Moore, A. M., Do, T., Simard, L., Adamkovics, M., Armus, L., Barth, A. J., Barton, E., Boyce, H., Cooke, J., Cote, P., Davidge, T., Ellerbroek, B., Ghez, A. M., Liu, M. C., Lu, J. R., Macintosh, B. A., Mao, S., Marois, C., Schoeck, M., Suzuki, R., Tan, J. C., Treu, T., Wang, L., and Weiss, J. (2014). The infrared imaging spectrograph (IRIS) for TMT: overview of innovative science programs. In *Ground-based and Airborne Instrumentation for Astronomy V*, volume 9147 of *Proc. SPIE*, page 91479S.

Zahnle, K., Marley, M. S., Freedman, R. S., Lodders, K., and Fortney, J. J. (2009). Atmospheric Sulfur Photochemistry on Hot Jupiters. *ApJ*, 701:L20–L24.

Zahnle, K. J. and Marley, M. S. (2014). Methane, Carbon Monoxide, and Ammonia in Brown Dwarfs and Self-Luminous Giant Planets. *ApJ*, 797:41.

Zellem, R. T., Swain, M. R., Roudier, G., Shkolnik, E. L., Creech-Eakman, M. J., Ciardi, D. R., Line, M. R., Iyer, A. R., Bryden, G., Llama, J., and Fahy, K. A. (2017). Forecasting the Impact of Stellar Activity on Transiting Exoplanet Spectra. *ApJ*, 844:27.